Micro- to nanoscale investigation of structures and chemical heterogeneities in geomaterials: Impacts on rheology

Renelle Dubosq

Thesis submitted to the University of Ottawa
in partial fulfillment of the requirements for the
doctoral degree in Earth Sciences

Department of Earth and Environmental Sciences
Faculty of Science
University of Ottawa

Résumé

La présence et les interactions entre les défauts structurels, les fluides et les éléments traces pendant la déformation jouent un rôle essentiel dans la manière dont les matériaux répondent à une contrainte appliquée. Bien que les liens entre les défauts cristallins et la mobilité des éléments traces soient à la frontière de la recherche en sciences de la Terre, le rôle des fluides et les processus physico-chimiques sous-jacents qui les relient restent mal compris. L'étude de ces processus à l'échelle nanométrique nécessite une approche corrélative combinant des techniques analytiques à haute résolution spatiale. Cette thèse intègre de nouvelles méthodes d’analyse structurelle et géochimique 2D et 3D, telles que l'imagerie de contraste par canalisation d'électrons, la diffraction par rétrodiffusion d'électrons, la microscopie électronique à transmission à balayage (STEM) et la tomographie par sonde atomique (APT), afin d'interroger la structure atomique et la composition des géomatériaux dans le but de mieux comprendre des questions de longue date en sciences de la Terre et d’établir des ponts entre la science des matériaux et les géosciences.

Les processus étudiés dans cette thèse comprennent : 1) les processus de diffusion sous-jacents qui mobilisent les éléments traces dans les nanostructures induites par la déformation; 2) les mécanismes de ségrégation des éléments traces associés aux inclusions fluides; 3) l'influence des inclusions fluides sur la mobilité des défauts structurels et des éléments traces; et 4) les étapes initiales de la nucléation des bulles en présence d'hétérogénéités chimiques à l'échelle nanométrique. Enfin, cette recherche interroge les rétroactions entre les processus de déformation et de diffusion d’éléments traces, en étudiant fondamentalement leur impact sur la rhéologie. Plus précisément, la thèse étudie l'influence de la déformation et des nanostructures associées sur la remobilisation des éléments traces et, à son tour, l'influence des éléments traces sur la nucléation et la mobilité des nanostructures.

Les travaux combinés ont permis d'identifier deux mécanismes de diffusion pour la mobilité des éléments traces induite par la déformation, de caractériser les inclusions fluides dans les données APT, de documenter deux processus qui ont conduit à proposer un nouveau modèle de durcissement induit par les inclusions fluides, et de documenter des preuves directes de la nucléation de bulles à la surface d'hétérogénéités chimiques à l'échelle nanométrique. Ces travaux repoussent non seulement les limites des techniques analytiques à haute résolution spatiale, notamment la STEM et l'APT, mais leurs résultats ont des implications transdisciplinaires importantes dans les domaines des géosciences, de la science des matériaux, de l'ingénierie et de la microscopie analytique.

Abstract

The presence of and interactions between structural defects, fluids, and trace elements during deformation play a vital role in the manner in which materials respond to an applied stress. Although the links between crystal defects and trace element mobility have been lying at the frontier of research in Earth sciences, the role of fluids and the underlying physico-chemical processes linking them remain poorly understood. Investigation of these nanometer scale processes requires a correlative approach combining high-spatial resolution analytical techniques. This thesis integrates novel 2D and 3D structural and geochemical mapping methods such as electron channeling contrast imaging, electron backscatter diffraction, scanning transmission electron microscopy (STEM) and atom probe tomography (APT) to interrogate the atomic structure and composition of geomaterials in an attempt to better understand long-standing questions in Earth sciences and build bridges between materials science and geoscience.

The processes investigated in this thesis include: 1) the underlying diffusion processes that mobilize trace elements into deformation-induced nanostructures; 2) the mechanisms of trace

element segregation associated with fluid inclusions; 3) the influence of fluid inclusions on the mobility of structural defects and trace element mobility; and 4) the initial stages of bubble nucleation in the presence of nanoscale chemical heterogeneities. Ultimately, this research interrogates the feedbacks between deformation and trace element diffusion processes, fundamentally investigating their impact on rheology. More specifically, the thesis investigates the influence of deformation and associated nanostructures on the remobilization of trace elements and, in turn, the influence of trace elements on the nucleation and mobility of nanostructures.

The combined work successfully identified two diffusion mechanisms for deformation-induced trace element mobility, characterized fluid-inclusions in APT data, documented two processes that led to proposing a new fluid inclusion-induced hardening model, and documented direct evidence of bubble nucleation on the surface of nanoscale chemical heterogeneities. This work not only pushes the limits of high-spatial resolution analytical techniques including STEM and APT, but the results have significant transdisciplinary implications in the fields of geoscience, materials science, engineering, and analytical microscopy.

Aknowledgements

First and foremost, I would like to thank my thesis advisor, David Schneider, who has been an incredible mentor during my time at uOttawa and especially over the last 4 years as I completed my PhD thesis. David has been immensely supportive of my, at times quite demanding, endeavours and has always encouraged me to pursue my curiosities and pushed me to collaborate with other researchers at home and abroad. He has given me endless opportunities which allowed me to develop a versatile and competitive skillset throughout the duration of my studies, including attending international conferences, participating in international field courses, and travelling to state-of-the art research facilities to perform my own analyses. More importantly, thank you for always staying positive and helping me grow to become a confident scientist and an overall better person.

I am very grateful to Anna Rogowitz for her guidance, time and knowledge for the duration of this project. Anna has spent endless hours instructing me about structural geology and given me extensive training on EBSD data acquisition and processing techniques as well as ECC imaging. She has been a great host during my many stays in Vienna and has been a great source of expertise throughout this project.

I extend a great thank you to Baptiste Gault who has also provided me with guidance and mentorship throughout my thesis. Baptiste has welcomed me in is group at the Max-Plank Institute for Iron Research in Düsseldorf on many occasions and provided me with training and expertise on state-of-the art analytical instruments. I am very fortunate to have had the chance to collaborate with Baptiste and his group, and I look forward to build on this relationship over my postdoctoral fellowship at MPIE.

I am also grateful for Kevin Schweinar for being a great host during my visits in Düsseldorf and for spending many hours assisting with APT specimen preparation, analysis, and data processing.

I am thankful to Brian Langelier who has welcomed me to the Canadian Centre for Electron Microscopy on a few occasions and provided me with training on APT data acquisition.

I thank the various sources of funding for this research. These include a Natural Sciences and Engineering Research Council of Canada (NSERC) Postgraduate Scholarship-Doctoral, an Ontario Graduate Scholarship, a Queen Elizabeth II Scholarship in Science and Technology and several research grant from the Geological Society of America, the Society of Economic Geologist Foundation, the Canadian Centre for Electron Microscopy, and Mitacs.

I thank Glenn Poirier for giving me the opportunity to work in the SEM/EMPA lab over the last 3 years. He has been a great teacher and thought me a lot about electron microscopy.

I would also like to thank Bernhard Grasemann for his continuous support. He has welcomed me into his group on many occasions and given me the opportunity to participate in many of his field courses in the Austrian Alps and in the Cyclades. I have enjoyed our many discussions about structural geology and I look forward to future collaborations.

I am especially thankful to the DAS group for all the great memories during my time at uOttawa. I would like to personally thank Jennifer Spalding and Sandra Wind who have been encouraging and supportive from the beginning and most importantly provided much needed distractions.

A very special thank you to my wonderful friend Anabelle Dufour Lamontagne who has been incredibly supportive and who has spent many hours listening to me talk about all my projects and trying really hard to understand what I was talking about.

I would like to express my gratitude to the review committee that evaluated my dissertation: Tom Al and Glenn Milne (University of Ottawa), Aaron Lussier (Canadian Museum of Nature), and Desmond Moser (University of Western Ontario).

Table of Contents

CHAPTER 1

Introduction

1.1 Introduction to crystalline defects

The presence of crystal defects and their interactions with each other and the crystal structure play a fundamental role in determining the physical and mechanical properties of a material, including its rheological behaviour. Investigating the microdynamics of defects can help us deepen our understanding of larger scale mass transfer processes on Earth.

Crystal defects are defined as any structure disrupting the ordered arrangement of atoms in a crystalline structure. They can be subclassified as: 1) *point defects* including vacancies (i.e., vacant atomic sites), self-interstitials (i.e., lattice atoms occupying interstitial spaces), substitutional impurities, and interstitial impurities; 2) *line defects* consisting of edge and screw dislocations as endmembers; 3) *planar defects*, which include stacking faults (i.e., irregularities in the stacking sequence of crystals), grain boundaries, twin boundaries, and phase boundaries; and 4) *bulk defects* including voids (i.e., vacancy aggregates), fluid inclusions, fractures, and precipitates (i.e., impurity clusters) (Schwartz and Lang 2016). Such crystalline imperfections can occur as a result of crystal growth processes, internal mechanical stresses, irradiation and crystal-plastic deformation (Burgers 1995; Dyar and Guntar 2008; Itoh and Stoneham 2001; Itoh et al. 2009; Klapper 2010; Seitz and Koehler 1956). The section below discusses some of the effects of these specific defects on the rheology of crystalline materials. For the purpose of this thesis, weakening and strengthening refer to decreases and increases in a material's yield stress, respectively; whereas softening and hardening refer to decreases and increases in Young's modulus (Figure 1.1).

1.2 Influence of crystalline defects on mineral rheology

The presence of point defects in a material introduces local stresses and subsequent intracrystalline strain fields that deform the crystal structure. For instance, the crystal structure surrounding interstitial atoms may expand to accommodate the defect, whereas the crystal structure surrounding vacancies can collapse to accommodate the space (Hoffman et al. 1953; Kanzaki 1957; Dederichs et al. 1978). In both cases, point defects act as pre-existing weaknesses, which can potentially lead to strain localization (e.g., Mushongera et al. 2020). At high homologous temperatures >0.9 ($T_H = T/T_{MP}$, where T_{MP} is the melting point temperature), the rheology of a crystalline material is controlled by the flux of point defects to accommodate differential stresses by ductile flow. During such deformation, known as Nabarro-Herring creep, the strain-rate is partially dependent on the density of point defects (Nabarro 1948; Herring 1950). The diffusion of vacancies during creep can either have a weakening or softening effect on crystals, and the aggregation of vacancies can lead to the growth and coalescence of intrinsic voids resulting in material failure (Benzerga et al. 2001; Fleck et al. 1989; Gao et al. 2005; Horstemeyer and Gokhale 1999; McVeigh et al. 2007; Orsini and Zikry 2001; Smallman 1972; Tvergaard 1989; Wilkinson 1987, 1988). During diffusion creep, vacancies can diffuse into dislocation cores enabling dislocation climb. This mechanism is extremely important during recovery and enables dislocations to climb over obstacles lying along their slip plane, which leads to strain softening (Smallman and Ngan 2014).

Ductile flow in materials can also be accommodated by the nucleation and propagation of dislocations within a crystal structure. The diffusion and interactions of dislocations during creep processes play a vital role in the way crystals respond to an applied stress. For instance, within the crystal-plastic regime, the nucleation and multiplication of dislocations can lead to their entanglement, which results in strain hardening and increases the yield strength of the material (Hansen et al. 2019). Strain hardening can additionally occur when dislocations are arrested by the strain field of other immobile defects (Cahn 2014; Chen et al. 2008; Cottrell and Bilby 1949; Vityk

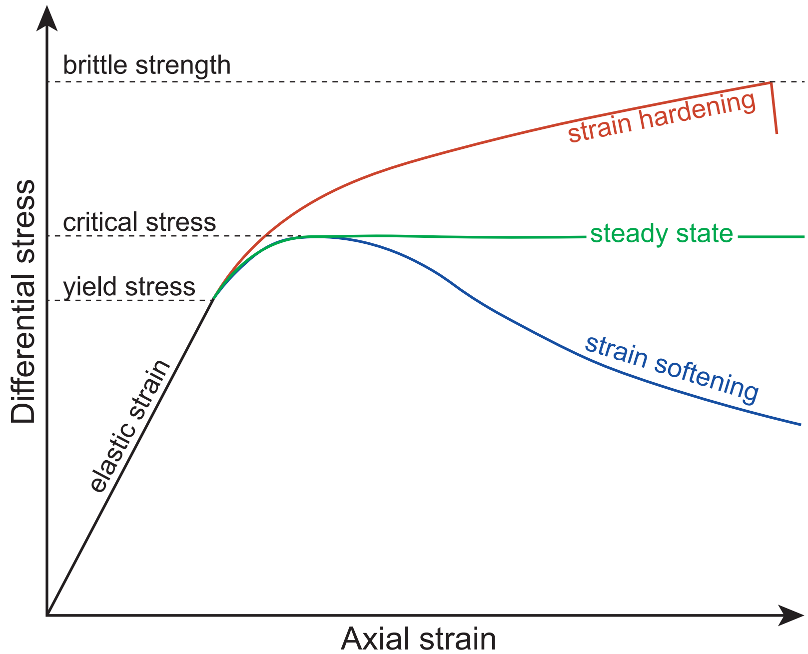

Figure 1.1. Idealised stress-strain curves obtained from rock deformation experiments illustrating the different rheological behaviours of crystalline materials. Modified from Tullis and Tullis (1986).

et al. 2000). In contrast, the untangling and annihilation of dislocations during recovery and dynamic recrystallization processes can lead to softening (Cottrell 1949).

Planar defects also have a significant impact on a material's rheology. On one hand, grain boundaries act as high-diffusivity pathways for point defects, facilitating ductile flow by cobble creep (i.e., the diffusion of point defects along grain boundaries; Cobble 1963). In the presence of fluids, grain boundaries facilitate pressure-solution creep and lead to mechanical weakening (Guren et al. 2020; Marti et al. 2018; Putnis and Ruiz-Agudo 2013; Renard et al. 2019; Wang and Putnis 2020). Grain boundaries also play an important role in dynamic recrystallization processes such as subgrain rotation recrystallization and grain boundary migration during which they act as dislocation sinks, lowering the overall dislocation density, thus having a softening effect on the material (Guillopé and Poirier 1979; Urai et al. 1986; Drury and Urai 1990). On the other hand, geometric effects (i.e., continuity of slip planes across grains and the change of Burgers vectors in adjacent grains) in addition to the local structural stabilization effects at grain boundary cores can lead to dislocation pileups and impede the movement of dislocations, inducing a significant increase in yield strength (Kondo et al. 2016). Similarly, twin boundaries and stacking faults can prevent the glide of dislocations and lead to strain hardening (Meyers et al. 2008; Tian et al. 2015). However, as grain sizes decrease into the nanoscale, grain boundaries can instead act as dislocation nucleation sites and facilitate plastic flow (Bagheripoor and Klassen 2020).

Lastly, bulk defects can also control a material's rheology and have either hardening or softening effects. The stress field surrounding bulk defects (e.g., voids, precipitates), for example, can temporarily arrest the movement of dislocations and lead to strain hardening (Cottrell 1953). However, previous experimental and numerically simulated studies have shown that dislocation loops can instead nucleate at the stress field of bulk defects (e.g., tip of microfractures, voids) and subsequently migrate away from the defect by dislocation glide and creep processes, leading to strain softening (Hatano 2004; Mitchell 1958; Moriarty et al. 2002; Rogowitz et al. 2018; Rudd 2009; Vityk et al. 2000). In addition, the compression and subsequent expansion of fluid inclusions under increasing temperature can result in the nucleation of dislocation loops and lead to mechanical softening (Bakker and Jansen 1994; McLaren et al. 1983).

1.3 Mechanisms of trace element diffusion

The diffusion of trace elements and their segregation into deformation-induced nanostructures (i.e., defects), including dislocations, low-angle grain boundaries, and stacking faults, can have a significant impact on material rheology. The segregation of trace elements into nanostructures can occur by three different intragrain diffusion mechanisms: 1) *volume diffusion*; 2) *high diffusivity pathway* (i.e., pipe) *diffusion*, and 3) *dislocation-impurity pair* (DIP) *diffusion*. Volume diffusion is a high temperature mechanism by which atoms migrate through a crystal structure in the presence of a chemical potential gradient or strain gradient (Klinger and Rabkin 1999). Pipe diffusion consists of the migration of atoms along single dislocations or low- and high-angle grain boundaries (i.e., high diffusivity pathways) where a chemical potential gradient is present (Love 1964). These gradients can result from the presence of chemical (e.g., precipitates) or structural (e.g., core-to-core overlap of entangled dislocations) sinks within, or at either end of dislocation cores and arrays (Legros et al. 2008; Piazolo et al. 2016). For DIP diffusion, chemical potential gradients are not required. Instead, impurities are attracted to dislocation cores by a strain field or 'capture zone' that is created by the dislocation (Cottrell 1953). The force attracting impurities to a dislocation can be explained by a gradient of the interaction energy, which is proportional to the relative spacing between atoms within the crystal structure (Cottrell 1953).

1.4 Influence of trace element diffusion on mineral rheology

Regardless of the responsible diffusion mechanism, the segregation of trace elements into crystal defects plays an important role in the rheology of crystals/minerals/materials. The accumulation of trace elements within dislocation cores, known as Cottrell atmospheres, can temporarily arrest or pin them (Cottrell and Bilby 1949; Cottrell 1953; Vityk et al. 2000), and as stresses increase to reach a critical value, dislocations can be unpinned and move at high velocities. This discontinuous motion of dislocations is known as the Portevin–Le Chatelier effect and can lead to hardening and brittle fracturing (Mohles et al. 1999; Portevin and Le Chatelier 1923). The accumulation of trace elements along grain boundaries can also exert a retarding force on migrating grain boundaries during dynamic recrystallization, which is called 'Zener pinning' (Smith 1948; Alley et al. 1986; Olgaard and Evans 1988). The role of pinning during growth processes produces reduced grain sizes promoting grain-size sensitive deformation mechanisms as diffusion creep leading to a linear viscous rheology rather than dislocation creep leading to a power-law behaviour (Poirier 1980; Hobbs et al. 1990).

1.5 Project objectives and hypotheses

The processes described in the sections above are not exhaustive, but they clearly illustrate how the various interactions between structural defects and trace elements can influence a material's response to an applied stress. In some instances, these deformation-induced interactions can have a strengthening or hardening effect on the material, while in others, they can instead have a weakening or softening effect. Although it is important to note that there are other factors that can influence the rheological behaviour of crystalline materials (i.e., chemical composition, temperature, confining pressure, pore fluid pressure, strain rate), the physico-chemical interactions between structural defects and trace elements, and their effects on material rheology, remain poorly understood and are the main focus of this thesis.

These physical and chemical processes have long been at the frontier of research within materials science. Although investigating these processes is essential to improve our understanding of large-scale mass transfer processes on Earth, there has been limited research studying similar processes in rocks and minerals. Therefore, the objective of this research is to interrogate the feedbacks between deformation and trace element diffusion processes in geomaterials. More specifically, investigate the influence of deformation and associated nanostructures on the remobilization of trace elements and, in turn, the influence of trace elements on the nucleation and mobility of nanostructures. For the purpose of this thesis, diffusion is broadly defined as the flux of atoms within a material as a result of energy gradients (e.g., chemical potential gradient, interaction energy gradient, thermal gradient, pressure gradient, electrostatic gradient, etc.). The hypotheses explored in this thesis are:

1) deformation-induced defects in minerals act as microstructural traps for trace-elements;
2) fluid inclusions behave similarly to voids in atom probe tomography analyses;
3) fluid inclusions have a weakening effect on mineral rheology; and
4) homogeneous bubble nucleation is a variety of heterogeneous nucleation.

Details regarding each of these projects are discussed in section 1.5.

1.6 Scientific approach

Investigation of sub-micrometer scale processes requires a correlative approach combining high-spatial resolution analytical techniques (Figure 1.2; Gault et al. 2021). Therefore, for each of the projects, I combine a suite of 2D and 3D micro- to nano-structural and geochemical analyses. Preliminary microstructural analysis of the samples is performed by combining scanning electron microscopy (SEM), electron channelling contrast imaging (ECCI), and electron backscatter diffraction (EBSD) mapping. ECCI is an SEM-based technique where an electron beam is scanned

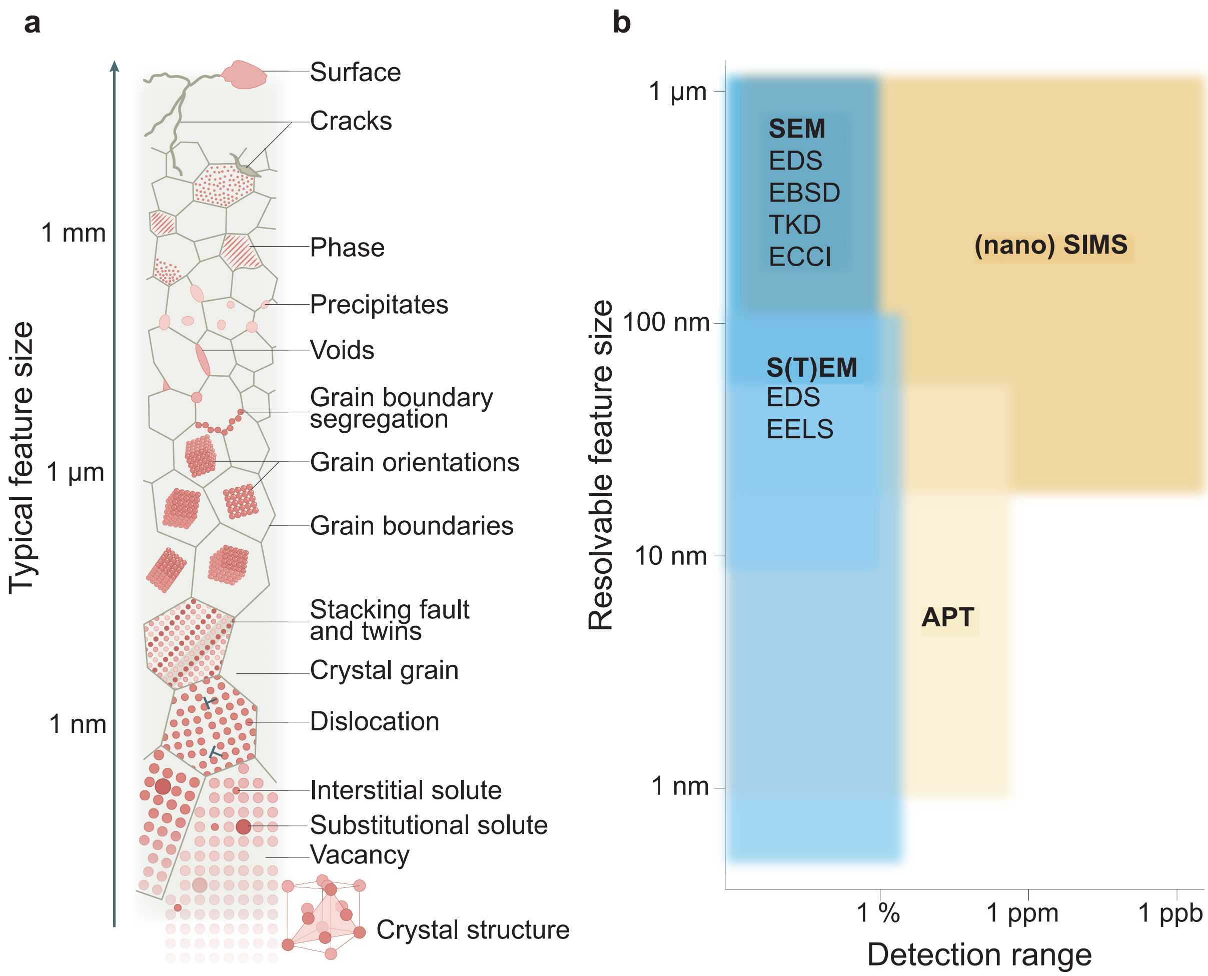

Figure 1.2. Schematic of typical microstructural feature sizes (a) and sensitivity and resolvable feature size of various material analysis techniques (b). Published in Gault et al. (2021).

Abbreviations: SEM: scanning electron microscopy; EBSD: electron backscatter diffraction; TKD: transmission kikuchi diffraction; ECCI: electron channelling contrast imaging; S(T)EM: scanning transmission electron microscopy; EDS: energy dispersive spectroscopy; EELS: electron energy loss spectroscopy; (nano) SIMS: nano secondary ion mass spectrometry; APT: atom probe tomography across an incrementally tilted sample until it is aligned at the Bragg angle with one of the lattice planes and is channelled through the crystal structure (Wilkinson and Hirsch 1997). Changes in crystallographic orientation or irregularities in the predicted crystal structure cause strong backscattering, which is observed with a backscatter electron detector and documented as bright features (Naresh-Kumar et al. 2012, 2013). This imaging technique is typically used for assessing crystal defects in metals, and this project is among the first to apply this technique to natural geological materials. The combined SEM and ECC images allow for the qualitative observation of crystal defects within the samples and are used for targeting specific microstructures (e.g., high dislocation density areas, low-angle grain boundaries, fluid inclusions, gas bubbles) to be further analyzed via EBSD techniques. EBSD is another SEM-based technique that allows for the qualitative and quantitative analysis of microstructures. Crystallographic information is obtained by scanning an electron beam across a titled crystalline sample. The interactions between the incident beam and the sample causes some of the electrons to diffract and exit the lattice at the Bragg angle, which is related to the spacing of the lattice planes. The diffraction pattern is detected with a fluorescent screen and can be used to determine the crystal orientation, characterize microstructures and discriminate between phases when combined with energy dispersive spectroscopy (Schwartz et al. 2009).

High-strain areas observed from EBSD-derived angle deviation and grain boundary maps are selected for further nano-structural and geochemical analyses via transmission electron microscopy (TEM), electron energy loss spectroscopy (EELS) mapping, and atom probe tomography (APT) analyses. TEM is an electron microscopy technique in which an electron source is transmitted through a thin (<150 nm) sample to obtain a high-spatial resolution (<0.05 nm) image as well as information on the internal structure of the samples (i.e., crystal structure, morphology, stress state; Williams and Carter 2009). Some TEM instruments can be operated in a scanning mode (STEM) during which the electron beam is rastered across the sample, and the scattered electrons are projected onto a detector to produce a higher contrast image with better signal-to-noise ratio (Pennycook and Nellist 2011). EELS instrumentation incorporated onto a TEM can be used to analyze the chemical content of a sample and create high-spatial resolution 2D compositional maps. Chemical and structural information is obtained by measuring the kinetic energy change of electrons from the primary beam after inelastic interactions with the material. Since the incident electrons respond differently to the field of the nucleus of different elements, an energy loss spectrum can be obtained (Pennycook and Nellist 2011). Although TEM is very effective at obtaining qualitative and quantitative information about the characteristics of crystal defects such as structure, morphology, and distribution, EELS is limited in its ability to quantify elemental compositions at the same scale. Therefore, selected nanostructures are additionally analyzed by APT. Atom probe tomography is a 3D sub-nanometer scale compositional mapping technique with high sensitivity in the range of tens of parts-per-million. During analyses, a high electrostatic field (V/nm) is produced by a high voltage or laser at the tip of a sharp needle-shaped specimen to induce the field evaporation of surface atoms. The ionized atoms are then projected onto a position sensitive detector with a high detection efficiency (up to 80%), which simultaneously measures the time-of-flight of the ions, allowing us to determine their mass over charge ratios. By combining the time-of-flight spectroscopy and the 3D spatial coordinate data of the evaporated atoms, the large datasets of 10^6–10^8 ions can be converted into 3D atomic point cloud reconstructions of the initial specimens (Gault et al. 2012; Gault et al. 2021). This technique is therefore ideal to obtain 3D quantitative compositional measurements and spatial imaging of materials at the near-atomic scale. In this project, APT analyses are performed on targeted nanostructures to interrogate the atomic structure of the deformed zones and to characterize the trace elements hosted within these features and in some cases determine the diffusion mechanisms driving them into the nanostructures (i.e., volume vs. pipe vs. DIP diffusion).

1.7 Relevance

Our understanding of the feedbacks between deformation and diffusion processes not only has significant impact for the mechanical behaviour of minerals and rocks but also has meaningful implications for other sub-disciplines of geology, including geochronology and economic geology, and trans-disciplinary research in the fields of materials science and engineering.

In geochronology, the reliability of accessory minerals as geochronometers relies on the assumption that trace elements diffuse negligeable distances through the crystal structure (Cherniak and Watson 2003; Fougerouse et al. 2019). However, a study by Piazolo et al. (2016) revealed that during deformation, dislocations move through the crystal structure and accumulate U and Pb within their cores. Furthermore, Piazolo et al. (2016) observed that when connected to a chemical or structural sink, trace elements migrate along dislocations and dislocation arrays leading to their continuous removal whereas trace elements in disconnected dislocations remain locked as isolated reservoirs. These results highlight the importance of deformation on the redistribution of radiogenic isotopes previously considered immobile and suggest that an understanding of the deformation microstructures in geochronometers is necessary for reliable and robust geochronological analyses. Other recent studies have revealed that deformational and metamorphic events can allow the diffusion of radiogenic isotopes leading to the formation of nanoscale clusters (Blum et al. 2018; Peterman et al. 2019; Verberne et al. 2020). The characterisation of these clusters has the potential to be used to resolve the timing of the nanoscale cluster-forming geological events.

In economic geology, it is well known that sulphide phases can incorporate significant concentrations of base- and precious-metals (Cook and Chryssoulis 1990; Reich et al. 2005). The characterization of these metal occurrences and their spatial relationship with nanostructures within the host minerals provides key information for understanding the dynamics that lead to the formation of viable economic deposits (Craig and Vokes 1993; Large et al. 2007; Tomkins and Mavrogenes 2001; Vukmanovic et al 2014). For example, Fougerouse et al. (2016) investigated Au-rich arsenopyrite from the Obuasi Au deposit in Ghana. Their study revealed that deformation-induced microstructures such as microfractures and low-angle grain boundaries act as high diffusivity pathways for fluids that subsequently leach lattice bound Au, consequently resulting in Au-depleted zones within the deformed sulphide phase. Results from my MSc research (Dubosq et al. 2018), however, suggest that deformational microstructures in pyrite can act as traps for Au and other trace elements. Therefore, investigating the interplay between deformation and the remobilization of metals has the potential to improve our understanding of metallic ore paragenesis.

The interplay between impurities and crystalline defects also plays an important role in understanding ice creep and dynamic flow properties which are essential to forecasting the regional feedback between glaciers and ice sheets and the changing climate. Impurities affect the mechanical properties and flow behaviour of ice causing localized enhanced deformation (Eichler et al. 2019; Kuiper et al. 2020; Paterson 1991). For example, it is well documented that elevated impurity content in ice cores correlates to decreased mean grain sizes (Cuffey et al. 2000; Fisher et al. 1986; Paterson 1991; Thorsteinsson et al. 1995). Based on this correlation, chemical impurities have been suggested to inhibit grain growth by exerting a retarding force on migrating grain boundaries through solute drag or pinning leading to a decrease in grain size (Alley et al.

1986; Olgaard et al. 1986; Rohrer 2010). The presence of impurities at grain boundaries also favours the growth of interfacial liquid films by reducing the pressure-melting point of ice (Dash 1995; Gilpin 1979). Liquid films reduce internal stresses at grain boundaries, which enhances the activity of the easiest intracrystalline slip system (De la Chapelle et al. 1999). These films can also act as dislocation sinks and enhance dislocation motion in ice, preventing hardening by dislocation entanglement and thus enhancing the strain rate (Kuiper et al. 2020). The presence of interstitial fluids can also promote grain-size sensitive deformation mechanisms such as grain boundary sliding and grain boundary diffusion (Samyn et al. 2005; Zhang et al. 1994). In addition to their effect on grain size, it has also been postulated that impurities enhance deformation by acting as dislocation sources and inducing defects along basal slip planes (Marshall 2005; Weikusat et al. 2017). Most of these mechanisms however, have been proposed based on correlative observations rather than direct documentation of the responsible mechanisms. Thus, more direct documentation is required to identify the underlying processes and responsible impurity species that lead to ice softening in order to improve our understanding of glacier and ice sheet flow.

In materials science and engineering, the subject of the interplay between impurities and crystalline defects has been lying at the research frontier and has had a significant impact on improving the design of synthetic materials (Meng et al. 2017; Park et al. 2018; Raabe et al. 2017; Seebauer and Wook Noh 2010; Yuan et al. 2018). For instance, since grain boundaries influence mechanical, functional, and kinetic properties of metallic alloys, solutes can be used to decorate the grain boundaries of alloys to introduce desired material properties–this process is known as segregation engineering (Raabe et al 2014; Randle 1999, 2004; Watanabe et al. 1980, 1999). Similarly, point defects engineering (i.e., intentional introduction of point defects in a material) is also used in material design. For example, dopants are used in the production of thin-film solar cells in order to introduce point defects, which can enhance photocurrent generation through sub-bandgap absorption (Park et al 2018). Thus, a better understanding of the rheological impacts on trace element segregation in crystalline materials can lead to improved material design.

In the first chapters of this thesis, pyrite was chosen as a material to study the interactions between deformation and trace element diffusion processes. The prevalence of pyrite as a base- and precious-metal-hosting sulphide phase within ore deposits make it an ideal mineral to evaluate prevailing models of metallic ore paragenesis that suggest metamorphism and crystal-plastic deformation of sulphides causes the liberation, remobilization and subsequent concentration of these metals into viable economic deposits (Craig and Vokes 1993; Large et al. 2007; Tomkins and Mavrogenes 2001). Investigating these micro- and nanoscale processes and their rheological impacts on sulphide phases can also help us better comprehend larger scale mass transfer processes within sulphide-rich terrains involved in the genesis of metallic ore deposits. Additionally, although pyrite is not one of the major mineral components that comprise the lithospheric crust, its relatively simple cubic crystalline structure and semi-conductive properties make it an ideal material to study nanoscale deformation and diffusion processes with the use of atom probe tomography. By investigating the interactions between crystal defects, fluids, and trace elements in pyrite, we can gain additional insight into the impact of these interactions on the rheological responses of minerals and potentially extrapolate our observations to major lithospheric components, such as silicate minerals, in order to better understand the larger tectonic scale mass transfer processes on Earth.

1.8 Thesis format

This doctoral thesis is divided into six chapters and presents a collection of four scientific articles. Three are published in peer-reviewed scientific journals and the fourth is in the final stages of preparation at the time of this doctoral thesis submission. For all papers produced out of this doctoral thesis, I helped conceive and develop the analytical method under the supervision of Dr. David Schneider (Ottawa) and guidance from Dr. Anna Rogowitz (Vienna) and Dr. Baptiste Gault (Düsseldorf). I conducted the experiments as a visiting PhD student at the University of Vienna, Austria (EBSD, ECCI), Max-Planck Institute for Iron Research in Düsseldorf, Germany (FIB, APT), and the Canadian Centre for Electron Microscopy in Hamilton, Ontario (TEM, APT). I performed data processing and analysis for each project and led discussions on the data interpretation. I took the lead in writing and revising all four manuscripts for which I am the first and corresponding author.

Chapter 1 is an introduction to the entire thesis and contains a short overview of the literature concerning the problem, the hypotheses, the objectives and the methodology.

Chapter 2 focusses on the first part of the aforementioned feedback loop which is to investigate the influence of deformation-induced nanostructures on trace element remobilization within the brittle-ductile transition regime, an important part of the strength profile of Earth's crust. In particular, this project examined the role of crystal-plastic deformation on base- and precious-metal remobilization in sulphide minerals from a mid-crustal orogenic Au deposit. In this chapter, I combined SEM-based nano- to microstructural characterization techniques and APT in an attempt to advance our understanding of the diffusion processes that occur during crystal-plastic deformation. The study focused on pyrite and the processes responsible for the observed link between chemical distribution of trace elements and defect structures, which are still highly debated, and, for the first-time, quantification of the orientation of crystal defects in geological materials directly from the APT data. The results advance our understanding of diffusion processes related to trace element distributions and their link to deformation structures, but also show which techniques can potentially be combined to maximize the data and knowledge that can be derived from nanoscale defect structures.

This work is published in *Contributions to Mineralogy and Petrology* (Dubosq et al. 2019). Anna Rogowitz (Vienna) provided guidance, assisted with EBSD analysis and ECC imaging and contributed to data interpretation and writing/editing of the manuscript; Kevin Schweinar (Düsseldorf) assisted with specimen preparation and APT analyses as well as with APT data processing; Baptiste Gault (Düsseldorf) provided guidance, assisted with APT data processing and contributed to data interpretation and writing/editing of the manuscript; David Schneider (Ottawa) provided supervision and guidance, and contributed to data interpretation and writing/editing of the manuscript.

The following chapters focus on the second part of the deformation cycle to understand the influence of trace element diffusion on the generation and mobility of crystal defects and to assess their impact on the rheology of geological materials.

Chapter 3 focusses on the characterization of fluid inclusions using APT. I have combined APT experiments and field evaporation simulations on pyrite to document trace-element segregation associated with nanovoids. I documented the first direct evidence of nanovoids in geomaterials as high point density features in both experimental and simulated 3D APT specimen reconstructions. Together with EBSD mapping and electron channeling contrast imaging I interpreted these voids to be nanoscale fluid inclusions. With these results, we now better understand how to identify and interpret voids in APT data, which had been a missing piece of the puzzle in the interpretation of complex nanostructures from atom probe data. These results not only have significant implications within the geosciences, but also have significant trans-disciplinary implications in materials science and analytical microscopy.

This work is published in *Ultramicroscopy* (Dubosq et al. 2020). Baptiste Gault (Düsseldorf) provided guidance, assisted with APT data processing and contributed to data interpretation and writing/editing of the manuscript; Constantinos Hatzoglou (Rouen) and François Vurpillot (Rouen) performed numerical simulations of APT experiments; Kevin Schweinar (Düsseldorf) assisted with APT analysis; Anna Rogowitz (Vienna) assisted with EBSD analysis and ECC imaging and contributed to data interpretation and writing/editing of the manuscript; Gerd Rantitsch (Leoben) performed Raman spectroscopy of carbonaceous material; David Schneider (Ottawa) provided supervision and guidance, and contributed to data interpretation and writing/editing of the manuscript.

Chapter 4 builds on the observations from Chapter 3 and investigates the influence of fluid inclusions on mineral rheology. In this chapter, I combined APT experiments and electron microscopy imaging techniques on naturally deformed pyrite to document the interactions between trace elements (impurities), fluid inclusions and crystal defects and assess their impact on mineral rheology. I have successfully documented a process that led me to propose a new model where fluids can have a hardening effect on minerals contrasted with the more commonly reported weakening and softening effect.

This work is published in *Contributions to Mineralogy and Petrology* (Dubosq et al. 2021). Anna Rogowitz (Vienna) provided guidance, assisted with EBSD analysis and ECC imaging and contributed to data interpretation and writing/editing of the manuscript; David Schneider (Ottawa) provided supervision and guidance and contributed to data interpretation and writing/editing of the manuscript; Kevin Schweinar (Düsseldorf) assisted with APT analysis; Baptiste Gault (Düsseldorf) provided guidance, assisted with APT data processing and contributed to data interpretation and writing/editing of the manuscript.

Although chapters 2-4 address the vital role of defects and diffusion in the manner minerals respond to an applied stress, in **Chapter 5** I address questions surrounding the kinetics of crystallite formation and the nucleation processes of gas bubbles (i.e., bulk defects) in rock melts. The relative timing and rate of these processes affect the rheological behaviors of magmas that control eruption dynamics. In this chapter I combine TEM, EELS and APT to investigate the initial stages of bubble nucleation. The combined data demonstrate the existence of nanoscale chemical heterogeneities within the melt and at the bubble-melt interface of bubbles that were previously interpreted to be nucleated homogeneously within the melt. These results contribute to the proposed hypothesis that homogeneous nucleation is simply a variety of heterogeneous nucleation where nucleation occurs on the surface of submicroscopic crystals and highlight the need to redefine homogeneous nucleation.

This work is prepared for submission to the *Journal of Volcanology and Geothermal Research*. David Schneider (Ottawa) provided supervision and guidance, and contributed to data interpretation and writing/editing of the manuscript; Xuyang Zhou (Düsseldorf) performed specimen preparation and APT analyses; Baptiste Gault (Düsseldorf) provided guidance and contributed to data interpretation; Pia Pleše (Ottawa) provided guidance contributed to data interpretation; Brian Langelier (Hamilton) provided training and assistance for APT analyses and assisted with APT data processing and interpretation.

Chapter 6 is a summary of the main findings of the overall research presented and the principal conclusions drawn from them. The chapter finishes with a suggested direction for future studies.

1.9 References

Alley R, Perepezko J, Bentley C (1986) Grain Growth in Polar Ice: II. Application. J Glaciol 32(112): 425–433. doi.org/10.3189/S0022143000012132

Bagheripoor M, Klassen R (2020). The effect of grain boundary on the local incipient plastic deformation of fcc metals during nanoindentation. J Appl Phys 128(2): 1.18. doi.org/10.1063/5.0010370

Bakker RJ, Jansen JBH (1994) A mechanism for preferential H_2O leakage from fluid inclusions in quartz, based on TEM observations. Contrib Mineral Petrol 116: 7–20. doi.org/10.1007/BF00310686

Benzerga AA, Besson J, Batisse R, Pineau A (2001) Synergistic effects of plastic anisotropy and void coalescence on fracture mode in plane strain. Model Simul Mater Sci Eng 10: 73–102. doi.org/10.1088/0965-0393/10/1/306

Blum TB, Reinhard DA, Chen Y, Prosa TJ, Larson DJ, Valley JW (2018) Uncertainty and sensitivity analysis for spatial and spectral processing of Pb isotopes in zircon by atom probe tomography. In: Moser DE, Corfu F, Darling JR, Reddy SM, Tait K (eds). Microstructural Geochronology: Planetary records down to atom scale, pp. 369–373. doi.org/10.1002/9781119227250.ch16

Burgers JM (1995) Physics. — Some considerations on the fields of stress connected with dislocations in a regular crystal lattice. I BT - Selected Papers of J. M. Burgers. In: Nieuwstadt FTM, Steketee JA (eds). Springer Netherlands, Dordrecht, pp 335–389.

Cahn JW (2014) Reprise: partial chemical strain dislocations and their role in pinning dislocations to their atmospheres. Philos Mag 94(27): 3170–3176. doi.org/10.1080/14786435.2014.951711

Chen S, Hiraga T, Kohlstedt DL (2006) Water weakening of clinopyroxene in the dislocation creep regime. J Geophys Res 111: 1–14. doi.org/10.1029/2005JB003885

Cherniak DJ, Watson EB (2003) Diffusion in zircon. Rev Mineral Geochem 53: 113–143.

Coble RL (1963) A model for boundary diffusion controlled creep in polycrystalline materials. J Appl Phys 34: 1679–1782. doi.org/10.1063/1.1702656

Cook NJ, Chryssoulis SL (1990) Concentrations of invisible gold in the common sulphides. Can Mineral 28: 1–16.

Cottrell AH (1949) Theory of dislocations. Prog Met Phys 1: 77–126. doi.org/10.1016/0502-8205(49)90004-0

Cottrell AH (1953) Theory of dislocations. Prog Met Phys 4: 205–264. doi.org/10.1016/0502-8205(53)90018-5

Cottrell AH, Bilby BA (1949) Dislocation theory of yielding and strain ageing of iron. Proc Phys Soc A 62: 49–62. doi.org/10.1088/0370-1298/62/1/308

Craig JR, Vokes FM (1993) The metamorphism of pyrite and pyritic ores: An overview. Mineral Mag 57 :3–18. doi.org/10.1180/minmag.1993.057.386.02

Cuffey, K. M., Thorsteinsson, T., and Waddington, E. D. (2000), A renewed argument for crystal size control of ice sheet strain rates, J Geophys Res, 105(B12), 27889– 27894, doi:10.1029/2000JB900270.

Dash JG, Fu H, Wettlaufer JS (1995) The pre-melting of ice and its environmental consequences. Rep Prog Phys 58(1): 115–167. doi.org/10.1088/0034-4885/58/1/003

De La Chapelle S, Milsch H, Duval CP (1999) Compressive creep of ice containing a liquid intergranular phase: Rate-controlling processes in the dislocation creep regime. Geophys Res Lett 26(2): 251–254. doi.org/10.1029/1998GL900289

Dedereichs PH, Lehmann C, Schober HR, Scholz A, Zeller R (1978) Lattice theory of point defects. J Nucl Mater 69–70: 176–199. doi.org/10.1016/0022-3115(78)90243-X

Drury MR, Urai JL (1990) Deformation-related recrystallization. Scripta Met 21: 879–884. doi.org/10.1016/0040-1951(90)90033-5

Dubosq R, Gault B, Hatzoglou C, Schweinar K, Vurpillot F, Rogowitz A, Rantitsch G, Schneider DA (2020) Analysis of nanoscale fluid inclusions in geomaterials by atom probe tomography: experiments and numerical simulations. Ultramic 218: 1–10. doi.org/10.1016/j.ultramic.2020.113092

Dubosq R, Lawley CJM, Rogowitz A, Schneider DA, Jackson S (2018) Pyrite deformation and connections to gold mobility: Insight from micro-structural analysis and trace element mapping. Lithos 310–311: 86–104. doi.org/10.1016/j.lithos.2018.03.024

Dubosq R, Rogowitz A, Schneider DA, Schweinar K, Gault B (2021) Fluid inclusion induced hardening: Nanoscale evidence from naturally deformed pyrite. Contrib Mineral Petrol 176: 1–14. doi.org/10.1007/s00410-021-01774-9.

Dubosq R, Rogowitz A, Schweinar K, Gault B, Schneider DA (2019) A 2D and 3D nanostructural study of naturally deformed pyrite: Assessing the links between trace element mobility and defect structures. Contrib Mineral Petrol 174(72): 1–16. doi.org/10.1007/s00410-019-1611-5

Dyar M, Guntar M (2008) Mineralogy and optical mineralogy. Am Mineral 93: 1481–1482. doi.org/ doi.org/10.2138/am.2008.524

Eichler J, Weikusat C, Wegner A, Twarloh B, Behrens M, Fischer H, Hörhold M, Jansen D, Kipfstuhl S, Ruth U, Wilhelms F and Weikusat I (2019) Impurity Analysis and

Microstructure Along the Climatic Transition From MIS 6 Into 5e in the EDML Ice Core Using Cryo-Raman Microscopy. Front. Earth Sci. 7:20. doi: 10.3389/feart.2019.00020

Fisher DA, Koerner RM (1986) On the special rheological properties of ancient microparticle-laden northern hemisphere ice as derived from borehole and core measurements. J Glaciol 32(112): 501-510.

Fleck NA, Hutchinson JW, Tvergaard V (1989) Softening by void nucleation and growth in tension and shear. J Mech Phys Solids 37:515–540. doi.org/10.1016/0022-5096(89)90027-6

Fougerouse D, Micklethwaite S, Halfpenny A, Reddy SM, Cliff JB, Martin LAJ, Kilburn M, Guagliardo P, Ulrich S (2016) The golden ark: Arsenopyrite crystal plasticity and the retention of gold through high strain and metamorphism. Terra Nova 28:181–187. doi.org/10.1111/ter.12206

Fougerouse D, Reddy SM, Kirkland CL, Saxey DW, Rickard WD, Hough RM (2019) Time-resolved, defect-hosted, trace element mobility in deformed Witwatersrand pyrite. Geosci Front 10 (1): 55–63. doi.org/10.1016/j.gsf.2018.03.010

Gao X, Wang T, Kim J (2005) On ductile fracture initiation toughness: Effects of void volume fraction, void shape and void distribution. Int J Solids Struct 42: 5097–5117. doi.org/10.1016/J.IJSOLSTR.2005.02.028

Gardner JE, Denis MH (2004) Heterogeneous bubble nucleation on Fe-Ti oxide crystals in high-silica rhyolitic melts. Geochim Cosmochim Acta 68(17): 3587–3597. doi.org/10.1016/j.gca.2004.02.021

Gault B, Chiaramonti A, Cojocaru-Mirédin O, Stender P, Dubosq R, Freysoldt C, Kumar Makineni S, Li T, Moody MP, Cairney JM (2021) Atom probe tomography. Nat Rev Methods Primers, 1, 1–30. doi: 10.1038/s43586-021-00047-w

Gault B, Moody M, Cairney J, SP R (2012) Atom Probe Microscopy. Springer-Verlag New York Inc.

Gilpin RR (1979) A model of the "liquid-like" layer between ice and a substrate with applications to wire regelation and particle migration. J Colloid Interface Sci 68(2): 235–251. doi.org/10.1016/0021-9797(79)90277-7

Guillopé M, Poirier JP (1979) Dynamic recrystallization during creep of single-crystalline halite: An experimental study. J Geophys Res B 84: 5557–5567. doi.org/10.1029/JB084iB10p05557

Guren MG, Putnis CV, Montes-Hernandez G, King HE, Renard F (2020) Direct imaging of coupled dissolution-precipitation and growth processes on calcite exposed to chromium-rich fluids. Chem Geol 552: 1–12. doi.org/10.1016/j.chemgeo.2020.119770

Hansen LN, Kumamoto KM, Thom CA, Wallis D, Durham WB, Goldsby DL, Breithaupt T, Meyers CD, Kohlstedt DL (2019) Low-temperature plasticity in olivine: Grain size, strain hardening, and the strength of the lithosphere. J Geophys Res B: Solid Earth 124: 5427–5449. doi.org/10.1029/2018JB016736

Hatano T (2004) Dislocation nucleation in shocked fcc solids: Effects of temperature and pre-existing voids. Phys Rev Lett 93: 1–4. doi.org/10.1103/PhysRevLett.93.085501

Herring C (1950) Diffusional viscosity of a polycrystalline solid. J Appl Phys 21: 437–445. doi.org/10.1063/1.1699681

Hobbs BE, Muhlhaus HB, Ord A (1990) Instability, softening and localization of deformation. In: Knipe RJ, Rutter EH (eds). Deformation mechanisms, rheology and tectonics. Geol Soc Lon Spec Publ 54, pp. 143–166. doi.org/10.1144/GSL.SP.1990.054.01.15

Hoffman RW, Anders FJ, Crittenden Jr. EC (1953) Evidence for collapse of lattice vacancy aggregates to form dislocation rings. J Appl Phys 24: 231–232. doi.org/10.1063/1.1721252

Horstemeyer MF, Gokhale AM (1999) A void–crack nucleation model for ductile metals. Int J Solids Struct 36: 5029–5055. doi.org/10.1016/S0020-7683(98)00239-X

Itoh N, Duffy DM, Khakshouri S, Stoneham AM (2009) Making tracks: Electronic excitation roles in forming swift heavy ion tracks. J Phys Condens Matter 21: 474205. doi.org/10.1088/0953-8984/21/47/474205

Itoh N, Stoneham AM (2001) Materials modification by electronic excitation. Radiat Eff Defects Solids 155: 277–290. doi.org/10.1080/10420150108214126

Kanzaki H (1957) Point defects in face-centred cubic lattice—I distortion around defects. J Phys Chem Solids 2(1): 24–36. doi.org/10.1016/0022-3697(57)90003-3

Klapper H (2010) Generation and Propagation of Defects During Crystal Growth. In: Dhanaraj G, Byrappa K, Prasad V, Dudley M (eds). Handbook of Crystal Growth. Springer, Berlin. pp. 93–132. doi.org/10.1007/978-3-540-74761-1_4

Klinger L, Rabkin E (1999) Beyond the Fisher model of grain boundary diffusion: Effect of structural inhomogeneity in the bulk. Acta Mater 47: 725–734. doi.org/10.1016/S1359-6454(98)00420-0

Kondo S, Mitsuma T, Shibata N, Ikuhara Y (2016) Direct observation of individual dislocation interaction processes with grain boundaries. Sci Adv 2(11): e1501926. doi.org/10.1126/sciadv.1501926

Kuiper EJN, de Bresser JHP, Drury MR, Eichler J, Pennock GM, Weikusat I (2020) Using a composite flow law to model deformation in the NEEM deep ice core, Greenland – Part 2: The role of grain size and pre-melting on ice deformation at high homologous temperature, Cryosph 14: 2449–2467. doi.org/10.5194/tc-14-2449-2020

Large RR, Maslennikov VV, Robert F, Danyushevsky LV, Chang Z (2007) Multistage sedimentary and metamorphic origin of pyrite and gold in the Giant Sukhoi Log deposit, Lena Gold Province, Russia. Econ Geol 102: 1233–1267. doi.org/10.2113/gsecongeo.102.7.1233

Legros M, Dehm G, Arzt E, Balk TJ (2008) Observation of giant diffusivity along dislocation cores. Science 319: 1646–1649. doi.org/10.1126/science.11517-71

Love GR (1964) Dislocation pipe diffusion. Acta Metal Mater 12: 731–737. doi.org/10.1016/0001-6160(64)90220-2

Marshall SJ (2005). Recent advances in understanding ice sheet dynamics. Earth Planet Sci Lett 240(2): 191–204. doi.org/10.1016/j.epsl.2005.08.016

Marti S, Stünitz H, Heilbronner R, Plümper O, Killian R (2018) Syn-kinematic hydration reactions, grain size reduction, and dissolution–precipitation creep in experimentally deformed plagioclase–pyroxene mixtures. Solid Earth 9: 985–1009. doi.org/10.5194/se-9-985-2018

McLaren AC, Cook RF, Hyde ST, Tobin RC (1983) The mechanisms of the formation and growth of water bubbles and associated dislocation loops in synthetic quartz. Phys Chem Miner 9: 79–94. doi.org/10.1007/BF00308151

McVeigh C, Vernerey F, Liu WK, et al (2007) An interactive micro-void shear localization mechanism in high strength steels. J Mech Phys Solids 55: 225–244. doi.org/10.1016/J.JMPS.2006.08.002

Meng X, Liu Z, Cui B, Qin D, Geng H, Cai W, Fu L, He J, Ren Z, Sui J (2017) Grain boundary engineering for achieving high thermoelectric performance in n-type skutterudites. Adv Energy Mater 7(13): 1–11. doi.org/10.1002/aenm.201602582

Meyers MA, Vohringer O, Lubarda VA (2001) The onset of twinning in metals: a constitutive description. Acta Mater 49: 4025–4039. doi.org/10.1016/S1359-6454(01)00300-7

Mitchell JW (1958) Growth and perfection of crystals. In: Doremus RH, Roberts BW and Turnbull D (eds). Wiley, New York, pp 386–389.

Mohles V, Rönnpagel D, Nembach E (1999) Simulation of dislocation glide in precipitation hardened materials. Comput Mater Sci 16(1–4): 144–150. doi.org/10.1016/S0927-0256(99)00056-7

Moriarty JA, Belak JF, Rudd RE, Söderlind P, Streitz FH, Yang LH (2002) Quantum-based atomistic simulation of materials properties in transition metals. J Phys: Condens Matter 14: 2825–2857. doi.org/10.1088/0953-8984/14/11/305

Mushongera LT, Kumar P, Sangid MD (2020) The interaction of point defects with stress fields generated by persistent slip bands in face-centered cubic nickel. Adv Eng Mater 22: 2000490. doi.org/10.1002/adem.202000490

Nabarro FRN (1948) Deformation of crystals by the motion of single ions. In: Report of a conference on the strength of solids. Phys Soc Lon: 75–90.

Naresh-Kumar G, Hourahine B, Edwards PR, Day AP, Winkelmann A, Wilkinson AJ, Parbrook PJ, England G, Trager-Cowan C (2012) Rapid non-destructive analysis of threading dislocations in wurtzite materials using the scanning electron microscope. Phys Rev Lett 108(13): 1–5. doi.org/10.1103/PhysRevLett.108.135503

Naresh-Kumar G, Mauder C, Wang KR, Kraeusel S, Bruckbauer J, Edwards PR, Hourahine B, Kalisch H, Vescan A, Giesen C, Heuken M, Trampert A, Day AP, Trager-Cowan C (2013) Electron channeling contrast imaging studies of non-polar nitrides using a scanning electron microscope. Appl Phys Lett 102:1–4. doi.org/10.1063/1.4801469

Olgaard DL, Evans B (1986) Effect of second-phase particles on grain growth in calcite. J Am Ceram Soc 69: C-272–C-277. doi.org/10.1111/j.1151-2916.1986.tb07374.x

Olgaard DL, Evans B (1988) Grain growth in synthetic marbles with added mica and water. Contrib Mineral Petrol 100(2): 246–260. doi.org/10.1007/BF00373591

Orsini V., Zikry M. (2001) Void growth and interaction in crystalline materials. Int J Plast 17: 1393–1417. doi.org/10.1016/S0749-6419(00)00091-7

Park JS, Kim S, Xie Z, Walsh A (2018) Point defect engineering in thin-film solar cells. Nature Rev Mater 3: 194–210. doi.org/10.1038/s41578-018-0026-7

Paterson WSB (1991) Why ice-age ice is sometimes "soft." Cold Reg Sci Technol 20(1): 75–98. doi.org/10.1016/0165-232X(91)90058-O

Pennycook SJ, Nellist PD (2011) Scanning transmission electron microscopy: Imaging and analysis. Springer. doi.org/10.1007/978-1-4419-7200-2

Peterman EM, Reddy SM, Saxey DW, Fougerouse D, Snoeyenbos D, Rickard W (2019) Nanoscale processes of trace element mobility in metamorphosed zircon. Contrib to Mineral Petrol 174: 92. doi.org/10.1007/s00410-019-1631-1

Piazolo S, La Fontaine A, Trimby P, Harley S, Yang L, Armstrong R, Cairney JM (2016) Deformation-induced trace element redistribution in zircon revealed using atom probe tomography. Nat Commun 7: 1–7. doi.org/10.1038/ncomm s1049 0

Poirier JP (1980) Shear localization and shear instability in materials in the ductile field. J Struc Geol 2: 135–142. doi.org/10.1016/0191-8141(80)90043-7

Portevin A, Le Chatelier F (1923) Sur un phénomène observation lors de l'essai de traction d'alliages en cours de transformation. C R Acad Sci Paris 176: 507–510.

Putnis CV, Ruiz-Agudo E (2013) The mineral–water interface: Where minerals react with the environment. Elements 9: 177–182. doi.org/1 0.2113/gselements.9.3.177

Raabe D, Herbig M, Sandlöbes S, Li Y, Tytko D, Kuzmina M, Ponge D (2014) Grain boundary segregation engineering in metallic alloys: A pathway to the design of interfaces. Curr Opin Solid State Mater Sci 18: 253–261. doi.org/10.1016/j.cossms.2014.06.002

Raabe D, Ponge D, Wang MM, Herbig M, Belbe M, Springer H (2017) 1 billion tons of nanostructure – segregation engineering enables confined transformation effects at lattice defects in steels. IOP Conf Ser: Mater Sci Eng 219: 012006. doi.org/10.1088/1757-899X/219/1/012006

Randle V (1999) Mechanism of twinning-induced grain boundary engineering in low stacking-fault energy materials. Acta Mater 47: 4187–4196. doi.org/10.1016/S1359-6454(99)00277-3

Randle V (2004) Twinning-related grain boundary engineering. Acta Mater 52: 4067–4081. doi.org/10.1016/j.actamat.2004.05.031

Reich M, Kesler S, Utsunomiya S, Palenik C, Chryssoulis S, Ewing R (2005) Solubility of gold in arsenian pyrite. Geochim Cosmochim Acta 69(11): 2781–2796. doi.org/10.1016/j.gca.2005.01.011

Renard F, Røyne A, Putnis CV (2019) Timescales of interface-coupled dissolution-precipitation reactions on carbonates. Geosci Front 10: 17–27. doi.org/10.1016/j.gsf.2018.02.013

Rogowitz A, Zaefferer S, Dubosq R (2018) Direct observation of dislocation nucleation in pyrite using combined electron channelling contrast imaging and electron backscatter diffraction. Terra Nova 30: 423–430. doi.org/10.1111/ter.12358

Rohrer GS (2010) Introduction to grains, phases, and interfaces—an interpretation of microstructure. Trans AIME 1948 175: 15–51, by CS Smith. Metall Mater Trans A 41: 1063–1100. doi.org/10.1007/s11661-010-0215-5

Rudd RE (2009) Void growth in bcc metals simulated with molecular dynamics using the Finnis-Sinclair potential. Philos Mag 89: 3133–3161. doi.org/10.1080/14786430903222529

Samyn D, Svensson A, Fitzsimons SJ (2008) Dynamic implications of discontinuous recrystallization in cold basal ice: Taylor Glacier, Antarctica. J Geophys Res 113: F03S90. doi.org/10.1029/2006JF000600

Schwartz AJ, Kumar M, Adams BL, Field D (2009). Electron backsatter diffraction in materials science. Springer Handbooks. doi.org/10.1007/978-0-387-88136-2

Schwartz K, Lang M (2016) Mineral Defects. In: White WM (ed). Encyclopedia of Geochemistry: A Comprehensive Reference Source on the Chemistry of the Earth. Springer International Publishing, pp 1–5.

Seebauer EG, Wook Noh K (2010) Trends in semiconductor defect engineering at the nanoscale. Mater Sci Eng: R: Rep 70(3–6): 151–168. doi.org/10.1016/j.mser.2010.06.007

Seitz F, Koehler J (1956) Solid state physics Vol. 2. In: Seitz F, Turnbull D (eds). Solid State Physics. Academic Press, New York, NY, pp 307–442

Smallman RE, Ngan AHW (2014) Point defect behaviour. In: Smallman RE, Ngan AHW (eds). Modern Physical Metallurgy. Butterworth-Heinemann, pp 251–285. doi.org/10.1016/B978-0-08-098204-5.00006-7.

Smallman RE, Westmacott KH (1972) Invited review: The nature and behaviour of vacancy clusters in close-packed metals. Mater Sci Eng 9:249–272. doi.org/10.1016/0025-5416(72)90042-0

Smith CS (1948) Grains, phases, and interfaces: an interpretation of microstructure. Trans Metall Soc AIME 175: 15–51.

Thorsteinsson T, Kipfstuhl J, Miller H (1997) Textures and fabrics in the GRIP ice core. J Geophys Res 102(C12): 26583–26599. doi.org/10.1029/97JC0016

Tian YZ, Zhao LJ, Chen S, Shibata A, Zhang ZF, Tsuji N (2015) Significant contribution of stacking faults to the strain hardening behavior of Cu-15%Al alloy with different grain sizes. Sci Rep 16: 16707. doi.org/10.1038/srep16707

Tomkins AG, Mavrogenes JA (2001) Redistribution of gold within arsenopyrite and löllingite during pro- and retrograde metamorphism: Application to timing of mineralization. Econ Geol 96: 525–534. doi.org/10.2113/gsecongeo.96.3.525

Tullis TE, Tullis J (1986) Experimental rock deformation techniques. In: Hobbs B, Heard H (eds). Mineral and Rock Deformation. Geophys Monogr Ser 36: 297–324. doi.org/10.1029/GM036p0297

Tvergaard V (1989) Material Failure by void growth to coalescence. Adv Appl Mech 27: 83–151. doi.org/10.1016/S0065-2156(08)70195-9

Urai JL, Means WD, Lister GS (1986) Dynamic recrystallization of minerals. Geophys Monograph Am Geophys Union 36: 161–199. doi.org/10.1029/GM036p0161

Verberne R, Reddy SM, Saxey DW, Fougerouse D, Rickard WDA, Plavsa D, Agangi A, Kylander-Clark ARC (2020) The geochemical and geochronological implications of nanoscale trace-element clusters in rutile. Geology 48(11): 1126–1130 doi.org/10.1130/G48017.1

Vityk MO, Bodnar RJ, Doukhan JC (2000) Synthetic fluid inclusions. XV. TEM investigation of plastic flow associated with re-equilibration of fluid inclusions in natural quartz. Contrib Mineral Petrol 139: 285–297. doi.org/10.1007/s004100000142

Vukmanovic Z, Reddy SM, Godel B, Barnes SJ, Fiorentini ML, Barnes SJ, Kilburn MR (2014) Relationship between microstructures and grain-scale trace element distribution in komatiite-hosted magmatic sulphide ores. Lithos 184–187: 42–61. doi.org/10.1016/j.lithos.2013.10.037

Wang L, Putnis CV (2020) Dissolution and precipitation dynamics at environmental mineral interfaces imaged by in situ atomic force microscopy. Acc Chem Res 53: 1196–1205. doi.org/10.1021/acs.accounts.0c00128

Watanabe T, Kitamure S, Karashima S (1980) Grain boundary hardening and segregation in alpha Iron-Tin alloy. Acta Metall 28: 455–463. doi.org/10.1016/0001-6160(80)90135-2

Watanabe T, Tsurekawa S (1999) The control of brittleness and development of desirable mechanical properties in polycrystalline systems by grain boundary engineering. Acta Mater 47: 4171–4185. doi.org/10.1016/S1359-6454(99)00275-X

Weikusat I, Jansen D, Binder T, Eichler J, Faria SH, Wilhelms F, Kipfstuhl S, Sheldon S, Miller H, Dahl-Jensen D, Kleiner T (2015) Physical analysis of an Antarctic ice core (EDML) –

towards an integration of micro- and macrodynamics of polar ice. Philos Trans A 375: 0347. doi.org/10.1098/rsta.2015.0347, 2017.

Wilkinson AJ, Hirsch PB (1997) Electron diffraction based techniques in scanning electron microscopy of bulk materials. Micron 28: 279–308. doi.org/10.1016/S0968-4328(97)00032-2

Wilkinson D (1988) The effect of a non-uniform void distribution on grain boundary void growth during creep. Acta Metall 36: 2055–2063. doi.org/10.1016/0001-6160(88)90307-0

Wilkinson DS (1987) The effect of time dependent void density on grain boundary creep fracture—i. Continuous void coalescence. Acta Metall 35: 1251–1259. doi.org/10.1016/0001-6160(87)90006-X

Williams DB, Carter CB (2009) Transmission electron microscopy. Springer. doi.org/10.1007/978-0-387-76501-3

Yuan L, Tian M, Lan J, Cao X, Wang X, Chai Z, Gibson JK, Shi W (2018) Defect engineering in metal–organic frameworks: A new strategy to develop applicable actinide sorbents. Chem Commun 54(4): 370–373. doi.org/10.1039/C7CC07527H

Zhang Y, Hobbs BE, Jessell MW (1994) The effect of grain-boundary sliding on fabric development in polycrystalline aggregates. J Struct Geol 16(9): 1315–1325. doi.org/10.1016/0191-8141(94)90072-8

CHAPTER 2

A 2D and 3D nanostructural study of naturally deformed pyrite: assessing the links between trace element mobility and defect structures

R. Dubosq[1], A. Rogowitz[2], K. Schweinar[3], B. Gault[3,4], D.A. Schneider[1]

[1]Department of Earth and Environmental Sciences, University of Ottawa, Ottawa, Canada

[2]Department of Geology, University of Vienna, Vienna, Austria

[3]Max-Planck-Institut für Eisenforschung GmbH, Düsseldorf, Germany

[4]Department of Materials, Royal School of Mines, Imperial College London, London, UK

Published in

Contributions to Mineralogy and Petrology, Volume 174

August 2019

doi.org/10.1007/s00410-019-1611-5

2.1 Abstract

The links between deformation-induced micro- and nanostructures and trace element mobility in sulphide minerals has recently become a popular subject of research in the Earth sciences due to its connections with metallic ore paragenesis. It has been shown that plastic deformation in pyrite creates diffusion pathways in the form of low-angle grain boundaries that act as traps for base- and precious-metals. However, the plastic behavior of pyrite and the physiochemical processes that concentrate these trace elements in deformation-induced micro- and nanostructures remain poorly understood. In this study, we develop strategies for 2D and 3D analysis of naturally deformed sulphides by combining electron backscatter diffraction, electron channeling contrast imaging and atom probe tomography on pyrite in an attempt to better understand the underlying diffusion processes that mobilize trace elements. The combined results reveal structures associated with crystal-plastic deformation in the form of dislocations, stacking faults, and low-angle grain boundaries that are decorated by As and Co. Although our data support a dislocation-impurity pair diffusion model, we have evidence that multiple diffusion mechanisms may have acted simultaneously. In this study, we applied new data processing techniques that allow for orientation measurement of nanostructural crystal defects. Dislocations within our studied sample occur along the {110} planes suggesting glide on (110).

2.2 Introduction

As part of metallic ore paragenesis, sulphide phases are known to incorporate significant concentrations of lattice-bound and ultrafine inclusions of base- and precious-metals such as Au, Ag, Bi, and Te (Cook and Chryssoulis, 1990; Reich et al., 2005). Prevailing models suggest that metamorphism and crystal-plastic deformation of sulphides can liberate these trace elements leading to their remobilization and concentration into economically viable deposits (Craig and

Vokes, 1993; Tomkins and Mavrogenes, 2001; Large et al., 2007). It has been demonstrated that crystal-plastically deformed arsenopyrite reveals microstructures in the form of low-angle grain boundaries, which act as conduits for fluids that leach lattice-bound gold from the host mineral under moderate temperature conditions (340-460°C; Fougerouse et al., 2016a). Consequently, arsenopyrite exhibits discrete, intra-crystalline gold-depleted zones. In marked contrast, comparable investigations of pyrite illustrate that plastic deformation creates diffusion pathways as low-angle grain boundaries that instead act as traps for base- and precious-metals (Dubosq et al., 2018). This phenomenon was documented in rocks that witnessed lower amphibolite facies conditions (550°C; Oliver et al., 2011). The broader implications of these results challenge a widely accepted model that gold from orogenic deposits is locally derived from diagenetic pyrite within the deforming and metamorphosing sedimentary successions (Large et al., 2007; Gaboury, 2013). Although we now know that crystal-plastic deformation of sulphides can not only result in the leaching of base- and precious-metals and creation of microstructural traps, the crystal-plastic behavior of pyrite and the geochemical and mechanical processes that concentrate these trace elements in deformation-induced nanostructures remain poorly understood.

Investigations on the chemical response of trace elements in minerals during crystal-plastic deformation, has previously been limited by the lack of micro-analytical tools with high spatial resolution. Initial studies that proved a clear spatial relationship between trace elements and deformation-induced microstructures combined a battery of 2D microstructural and geochemical analyses, most commonly including orientation contrast imaging (OC), electron backscatter diffraction (EBSD), electron microprobe analyses (EMPA), laser ablation inductively coupled mass spectrometry (LA-ICP-MS), sensitive high-resolution ion microprobe (SHRIMP), and secondary ion mass spectrometry (SIMS) (Büttner and Kasemann, 2007; Dubosq et al., 2018;

Fougerouse et al., 2016b; Moser et al., 2009, 2011; Piazolo et al., 2012; Reddy et al., 2006, 2009; Timms et al., 2006, 2011; Vukmanovic et al., 2014). Whereas many diffusion models have been proposed to explain this relationship, identifying the specific mechanisms responsible for the nano-scale heterogeneities remained unclear. In recent years, 3D nanostructural and nanochemical analytical techniques typically used in material sciences are rapidly finding new applications in the fields of Earth sciences. Investigations into the diffusion of trace elements relative to microstructures now integrate innovative techniques such as transmission electron microscopy (TEM; Ando et al., 2001; Plümper et al., 2012; Reddy et al., 2007; Timms et al., 2012) and atom probe tomography (APT; Fougerouse et al., 2019; Kirkland et al., 2018; Peterman et al., 2016; Piazolo et al., 2016; Reddy et al., 2016; Seydoux-Guillaume et al., 2018). These studies have made significant advancements in understanding the diffusion mechanisms that can occur at the submicrometer scale, however, most investigate the impacts of trace element mobility on the reliability of geochronometers. Consequently, the impacts of trace element segregation during crystal plasticity on mineral micro-rheology and mineralization remain elusive.

In this study, we attempt to document the diffusion processes driving trace elements into deformation-induced microstructures of sulphides by developing new applications to 2D and 3D nanostructural and geochemical imaging techniques. Herein, we integrate EBSD mapping, electron channeling contrast imaging (ECCI) and APT on crystal-plastically deformed pyrite. While APT is currently the best tool with the capacity to measure 3D chemistry at the near-atomic resolution, it is limited by its spatial resolution in capturing structural and crystallographic information. Hence, recent studies have combined TEM, which is an excellent tool for 3D structural analysis at the nanoscale, together with APT (Herbig et al., 2015; Seydoux-Guillaume et al., 2018). However, challenges that arise by conducting TEM imaging before APT analysis, including carbon contamination, absorption of gaseous species, and formation of oxide layers, can cause embrittlement of the specimen and a reduction of the yield during APT analysis (Herbig et al., 2015). Thus, our study pushes the limits of the 3D tools' abilities by applying new data processing techniques (Kwiatkowski da Silva et al., 2017) that allow crystallographic-orientation measurement of nanostructural crystal defects using APT data alone. Using these protocols, we show metal enrichment within nanostructural defects, shedding light on the mechanisms of metal migration through the pyrite crystal during and following deformation events.

2.3 Methods

2.3.1 Electron backscatter diffraction mapping

Primary EBSD mapping was conducted on pyrite sites of interest to quantify the crystal-plastic deformation within the grains. All crystallographic data was collected at the Department for Lithospheric Research (University of Vienna, Austria) using a FEI Quanta 3D FEG instrument equipped with a field-emission electron source and an EDAX Pegasus Apex 4 System, which consists of a Digiview IV EBSD camera and an Apollo XV silicon drift detector for EDX-spectrometry. Thin sections for EBSD mapping were chemomechanically polished with an alkaline colloidal silica suspension (SYTON©) and subsequently carbon-coated to establish conductivity. Analytical conditions were set at a 15kV accelerating voltage with a spot size of 1 in analytical modus, a 4 nA probe current, at working distance of 14 mm and a sample tilt of 70°. EBSD mapping was performed using a hexagonal grid and a step size of 40 to 80 nm. EBSD data was cleaned using the OIM Data Collection and Analysis software by combining the neighbour orientation correlation (clean-up level: 1) and confidence index standardization (CI: 0.1) functions. Misorientation deviation angle (misorientation of each pixel relative to grain average) and grain boundary maps were then created by using the MTEX toolbox in Matlab (Bachmann et al., 2010).

The EBSD data allowed us to target two specific pyrite domains for further analyses via ECCI and APT: (1) the boundary between two pyrite grains; and (2) a pyrite grain with healed microfractures.

2.3.2 Electron channelling contrast imaging

In an attempt to further characterize deformation-induced microstructures within the sites of interest, we conducted ECC imaging. This imaging is a scanning electron microscopy (SEM) technique that allows for the direct observation of crystal defects using the backscatter electron detector (Naresh-Kumar et al., 2012, 2013; Zaefferer and Elhami, 2014; Rogowitz et al., 2018). Imaging via ECC was conducted at the Max-Planck-Institut Für Eisenforschung GmbH (Düsseldorf, Germany) using a Zeiss Merlin SEM with a Gemini-type field emission gun electron column and a Bruker e-Flash HR EBSD detector. Analytical conditions for imaging were set to a 30 kV accelerating voltage, a 2-4 nA probe current and a working distance between 6 and 8 mm.

2.3.3 Atom probe tomography

Further sites of interest within the ECC images were selected for 3D imaging and geochemical mapping. APT analyses were conducted to interrogate the atomic structure of the deformed zones in an attempt to characterize the physical state of base- and precious-metal hosted within these features giving insight into the transport mediums and the diffusion processes that mobilize them. Three of the selected sites are presented in this study.

2.3.3.1 Sample preparation and APT analytical conditions

Specimens for APT were prepared by in-situ lift-out following the protocol outlined in Thompson et al. (2007) on a dual beam scanning electron microscope / focused ion beam FEI Helios Nanolab 600i. Following sharpening by annular milling at 30kV, the specimens were cleaned by using the Ga-beam at 2 kV to remove the part of the specimen potentially severely damaged by the implantation of the energetic ions. Specimens were then analysed by APT in a Cameca LEAP 5000 XS or LEAP 5000 XR (Table S2.1), the former being a straight flight path instrument with a detector efficiency of ~80%, whereas the latter is fitted with a reflectron-lens with a detector efficiency of ~40-50%. The base temperature was maintained at 55 K, the specimens were analysed in laser pulsing mode, with a laser pulse energy of 45 pJ focused on an area estimated to be <3 micrometers in diameter. The detection rate was maintained on average at 1 ion detected for 100 pulses by progressively increasing the high-voltage. The laser pulse repetition rate was 125 kHz on the LEAP 5000 XR and 200 kHz on the LEAP 5000 XS allowed by the shorter times of flight of the ions in the straight flight path. The ranged mass spectrum used for all analytical specimens is shown in Figure S2.1.

2.3.3.2 Orientation analysis to optimize 3D reconstruction

The data processing and reconstruction was done with the commercial software package IVAS 3.8.2. Compositional profiles and 2D contour plots presented herein were generated from cubic regions of interest (ROI) using the 1D concentration profile and 2D contour plot function and computed using the *fixed bin width profile*, *atomic*, and *decompose complex ions* options. The bin size was adjusted for each profile (0.2-0.5 nm) to optimize the quantitative results.

The details of the reconstruction protocol can be found in Larson et al. (2013). To ensure an accurate reconstruction of the data, the image compression factors (ξ) were calibrated by using the relationship:

$$\xi = \frac{\theta_{crys}}{\theta_{obs}} \qquad \text{(Eq 1)}$$

where θ_{crys} is the theoretical angle between two crystallographic directions and θ_{obs} is the observed angle (Gault et al., 2008). Herein we identified the 111 and 002 poles projected onto the detector event histogram of each dataset, which occur as low detected event areas due to the deviation of the electrical field by facets centered around major crystallographic poles (Figure S2.2a; Gault et al., 2012a). The identification of the poles was confirmed by comparing the measured ratio of the of the lattice spacing along each pole ($D_{002\ measured}/D_{111\ measured}$) to the theoretical ratio ($D_{002\ theory}/D_{111\ theory}$). Note the crystallographic poles in each dataset were identified by overlaying a stereographic projection of a face-centered-cubic (fcc) structure with a unit cell of 5.47 Å produced using the WinWULFF 1.6.0 software (Weber, 2018). The value of θ_{crys} of 54.7° is known, and we calculated θ_{obs} by using:

$$\theta_{obs} = \frac{\tan^{-1}(d/L)}{\pi} * 180 \qquad \text{(Eq 2)}$$

where *d* is the measured distance between the two crystallographic directions (measured from the detector event histogram) and *L* is the flight distance from the specimen of the analysed specimen and the detector (Gault et al., 2012a), which is 100 mm for the LEAP 5000 XS. For the LEAP 5000 XR, a similar protocol could not be directly applied because of the reflectron that is on the path of the ions which curves the ion trajectories. For these datasets, we used a value for the flight path of ~40 mm that is a reasonable approximation of the distance where the angular field-of-view corresponds to that observed on the detector past the reflectron (Humphrey-Baker, 2009). We then calculated the initial specimen radius, R_0, by using:

$$R_0 = \frac{V}{k_f F_e} \qquad \text{(Eq 3)}$$

where *V* is the applied voltage, K_f is the field reduction factor and F_e is the evaporation field (Gault et al., 2009), assuming a F_e value of 30 Vnm^{-1} (Ohnuma, 2017), which is the tabulated value for pure Fe. The value K_f was adjusted so as to obtain an interplanar spacing consistent with the structure of pyrite (Figure S2.2b). Reconstruction parameters were set to an image compression factor (ξ) ranging from 1.71-1.74 (LEAP 5000 XS) and 1.46-1.54 (LEAP 5000 XR) and an R_0 ranging from 11.8-14.5 nm (LEAP 5000 XS) and 18.8-43.5 nm (LEAP 5000 XR).

By using these parameters, we were able to manually add the 002 and 111 crystallographic poles previously identified from the detector event histograms for each APT dataset in the respective reconstruction. The (x,y) positioning of the poles was achieved by generating 2D contour plots of all detected ions perpendicular to the analytical axis (z) of the specimen, which revealed the poles as low concentration areas (similar to detector event histograms; Figure S2.3a). The orientation of the poles was then manually adjusted to plot perpendicular to the corresponding crystallographic planes, which were visible in the APT data reconstructions (Figure S2.3b-c). Once plotted in the reconstruction, we were able to measure their angles relative to the observed nanostructures (Figure S2.3d; Gault et al., 2012b). The orientation of each structure has been plotted onto a stereographic projection for analysis.

2.4 Sample description and selection of sites of interest

The investigated sample of our study possesses a brecciated pyrite layer at the margin of a mineralized sulphidized quartz-calcite vein hosted in a mafic volcanic rock from the Detour Lake deposit, Canada (Figure 2.1a; Dubosq et al., 2018; Oliver et al., 2011; Rogowitz et al., 2018). Grains within the pyrite layer are strongly fractured with a wide range of fragment sizes (50 to 3000 µm; Figure 2.1b). Observations from a previous study suggest the investigated sample has been affected by at least two elevated fluid-pressure events of which one is causing the brecciation of the pyrite layer (Rogowitz et al., 2018). The host rock's metamorphic mineral assemblage (actinolite- biotite- plagioclase- epidote- almandine ± calcite ± quartz ± ilmenite; Oliver et al., 2011) suggest the sample was subjected to lower amphibolite facies conditions. However, sutured

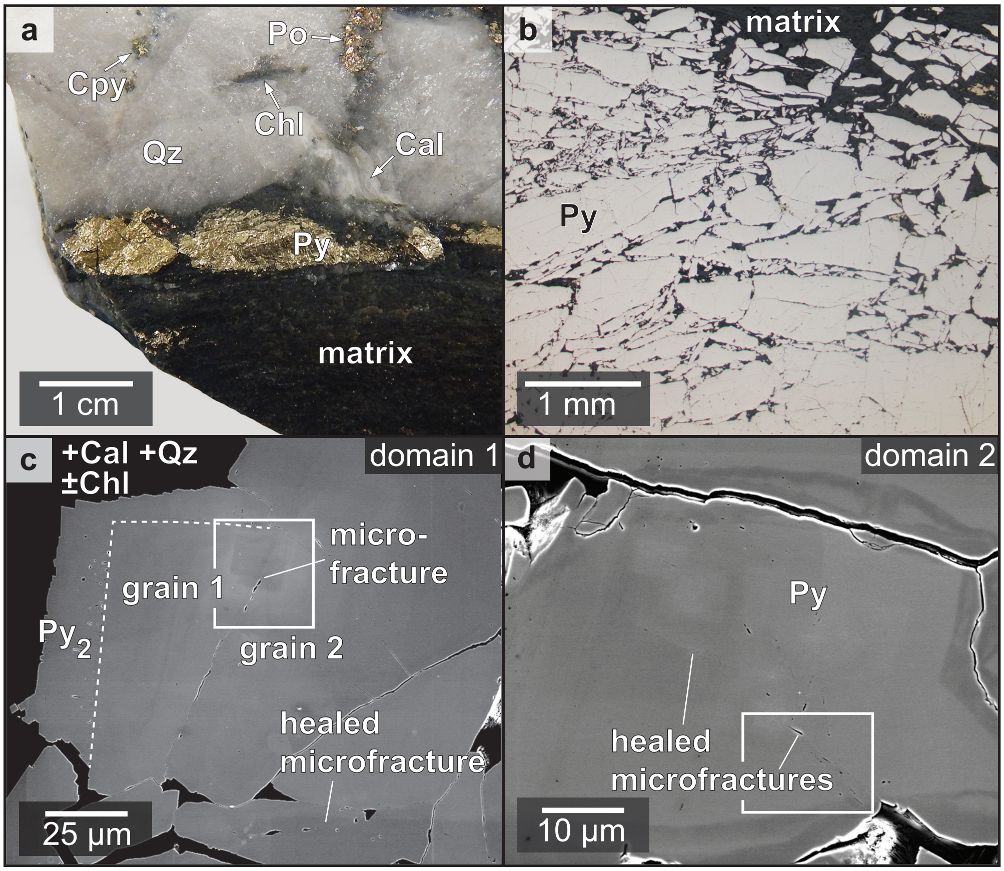

Figure 2.1. a. Hand sample photo of the brecciated pyrite layer at the margin of a sulphidized quartz-calcite vein and a mafic volcanic host rock composed of actinolite-biotite-plagioclase-epidote-almandine ±calcite ±quartz ±ilmenite (modified from Rogowitz et al., 2018). **b.** Reflected light photomicrograph of the brecciated fragment layer revealing the wide range of fragment sizes (50 to 3000 µm; modified from Rogowitz et al., 2018) **c.** Backscatter image of pyrite fragments in domain 1 highlighting the site of interest at the intergranular microfracture between grains 1 and 2. Note, pyrite overgrowth at the rim of grain 1 delineated by inclusion trail (dashed white line). White box indicates location for Figure 2.2b. **d.** Backscatter image of pyrite fragment in domain 2 displaying healed microfractures traced by inclusion trails. White box indicates location for Figure 2.4a.

grain boundaries with minor bulging in vein quartz and cracks sealed by carbonate, quartz, and chlorite indicate that brecciation and ongoing deformation were at greenschist facies conditions (Rogowitz et al., 2018).

In this study, we focus on two pyrite domains within the brecciated layer. Domain 1 consists of pyrite fragments ranging between 25-100 μm in diameter forming a puzzle-like structure (Figure 2.1c; also see Figure 2.1c of Rogowitz et al., 2018). Healed microfractures resulting in inclusion trails can be observed in some pyrite fragments. A secondary pyrite growth, which is delineated by an inclusion trail, is documented at the margins of grain 1. The main site of interest within this pyrite domain is the high strain area between pyrite grains 1 and 2 showing a microfracture at their grain boundary (Figure 2.1c). Domain 2 consists of a single pyrite fragment ~75 μm in diameter with multiple healed microfractures, similarly evinced by inclusion trails (Figure 2.1d).

2.5 Results

2.5.1 2D microstructural analysis

EBSD maps of pyrite domain 1 exhibit evidence for crystal-plastic deformation within the brittle-dominated pyrite fragments (Figure 2.2). Deviation angle and grain boundary maps of the area reveal linear to more heterogeneous misorientation patterns with a maximum misorientation of 10° (Figure 2.2a). Minor development of partial low-angle grain boundaries (5-10°) occurs at or near the boundary of larger deformed grains (Figure 2.2). The grain boundary between the two largest grains was selected for further analysis (Figure 2.2b). Grain 1 reveals very minor to no crystal-structure rotation barely detectable by conventional EBSD (<1°). Comparatively, grain 2 reveals more significant crystal-structure rotation with a maximum misorientation angle of 10° from the calculated grain average misorientation. Higher strain areas in domain 1 occur close to grain

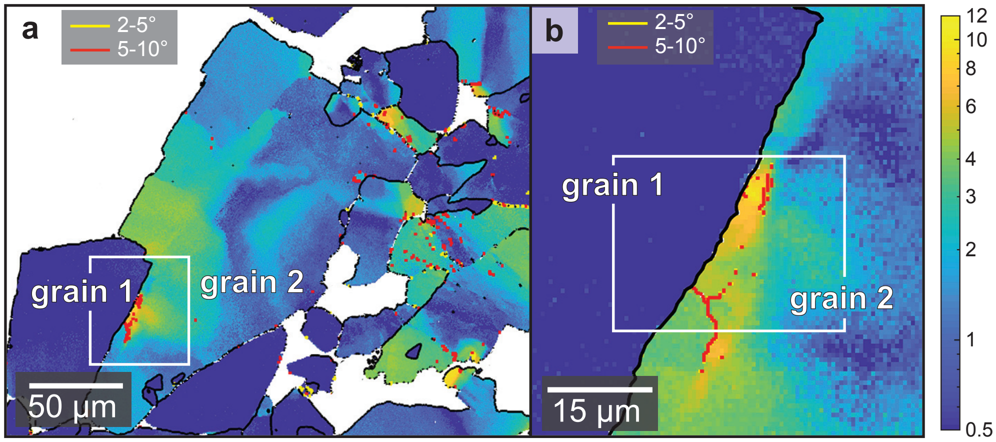

Figure 2.2. Deviation angle and grain boundary maps (via EBSD) of pyrite domain 1 within brecciated pyrite layer. Note the logarithmic color scale. **a.** Overview of area showing linear to more complex misorientation patterns with a maximum crystal lattice rotation of 10° and low-angle grain boundary (red and yellow) development within pyrite fragments. Smaller recrystallized grains (black boundary) also occur at the rim of the larger pyrite fragment (grain 2). **b.** Close-up view of area of interest (white box in a.) near the grain boundary between two pyrite grains revealing almost no evidence for plastic deformation within grain 1 and more significant evidence within grain 2 in the form of a heterogeneous misorientation pattern and low-angle grain boundary development. White box indicates location for Figure 2.3a.

boundaries and are made evident by crystal-structure misorientations of up to 10° and the development of partial low-angle grain boundaries at the boundary between the grains. One of these high-strain areas occurs at the boundary between grains 1 and 2 (Figure 2.2b).

Further analysis of pyrite domain 1 using ECCI reveals a microfracture between the two pyrite grains that was otherwise not observed (Figure 2.3a, b). These images also show possible fluid- and metal-inclusions at the tip of this microfracture (black and white spots, respectively; Figure 2.3b). In accordance with EBSD results, ECCI documents the presence of crystal defects within the two pyrite grains. Similar to the low detection of misorientation within grain 1, ECC images reveal a small density of free dislocations (Figure 2.3a). Comparatively, grain 2 evinces significant crystal-plastic deformation by revealing a higher dislocation density, stacking faults, bend contours, and low-angle grain boundaries (Figure 2.3a, b). In both grains, dislocations are visible as white dots and rather short and curved bright line segments. Stacking faults appear as very narrow and discrete straight lines with grey value variations on either side, perpendicular to dislocations. The bend contours in grain 2 appear as wider (0.25-0.5 μm) bands of varying grey value in a zone of increased dislocation density, which appears to propagate from the microfracture in a step-like pattern (Figure 2.3). These bend contours appear very similar to low-angle grain boundaries in ECCI and can only be confirmed by EBSD. The EBSD misorientation angle deviation map in Figure 2.2b confirms that one of the lines occurring with the bend contours is in fact a low-angle grain boundary. We assume that this low-angle grain boundary is the line with the largest grey value variation on either side of it in the ECC image. The subgrain within grain 2 appears as an area of brighter grey value delineated by aligned dislocations forming a low-angle grain boundary. On the basis of these micro- to nanostructural observations, we prepared two specimens specifically from this area for further structural and geochemical analysis by APT ('i'

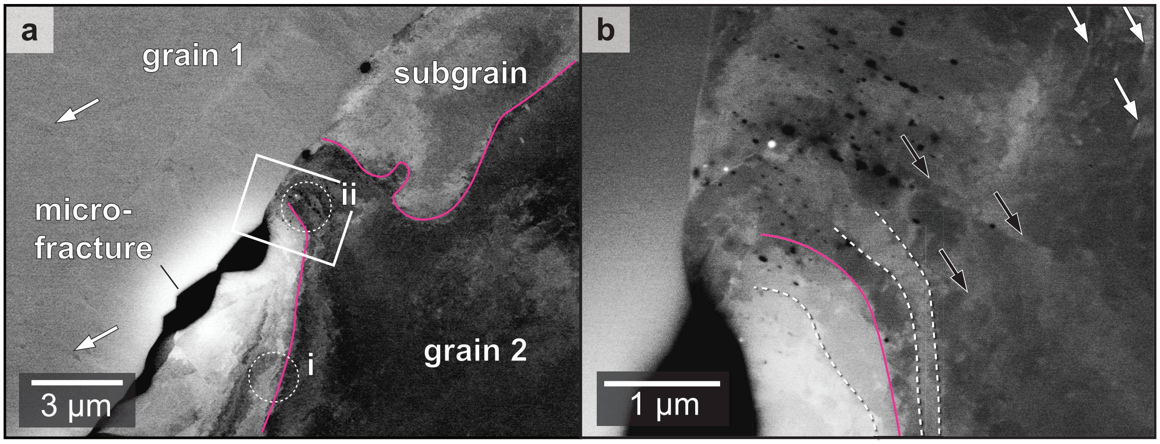

Figure 2.3. a. ECC image of site of interest at the grain boundary within pyrite domain 1 between the mostly undeformed grain 1 (few free dislocations illustrated by white arrows) and the more significantly crystal-plastically deformed grain 2. The image unveils a microfracture at the grain boundary, significant crystal distortion within grain 2 (grey value variations), a subgrain within grain 2 near the specimen of the microfracture, and a subgrain boundary on the right of the microfracture (subgrain boundaries are traced by pink lines). Locality of APT specimens ‘i’ and ‘ii’ are indicated by white dashed circles. **b.** Close-up view at the specimen of the microfracture (white box in a.) revealing fluid and metal inclusions (black and white spots, respectively), dislocations (white arrows), stacking faults (black arrows), bend contours (white dashed lines), and a subgrain boundary (pink line).

and 'ii'; Figure 2.3a). Specimen 'i' is located in the area with an increased dislocation density within the bend contours and specimen 'ii' is located at the tip of the microfracture, which contains the fluid- and metal-inclusions.

EBSD data of pyrite domain 2 reveal much less evidence for crystal-plastic deformation (Figure 2.4a). Only a very subtle linear misorientation pattern is observed with a maximum misorientation of 3° relative to the grain's average orientation. Minor low-angle grain boundaries can be observed at the healed microfractures. An area at the tip of a microfracture was selected for further analysis (Figure 2.4a).

ECC images of this pyrite domain reveal the tip of a microfracture containing metal-inclusions (Figure 2.4b). In accordance with EBSD data, the ECC images do not show a significant amount of crystal defects. Only very minor crystal distortion is observed in the form of grey value variation, free dislocations and stacking faults (Figure 2.4). However, compared to domain 1, the density of observed linear and planar defects appears significantly lower within domain 2. Based on these observations, we selected an area that appeared to be the least deformed and prepared one needle-shaped specimen from this pyrite domain for further 3D nanostructural and geochemical analysis (APT specimen 'iii'; Figure 2.4a). This specimen allows for the comparison of trace element distribution between the significantly more crystal-plastically deformed specimens of pyrite domain 1 and this less deformed pyrite domain 2.

2.5.2 3D nanostructural and geochemical analysis

Based on APT analysis, the reconstruction of specimen 'i' reveals individual linear defects (i.e., dislocations) highlighted by elevated As compositions ranging from 0.25-0.52 at% (Figure 2.5a, Figure S2.4; Makineki et al., 2018a, 2018b, 2018c). A subgrain (low-angle grain) boundary composed of three aligned dislocations occurs at high-angles from the specimen axis (Figure 2.5c-

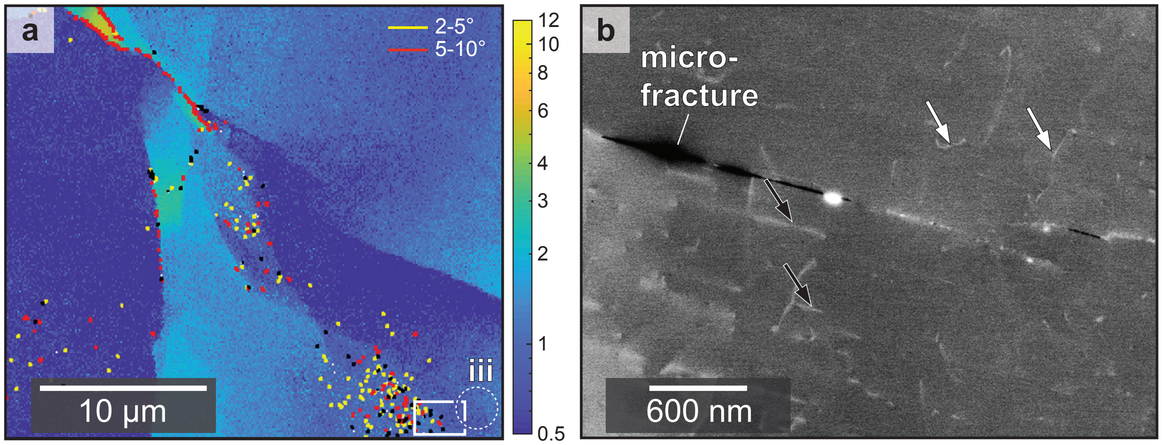

Figure 2.4. a. Deviation angle and grain boundary maps (via EBSD) of pyrite domain 2 within brecciated pyrite layer revealing minor crystal lattice rotation (logarithmic color scale) with a maximum misorientation of 3° relative to the grain's average orientation. Low-angle boundaries (red and yellow) occur at microfractures within the pyrite grain. Note the smaller red, yellow and black circles near the lower right corner of the map represent misindexed points rather than high- and low-angle grain boundaries. The location of APT specimen 'iii' is demontrated in the dashed white circle. **b.** ECC image of site of interest within pyrite domain 2 revealing minor crystal distortion in the form of grey value variation, dislocations (white arrows), and stacking faults (black arrows). Metal inclusions (bright spots) occur within microfractures.

d). The structures are enriched in As at compositions ~2-3x above matrix-level background (0.00-0.18 at%), confirmed by composition profiles across the linear and planar structures (Figure 2.5e, Figure S2.4). One of these profiles across a dislocation reveals a depletion in As directly adjacent to (within 0-2 nm) the defect (Figure 2.5c). Some of these documented defects are additionally decorated by Co with compositions ranging from 0.41-0.74 at%, that are ~2x above the matrix-level compositions (0.10-0.42 at%), however the distribution of Co within the specimen is mostly homogeneous (Figure 2.5b). Another composition profile through the matrix between the documented nanostructures reveals As compositions ranging between 0.01-0.02 at% and Co compositions ranging from 0.17-0.24 at% with averages of 0.03 at% and 0.21 at%, respectively (Figure S2.5a, Table S2.2).

The reconstruction of specimen 'ii' also reveals individual dislocations that are enriched in As, Co, or both (As: 0.27-0.88 at%; Co: 0.39-0.69 at%; Figure 2.6a-c, S2.6). Most of the dislocations in this reconstruction also occur at high-angle to the specimen's main axis. Peak As compositions within the dislocations are elevated ~2-4x above that of the matrix (0.00-0.20 at%) whereas the peak Co composition are only ~1.5-2x above that of the matrix (0.10-0.30 at%; Figure S2.6). In addition to dislocations, the reconstruction shows planar defects in the form of stacking faults that are again enriched in As and Co (Figure 2.6a-c, S2.6). Stacking faults in APT reconstructions occur as planar features highlighted by solute enrichment trailing a leading dislocation front with elevated solute concentrations ahead of the leading dislocation (Figure 2.6f; Makineki et al., 2018a, 2018b, 2018c). Compositional values of As and Co within the stacking faults' dislocation fronts are 0.63-1.02 at% and 0.44-0.70 at%, respectively (Figure 2.6d, S2.6). Composition profiles along these planar structures (perpendicular to the dislocation front) show a monotonic increase in As composition, which is at a high point at the dislocation front (Figure

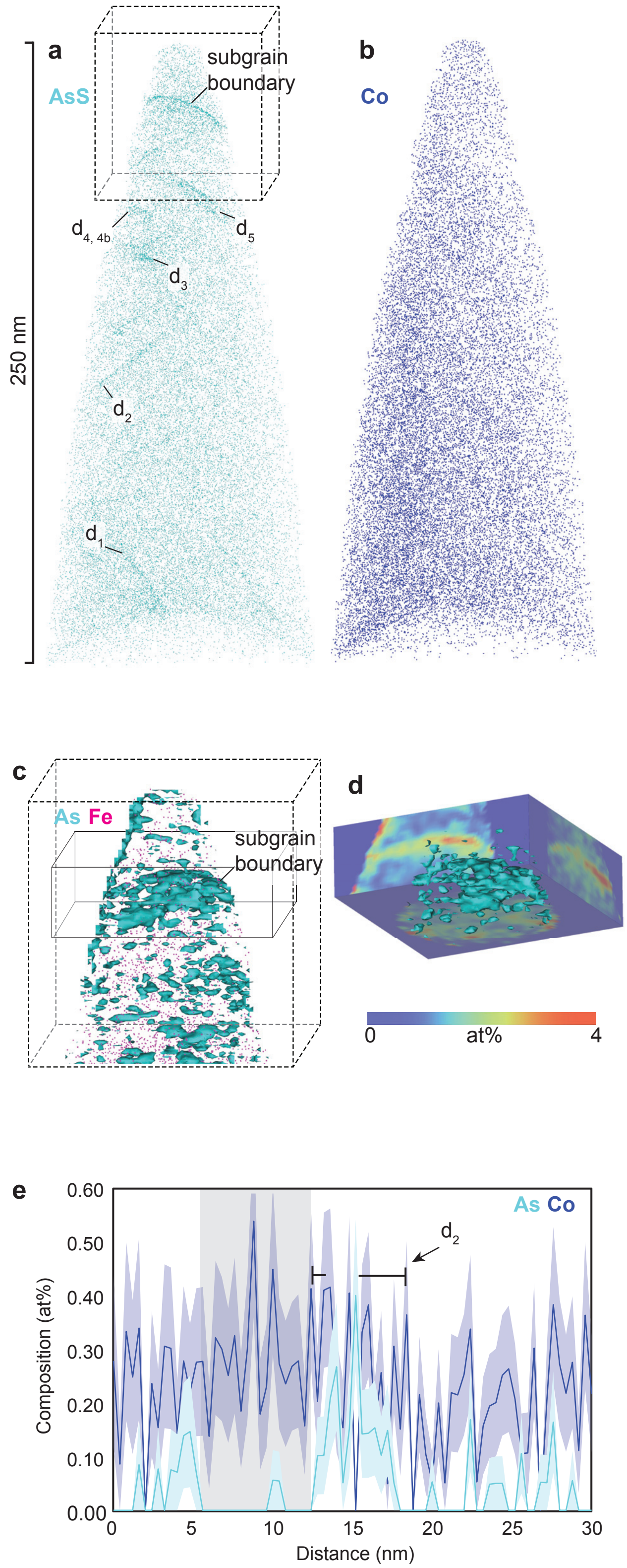

Figure 2.5. a. Reconstruction of APT specimen 'i' displaying the distribution of AsS ions (turquoise dots) and revealing microstructures in the form of dislocations and low-angle grain (subgrain) boundaries. **b.** Reconstruction of APT specimen 'i' demonstrating the homogeneous distribution of Co atoms (blue dots). **c.** Close-up reconstruction of the tip from specimen 'i' illustrating the distribution of Fe atoms (pink dots) and increased As concentrations in a subgrain boundary (turquoise isosurfaces; 0.3% isovalue). **d.** Clipping of region of interest surrounding subgrain boundary with 2D contour plots of As along x-, y-, and z-axes revealing elevated As concentration along a planar feature. **e.** Concentration profile across dislocation 2 showing a As peak near 0.4 at% which is preceded by a As depletion (vertical grey box) in the vicinity of the dislocation and a relatively homogeneous distribution of Co concentrations.

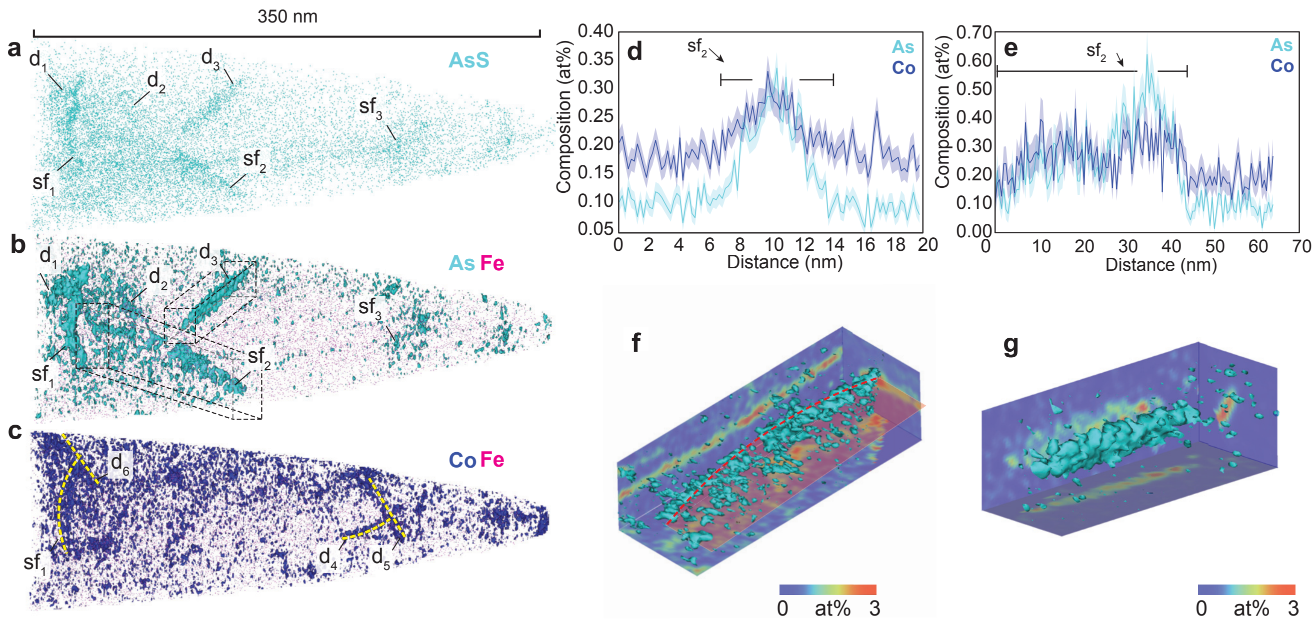

Figure 2.6. a. Reconstruction of APT specimen 'ii' showing the distribution of AsS ions (turquoise dots) and revealing microstructures in the form of dislocations and stacking faults. **b.** Reconstruction of APT specimen 'ii' displaying the distribution of Fe atoms (pink dots) and elevated As concentrations (turquoise isosurfaces, 0.35% isovalue). Arsenic isosurfaces also reveal microstructures in the form of dislocations and stacking faults decorated with elevated As concentrations. **c.** Reconstruction of APT specimen 'ii' displaying the distribution of Fe atoms (pink dots) and elevated Co concentrations (blue isosurfaces, 0.7% isovalue). Cobalt isosurfaces unveil microstructures in the form of dislocations and stacking faults decorated with elevated Co concentrations (outline in yellow dashed lines). **d.** Concentration profile across stacking fault 2 with As and Co peaking at the dislocation front (0.34 and 0.33 at%, respectively). **e.** Concentration profile along stacking fault 2 (perpendicular to dislocation front) showing a steady increase of As concentration, reaching a maximum at the dislocation front, and a more constant Co concentration only slightly reaching maximum values at the dislocation front. **f.** Clipping of region of interest surrounding stacking fault 2 with 2D contour plots of As along x-, y-, and z-axes illustrating elevated As concentration along a planar feature (traced by red plane) with higher concentrations along a linear (dislocation) front (outlined in red dashed line). **g.** Clipping of region of interest surrounding dislocation 3 with 2D contour plots of As along x-, y-, and z-axes revealing elevated As concentration along a linear feature.

2.6e, 2.S4), consistent with observations of Makineni et al. (2018a, b). Cobalt profiles, however, reveal a homogeneous composition along the stacking fault only slightly rising at the dislocation front (Figure 2.6e, S2.6). A composition profile through the matrix between the documented nanostructures reveals As compositions ranging between 0.00-0.06 at% and Co compositions ranging from 0.02-0.07 at% with averages of 0.04 at% and 0.06 at%, respectively (Figure S2.5b, Table S2.2).

In comparison, the reconstruction of specimen 'iii' did not reveal any linear or planar defects and instead shows a mostly homogeneous distribution of trace elements including As and Co (Figure 2.7a-b). A composition profile across the entire specimen reveals As compositions ranging between 0.01-0.07 at% and Co compositions ranging from 0.40-0.66 at% (Figure 2.7c, S2.7), providing a view of the amplitude of compositional heterogeneity that can be expected within the specimen's undeformed domains. The As composition documented in this specimen falls within the range of As matrix compositions of specimens 'i' and 'ii', whereas the Co composition significantly exceeds the range of Co matrix compositions within these.

In addition to the 3D imaging and geochemical analysis of the nanostructures observed within domain 1, further processing of the APT data allowed for the orientation of each documented structures to be measured. The orientations of the linear structures, and the poles to the planar structures (i.e., low-angle grain boundary, stacking faults) for both specimens were plotted on an azimuthal equidistant stereographic projection (Figure 2.8; De Geuser and Gault, 2017). The APT data shows that most of the dislocations and poles to planar structures plot along (±5°) the 110 planes.

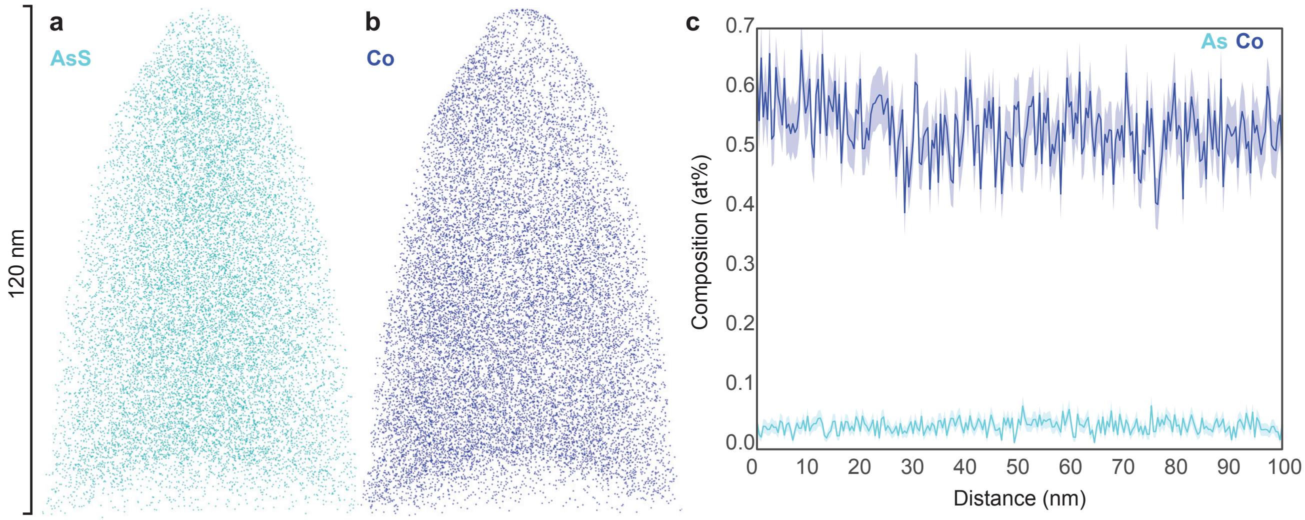

Figure 2.7. Reconstruction of APT specimen ‘iii’ showing the homogeneous distribution of **a.** AsS ions (turquoise dots) and **b.** Co atoms (blue dots). **c.** Concentration profile across the specimen supporting the observation of the homogeneous distribution of As and Co with matrix concentrations ranging between 0.02-0.05 at% and 0.40-0.65 at%, respectively.

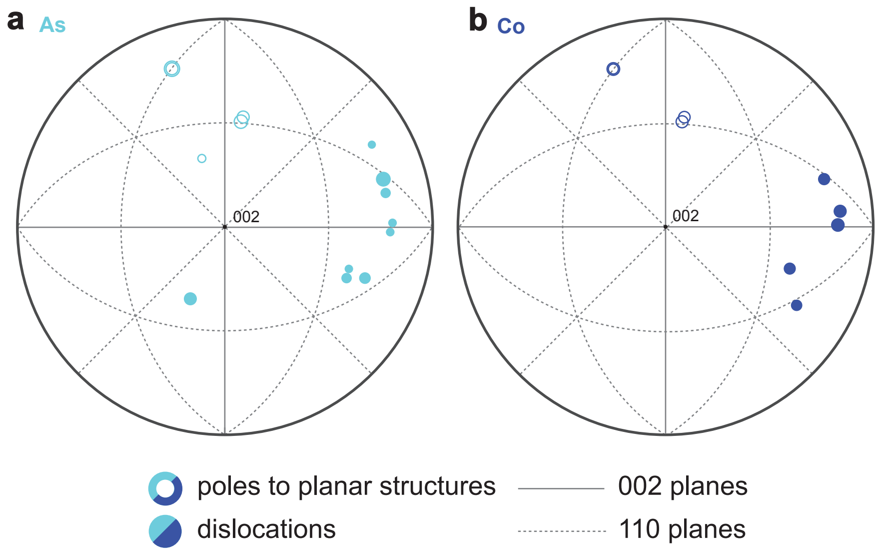

Figure 2.8. a. Scatter plot of As-rich microstructures onto an azimuthal equidistant stereographic projection relative to 002 and 110 planes. Marker sizes correspond to the peak As atomic concentrations within the plotted structures. **b.** Scatter plot of Co-rich microstructures onto an azimuthal equidistant stereographic projection relative to 002 and 110 planes. Marker sizes correspond to the peak atomic Co concentrations within the plotted structures. Both As- and Co-rich microstructures appear to be preferentially oriented (±5°) along the 110 planes.

2.6 Discussion

2.6.1 Crystal-plastic deformation of pyrite

Our 2D and 3D nano- and microstructural data reveal linear to more complex misorientation patterns and the development of low-angle grain boundaries (Figure 2.2, 2.4a). Upon closer inspection, nanoscale structures including dislocations, stacking faults, and possibly bend contours are observed (Figure 2.3, 2.4b, 2.5, 2.6). The herein identified bend contours described as wide bands of varying orientation in a zone of increased dislocation density, could possibly be a result of microfracturing rather than dislocation-glide and creep. These combined nano- and microstructures show evidence for notable crystal-plastic deformation within the fractured pyrite layer. Although the metamorphic assemblage of the host rock indicate peak conditions of lower amphibolite facies, the occurrence of crystal-plastic microstructures in the vicinity of brittle features (i.e., microfractures) indicates that brittle and crystal-plastic deformation were coeval, suggesting the sample was deformed within the brittle-ductile transition zone, proposed to range from 260°C (Barrie et al., 2011) to 450°C (Cox et al., 1981; Graf et al., 1981) for pyrite. Such conditions are also consistent with the second brecciation event reported by Rogowitz et al. (2018) where cracks sealed by fluid inclusion-rich quartz and chlorite indicate ongoing deformation at greenschist facies conditions. Although the development of low-angle grain boundaries in domain 1 (Figure 2.3) can be linked to strain accommodation by dislocation-creep, the rather low crystal defect density and lack of dislocation arrays together with micro-cracks in domain 2 argues that low-angle grain boundaries detected by EBSD are likely relicts of healed micro-fractures.

Previous studies on naturally and experimentally deformed pyrite have documented three slip systems for accommodating strain in pyrite, including {001}<100>, {001}<110>, and {110}<001>, with the first being the most commonly reported (Barrie et al., 2008; Couderc et al., 1980; Levade et al., 1982; Shyh-Long and Pouyan, 1987). Our orientation analysis of the documented nanostructures within the APT data shows that most dislocations and poles to planar structures (i.e., stacking faults and subgrain boundaries) plot along (parallel) the 110 planes (Figure 2.8) suggesting possible slip on {110}. The results of our orientation analysis are consistent with the results of the slip lines trace analysis on ECCI images of this sample reported in Rogowitz et al. (2018), which suggest a possible active slip plane of (110) with Burgers vectors [001] and [00-1]. This APT-based orientation analysis has the capacity to analyze small features that otherwise cannot be resolved by other orientation imaging microscopy techniques such as transmission Kikuchi diffraction (TKD; Trimby, 2012). The precision of the structural measurements, however, is limited by the spatial resolution of the APT data, which is dependent on the material and the measurement conditions. The ideal material for crystallographic analyses has few alloying elements, thus the complex compositional range of pyrite poses some challenges. The irregular field evaporation behavior the atomic planes due to the compositional variability obscures the resolution of crystallographic poles on event detector histograms and consequently lattice planes in reconstructions. Since our orientation analysis is based on the identification and positioning of crystallographic poles in APT reconstructions, the error associated with each measurement increases with lower spatial resolution. Although we have identified the possible slip planes, we were not able to constrain the specific slip systems. Thus, orientation analysis of nanostructures within the APT data should be combined with EBSD or ECCI analyses for higher precision.

2.6.2 Diffusion mechanisms of trace elements

Our 3D nanostructural and geochemical data reveals the segregation of trace elements such as As and partially Co into deformation-induced nanostructures including dislocations, low-angle boundaries, and stacking faults (Figure 2.5a, 2.6a-c). Although trace element segregation into deformation nanostructures has been the subject of many studies in material sciences, only a few studies have reported this phenomenon in geological materials (Fougerouse et al., 2019; LaFontaine et al., 2017; Peterman et al., 2016; Piazolo et al., 2016; Reddy et al., 2016). A recent study on zircon documents the atomic-scale distribution of trace elements including Al, Pb, U and Y within single dislocations and dislocation arrays arguing for a 'pipe' diffusion model where trace elements move along dislocation arrays that are connected to chemical or structural sinks (Piazolo et al., 2016). An investigation on trace element mobility in pyrite reported similar results where Pb, Sb, Ni, Tl and Cu decorate entangled dislocations and Pb, As, Ni, Co, Sb and Bi decorate high-angle grain boundaries (Fougerouse et al., 2019). Although these data suggest 'pipe' diffusion of trace elements along dislocation cores into structural sinks and along high-angle grain boundaries (Love, 1964), the results also support a model where the trace elements are initially captured by Cottrell atmospheres created by the moving dislocations (Cottrell and Bilby, 1949). The latter is consistent with dislocation-impurity pair (DIP) diffusion (Petukhov and Klyuchnik, 2012).

Both 'pipe' and DIP diffusion mechanisms can result in local trace element enrichment and can possibly explain our observations, nevertheless the driving forces are different. 'Pipe' diffusion requires a chemical potential gradient and is often associated with dislocation arrays (Love, 1964), although some studies have shown that 'pipe' diffusion can occur along single dislocations where a chemical potential gradient is present (i.e., precipitates; Legros et al., 2008). This gradient can result from the presence of chemical or structural sinks within, or at either end of, dislocation cores and arrays. Chemical sinks can consist of precipitates and chemically enriched or depleted zones (Legros et al., 2008; Piazolo et al., 2016), whereas structural sinks can consist of the core-to-core overlap of entangled dislocations, which can lead to the trapping of trace elements and the formation of precipitates (Fougerouse et al., 2019). Since we do not record any evidence of a chemical potential gradient, we propose that our dataset dominantly records DIP diffusion. However, although we do not have any unequivocal proof of 'pipe' diffusion in the investigated sample, we document a low-angle grain boundary that is enriched in As in specimen 'i' (Figure 2.5a, 5c-d), therefore we cannot completely reject the activity of 'pipe' diffusion.

Unlike simple volume or 'pipe' diffusion, DIP diffusion does not require any assumptions about chemical potential gradients. Instead, impurities are attracted to dislocation cores by a strain field or 'capture zone' that is created by the dislocations. The force attracting impurities to a dislocation can be explained by a gradient of the interaction energy, which is proportional to the relative spacing between atoms within the crystal-structure (Cottrell, 1953a). Trace element depletion below matrix (background) composition level on one side of a dislocation is also consistent with DIP diffusion. This can be observed in the composition profile across dislocation 2 (d_2) within specimen 'i' where the As compositions are below the matrix average composition of ~0.10 at% to 0 at% before climbing to ~0.40 at% within the dislocation core (Figure 2.5e). This phenomenon has been observed in other mineral phases as well, where trace element depleted zones were attributed to a 'capture zone' or a Cottrell atmosphere (Cottrell and Bilby, 1949; Fougerouse et al., 2019; Piazolo et al., 2016). Such depletion however is not observed at or near every dislocation within the pyrite specimens we investigated. The absence of depleted zones in the wake of dislocations can possibly be explained by volume diffusion or the compositional variations may simply be below detection limits of the instrument. The attraction of impurities to dislocation cores would results in a chemical potential gradient that could drive As from within the pyrite matrix to redistribute into the depleted zones adjacent to the dislocations. However, it is also possible that we simply do not document the depletion due to the difficulty of positioning our analytical region of interest along the specific slip plane of the dislocation.

Our preferred model, however, becomes more complex when we compare the trace element compositions within the matrices of the mostly undeformed and strongly deformed specimens. In an ideal scenario, where the trace elements trapped within the dislocation cores originated from the crystal matrix, we would expect the trace element composition within the matrix of a deformed crystal to be lower than its initial composition before deformation. In our sample, the As composition of the matrix between nanostructures in specimens 'i' and 'ii' ranges between 0.01-0.02 at% and 0.00-0.06 at%, respectively (Figure S2.4-S2.6), which is slightly lower than the matrix composition of the mostly undeformed specimen ‘iii’ ranging between 0.01-0.07 at% (Figure 2.7c). This observation also supports our DIP diffusion model where As from the matrix is driven into the deformation-induced nanostructures as they migrate through the crystal structure. As for Co, its composition in the undeformed specimen (0.40-0.66 at%; Figure S2.5) also exceed that of the matrix within the deformed specimens 'i' and 'ii', which range between 0.17-0.24 at% and 0.02-0.07 at%, respectively (Figure 2.6d-e, Figure S2.4-S2.6). This observation could indicate that the Co was also internally derived and trapped within the nanostructures through DIP diffusion. However, the Co matrix composition within the undeformed specimen also exceeds the peak Co compositions of the dislocation cores within the deformed specimens (0.39-0.74; Figures 2.6d-e, S2.4, S2.6). The lower composition of Co within the dislocation cores in specimen 'i' compared to specimen 'ii' could either be attributed to less effective DIP diffusion due to lower Co concentrations or could be indicative of a second diffusion mechanism, such as 'pipe' diffusion, displacing Co out of the deformed crystal into a structural sink (i.e., microfractures). Unfortunately, there is no way of knowing whether the initial (undeformed) As and Co compositions between pyrite domains 1 and 2 were equivalent. Thus, any variations between their trace element matrix compositions may not be necessarily due to a diffusion mechanism and could simply represent a heterogeneous distribution of trace elements within the pyrite layer. Therefore, no definite conclusions can be made by comparing the relative trace element compositions within the matrices of strongly deformed specimens 'i' and 'ii' and mostly undeformed specimen 'iii'.

To summarize, our data best support a dislocation-impurity pair diffusion model and demonstrates that there may have been multiple diffusion mechanisms active during the brittle to crystal-plastic deformation of pyrite. We have provided nanostructural and geochemical evidence of trace elements (i.e., impurities) that have migrated toward dislocation cores leaving trace element depleted zones in the wake of the dislocations. This process results in a chemical potential gradient that can potentially drive volume diffusion within the crystal structure to homogenize the distribution of trace elements. The entrainment of trace elements within migrating dislocations leads to the formation of dislocation arrays (i.e., subgrain boundaries) that are consequently enriched in trace elements, create high diffusivity pathways and can potentially allow for 'pipe' diffusion to occur. Despite documenting a low angle grain boundary enriched in As, we do not have conclusive evidence for chemical potential gradients or trace element enriched structural sinks at either ends of the dislocation array to confirm that 'pipe' diffusion did occur within our sample.

2.6.3 Dislocation-impurity pair kinetics

The subject of the interplay between impurities and crystalline defects, including dislocations, has been lying at the research frontier of material sciences and has had a significant impact on improving the design of synthetic materials (Meng et al., 2017; Park et al., 2018; Raabe et al., 2017; Seebauer and Wook Noh, 2010; Yuan et al., 2018). Dislocation-impurity pair kinetics and their implications for the crystal-plastic behavior of geological materials however remains little investigated. As discussed, we know that impurities tend to be attracted to dislocation cores because their presence help reduce the free energy of the system by accommodating the stress field (Cottrell, 1953a). The size of this field is dependent on the lattice diffusion rate, which varies with temperature, relative ionic radii of impurities, and the bonding type (Heitjans and Karger, 2005). Although there is very little information on diffusion coefficients for As and Co in sulphides, it has been observed that elements with larger ionic radii tend to show a positive correlation with microstructures (Shannon, 1976). The similar ionic radius of As and Co however, makes it difficult to assess why most of our microstructures within the pyrite are decorated with As, whereas only a few are decorated with Co. Unfortunately, the spatial resolution of APT is insufficient to resolve whether As and Co are segregated to the same side of dislocations (i.e., compressive or tensile region).

It is generally understood that the presence of impurities within dislocation cores decreases the velocity of the dislocation and can potentially act as a barrier. It has recently been demonstrated that slower moving dislocations can trap impurities more efficiently (Petukhov and Klyuchnik, 2012); however, previous studies have suggested that at elevated temperatures and stress, the composition of impurities within a dislocation core can increase the dislocation's mobility by decreasing its activation energy (Imai and Sumino, 1983). These contradicting statements can be explained by the Portevin–Le Chatelier (PLC) effect (Chihab et al., 1987; Hähner et al., 2002; Kalk and Schink, 1992, 1998; Portevin and Le Chatelier, 1923). The PLC effect consists of a discontinuous mechanical response to a constant applied strain rate. The discontinuous or stick-slip motion of dislocations occurs when they encounter mobile impurities, which can temporarily arrest or pin the structures (Butt and Feltham, 1993; Neuhäuser, 1993). Note, pinning of dislocations requires large misfitting impurities within dislocation cores and dense Cottrell atmospheres (Cottrell and Bilby, 1949). As stress increases and reaches a critical value, the dislocations can be unpinned and move at high velocities (Ananthakrishna, 2007). This effect can be observed on stress-versus-strain curves as a series of stress drops and reloading sequences (Cottrell and Bilby, 1949; Cottrell, 1953b; Kubin and Estrin, 1985; Louat, 1981; McCormick, 1973; Penning, 1972; Van den Beukel, 1980). Under constant strain rate and temperature conditions, PLC stress serrations can only occur when the diffusivity of impurities and dislocations are of the same magnitude (Ananthakrishna, 2007). These nano-scale phenomena, which have been labeled as 'elastic depinning' (Fisher, 1998) also occur at the macroscale and mimic the motion of geological faults. Thus, it is a safe assumption that these stick-slip events at the nano-scale that result in localized crystal-plastic deformation can lead to hardening of materials and brittle fracturing (Mohles et al., 1999). Based on this theory, trace element diffusion induced by crystal-plastic deformation within minerals could potentially lead to premature strain-hardening and play a significant role in their deformational behavior. Taking this model further, the accumulation of impurities in dislocations produced at the tip of microfractures (Rogowitz et al., 2018; Gerberich et al., 2013) could lead to their pinning causing strain-hardening and potentially fracture propagation. Further investigations on DIP diffusion could lead to a better understanding of the behavior of materials and minerals and have a significant impact in the material sciences and geosciences.

2.6.4 Implications of As diffusion

Arsenic concentrations in pyrite have been strongly associated with the incorporation of Au at many types of metallic ore deposits (Agangi et al., 2013; Cline, 2001; Cook and Chryssoulis, 1990; Deditius et al., 2008; Emsbo et al., 2003; Foster et al., 2007; Frimmel et al., 2005; Huston et al., 1995; Large et al., 2007; McClenaghan et al., 2004; Morey et al., 2008; Muntean et al., 2011; Reich et al., 2005, 2013). In such deposits, Au in pyrite typically occurs as substitutional Au^{1+} or interstitial impurities (i.e., nanoparticules; Ciobanu et al., 2012; Palenik et al., 2004; Saunders, 1990; Simon et al., 1999a). Prevailing models suggest that the substitution of anionic As for S in tetrahedral structural sites enhances the incorporation of Au into Fe octahedral sites by distorting the crystal-structure (Deditius et al., 2008; Palenik et al., 2004; Simon et al., 1999b). As a result, the empirical solubility of Au in As-rich pyrite has been defined as $\boldsymbol{C_{Au} = 0.02 \times C_{As} + 4 \times 10^{-5}}$ at temperatures ranging between 150-250°C. Consequently, Au concentrations exceeding the solubility limit (Au:As = 1:200) results in the occurrence of Au nanoparticules instead of solid-solution Au (Au^{1+}; Chouinard et al., 2005; Reich et al., 2005; Simon et al., 1999a). Considering the metastable nature of solid-solution Au in pyrite, it is probable to assume that the migration of As into nanostructures in pyrite through DIP diffusion could lead to an overall As-depletion within the crystal matrix. This would increase the Au:As ratio and potentially exceed the solubility limit for Au in the pyrite crystal. The diffusion of As in pyrite could lead to the exsolution of structurally-bound Au in the form of liberated nanoparticules of native Au.

2.7 Conclusions

We have combined a battery of 2D and 3D nanostructural and geochemical analyses to reveal the diversity of intragrain nanostructures and their relationship with trace elements within deformed pyrite. Our data demonstrates that pyrite deformation in the investigated sample occurred at the brittle-ductile transition zone for pyrite under greenschist facies conditions. Intragrain nanostructures indicative of crystal-plastic deformation include: dislocations, stacking faults, and low-angle grain boundaries. These structures suggest that strain was accommodated by dislocation-glide and -creep with orientation measurements from APT data revealing slip occurred along {110} planes. APT analyses also revealed that single isolated dislocations, stacking faults, and low-angle grain boundaries have elevated compositions of As and Co. Although our APT specimen reconstructions and composition profiles best support a DIP diffusion model for the migration of trace elements during pyrite deformation, we also acknowledge that other diffusion mechanisms including volume and 'pipe' diffusion likely occurred simultaneously.

2.8 Acknowledgments

This project was funded by Detour Gold Corp., an SEGF student research grant (to RD), a GSA research grant (to RD), an NSERC grant (to DAS) and a postdoctoral award of the FGGA, Vienna (to AR). KS is grateful for financial support from the IMPRS-SURMAT graduate school. We greatly appreciated discussions and technical assistance from Gerlinde Habler (Vienna) and Stefan Zaefferer (Düsseldorf). Uwe Tezins and Andreas Sturm are thanked for their support of the APT and FIB facilities at MPIE. This paper benefitted from the thorough reviews by Denis Fougerouse, Sandra Piazolo, and Steve Reddy as editor.

2.9 References

Agangi A, Hofman A, Wohlgemuth-Uberwasser CC (2013) Pyrite zoning as a record of mineralization in the Ventersdorp contact reef, Witwatersrand Basin, South Africa. Econ Geol 108:1243–1272. doi.org/10.2113/econgeo.108.6.1243

Ananthakrishna G (2007) Current theoretical approaches to collective behavior of dislocations. Phys Rep 440(4–6): 113–259. doi.org/10.1016/j.physrep.2006.10.003

Ando J, Shibata Y, Okajima Y, Kanagawa K, Furusho M, Tomioka N (2001) Striped iron zoning of olivine induced by dislocation creep in deformed peridotites. Nature 414: 893–895. doi.org/10.1038/414893a

Bachmann F, Hielscher R, Jupp PE, Pantleon W, Schaeben H, Wegert E (2010) Inferential statistics of electron backscatter diffraction data from within individual crystalline grains. J Appl Crystallogr 43: 1338–1355. doi.org/10.1107/S002188981003027X

Barrie CD, Boyle AP, Cox SF, Prior DJ (2008) Slip systems and critical resolved shear stress in pyrite: An electron backscatter diffraction (EBSD) investigation. Mineral Mag 72: 1181–1199. doi.org/10.1180/minmag.2008.072.6.1181

Barrie CD, Pearce MA, Boyle AP (2011) Reconstructing the pyrite deformation mechanism map. Ore Geol Rev 39(4): 265–276. doi.org/10.1016/j.oregeorev.2011.03.006

Butt MZ, Feltham P (1993) Solid solution hardening. J Mater Sci 28(10): 2557–2576. doi.org/10.1007/BF00356192

Büttner SH, Kasemann SA (2007) Deformation-controlled cation diffusion in tourmaline: A microanalytical study on trace elements and boron isotopes. Am Mineral 92: 1862–1874. doi.org/10.2138/am.2007.2567

Chihab K, Estrin Y, Kubin LP, Vergnol J (1987) The kinetics of the Portevin-Le Chatelier bands in an Al-5at%Mg alloy. Scr Metall 21(2): 203–208. doi.org/10.1016/0036-9748(87)90435-2

Chouinard A, Paquette J, Williams-Jones AE (2005) Crystallographic controls on trace-element incorporation in auriferous pyrite from the Pascua epithermal high-sulfidation deposit, Chile-Argentina. Can Mineral 43: 951–963. doi.org/10.2113/gscanmin.43.3.951

Ciobanu CL, Cook NJ, Utsunomiya S, Kogagwa M, Green L, Gilbert S, Wade B (2012) Gold-telluride nanoparticles in arsenic-free pyrite. Am Mineral 97: 1515–1518. doi.org/10.2138/am.2012.4207

Cline JS (2001) Timing of gold and arsenic sulfide mineral deposition at the Getchell Carlin-type gold deposit, Northcentral Nevada. Econ Geol 96: 75–89. doi.org/10.2113/gsecongeo.96.1.75

Cook NJ, Chryssoulis SL (1990) Concentrations of invisible gold in the common sulphides. Can Mineral 28: 1–16.

Cottrell AH (1953a) Theory of dislocations. Prog Met Phys 4: 205–264. doi.org/10.1016/0502-8205(53)90018-5

Cottrell AH (1953b) A note on the Portevin-Le Chatelier effect. Philos Mag 44(355): 829–832. doi.org/10.1080/14786440808520347

Cottrell AH, Bilby BA (1949) Dislocation theory of yielding and strain ageing of iron. Proc Phys Soc A 62(1): 49–62. doi.org/10.1088/0370-1298/62/1/308

Couderc JJ, Bras J, Fagot M, Levade C (1980) Etude par microscopie electronique en transmission d'echantillons de blende de diverses provenances. Bull Mineral 103: 547–557. doi.org/10.3406/bulmi.1980.7419

Craig JR, Vokes FM (1993) The metamorphism of pyrite and pyritic ores: An overview. Mineral Mag 57: 3–18. doi.org/10.1180/minmag.1993.057.386.02

Cox SF, Etheridge MA, Hobbs BE (1981) The experimental ductile deformation of polycrystalline and single-crystal pyrite. Econ Geol 76: 2105–2117. doi.org/10.2113/gsecongeo.76.8.2105

De Geuser F, Gault B (2017) Reflections on the projection of ions in atom probe tomography. Microsc Microanal 23(2): 238–246. doi.org/10.1017/S1431927616012721

Deditius AP, Utsunomiya S, Renock D, Ewing RC, Ramana CV, Becker U, Kesler SE (2008) A proposed new type of arsenian pyrite: composition, nanostructure and geological significance. Geochim Cosmochim Acta 72: 2919–2933.

doi.org/10.1016/j.gca.2008.03.014

Dubosq R, Lawley CJM, Rogowitz A, Schneider DA, Jackson S (2018) Pyrite deformation and connections to gold mobility: Insight from micro-structural analysis and trace element mapping. Lithos 310-311: 86–104. doi.org/10.1016/j.lithos.2018.03.024

Emsbo P, Hofstra AH, Lauha EA, Griffin GL, Hutchinson RW (2003) Origin of high-grade gold ore, source of ore fluid components, and genesis of the Miekle and neighboring Carlin-type deposits, Northern Carlin Trend, Nevada. Econ Geol 98: 1069–1105. doi.org/10.2113/gsecongeo.98.6.1069

Fisher DS (1998) Collective transport in random media: from superconductors to earthquakes. Phys Rep 301(1): 113–150. doi.org/10.1016/S0370-1573(98)00008-8

Foster AR, Williams PJ, Ryan CG (2007) Distribution of gold in hypogene ore at the Ernest Henry iron oxide copper gold deposit, Cloncurry District, NW Queensland. Explor Min Geol 16:125–143.

Fougerouse D, Micklethwaite S, Halfpenny A, Reddy SM, Cliff JB, Martin LAJ, Kilburn M, Guagliardo P, Ulrich S (2016a) The golden ark: Arsenopyrite crystal plasticity and the retention of gold through high strain and metamorphism. Terra Nova 28: 181–187. doi.org/10.1111/ter.12206

Fougerouse D, Reddy SM, Saxey DW, Rickard WDA, van Riessen A, Micklethawaite S (2016b) Nanoscale gold clusters in arsenopyrite controlled by growth rate not concentration: Evidence from atom probe microscopy. Am Mineral 101: 1916–1919. doi.org/10.2138/am-2016-5781CCBYNCND

Fougerouse D, Reddy SM, Kirkland CL, Saxey DW, Rickard WD, Hough RM (2019) Time-resolved, defect-hosted, trace element mobility in deformed Witwatersrand pyrite. Geosci Front 10: 55–63. doi.org/10.1016/j.gsf.2018.03.010

Frimmel HE, Groves DI, Kirk J, Ruiz J, Chesley J, Minter WEL (2005) The formation and preservation of the Witwatersrand goldfields the largest gold province in the world. Econ Geol 100th Anniversary 100: 769–797. doi.org/10.5382/AV100.23

Gaboury D (2013) Does gold in orogenic deposits come from pyrite in deeply buried carbon-rich sediments?: Insight from volatiles in fluid inclusions. Geology 41: 1207–1210. doi.org/10.1130/G34788.1

Gault B, De Geuser F, Stephenson LT, Moody MP, Muddle BC, Ringer SP (2008) Estimation of the reconstruction parameters for atom probe tomography. Microsc Microanal 14 (4): 296–305. doi.org/10.1017/S1431927608080690

Gault B, Moody MP, Cairney JM, Ringer SP (2012a) Atom probe microscopy. Series in Materials Science. Springer, Heidelberg.

Gault B, Mood MP, Cairney JM, Ringer SP (2012b) Atom probe crystallography. Mater Today 15(9): 378–386. doi.org/10.1016/S1369-7021(12)70164-5

Gault B, Moody MP, De Geuser F, Tsafnat G, LaFontaine A, Stephenson LT, Haley D, Ringer, SP (2009) Advances in the calibration of atom probe tomographic reconstruction. J Appl Phys 105 (3): 1–10. doi.org/10.1063/1.3068197

Gerberich W, Jungk JM, Mook WM (2003) Crack–Dislocation Interactions. In: Milne I, Ritchie RO, Karihaloo B (eds) Comprehensive structural integrity, Pergamon, pp 357–381.

Graf JL, Skinner BJ, Bras J, Fagot M, Levade C, Couderc JJ (1981) Transmission electron-microscopic observation of plastic deformation in experimentally deformed pyrite. Econ Geol, 76: 738–742. doi.org/10.2113/gsecongeo.76.3.738

Hähner P, Ziegenbein A, Rizzi E, Neuhäuser H (2002) Spatiotemporal analysis of Portevin–Le Châtelier deformation bands: Theory, simulation, and experiment. Phys Rev B 65(13): 134109–134128. doi.org/10.1103/PhysRevB.65.134109

Heitjans P, Karger J (Eds) (2005) Diffusion in condensed matter: Methods, Materials, Models, Springer, Heidelberg.

Humphrey-Baker S (2009) Atomic-scale studies of fusion materials. Dissertation, Oxford University, 121 p.

Huston DL, Sie SH, Suter GF, Cooke DR, Both RA (1995) Trace elements in sulfide minerals from Eastern Australian volcanic-hosted massive sulfide deposits: Part I: proton microprobe analyses of pyrite, chalcopyrite, and sphalerite, and Part II. Selenium levels in pyrite: comparison with delta 34 S values and implications for the source of sulfur in volcanogenic hydrothermal systems. Econ Geol 90: 1167–1196. doi.org/10.2113/gsecongeo.90.5.1167

Hwang C, Bernstein IM (1986) Dislocation transport of hydrogen in iron single crystals. Acta Metall 34(6): 1001–1010. doi.org/10.1016/0001-6160(86)90209-9

Imai M, Sumino K (1983) In situ X-ray topographic study of the dislocation mobility in high-purity and impurity-doped silicon crystals. Philos Mag A 47: 599–621. doi.org/10.1080/01418618308245248

Kalk A, Schwink Ch (1992) On sequences of alternate stable and unstable regions along tensile deformation curves. Phys Status Solidi B 172(1): 133–144. doi.org/doi.org/10.1002/pssb.2221720114

Kalk A, Schwink Ch (1995) On dynamic strain ageing and the boundaries of stable plastic deformation studied on Cu-Mn polycrystals. Philos Mag A 72(2): 315–339. doi.org/10.1080/01418619508239928

Kirkland CL, Fougerouse D, Reddy SM, Hollis J, Saxey DW (2018) Assessing the mechanisms of common Pb incorporation into titanite. Chem Geol 483: 558–566. doi.org/10.1016/j.chemgeo.2018.03.026

Kubin LP, Estrin Y (1985) The Portevin-Le Chatelier effect in deformation with constant stress rate. Acta Metall 33(3): 397–407. doi.org/10.1016/0001-6160(85)90082-3

Kwiatkowski da Silva A, Leyson G, Kuzmina M, Ponge D, Herbig M, Sandlöbes S, Gault B, Neugebauer J, Raabe D (2017) Confined chemical and structural states at dislocations in Fe-9 wt% Mn steels: A correlative TEM-atom probe study combined with multiscale modelling. Acta Mater 124: 305–315. doi.org/0.1016/j.actamat.2016.11.013

La Fontaine A, Piazolo S, Trimby P, Yang L, Cairney JM (2017) Laser-assisted atom probe tomography of deformed minerals: A zircon case study. Micros Microanal 23(2): 1–10. doi.org/10.1017/S1431927616012745

Large RR, Maslennikov VV, Robert F, Danyushevsky LV, Chang Z (2007) Multistage sedimentary and metamorphic origin of pyrite and gold in the Giant Sukhoi log deposit, Lena Gold Province, Russia. Econ Geol 102: 1233–1267. doi.org/10.2113/gsecongeo.102.7.1233

Larson DJ, Prosa TJ, Ulfig RM. Geiser BP, Kelly TF (2013) Local electrode atom probe tomography: A user's guide. Springer, Heidelberg, 318 p.

Legros M, Dehm G, Arzt E, Balk TJ (2008) Observation of giant diffusivity along dislocation cores. Science 319: 1646–1649. doi.org/10.1126/science.1151771

Levade C, Couderc JJ, Bras J, Fagot M (1982) Transmission electron microscopy study of experimentally deformed pyrite. Philos Mag 46: 307–325. doi.org/10.1080/01418618208239921

Louat N (1981) On the theory of the Portevin-Le Chatelier effect. Scr Metall 15(11): 1167–1170. doi.org/10.1016/0036-9748(81)90290-8

Love GR (1964) Dislocation pipe diffusion. Acta Metall Mater 12(6): 731–737. doi.org/10.1016/0001-6160(64)90220-2

Makineni SK, Kumar A, Lenz M, Kontis P, Meiners T, Zenk C, Zaefferer S, Eggler G, Neumeier S, Spiecker E, Raabe D, Gault B (2018a) On the diffusive phase transformation mechanism assisted by extended dislocations during creep of a single crystal CoNi-based superalloy. Acta Mater 155: 362–371. doi.org/10.1016/j.actamat.2018.05.074

Makineni SK, Lenz M, Neumeier S, Spiecker E, Raabe D, Gault B (2018b) Elemental segregation to antiphase boundaries in a crept CoNi-based single crystal superalloy. Scr Mater 157: 62–66. doi.org/10.1016/j.scriptamat.2018.07.042

Makineni SK, Lenz M, Kontis P, Li Z, Kumar A, Felfer PJ, Neumwier S, Herbig M, Spiecker E, Raabe D, Gault B (2018c) Correlative microscopy—novel methods and their applications to explore 3D chemistry and structure of nanoscale lattice defects: A case study in superalloys. JOM 70 (9). 1736–1743. doi.org/10.1007/s11837-018-2802-7

McClenaghan SH, Lentz DR, Cabri LJ (2004) Abundance and speciation of gold in massive sulfide of the Bathurst mining camp, New Brunswick, Canada. Can Mineral 42: 851–871. doi.org/10.2113/gscanmin.42.3.851

McCormick PG (1973) The Portevin-Le Chatelier effect in a pressurized low carbon steel. Acta Metall 21(7): 873–878. doi.org/10.1016/0001-6160(73)90144-2

Meng X, Liu Z, Cui B, Qin D, Geng H, Cai W, Fu L, He J, Ren Z, Sui J (2017) Grain boundary engineering for achieving high thermoelectric performance in n-type skutterudites. Adv Energy Mater 7(13): 1–11. doi.org/10.1002/aenm.201602582

Mohles V, Rönnpagel D, Nembach E (1999) Simulation of dislocation glide in precipitation hardened materials. Comput Mater Sci 16(1–4): 144–150. doi.org/10.1016/S0927-0256(99)00056-7

Morey AA, Tomkins AG, Bierlin FP, Weinberg RF, Davidson GJ (2008) Bimodal distribution of gold in pyrite and arsenopyrite: Examples from the Archean Boorara and Bardoc shear systems, Yilgarn craton, Western Australia. Econ Geol 103: 599–614. doi.org/10.2113/gsecongeo.103.3.599

Moser DE, Davis WJ, Reddy SM, Flemming RL, Hart RJ (2009) Zircon U–Pb strain chronometry reveals deep impact-triggered flow. Earth Planet Sci Lett 277: 77–79. doi.org/10.1016/j.epsl.2008.09.036

Moser DE, Cupelli CL, Barker IR, Flowers RM, Bowman JR, Wooden J, Hart RJ (2011) New zircon shock phenomena and their use for dating and reconstruction of large impact structures revealed by electron nanobeam (EBSD, CL, EDS) and isotopic U–Pb and (U–

Th)/He analysis of the Vredefort dome. Can J Earth Sci 48: 117–139. doi.org/10.1139/E11-011

Muntean JL, Cline JS, Simon AC, Longo AA (2011). Magmatic-hydrothermal origin of Nevada's Carlin-type gold deposits. Nature Geosci 4: 122–127. doi.org/10.1038/ngeo1064

Naresh-Kumar G, Hourahine B, Edwards PR, Day AP, Winkelmann A, Wilkinson AJ, Parbrook PJ, England G, Trager-Cowan C (2012) Rapid nondestructive analysis of threading dislocations in wurtzite materials using the scanning electron microscope. Phys Rev Lett 108(13): 1–5. doi.org/10.1103/PhysRevLett.108.135503

Naresh-Kumar G, Mauder C, Wang KR, Kraeusel S, Bruckbauer J, Edwards PR, Hourahine B, Kalisch H, Vescan A, Giesen C, Heuken M, Trampert A, Day AP, Trager-Cowan C (2013) Electron channeling contrast imaging studies of non-polar nitrides using a scanning electron microscope. Appl Phys Lett 102: 1–4. doi.org/10.1063/1.4801469

Neuhäuser H (1993) Problems in solid solution hardening. Phys Scr T49B: 412–419. doi.org/10.1088/0031-8949/1993/T49B/005

Ohnuma T (2017) First-principles calculation of field evaporation and surface diffusion on BCC Fe (001). Microsc Microanal 23(S1): 650-651. doi.org/10.1017/S1431927617003919

Oliver J, Ayer J, Dubé B, Aubertin R, Burson M, Panneton G, Friedman R, Hamilton M (2011) Structure, stratigraphy, U-Pb geochronology and alteration characteristics of gold mineralization at the Detour Lake deposit, Ontario, Canada. Explor Min Geol 20: 1–30.

Palenik CS, Ustunomiya S, Reich M, Kesler SE, Wang L, Ewing RC (2004) “Invisible” gold revealed: direct imagining of gold nanoparticles in a Carlin-type deposit. Am Mineral 89: 1359–1366. doi.org/10.2138/am-2004-1002

Park JS, Kim S, Xie Z, Walsh A (2018) Point defect engineering in thin-film solar cells. Nature Rev Mater 3: 194–210. doi.org/10.1038/s41578-018-0026-7

Penning P (1972) Mathematics of the Portevin-Le Chatelier effect. Acta Metall 20(10): 1169–1175. doi.org/10.1016/0001-6160(72)90165-4

Peterman EM, Reddy SM, Saxey DW, Snoeyenbos DR, Rickard WDA, Fougerouse D, Kylander-Clark ARC (2016) Nanogeochronology of discordant zircon measured by atom probe microscopy of Pb-enriched dislocation loops. Science Advances 2(9): 1–9. doi.org/10.1126/sciadv.1601318

Petukhov BV, Klyuchnik PA (2012) Dynamic interaction of dislocations with impurity subsystem in crystalline materials. Crystallogr Rep 57: 388–392. doi.org/10.1134/S1063774512030169

Piazolo S, Austrheim H, Whitehouse M (2012) Brittle-ductile microfabrics in naturally deformed zircon: Deformation mechanisms and consequences for U-Pb dating. Am Mineral 97: 1544–1563. doi.org/10.2138/am.2012.3966

Piazolo S, La Fontaine A, Trimby P, Harley S, Yang L, Armstrong R, Cairney JM (2016) Deformation-induced trace element redistribution in zircon revealed using atom probe tomography. Nature Comm 7: 1–7. doi.org/10.1038/ncomms10490

Plümper O, King H, Vollmer C, Ramasse Q, Jung H, Austrheim H (2012) The legacy of crystal-plastic deformation in olivine: high-diffusivity pathways during serpentinization. Contrib Mineral Petrol 163: 701–724. doi.org/10.1007/s00410-011-0695-3

Portevin A, Le Chatelier F (1923) Sur un phénomène observé lors de l'essai de traction d'alliages en cours de transformation. C R Acad Sci Paris 176:507–510.

Raabe D, Ponge D, Wang MM, Herbig M, Belbe M, Springer H (2017) 1 billion tons of nanostructure – segregation engineering enables confined transformation effects at lattice defects in steels. IOP Conf Ser: Mater Sci Eng 219: 1–12. doi.org/10.1088/1757-899X/219/1/012006

Reddy SM, Timms NE, Trimby P, Kinny PD, Buchan C, Blake K (2006) Crystal-plastic deformation of zircon: A defect in the assumption of chemical robustness. Geol 34(4): 257–260. doi.org/10.1130/G22110.1

Reddy SM, Timms NE, Pantleon W, Trimby P (2007) Quantitative characterization of plastic deformation of zircon and geological implications. Contrib Mineral Petrol 153: 625–645. doi.org/10.1007/s00410-006-0174-4

Reddy SM, Timms NE, Hamilton PJ, Smyth HR (2009) Deformation-related microstructures in magmatic zircon and implications for diffusion. Contrib Mineral Petrol 157: 231–244. doi.org/10.1007/s00410-008-0331-z

Reddy SM, van Riessen A, Saxey DW, Johnson TE, Rickard WDA, Fougerouse D, Fischer S, Prosa TJ, Rice KP, Reinhard DA, Chen Y, Olson D (2016) Mechanisms of deformation-induced trace element migration in zircon resolved by atom probe and correlative microscopy. Geochim Cosmochim Acta 195: 158–170. doi.org/10.1016/j.gca.2016.09.019

Reich M, Deditius A, Chryssoulis S, Li JW, Ma CQ, Parada MA, Barra F, Mittermayr F (2013) Pyrite as a record of hydrothermal fluid evolution in a porphyry copper system: a

SIMS/EMPA trace element study. Geochim Cosmochim Acta 104: 42–62. 10.1016/j.gca.2012.11.006

Reich M, Kesler S, Utsunomiya S, Palenik C, Chryssoulis S, Ewing R (2005) Solubility of gold in arsenian pyrite. Geochim Cosmochim Acta 69(11): 2781–2796. doi.org/10.1016/j.gca.2005.01.011

Rogowitz A, Zaefferer S, Dubosq R (2018) Direct observation of dislocation nucleation in pyrite using combined electron channelling contrast imaging and electron backscatter diffraction. Terra Nova 30: 423–430. doi.org/10.1111/ter.12358

Saunders JA (1990) Colloidal transport of gold and silica in epithermal precious-metal systems: evidence from the Sleeper deposit, Nevada. Geol 18: 757–760. doi.org 10.1130/0091-7613(1990)018<0757:CTOGAS>2.3.CO2

Seebauer EG, Wook Noh K (2010) Trends in semiconductor defect engineering at the nanoscale. Mater Sci Eng: R: Rep 70(3–6): 151–168. doi.org/10.1016/j.mser.2010.06.007

Seydoux-Guillaume AM, Fougerouse D, Laurent AT, Gardés E, Reddy SM, Saxey DW (2018) Nanoscale resetting of the Th/Pb system in an isotopically-closed monazite grain: A combined atom probe and transmission electron microscopy study. Geosci Front 10(1): 65–76. doi.org/10.1016/j.gsf.2018.09.004

Shannon R (1976) Revised effective ionic radii and systematic studies of interatomic distances in halides and chalcogenides. Acta Crystallogr A 32: 751–767. doi.org/10.1107/S0567739476001551

Shyh-Long H, Pouyan S (1987) Application of anisotropic electron diffraction to determine the displacement vector of stacking fault in pyrite. J Mater Sci Lett 6: 1238–1240. doi.org/10.1007/BF01729197

Simon G, Huang H, Penner-Hahn JE, Kesler SE, Kao LS (1999a) Oxidation state of gold and arsenic in gold-bearing arsenian pyrite. Am Mineral 84: 1071–1079. doi.org/10.2138/am-1999-7-809

Simon G, Kesler SE, Chryssoulis S (1999b) Geochemistry and textures of gold-bearing arsenian pyrite, Twin Creeks, Nevada: implications for deposition of gold in Carlin-type deposits. Econ Geol 94: 405–422.

Thompson K, Lawrence D, Larson DJ, Olson JD, Kelly TF, Gorman B (2007) In situ site-specific specimen preparation for atom probe tomography. Ultramic 107 (2-3): 131–139. doi.org/10.1016/j.ultramic.2006.06.008

Timms NE, Kinny PD, Reddy SM (2006) Enhanced diffusion of uranium and thorium linked to crystal plasticity in zircon. Geochem Trans 7 (1):1–16. doi.org/10.1186/1467-4866-7-10

Timms NE, Kinny PD, Reddy SM, Evans K, Clark C, Healy D (2011) Relationship among titanium, rare earth elements, U–Pb ages and deformation microstructures in zircon: Implications for Ti-in-zircon thermometry. Chem Geol 280: 33–46. doi.org/10.1016/j.chemgeo.2010.10.005

Timms NE, Reddy SM, Fitz Gerald JD, Green L, Muhling JR (2012) Inclusion-localised crystal-plasticity, dynamic porosity, and fast-diffusion pathway generation in zircon. J Struct Geol 35: 78–89. doi.org/10.1016/j.jsg.2011.11.005

Tomkins AG, Mavrogenes JA (2001) Redistribution of gold within arsenopyrite and löllingite during pro- and retrograde metamorphism: Application to timing of mineralization. Econ Geol 96: 525–534. doi.org/10.2113/gsecongeo.96.3.525

Trimby PW (2012) Orientation mapping of nanostructured materials using transmission Kikuchi diffraction in the scanning electron microscope. Ultramic 120: 16–24. doi.org/10.1016/j.ultramic.2012.06.004

Van den Beukel A (1980) On the mechanism of serrated yielding and dynamic strain ageing. Acta Metall 28(7): 965–969. doi.org/10.1016/0001-6160(80)90114-5

Vukmanovic Z, Reddy SM, Godel B, Barnes SJ, Fiorentini ML, Barnes SJ, Kilburn MR (2014) Relationship between microstructures and grain-scale trace element distribution in komatiite-hosted magmatic sulphide ores. Lithos 184–187: 42–61. doi.org/10.1016/j.lithos.2013.10.037

Weber S (2018) WinWULFF [computer software]. JCrystalSoft. Retrieved from www.jcrystal.com/products/winwulff/index.htm

Yuan L, Tian M, Lan J, Cao X, Wang X, Chai Z, Gibson JK, Shi W (2018) Defect engineering in metal–organic frameworks: a new strategy to develop applicable actinide sorbents. Chem Commun 54(4): 370–373. doi.org/10.1039/C7CC07527H

Zaefferer S, Elhami NN (2014) Theory and application of electron channeling contrast imaging under controlled diffraction conditions. Acta Mater 75(154): 20–50. doi.org/10.1016/j.actamat.2014.04

CHAPTER 3

Analysis of nanoscale fluid inclusions in geomaterials by atom probe tomography: experiments and numerical simulations

R. Dubosq[1], B. Gault[2,3], C. Hatzoglou[4], K. Schweinar[2], F. Vurpillot[4], A. Rogowitz[5], G. Rantitsch[6], D.A. Schneider[1]

[1]Department of Earth and Environmental Sciences, University of Ottawa, Ottawa, Canada

[2]Max-Planck-Institut für Eisenforschung GmbH, Düsseldorf, Germany

[3]Department of Materials, Royal School of Mines, Imperial College London, London, UK

[4]Normandie Université, UNIROUEN, INSA Rouen, CNRS, Groupe de Physique des Matériaux, 76000 Rouen, France.

[5]Department of Geology, University of Vienna, Vienna, Austria

[6]Department of Geology and Economic Geology, University of Leoben, Leoben, Austria

Published in

Ultramicroscopy, Volume 218

November 2020

doi.org/10.1016/j.ultramic.2020.113092

3.1 Abstract

The spatial correlation between defects in crystalline materials and trace element segregation plays a fundamental role in determining the physical and mechanical properties of a material, which is particularly important in naturally deformed materials. Herein, we combine electron backscatter diffraction, electron channelling contrast imaging, scanning transmission electron microscopy and atom probe tomography on a naturally occurring metal sulphide in an attempt to document mechanisms of element segregation in a brittle-dominated deformation regime. Within APT reconstructions, features with a high point density comprising O-rich discs stacked over As-rich spherules are observed. The combined microscopy data allow us to interpret these as nanoscale fluid inclusions. Our observations are confirmed by simulated APT experiments of core-shell particles with a core exhibiting a very low evaporation field and the shell emulating a segregated layer at the inclusion interface. Our data has significant trans-disciplinary implications to the geosciences, the material sciences, and analytical microscopy.

3.2 Introduction

Recent developments in micro- to nano-scale analytical techniques have enabled unique observations of physical and chemical complexities in crystalline materials. Crystal defects can be defined as disruptions of the regular arrangement of atoms in an organized crystalline structure. Defects are subclassified as point defects including vacancies and impurities, line defects consisting of dislocations, plane defects that are stacking faults and grain boundaries, and bulk defects including voids, fluid inclusions, cracks, and impurity clusters (Schwartz and Lang 2016). Such crystalline imperfections can occur as a result of inherent crystal growth (Klapper 2010), crystal plastic deformation (Burgers 1995), or radiation damage (Seitz and Koehler 1956; Itoh and Stoneham 2001; Dyar and Guntar 2008; Itoh et al. 2009). The interaction of trace components with crystal defects can control the distribution and redistribution of these elements, which can, in turn, significantly impact a material's physical properties. For example, in a recent study combining electron backscatter diffraction (EBSD), electron channelling contrast imaging (ECCI) and atom probe tomography (APT) on pyrite, a naturally occurring sulphide metal, we documented the migration of trace metals into deformation-induced microstructures through dislocation-impurity pair diffusion during crystal-plasticity (Dubosq et al. 2019). The links between trace element segregation and crystalline defects including dislocations, grain-, phase-, and twin-boundaries and precipitate-matrix interfaces has also been commonly reported in many studies on other minerals (Moser et al. 2011; Timms et al. 2012; Fougerouse et al. 2016; Piazolo et al. 2016; Reddy et al. 2016), metallic alloys (Miller 2006; Smith et al. 2013; Makineni et al. 2018; Katnagallu et al. 2019; He et al. 2020) and semiconductors (Thompson et al. 2007), including thermoelectric materials (Yu et al. 2018, 2019). However, the interaction between trace component segregation and nanoscale fluid inclusions, and its effect on a material's physical properties remains poorly understood due to the challenges of characterizing fluid inclusions using conventional analytical microscopy techniques.

Nanoscale fluid inclusions are features undistinguishable from voids by conventional microscopy techniques that can occur in either natural or engineering materials (i.e., minerals, ceramics, polymers, etc.) and can play a vital function in determining their physical properties including their strength, modulus, and thermal conductivity. The presence of voids or fluid inclusions in materials can either have a detrimental or beneficial effect on its properties. For example, the diffusion of vacancies during creep can lead to the growth and coalescence of intrinsic voids and result in material failure, thus the presence of voids can have a weakening effect on materials (Smallman and Westmacott 1972; Wilkinson 1987, 1988; Fleck et al. 1989; Tvergaard

1989; Horstemeyer and Gokhale 1999; Orsini and Zikry 2001; Benzerga et al. 2001; Gao et al. 2005; McVeigh et al. 2007). On the other hand, voids can introduce desirable physical properties such as low density, high compressive strength, good energy absorption, and noise control (Klempner and Frisch 1991; Banhart 2001; Ohji 2013). Thus, characterizing these nanoscale features is important to understand and predict how a material will perform under specific conditions. Current microscopy techniques that are used for the characterization and quantification of nanoscale voids in materials include various electron microscopy techniques such as scanning electron microscopy (SEM), transmission electron microscopy (TEM), scanning TEM and high-resolution TEM (Armstrong and Goodhew 1983; Rothaut et al. 1983; Harrison et al. 2017). Although these techniques are very effective for obtaining quantitative information about void characteristics including structure, volume fraction, distribution, and morphology, acquiring compositional measurements remains a challenge due to the small nature of the voids. More recently, studies on nanoporous materials have used field ion microscopy and atom probe tomography (APT) for sub-nanometer scale characterization and report apparent increases in atomic density through trajectory aberrations in the vicinity of voids (Brenner and Seidman 1975; Miller et al. 2011; Edmondson et al. 2013; Schmidt et al. 2018; Lloyd et al. 2019). These ion trajectory artefacts have also been observed in field evaporation simulations(Larson et al. 2015). Although it is recognized that voids act as field concentrators, the complex atomic displacements around voids and their limiting effect on the accuracy of APT data reconstructions, more specifically when voids are filled with fluids, continue to be poorly understood.

Herein, we have conducted EBSD, ECCI, STEM and APT on natural pyrite. The APT data reveals patterns of void-like features that appear to not be empty but filled with loosely-bonded atoms or molecule, herein referred to as fluid inclusions. This pattern was subsequently emulated through numerical APT experiments performed using a state-of-the art finite-element method framework (Rolland et al. 2015), confirming our hypothesis. The combined data has significant trans-disciplinary implications to the geosciences (structural geology, geochemistry, economic geology, geochronology), the material sciences (metals, ceramics, polymers), and analytical microscopy.

3.3 Materials and Methods

3.3.1 Pyrite

The material investigated in this study is a polycrystalline pyrite (FeS_2) aggregate within a black shale matrix mostly composed of fine-grained (5-20 μm) graphite (C), white mica ($KAl_2(AlSi_3O_{10})(FOH)_2$) and quartz ($SiO_2$) from the Archean Abitibi Subprovince of Canada (Figure 3.1). Raman spectroscopy of carbonaceous material (RSCM) was conducted (Lünsdorf et al. 2017) to determine the peak temperature that the rock has attained, yielding conditions of 302 ± 27°C for the sample (Table S3.1; see supplementary files for methodological details). The iron sulphide mineral is a face-centered-cubic structure belonging to the Pa3 space group with a symmetry of 2/m3 and unit cell dimensions of a = 5.418 Å, Z = 4, H = 6-6.5, and G = 5.02. The centers of the cubic cell's edges are occupied by S_2 pairs covalently bonded by sp^3 hybrid orbitals. Each S_2 pair is also covalently bonded to three Fe atoms by d^2sp^3 hybrid orbitals resulting in the overlap of Fe conduction band with the valance band, giving pyrite metallic characteristics (Nesse 2000).

3.3.2 Electron backscatter diffraction and electron channelling contrast imaging

Primary characterization of the investigated pyrite metal was performed by combining EBSD mapping and ECC imaging to obtain quantitative and qualitative information of the crystalline

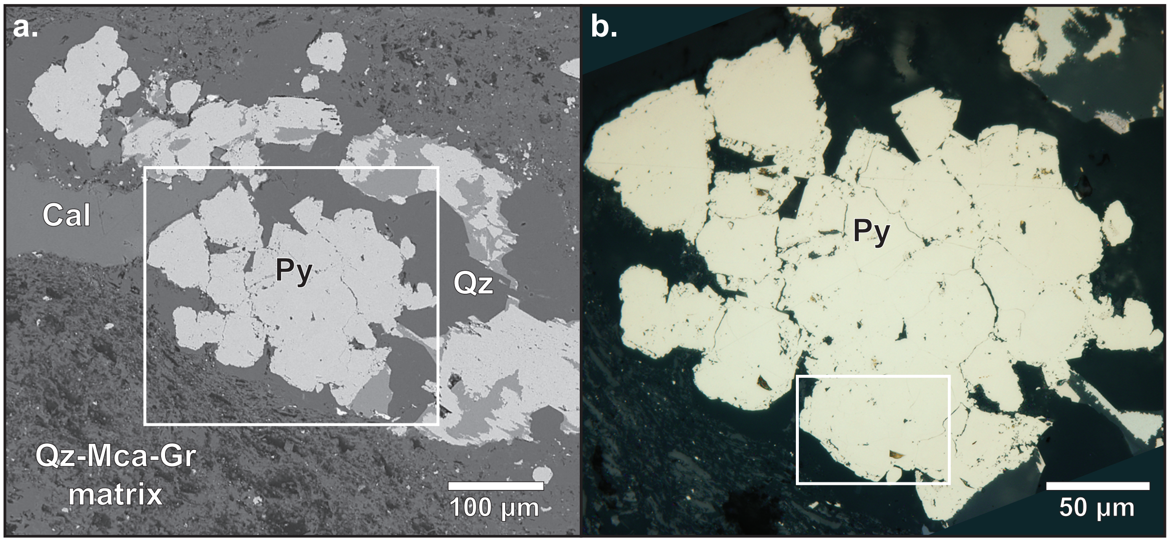

Figure 3.1. a. Electron backscatter scanning electron microscope image of polycrystalline pyrite grains in a black shale (quartz (Qz), mica (Mca), graphite (Gr)) matrix surrounded by a quartz (Qz) and calcite (Cal) strain shadow. White box indicates the location of Figure 3.1b. **b.** Reflected light photomicrograph of the investigated polycrystalline pyrite grain. White box showing the location of Figure 3.2a.

structure and deformation state of the sample. All crystallographic data were collected at the Department of Lithospheric Research (University of Vienna, Austria) using a FEI Quanta 3D FEG instrument equipped with a field-emission electron source and an EDAX Pegasus Apex 4 System consisting of a Digiview IV EBSD camera and an Apollo XV silicon drift detector for EDX-spectroscopy. Prior to analysis, the thin section was chemomechanically polished with an alkaline colloidal silica suspension (SYTON©) and carbon-coated to establish conductivity. EBSD mapping was conducted first with analytical conditions set to an accelerating voltage of 15 kV with a spot size of 1.5 in analytical modus and a probe current of 4 nA. The sample was tilted to 70° and brought to a working distance of 14 mm. Mapping was performed by using a hexagonal grid and a step size of 26 nm. EBSD data was cleaned using the OIM Data Collection and Analysis software by combining the neighbour orientation correlation (clean-up level: 2) and confidence index standardization (CI: 0.1) functions. Misorientation deviation angle (misorientation of each pixel relative to grain average) and grain boundary maps were then created using the MTEX toolbox in Matlab (Bachmann et al. 2010).

ECC imaging was subsequently conducted at specific pyrite domains identified in EBSD maps to further investigate the targeted microstructures. This imaging was also performed on the FEI Quanta 3D FEG instrument at the University of Vienna. Analytical conditions for imaging were set to a 30 kV accelerating voltage, a spot size of 2 in analytical modus, a 2–4 nA probe current and a working distance between 7.5 and 8 mm, allowing for the direct observation of crystal defects.

3.3.3 Atom probe tomography

A series of specimens was prepared from the investigated pyrite by in situ lift-out (Thompson et al. 2007) targeting a grain boundary for APT in an attempt to investigate the detailed composition of some of the microstructural features at the near-atomic scale. The needle-shaped specimen was sharpened by annular milling at 30 kV on a dual-beam scanning electron microscope/focused ion beam FEI Helios Nanolab 600i at the Max-Planck-Institut für Eisenforschung GmbH (Düsseldorf, Germany) and subsequently cleaned using the Ga-beam at 2 kV to remove regions potentially severely damaged by the implantation of energetic Ga ions. Note, the grain boundary remained visible throughout the tip preparation process. The specimen was then analysed by APT in a Cameca LEAP 5000 XR (Table S3.2) fitted with a reflectron-lens which has a detector efficiency of ~50%. The specimen was analysed in laser pulsing mode at 55 K with a laser pulse energy of 45 pJ focused on an area estimated to be <3 μm in diameter, a detection rate of 0.5 ion per 100 pulses and a laser pulse repetition rate of 125 kHz. The data processing and reconstruction were done with the commercial software package IVAS 3.8.2. Compositional profiles presented herein were generated from cylindrical regions of interest (ROI) using the 1D concentration profile function and computed using the fixed bin width profile, atomic, and decompose complex ions options. The bin size was adjusted for each profile (0.2–0.4 nm) to maximise the ratio of the peak signal to the statistical fluctuations. Ion identities within the measured dataset were assigned by defining ranges within the mass spectrum that best fit theoretical isotopic ratios (Exertier et al. 2018; Blum et al. 2018; Reddy et al. 2020). The ranged mass spectrum used for the specimen is shown in Figure S3.1.

3.3.4 Scanning transmission electron microscopy

A TEM specimen was prepared by in-situ lift-out using a Thermo Scientific Helios G4 UXe DualBeam Plasma-FIB at the Canadian Centre for Electron Microscopy, McMaster University (Hamilton, Canada). The region of interest was marked by an electron-deposited tungsten layer and subsequently protected by xenon deposition of tungsten and mixture of carbon and platinum.

A ~1 μm thick lamella was obtained by trenching adjacent areas and was then attached to a copper grid. The lamella was thinned to ~80 nm by an ion beam with gradually decreased currents at 30 KeV and cleaned with progressively reduced low voltages until 5 keV in order to remove the amorphorized layers resulting from ion bombardment.

High-angle annular dark field (HAADF) imaging was performed using a FEI Titan 80-300 TEM equipped with a CEOS probe and image corrector operated in STEM mode at a convergence angle of 19.1 mrad. The microscope was operated at an acceleration voltage of 300 kV and micrographs were captured using a HAADF detector (Fischione). The images were collected using a dwell time of 4 μs, a total frame time of 20.1 s, a camera length of 185 mm, a spot size of 11 and a screen current of ~100 pA.

3.3.5 Numerical simulations

Several frameworks for simulating the field evaporation process to emulate atom probe tomography currently exist (Vurpillot and Oberdorfer 2015). In our study, we apply a model developed by the Groupe de Physique des Matériaux (GPM) at the University of Rouen (Normandy, France) (Vurpillot 2001; Blavette et al. 2001). The model was subsequently optimized (Gruber et al. 2011) in order to introduce the thermally activated process of the field evaporation (Blavette et al. 2001). This model was chosen for its ability to quantify, and therefore correct, the APT biases related to local magnification effects (Gault et al. 2012; Lefebvre et al. 2016; Hatzoglou et al. 2018, 2019).

The morphology of APT specimens is here simplified into a hemisphere on a cylinder, with a simple cubic crystallographic structure with a lattice parameter of 0.2 nm. The analysis temperature is set to 50 K, which is an average value of the temperature range (20 to 80 K) commonly used in APT analysis. The simulated microstructures are simplified as particles with a spherical outer layer herein referred to as shell, and an inner content herein referred to as core, which are embedded in a pure matrix. The core is considered as a pure element with an evaporation field (F_{Core}), which is the field necessary to provoke the field evaporation of an atom from the surface, that is ten times lower than the matrix evaporation field F_{Matrix} (i.e., $F_{Core} = 0.1 \times F_{Matrix}$). The shell is composed of two elements: shell atoms and matrix atoms in a ratio referred to as X_S. The shell atoms have an evaporation field slightly higher than the matrix ($F_{Shell} = 1.1 \times F_{Matrix}$). Due to limitation in the simulation code, the radius of curvature of the specimen's apex is limited to 17.6 nm, smaller than typical experimental values (between 40–100 nm). To enable direct comparisons with APT reconstructions, a scale factor is introduced. Reduced size ratios (P), which correspond to the core diameter divided by the specimen's curvature radius, are used to reflect particles size. For example, an experimental APT specimen with a radius of curvature between 40 nm to 50 nm containing core particles with a diameter of 5 nm and a shell thickness of 1 nm would have a P of 10% to 12.5%.

3.4 Results and Discussion

3.4.1 2D microstructural analysis

EBSD mapping and ECC imaging were conducted on the polycrystalline pyrite aggregate in order to quantify deformation within the sample and identify the dominant behavioural regime. EBSD maps of the pyrite reveal minor evidence for crystal-plastic deformation within the polycrystalline aggregate. Deviation angle and grain boundary maps of a targeted domain (Figure 3.2a) exhibit a more heterogeneous misorientation pattern within crystal 1 and a linear misorientation pattern within crystal 2, both displaying a maximum misorientation of 6.5° relative to their respective grain average orientation. Minor development of partial low-angle grain boundaries (2-5°) occur in crystal 1, separating higher strain domains from undeformed crystal-structure. ECC imaging of

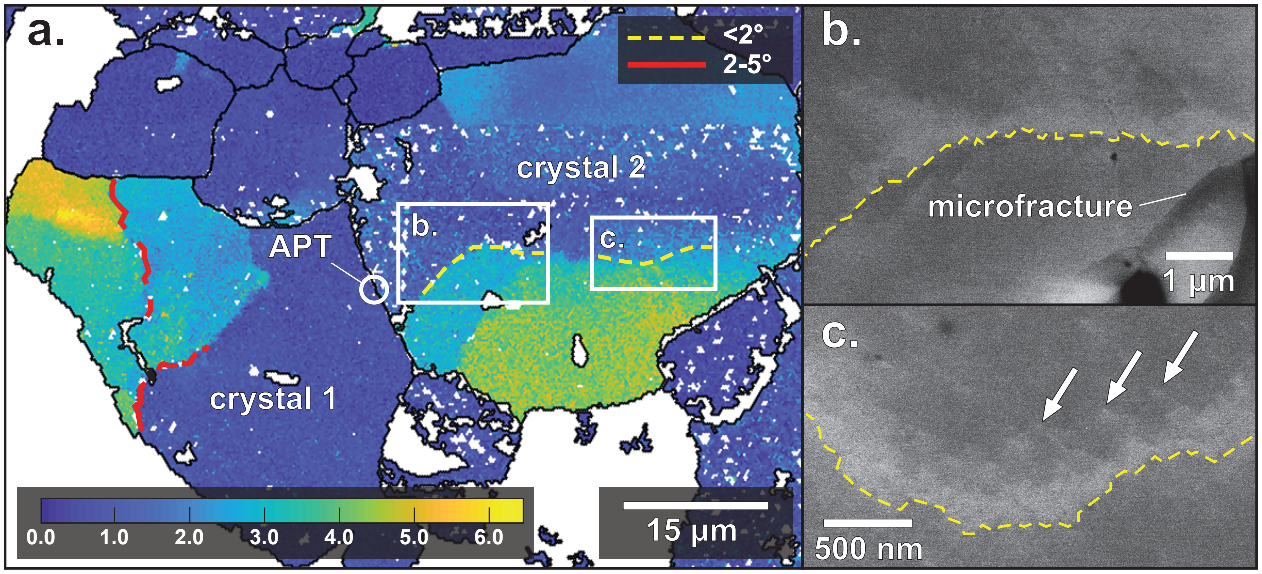

Figure 3.2. a. EBSD misorientation and grain boundary map of pyrite region of interest revealing heterogeneous and linear misorientation pattern with a maximum misorientation of 6.5° relative to the average grain orientation and low-angle grain boundaries (red and dashed yellow lines). Note the low-angle grain boundaries are due to lattice rotation during micro-fracturing rather than dislocation glide and creep. The <2° low-angle grain boundaries were observed in the ECC images as aligned dislocations and were subsequently added onto the EBSD map. White boxes indicate locations of Figure 3.2b. and 3.2c. and white circle indicates location of analysed APT specimen. **b-c.** ECC images of pyrite domains with linear misorientation patterns revealing increased dislocation density (white arrows), micro-fracturing and associated low-angle grain boundaries (yellow dashed lines).

crystal 2 (Figure 3.2b-c) reveals areas of increased free dislocation density and low-angle grain boundaries (<2°), otherwise not observed in EBSD maps, adjacent to microfractures. Dislocations are visible as white dots with rather short bright line segments (Figure 3.2c) whereas low-angle grain boundaries appear as aligned or partially-aligned dislocation walls with varying crystallographic orientation (grey value) on either sides (Figure 3.2b-c).

Although these observed microstructures are typically associated with crystal-plasticity, the relatively low degree of misorientation within the sample (<6.5°) and the proximity of the microstructures to microfractures suggests minimal crystal-plastic deformation in a dominantly brittle regime. Therefore, the low-angle grain boundaries documented in EBSD maps represent crystal-structure rotation (2-5°; Figure 3.2a) on either sides of microfractures. The aligned dislocation walls (low-angle boundaries <2°; Figure 3.2b-c) documented in ECC images most likely represent dislocations that have nucleated in the vicinity of a microfracture rather than the migration of pre-existing dislocations by dislocation glide and creep processes (Rogowitz et al. 2018). Our RSCM data indicate peak temperature conditions for the investigated sample at 302 ± 27°C (Table S3.1), which falls within the lower most range of the brittle to crystal-plastic behaviour of pyrite, estimated to be between 260–450°C (Graf et al. 1981; Cox et al. 1981; Barrie et al. 2011), supporting our observations of brittle-dominated deformation mechanisms.

3.4.2 3D nanostructural and geochemical analysis

In an attempt to identify nanoscale crystal-defects and quantify elemental segregation within the brittlely deformed iron sulphide, one APT specimen from the boundary between crystals 1 and 2 was analysed and yielded >25 million ions. The 3D reconstruction of the specimen from the APT analysis reveals a homogeneous distribution of the major pyrite components Fe (40.18 at%) and S (59.58 at%). Note, the measured composition of S is lower than expected from the stoichiometry,

~60 at% instead of 66.6 at%, even following peak deconvolution as available within the commercial software package IVAS. This can be related to typical issues of having S_2^{2+} overlapped with S^{1+}. In addition, the isotopic distribution of S does not allow precise deconvolution, which is expected from most APT analysis of ionically and covalently bonded materials. Dissociations of emitted molecular ions can also lead to neutrals, which is common in these systems(Gault et al. 2016). In contrast, ubiquitous high-point-density features (133-275 ions/nm^3), approximately a factor of two compared to the surrounding matrix, measuring 3 to 8 nm in diameter are heterogeneously dispersed within the specimen (at <25 nm spacing). These sudden changes in point density within the tomographic reconstruction result from trajectory aberrations associated to microstructural features typically requiring a lower electrostatic field to trigger the field evaporation process (Miller 1987; Vurpillot et al. 2000).

Here, these features are also associated to As-enriched spherules with As compositions of 3.27-5.97 at%, which is ~20× to 40× that of the matrix composition (0.16 ± 0.07 at%), superimposed by, in the direction of field evaporation, O-rich discs with O compositions of 3.20-4.92 at%, exceeding the matrix level compositions by two orders of magnitude (0.03 ± 0.02 at%; Figure 3.3a-d). Although the O-rich discs are mostly stacked directly on top of the As spherules, they also occur in various directions (Figure 3.3a, S3.2). Note, O compositions were obtained by decomposing all O-bearing ions (11.89% O; 3.35% OH; 3.28% H_2O; 10.75% H_3O; 59.13% FeO; 2.15% Fe_3O; 3.03% CoOH and 6.39% OS_2; Figure S3.2a-b). Composition profiles across the high-density features confirm the elevated As and O compositions by illuminating narrow (1-2 nm) O composition peaks preceding and/or slightly overlapping wider (4-6 nm) As composition peaks, which appear to be positively correlated with an increased ionic point density (Figure 3.3e). APT data of two other specimens from the same lift-out reveal the same high-density features

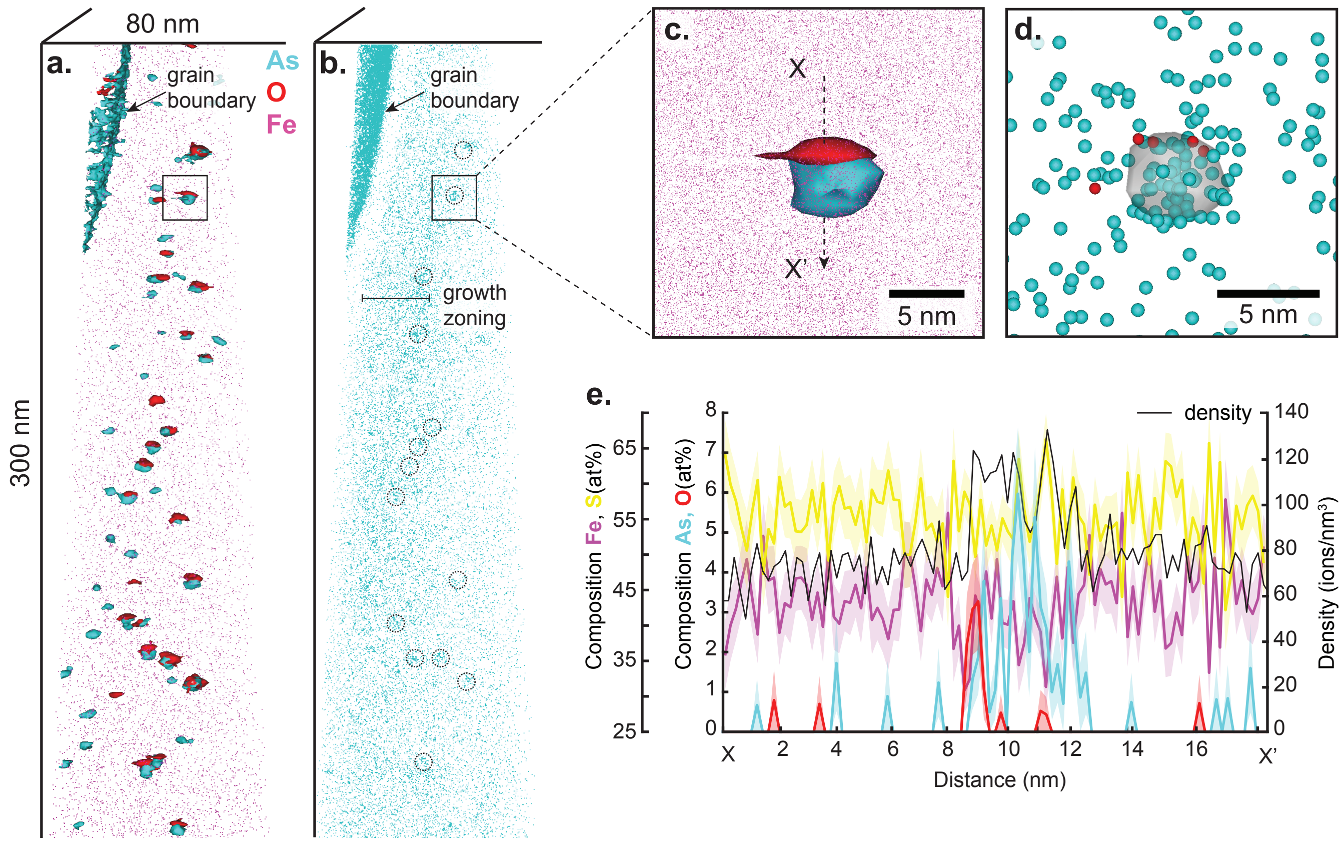

Figure 3.3. a. Reconstruction of APT specimen displaying the distribution on Fe ions (pink dots) and As (turquoise isosurfaces; 1 at% isovalue) and O compositions (red isosurfaces; 0.5 at% isovalue), revealing a grain boundary and other high-density features. **b.** Reconstruction of APT specimen displaying the distribution of AsS ions (turquoise dots) and revealing a grain boundary, an AsS-rich band parallel to the grain boundary, and other high-density features. **c.** Close-up reconstruction of a high-density feature showing an As-rich globule (turquoise isosurfaces; 1.40 at% isovalue) and superimposed O-rich disc (red isosurfaces; 0.67 at% isovalue). **d.** Close-up reconstruction of a high-density feature (grey isosurfaces; 22.47 ions/nm^3 isovalue) showing the distribution of AsS and H_2O ions. Note, the direction of evaporation is upwards in a-d. **e.** Composition profile across high-density feature showing the composition pyrite's major components and the elevated As- and O-rich compositions by revealing a narrow (1 nm) O peak of 3.27 at% preceding a wider (4 nm) As peak of 5.97 at%.

occurring as apparent As and O clusters measuring up to 15-30 nm in diameter (Figure S3.3). Whereas the features are dominantly composed of As and O, other trace elements including H, Co, Cu, and Zn are present in slightly elevated compositions relative to the matrix (Figure S3.2a).

A planar feature highlighted by an elevated As composition ranging between 1.00-2.68 at% occurs at the tip of the specimen, which we interpret to be a high-angle grain boundary based on the locality of the specimen lift-out illustrated on the EBSD map (Figure 3.2a). A wide band (~25 nm) of elevated As composition (0.56-1.89 at%), relative to the more dominant part of the matrix ranging between 0.00-0.50 at% (Figure 3.3b), is parallel to the high-angle grain boundary. Due to the ability of As to form limited solid-solution series with pyrite and form discrete growth zones during crystallization(Fleet et al. 1993; Craig et al. 1998; Large et al. 2009; Dubosq et al. 2018), we interpret the As-rich band within the specimen matrix to be a growth band that represents the evolving availability of As within the primary crystallizing fluid. Upon closer inspection, a significant portion of the observed high-density features appear to be aligned at the boundary between the As-rich growth band and the As-depleted matrix (Figure 3.3b). A typical feature that forms during crystal growth includes fluid inclusions, which are described as small volumes containing fluid contents (gas and/or liquid phase) that were trapped in a mineral during nucleation and crystallization. The description of fluid inclusions resembles that of a void, which is a volume within a solid material occupied by a vacuum or fluid, and in contrast to our APT results, consists of a low-density feature.

To confirm the presence of such inclusions within the investigated sample, STEM imaging of a pyrite crystal proximal to the analysed APT specimen was performed. The images revealed ubiquitous closed-cell void-like features, which appear as semi-spherical areas of darker grey-scale value as a result of the z-contrast in HAADF imaging mode. The apparent voids are heterogeneously distributed in the grain and vary between <5 nm to 15 nm in diameter. The images also show a wide range of volume fractions from densely packed (2-4 nm between features; Figure 3.4a) to more dispersed (>10 nm between features; Figure 3.4b). The STEM images confirm the presence of nanoscale voids-like features in the sample and supports our hypothesis that the high-density features in the experimental APT data could potentially be fluid inclusions. However, in contrast to the documented high-density features observed in the experimental APT data, we would intuitively expect fluid inclusions to be represented by low-density features in the 3D reconstructions.

A similar distribution of O as observed in our APT reconstructions has been previously observed in metals and metal oxides by several authors and has been attributed to the field induced migration of O ions towards a metallic matrix due to the difference in the charge carrier concentration (Cranstoun and Anderson 1973; Brocq et al. 2010; MARQUIS et al. 2011; Lardé et al. 2011; Kitaguchi et al. 2015; Lee et al. 2015; Bachhav et al. 2019). However, in this study, there is no such metal/semiconductor-insulator interface, and the diffusion of O inside the pyrite is not expected to be particularly easy. Alternatively, migrations driven by the electrostatic field have been reported on the surface metals and associated to high-evaporation field species retained on the specimen's surface and driven towards high-field regions, typically poles and zone lines. The point density associated to the inclusions are indicative of a low-field region, and no strong indication of poles and zone lines specifically in these areas can be seen. It is hence very unlikely that the O observed here can be related to migration induced by the electrostatic field. Thus, we have performed a series of field evaporation numerical simulations to investigate the flight path of ions surrounding fluid inclusions during APT analyses and explain the observed high-density features in the experimental APT reconstructions.

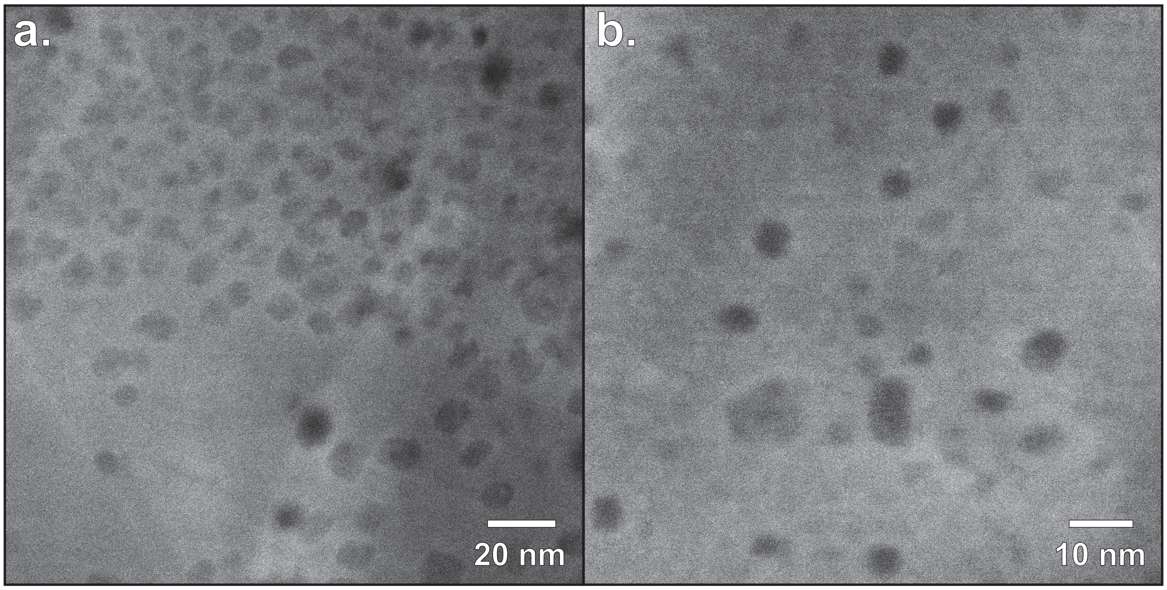

Figure 3.4. HAADF STEM images of nanovoids (<5 nm to 15 nm in diameter) in pyrite showing a heterogeneous distribution and a wide range of void volume fractions from densely packed (2-4 nm between voids) in 3.4a. to more dispersed (>10 nm between voids) in 3.4b.

3.4.3 Reconstruction of numerical simulations

A pre-evaporation morphology of core-shell particles, as described in section 2.5, was used for the simulations to represent the fluid inclusions with an As-rich shell and an O-rich core. The evaporation field of the core is set very low in comparison to the surrounding matrix. Even though the link between bond strength and evaporation field is not straightforward (Ge et al. 1999), this is expected to qualitatively reproduce the behaviour of loosely bonded atoms within the inclusion, i.e. a liquid or a gas adsorbed on the surface. To maintain the same size ratio as the experimental data (i.e., fluid inclusions with a ~5 nm core diameter and a ~50 nm specimen curvature radius), we simulated particles defined as a core with a reduced size ratio of 9.1%, and a shell thickness 5 times smaller than the core diameter. To investigate the influence of particles size, we additionally simulated particles approximately twice as large as the initial simulation with a reduced size ratio of 20.6% and a shell whose thickness still maintains the experiment ratio with the core. In addition, we investigated the influence of the composition of shell atoms by simulating three different concentrations of X_S: 10 at% (Figure S3.4a), 50 at% (Figure S3.4b) and 100 at% (Figure S3.4c), for a total of six simulations (Figure 3.5).

The 3D reconstructions of the simulated core-shell particles, which are comparable to fluid inclusions within a solid material, reveal similar post-evaporation morphologies for all six simulations. In each simulated APT reconstruction, the pre-evaporation spherical shell mostly retains its morphology after evaporation and only appears to have a slightly dispersed arrangement of ions. Comparatively, the initially spherical simulated cores consistently produced dense and irregular ion clusters amalgamated into disc-like geometries at the tip or edge of the post-evaporation shells. Compositional profiles across the 3D reconstructions of the core-shell particles

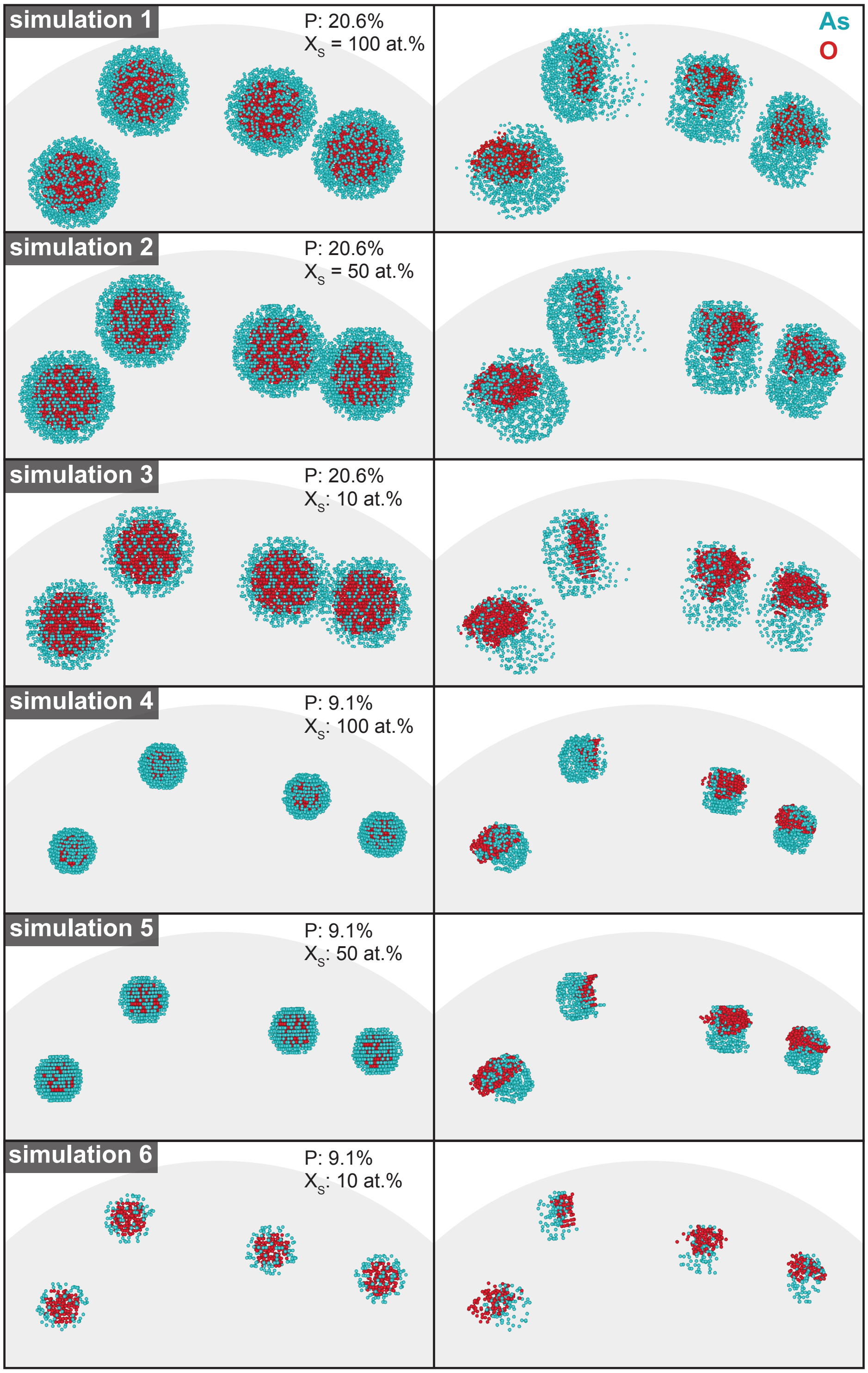

Figure 3.5. Illustration of input dimensions of core-shell particles (left) and reconstruction of the core-shell particles after simulated APT experiments (right) for six simulations. Note, the grey shaded region represents the specimen matrix to illustrate the specimen tip radius. Elemental segregation shells have a thickness that is 20% of the particle diameter and an evaporation field 1.1 that of the matrix whereas cores have an evaporation field 10 lower than the matrix. All six simulations show similar results regardless of P and XS parameters revealing a mostly intact shells overlain by clusters of core ions. Note the particle shells do not retain their initial geometry. P: particle diameter/specimen tip radius*100 (%); XS: shell composition (at%)

show a strong positive correlation between the particles' ionic density and its core composition (Figure 3.6; S3.5, S3.6). This correlation is attributed to the crossing trajectories of the core ions, which result in apparent elevated ionic densities. By comparing the compositional profiles between the smaller reduced size ratio particles (9.1%) versus the larger reduced size ratio particles (20.6%), we notice a stronger correlation of the ionic density and core compositions in the larger particles. The phenomena can be explained through the masking of the core ion trajectories by the magnification effect of the ions evaporated from the hemispherical specimen surface. Thus, when the ratio between a nanoparticle's core diameter and the specimen's curvature radius is larger, the magnification effect of the ions evaporated from the specimen surface is not as strong and cannot effectively mask the effect of the core's crossing ion trajectories (Larson et al. 2013).

3.4.4 Field evaporation ion flight path near fluid inclusions

The simulated APT data of core-shell particles are representative of fluid inclusions with an As-coated shell and an O-rich core that reveal high-density features, in accordance with the experimental data. The morphology of these structures in APT reconstructions can be explained by the erratic, converging and crossing flight paths of ions during the field evaporation in a region surrounding a fluid inclusion. Ions at the surface of a perfect concave-shaped hemisphere start their flight at a 90° angle from the specimen's local normal in a radiating flight path that curves according to the electrostatic field distribution (Smith 1978). However, in reality specimens do not exhibit a regular hemispherical geometry, which results in a homogeneous angular compression of the ion flight paths. The relationship between an ions' evaporation field (F_{evap}) and its evaporation rate (Φ_{evap}) can be estimated by:

$$\Phi_{evap} \approx v_0 e^{\left(\frac{Q_0}{k_B T}\right)\left(\frac{F}{F_{evap}}-1\right)}$$

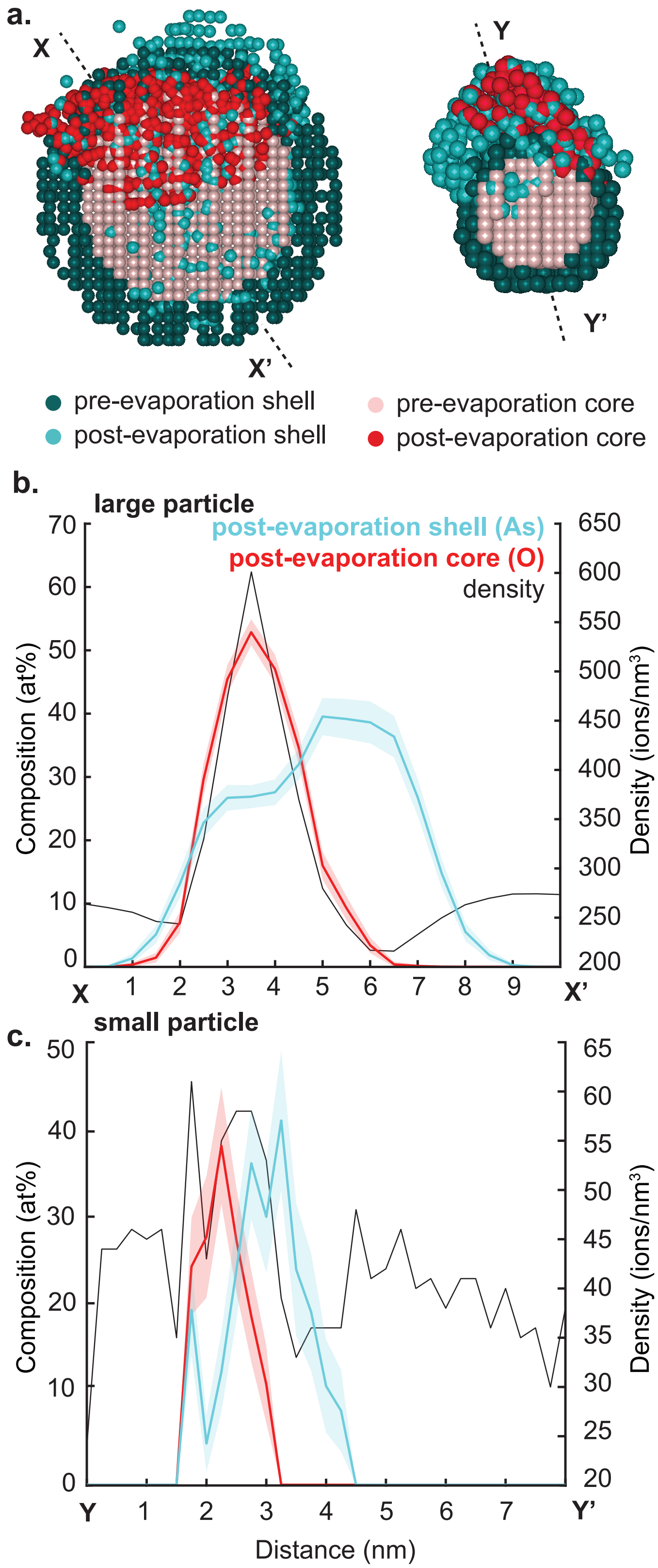

Figure 3.6. a. APT reconstruction of the large and small simulated pre- and post-evaporation core-shell particles with respective reduced size ratios of 9.1% and 20.6%. Note, the direction of evaporation is to the top of the image. **b-c.** Compositional profile across the X-X' and Y-Y' axes of the large and small particles showing As peaks of 52 at% and 62 at% preceded by slightly narrower O peaks of 53 at% and 38 at%. The density curve is also plotted in each profile, revealing a positive correlation between ionic density and core compositions. Note this correlation appears stronger in the larger particle.

where v_0 is the normal component of vibrations from thermal agitation of atoms, Q_0 is the initial energy barrier, k_B is the Boltzmann constant, T is the absolute temperature, and F is the electric field. Based on this relationship, ions with a higher evaporation field leave the surface at a lower rate than ions with a lower evaporation field under an identical electric field. Thus, in a homogeneous single-phase specimen, atoms from a perfectly curved needle surface should evaporate at the same rate and strike the detector with a uniform density of hits (Figure 3.7a). However, when a specimen surface is composed of two or more elements (Figure 3.7b) where the inclusion shell is exposed at the surface of the needle, the evaporation rate varies depending on each elements' evaporation field, which can lead to atoms striking the detector a different times and result in a heterogeneous density of hits on the detector. In our case, the evaporation field of pure As (42 V/nm (Tsong 1978)), which defines the shell, is slightly higher than the evaporation field estimated for pure Fe (33 V/nm (Tsong 1978)), a main component of pyrite, thus the evaporated ions from the shell and the matrix strike the detector in approximately the same period also resulting in a near homogenous density of hits (Figure 3.7b). If ions continue to evaporate from the shell surface, the core of the inclusion is eventually exposed and its contents (H_2O/FeO), with a significantly lower evaporation field (~13 V/nm (Müller et al. 1965; Kuo et al. 2009)) relative to that of the shell and matrix, evaporate at a much faster rate striking the detector at once, leaving behind a void with a locally concave curvature region (Figure 3.7c). Once the shell contents are evaporated, ions surrounding the emerged concave surface initially evaporate at a 90° angle from the surface and are deflected towards the specimen axis due to the imperfect void geometry that results in converging and possibly crossing ion flight paths (Birdeye et al. 1973; Larson et al. 2015) leading to a high-density of hits on the detector (Figure 3.7d). The observed high-density features in the pyrite specimen can be explained by the fast evaporation of an O-rich

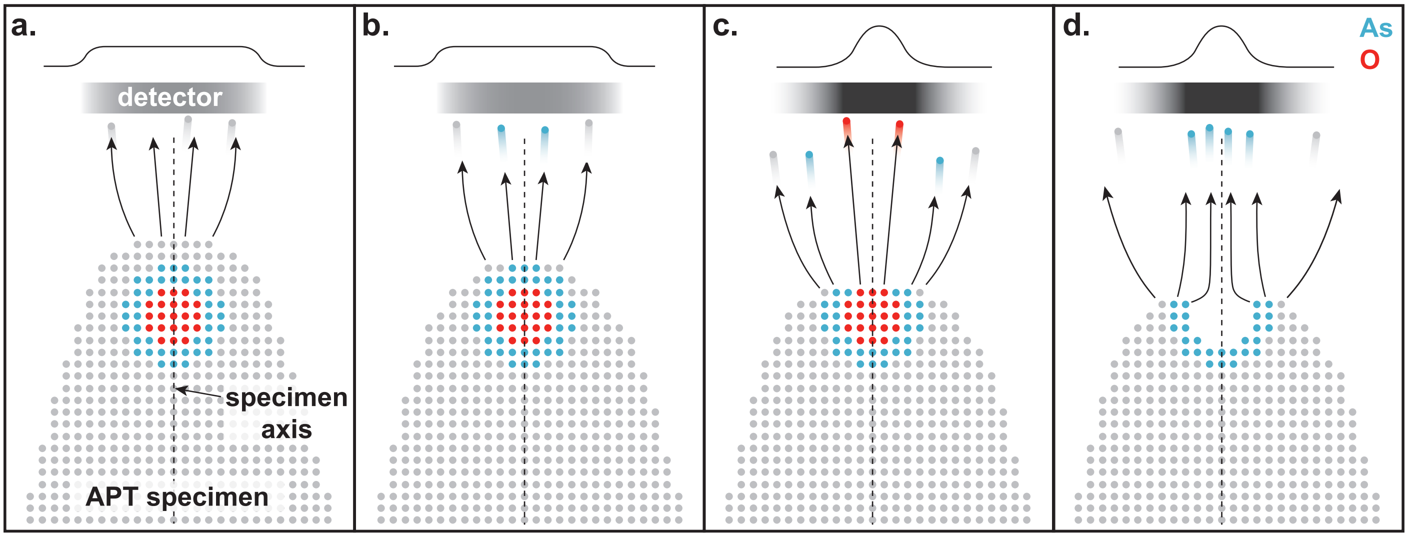

Figure 3.7. Schematic ion flight paths of local compositions surrounding a void during field evaporation. **a.** Ions from the specimen matrix (grey dots) evaporating at an initial 90° to the hemispherical surface and deflecting towards the specimen main axis, resulting in a homogeneous density of hits on the detector. **b.** Ions from the specimen matrix (grey dots) and the void shell (turquoise dots) with a slightly higher evaporation field evaporating from the specimen surface at approximately the same rate homogeneously hitting the detector. **c.** Void opening and evaporation of the content (red dots) with a significantly lower evaporation field at a much faster rate resulting in a very localized high density of hits on the detector. **d.** Ions from the void shell evaporate 90° from its concave surface resulting in converging flight paths and localized high-density region on the detector.

core in an As-coated fluid inclusion, creating a 3D image of O-rich flat discs and As-rich spherules in the reconstruction of the experimental data.

The comparable simulated and experimental APT data show us how we can identify and interpret complex nanostructures such as fluid inclusions or core-shell nanoparticles in APT, which is essential for material characterization. By learning to recognize these nanoscale features in APT data, we can now obtain compositional data and quantify elemental segregation associated with fluid inclusions. However, as a result of the erratic flight path of ions in the vicinity of a void, the distortion of its morphology as shown in our simulated APT results (Figure 3.5) limits the use of APT to quantitative volumetric and compositional measurements rather than qualitative information about its structure.

3.5 Conclusions

Our combined 2D and 3D microstructural analyses document nanoscale fluid inclusions (voids) in a pyrite sample composed of As segregation shells with O-rich (H_2O/FeO) cores, which were confirmed by simulated APT experiments. With these results, we now can identify and interpret fluid inclusions in APT data that had been a missing piece of the puzzle in the interpretation of complex nanostructures from atom probe data. These findings have significant trans-disciplinary implications to the geosciences (structural geology, geochemistry, mineralogy, geochronology, economic geology,), the material sciences (metals, ceramics, polymers), and analytical microscopy. In mineralogy, the characterization of fluid inclusions can provide crucial information to understand the growth of minerals and inclusion of impurities in minerals. Within geochronology voids and dislocations such as these in dated minerals may host elements or isotopes that negatively affect their isotopic age. Within ore deposit geology, voids in precious metal-hosting minerals may provide information about the temperature, pressure and composition of the ore forming fluids and/or act as the necessary traps to structurally prevent the metals (gold, silver, copper) from migrating or diffusing out of the host mineral. In material sciences, the presence of such crystalline features can either limit or enhance the performance of engineering materials. Thus, performing APT analysis on crystalline material can help us better understand and predict their physical properties.

3.6 Acknowledgements

This project was funded by a Mitacs Globalink award and CCEM seed grant (to RD) and NSERC grant (to DAS). We greatly appreciated discussions with Tyler Blum (UW-Madison) and Paraskevas Kontis (MPIE, Düsseldorf). Andreas Sturm and Uwe Tezins are thanked for their training and support of the APT and FIB facilities at MPIE. We thank Lola Lilensten (MPIE, Düsseldorf) for assistance during APT experiments, and Hui Yuan (CCEM, Hamilton) and Natalie Hamada (CCEM Hamilton) for their assistance at on PFIB and STEM instruments at CCEM. Two anonymous reviewers and Angus Kirkland provided valuable comments during the review process.

3.7 References

Armstrong TR, Goodhew PJ (1983) Helium bubble growth in 316 stainless steel. Radiat Eff 77: 35–48. doi.org/10.1080/00337578308224720

Bachhav M, Pawar G, Vurpillot F, Danoix R, Danoix F, Hannoyer B, Dong Y, Marquis E (2019) Interpreting the Presence of an Additional Oxide Layer in Analysis of Metal Oxides–Metal Interfaces in Atom Probe Tomography. J Phys Chem C 123:1313–1319. doi.org/10.1021/acs.jpcc.8b10895

Bachmann F, Hielscher R, Jupp PE, Pantleon W, Schaeben H, Wegert E (2010) Inferential statistics of electron backscatter diffraction data from within individual crystalline grains. J

Appl Crystallogr 43: 1338–1355. doi.org/10.1107/S002188981003027X

Banhart J (2001) Manufacture, characterisation and application of cellular metals and metal foams. Prog Mater Sci 46: 559–632. doi.org/10.1016/S0079-6425(00)00002-5

Barrie CD, Pearce MA, Boyle AP (2011) Reconstructing the pyrite deformation mechanism map. Ore Geol Rev 39: 265–276. doi.org/10.1016/J.OREGEOREV.2011.03.006

Benzerga AA, Besson J, Batisse R, Pineau A (2001) Synergistic effects of plastic anisotropy and void coalescence on fracture mode in plane strain. Model Simul Mater Sci Eng 10: 73–102. doi.org/10.1088/0965-0393/10/1/306

Birdeye P, Smith D, Smith G (1973) Analogue investigations of electric field distribution and ion trajectories in the field ion microscope. J Phys D 7: 1642–1651. doi.org/10.1088/0022-3727/7/12/310

Blavette D, Vurpillot F, Pareige P, Menand A (2001) A model accounting for spatial overlaps in 3D atom-probe microscopy. Ultramic 89: 145–153. doi.org/10.1016/S0304-3991(01)00120-6

Blum TB, Darling JR, Kelly TF, Larson DJ, Moser DE, Perez-Huerta A, Prosa TJ, Reddy SM, Reinhard DA, Saxey W, Ulfig RM, Valley JW (2018) Best practices for reporting atom probe analysis of geological materials. In: Moser DE, Corfu F, Darling JR, Reddy SM, Tait K (eds) Microstructuctural geochronology: Planetary records down to atom scale, pp. 369–373. doi.org/10.1002/9781119227250.ch18

Brenner SS, Seidman DN (1975) Field ion microscope observations of voids in neutron irradiated molybdenum. Radiat Eff 24: 73–78. doi.org/10.1080/00337577508240789

Brocq M, Radiguet B, Le Breton J-M, Cuvilly F, Pareige P, Legendre F (2010) Nanoscale characterisation and clustering mechanism in an Fe–Y2O3 model ODS alloy processed by reactive ball milling and annealing. Acta Mater 58: 1806–1814. doi.org/10.1016/j.actamat.2009.11.022

Burgers JM (1995) Physics.—Some considerations on the fields of stress connected with dislocations in a regular crystal lattice. I BT - Selected Papers of J. M. Burgers. In: Nieuwstadt FTM, Steketee JA (eds). Springer Netherlands, Dordrecht, pp 335–389.

Cox SF, Etheridge MA, Hobbs BE (1981) The experimental ductile deformation of polycrystalline and single crystal pyrite. Econ Geol 76: 2105–2117. doi.org/10.2113/gsecongeo.76.8.2105

Craig JR, Vokes FM, Solberg TN (1998) Pyrite: physical and chemical textures. Miner Depos 34: 82–101. doi.org/10.1007/s001260050187

Cranstoun GKL, Anderson JS (1973) Hydrogen promoted corrosion of tungsten by oxygen in an electric field: A field ion microscope study. Surf Sci 35: 319–335. doi.org/ doi.org/10.1016/0039-6028(73)90222-7

Dubosq R, Lawley CJM, Rogowitz A, Schneider DA, Jackson S (2018) Pyrite deformation and connections to gold mobility: Insight from micro-structural analysis and trace element mapping. Lithos 310–311: 86–104. doi.org/10.1016/J.LITHOS.2018.03.024

Dubosq R, Rogowitz A, Schweinar K, Gault B, Schneider DA (2019) A 2D and 3D nanostructural study of naturally deformed pyrite: assessing the links between trace element mobility and defect structures. Contrib to Mineral Petrol 174:72. doi.org/10.1007/s00410-019-1611-5

Dyar M, Guntar M (2008) Mineralogy and Optical Mineralogy. Am Mineral 93: 1481–1482. doi.org/ doi.org/10.2138/am.2008.524

Edmondson PD, Parish CM, Zhang Y, Hallén A, Miller MK (2013) Helium bubble distributions in a nanostructured ferritic alloy. J Nucl Mater 434: 210–216. doi.org/10.1016/J.JNUCMAT.2012.11.049

Exertier F, La Fontaine A, Corcoran C, Piazolo S, Belousova E, Peng Z, Gault B, Saxey DW, Fougerouse D, Reddy SM, Pedrazzini S, Bagot PAJ, Moody MP, Langelier B, Moser DE, Botton GA, Vogel F, Thompson GB, Blanchard PT, Chiaramontu AN, Reinhard DA, Rice KP, Schreiber DK, Kruska K Wang J, Cairney JM (2018) Atom probe tomography analysis of the reference zircon gj-1: An interlaboratory study. Chem Geol 495: 27–35. doi.org/doi.org/10.1016/j.chemgeo.2018.07.031

Fleck NA, Hutchinson JW, Tvergaard V (1989) Softening by void nucleation and growth in tension and shear. J Mech Phys Solids 37: 515–540. doi.org/10.1016/0022-5096(89)90027-6

Fleet ME, Chryssoulis SL, MacLean PJ, Davidson R, Weisener CG (1993) Arsenian pyrite from gold deposits; Au and As distribution investigated by SIMS and EMP, and color staining and surface oxidation by XPS and LIMS. Can Mineral 31: 1–17.

Fougerouse D, Reddy SM, Saxey DW, Rickard WDA, van Riessen A, Micklethawaite S (2016) Nanoscale gold clusters in arsenopyrite controlled by growth rate not concentration: evidence from atom probe microscopy. Am Mineral 101:1916–1919

Gao X, Wang T, Kim J (2005) On ductile fracture initiation toughness: Effects of void volume fraction, void shape and void distribution. Int J Solids Struct 42: 5097–5117. doi.org/10.1016/J.IJSOLSTR.2005.02.028

Gault B, Moody M, Cairney J, SP R (2012) Atom Probe Microscopy. Springer-Verlag New York Inc.

Gault B, Saxey DW, Ashton MW, Sinnott SB, Chiaramonti AN, Moody MP, Schreiber DK (2016) Behavior of molecules and molecular ions near a field emitter. New J Phys 18: 1–16. doi.org/10.1088/1367-2630/18/3/033031

Ge X, Chen N, Zhang W, Zhu F (1999) Selective field evaporation in field-ion microscopy for ordered alloys. J Appl Phys 85: 3488–3493. doi.org/10.1063/1.369706

Graf JL, Skinner BJ, Bras J, Fagot M, Levade C, Couderc JJ (1981) Transmission electron microscopic observation of plastic deformation in experimentally deformed pyrite. Econ Geol 76: 738–742. doi.org/10.2113/gsecongeo.76.3.738

Gruber M, Vurpillot F, Bostel A, Deconihout B (2011) Field evaporation: A kinetic Monte Carlo approach on the influence of temperature. Surf Sci 605: 2025–2031. doi.org/10.1016/J.SUSC.2011.07.022

Harrison RW, Greaves G, Hinks JA, Donnelly SE (2017) Engineering self-organising helium bubble lattices in tungsten. Sci Rep 7: 7724–7728. doi.org/10.1038/s41598-017-07711-w

Hatzoglou C, Radiguet B, Da Costa G, Pareige P, Roussel M, Hernandez-Mayoral M, Pareige C (2019) Quantification of APT physical limitations on chemical composition of precipitates in Fe–Cr alloys. J Nucl Mater 522: 64–73. doi.org/10.1016/J.JNUCMAT.2019.05.022

Hatzoglou C, Radiguet B, Vurpillot F, Pareige P (2018) A chemical composition correction model for nanoclusters observed by APT - Application to ODS steel nanoparticles. J Nucl Mater 505: 240–248. doi.org/10.1016/J.JNUCMAT.2018.03.057

He J, Zenk CH, Zhou X, Neumeier S, Raabe D, Gault B, Makineni SK (2020) On the atomic solute diffusional mechanisms during compressive creep deformation of a Co-Al-W-Ta single crystal superalloy. Acta Mater 184: 86–99. doi.org/10.1016/J.ACTAMAT.2019.11.035

Horstemeyer MF, Gokhale AM (1999) A void–crack nucleation model for ductile metals. Int J Solids Struct 36: 5029–5055. doi.org/10.1016/S0020-7683(98)00239-X

Itoh N, Duffy DM, Khakshouri S, Stoneham AM (2009) Making tracks: electronic excitation roles in forming swift heavy ion tracks. J Phys Condens Matter 21: 1–14. doi.org/10.1088/0953-

8984/21/47/474205

Itoh N, Stoneham AM (2001) Materials modification by electronic excitation. Radiat Eff Defects Solids 155: 277–290. doi.org/10.1080/10420150108214126

Katnagallu S, Stephenson LT, Mouton I, Freysoldt C, Subramanyam APA, Jenke J, Ladines AN, Neumeier S, Hammerschmidt T, Drautz R, Neugebauer J, Vurpillot F, Raabe D, Gault B (2019) Imaging individual solute atoms at crystalline imperfections in metals. New J Phys 21: 1–10. doi.org/10.1088/1367-2630/ab5cc4

Kitaguchi HS, Moody MP, Li HY, Evans HE, Hardy MC, Lozano-Perez S (2015) An atom probe tomography study of the oxide–metal interface of an oxide intrusion ahead of a crack in a polycrystalline Ni-based superalloy. Scr Mater 97: 41–44. doi.org/10.1016/j.scriptamat.2014.10.025

Klapper H (2010) Generation and propagation of defects during crystal growth. In: Dhanaraj G, Byrappa K, Prasad V, Dudley M (eds) Handbook of crystal growth. Springer, Berlin.

Klempner D, Frisch K (1991) Polymeric foams. Hanser, New York, NY.

Kuo H-S, Hwang I-S, Fu T-Y, Hwang Y-S, Lu Y-H, Lin C-Y, Hou J-L, Tsong TT (2009) A single-atom sharp iridium tip as an emitter of gas field ion sources. Nanotechnology 20: 1–5. doi.org/10.1088/0957-4484/20/33/335701

Lardé R, Talbot E, Pareige P, Bieber H, Schmerber G, Colis S, Pierron-Bohnes V, Dinia A(2011) Evidence of superparamagnetic Co clusters in pulsed laser deposition-grown Zn0.9Co0.1O Thin films using atom probe tomography. J Am Chem Soc 133: 1451–1458. doi.org/10.1021/ja108290u

Large RR, Danyushevsky L, Hollit C, Maslennikov V, Meffre S, Gilbert S, Bull S, Scott R, EMsbo P, Thomas H, Singh B, Foster J (2009) Gold and trace element zonation in pyrite using a laser imaging technique: Implications for the timing of gold in orogenic and carlin-style sediment-hosted deposits. Econ Geol 104: 635–668. doi.org/10.2113/gsecongeo.104.5.635

Larson DJ, Gault B, Geiser BP, DeGeuser F, Vurpillot F (2013) Atom probe tomography spatial reconstruction: Status and directions. Curr Opin Solid State Mater Sci 17: 236–247. doi.org/10.1016/J.COSSMS.2013.09.002

Larson DJ, Giddings AD, Wu Y, Verheijen MA, Prosa TJ, Roozeboom F, Rice KP, Kessels WMM, Geiser BP, Kelly TF (2015) Encapsulation method for atom probe tomography analysis of nanoparticles. Ultramic 159: 420–426. doi.org/10.1016/J.ULTRAMIC.2015.02.014

Lee JH, Cha EJ, Kim YT, Chae BK, Kim JJ, Lee SY, Hwang HS, Park CG (2015) A study of threshold switching of NbO2 using atom probe tomography and transmission electron microscopy. Micron 79: 101–109. doi.org/10.1016/j.micron.2015.07.015

Lefebvre W, Vurpillot F, Sauvage X (2016) Atom probe tomography: put theory into practice. Elsevier, Boston, MA.

Lloyd MJ, Abernethy RG, Gilbert MR, Griffiths I, Bagot PAJ, Nguyen-Manh D, Moody MP, Armstrong DEJ (2019) Decoration of voids with rhenium and osmium transmutation products in neutron irradiated single crystal tungsten. Scr Mater 173: 96–100. doi.org/10.1016/J.SCRIPTAMAT.2019.07.036

Lünsdorf NK, Dunkl I, Schmidt BC, Rantitsch G, Eynatten H (2017) Towards a higher comparability of geothermometric data obtained by Raman spectroscopy of carbonaceous material. Part 2: A revised geothermometer. Geostand Geoanalytical Res 41: 593–612. doi.org/10.1111/ggr.12178

Makineni SK, Kumar A, Lenz M, Kontis P, Meiners T, Zenk C, Zaefferer S, Eggler G, Neumeier

S, Spiecker E, Raabe D, Gault B (2018) On the diffusive phase transformation mechanism assisted by extended dislocations during creep of a single crystal CoNi-based superalloy. Acta Mater 155: 362–371. doi.org/10.1016/J.ACTAMAT.2018.05.074

Marquis EA, Geiser BP, Prosa TJ, Larson DJ (2011) Evolution of tip shape during field evaporation of complex multilayer structures. J Microsc 241: 225–233. doi.org/10.1111/j.1365-2818.2010.03421.x

McVeigh C, Vernerey F, Liu WK, Moran B, Olson G (2007) An interactive micro-void shear localization mechanism in high strength steels. J Mech Phys Solids 55: 225–244. doi.org/10.1016/J.JMPS.2006.08.002

Miller MK (2006) Atom probe tomography characterization of solute segregation to dislocations and interfaces. J Mater Sci 41: 7808–7813. doi.org/10.1007/s10853-006-0518-5

Miller MK (1987) The effects of local magnification and trajectory aberrations on atom probe analysis. J Phys 48: 565–570. doi.org/10.1051/jphyscol:1987692

Miller MK, Longstreth-Spoor L, Kelton KF (2011) Detecting density variations and nanovoids. Ultramic 111: 469–472. doi.org/10.1016/j.ultramic.2011.01.027

Moser DE, Cupelli CL, Barker IR, Flowers RM, Bowman JR, Wooden J, Hart RJ (2011) New zircon shock phenomena and their use for dating and reconstruction of large impact structures revealed by electron nanobeam (EBSD, CL, EDS) and isotopic U–Pb and (U–Th)/He analysis of the Vredefort dome. Can J Earth Sci 48: 117–139. doi.org/10.1139/E11-011

Müller EW, Nakamura S, Nishikawa O, McLane SB (1965) Gas-surface interactions and field-ion microscopy of nonrefractory metals. J Appl Phys 36: 2496–2503. doi.org/10.1063/1.1714519

Nesse W (2000) Introduction to Mineralogy. Oxford University Press, New York, NY.

Ohji T (2013) Porous ceramic materials. In: Somiya S (ed) Handbook of Advanced Ceramics, second edition. Academic Press, Oxford, pp 1131–1148.

Orsini V., Zikry M. (2001) Void growth and interaction in crystalline materials. Int J Plast 17: 1393–1417. doi.org/10.1016/S0749-6419(00)00091-7

Piazolo S, La Fontaine A, Trimby P, Harley S, Yang L, Armstrong R, Cairney JM (2016) Deformation-induced trace element redistribution in zircon revealed using atom probe tomography. Nat Commun 7: 10490. doi.org/10.1038/ncomms10490

Reddy SM, Saxey DW, Rickard WDA, Fougerouse D, Montalvo SD, Verberne R, Riessen A (2020) Atom Probe Tomography: Development and Application to the Geosciences. Geostand Geoanalytical Res 44: 5–50. doi.org/10.1111/ggr.12313

Reddy SM, van Riessen A, Saxey DW, Johnson TE, Rickard WDA, Fougerouse D, Fischer S, Prosa TJ, Rice KP, Reinhard DA, Chen Y, Olson D (2016) Mechanisms of deformation-induced trace element migration in zircon resolved by atom probe and correlative microscopy. Geochim Cosmochim Acta 195: 158–170. doi.org/10.1016/J.GCA.2016.09.019

Rogowitz A, Zaefferer S, Dubosq R (2018) Direct observation of dislocation nucleation in pyrite using combined electron channelling contrast imaging and electron backscatter diffraction. Terra Nov 30: 423–430. doi.org/10.1111/ter.12358

Rolland N, Vurpillot F, Duguay S, Blavette D (2015) A meshless algorithm to model field evaporation in atom probe tomography. Microsc Microanal 21: 1649–1656. doi.org/10.1017/S1431927615015184

Rothaut J, Schroeder H, Ullmaier H (1983) The growth of helium bubbles in stainless steel at high temperatures. Philos Mag A 47: 781–795. doi.org/10.1080/01418618308245265

Schmidt JE, Peng L, Poplawsky JD, Weckhuysen BM (2018) Nanoscale Chemical Imaging of Zeolites Using Atom Probe Tomography. Angew Chemie Int Ed 57: 10422–10435. doi.org/10.1002/anie.201712952

Schwartz K, Lang M (2016) Mineral defects. In: White WM (ed) Encyclopedia of Geochemistry: A Comprehensive Reference Source on the Chemistry of the Earth. Springer International Publishing, pp 1–5.

Seitz F, Koehler J (1956) Solid State Physics Vol.2. In: Seitz F, Turnbull D (eds) Solid state physics. Academic Press, New York, NY, pp 307–442.

Smallman RE, Westmacott KH (1972) Invited review: The nature and behaviour of vacancy clusters in close-packed metals. Mater Sci Eng 9: 249–272. doi.org/10.1016/0025-5416(72)90042-0

Smith GDW, Hudson D, Styman PD, Williams CA (2013) Studies of dislocations by field ion microscopy and atom probe tomography. Philos Mag 93: 3726–3740. doi.org/10.1080/14786435.2013.818257

Smith R (1978) Ion trajectories in field-ion microscope. J Phys D-Applied Phys 11: 409–419.

Thompson K, Lawrence D, Larson DJ, Olson JD, Kelly TF, Gorman B (2007) In situ site-specific specimen preparation for atom probe tomography. Ultramic 107: 131–139. doi.org/10.1016/J.ULTRAMIC.2006.06.008

Timms NE, Reddy SM, Fitz Gerald JD, Green L, Muhling JR (2012) Inclusion-localised crystal-plasticity, dynamic porosity, and fast diffusion pathway generation in zircon. J Struct Geol 35: 78–89. doi.org/10.1016/j.jsg.2011.11.005

Tsong TT (1978) Field ion image formation. Surf Sci 70: 211–233. doi.org/10.1016/0039-

6028(78)90410-7

Tvergaard V (1989) Material Failure by Void Growth to Coalescence. Adv Appl Mech 27: 83–151. doi.org/10.1016/S0065-2156(08)70195-9

Vurpillot F (2001) Étude de la fonction de transfert pointe-image de la sonde atomique tomographique. Université de Rouen, 197 p.

Vurpillot F, Bostel A, Blavette D (2000) Trajectory overlaps and local magnification in three-dimensional atom probe. Appl Phys Lett 76: 3127–3129. doi.org/10.1063/1.126545

Vurpillot F, Oberdorfer C (2015) Modeling atom probe tomography: A review. Ultramic 159: 202–216. doi.org/10.1016/J.ULTRAMIC.2014.12.013

Wilkinson D (1988) The effect of a non uniform void distribution on grain boundary void growth during creep. Acta Metall 36: 2055–2063. doi.org/10.1016/0001-6160(88)90307-0

Wilkinson DS (1987) The effect of time dependent void density on grain boundary creep fracture—i. continuous void coalescence. Acta Metall 35: 1251–1259. doi.org/10.1016/0001-6160(87)90006-X

Yu Y, Zhang S, Mio AM, Gault B, Sheskin A, Scheu C, Raabe D, Zu F, Wuttig M, Amouyal Y, Cojocaru-Mirédin O (2018) Ag-Segregation to Dislocations in PbTe-Based Thermoelectric Materials. ACS Appl Mater Interfaces 10: 3609–3615. doi.org/10.1021/acsami.7b17142

Yu Y, Zhou C, Zhang S, Zhu M, Wuttig M, Scheu C, Raabe D, Snyder GF, Gault B, Cojocaru-Mirédin O (2019) Revealing nano-chemistry at lattice defects in thermoelectric materials using atom probe tomography. Mater Today 32: 260–274. doi.org/10.1016/J.MATTOD.2019.11.010

CHAPTER 4

Fluid inclusion induced hardening: nanoscale evidence from naturally deformed pyrite

R. Dubosq[1], A. Rogowitz[2], D.A. Schneider[1], K. Schweinar[3], B. Gault[3,4]

[1]Department of Earth and Environmental Sciences, University of Ottawa, Canada

[2]Department of Geodynamics and Sedimentology, University of Vienna, Austria

[3]Max-Planck-Institut für Eisenforschung GmbH, Germany

[4]Department of Materials, Royal School of Mines, Imperial College London, UK

Published in

Contributions to Mineralogy and Petrology, Volume 176

January 2021

doi.org/10.1007/s00410-021-01774-9

4.1 Abstract

The interaction of trace elements, fluids and crystal defects plays a vital role in a crystalline material's response to an applied stress. Fluid inclusions are typically known to facilitate crystal-plastic deformation in minerals. Herein we discuss a model of fluid hardening whereby dislocations are pinned at fluid inclusions during crystal-plastic deformation, initiating pipe diffusion of trace elements from the fluid inclusions into crystal defects that leads to their stabilization and local hardening. We derive this hypothesis from atom probe tomography data of naturally deformed pyrite, combined with electron backscatter diffraction mapping, electron channelling contrast imaging and scanning transmission electron microscopy. The 2D and 3D micro- to nanoscale structural and chemical data reveal nanoscale fluid inclusions enriched in As, O, Na and K that are linked by As-enriched dislocations. Our efforts advance the understanding of the interplay between nanostructures and impurities during relatively low temperature deformation, which yields insight into the larger scale mass transfer processes on Earth.

4.2 Introduction

Structural defects strongly influence the response of a crystalline material, including natural minerals and metals, to an applied stress. Such as within the crystal-plastic regime, the multiplication of dislocations can lead to their entanglement, resulting in strain hardening thus increasing the yield strength (Hansen et al. 2019). Strain hardening can also occur when dislocations are arrested by the strain fields of immobile defects (i.e., particles or precipitates) or by the accumulation of mobile solutes in dislocation cores, known as Cottrell atmospheres (Cahn 2014; Chen et al. 2008; Cottrell and Bilby 1949; Vitik et al. 2000). These imperfections have a role in trace element mobility, since grain or phase boundaries and dislocations offer pathways for accelerated diffusion (Dubosq et al. 2019; Kovaleva et al. 2017; Legros et al. 2008; Love 1964;

Piazolo et al. 2016). For example, Fougerouse et al. (2019) documented Pb isotopes within recrystallized high-angle grain boundaries in pyrite that have been interpreted to be externally-derived Pb, which suggests grain boundaries act as open systems for trace element mobility. In another study, Cukjati et al. (2019) showed that the diffusion of trace elements at phase boundaries can be a controlling factor for diffusion creep processes, therefore having an effect on rheology.

The rheology of minerals is similarly influenced by interactions with fluids. Under relatively high pressure and temperature conditions, minerals are typically softened when exposed to a hydrous environment. One such example is the compression and subsequent expansion of fluid inclusions under increasing temperature resulting in the nucleation of dislocation loops and mechanical softening (Bakker and Jansen 1994; McLaren et al. 1983). Furthermore, water can soften minerals through hydrolytic weakening. This process occurs when water molecules penetrate into a mineral converting strong silicon–oxygen bonds to weaker hydrogen bonds in silicate minerals, facilitating dislocation creep processes (Griggs 1967). Based on deformation experiments under wet conditions, hydrolytic weakening can lower the mineral strength up to three orders of magnitude (Chen et al. 2006; Mei et al. 2010; Tielke et al. 2017; Xu et al. 2019). In addition, since the rate of the recovery processes is controlled by dislocation creep, and recovery is essential for the nucleation of recrystallized grains, the presence of water in silicate minerals reduces the critical temperature required for recrystallization at low strain rates (Griggs 1967; Hobbs 1968; Hobbs et al. 1972; Tullis et al. 1973; Bell and Etheridge 1976). Water can also reduce a mineral's strength by enhancing volume diffusion. The increased oxygen density in the crystal structure introduces more point defects resulting in faster diffusion (Ahrens and Schubert 1975). Mechanical weakening can also occur by solution creep. Under high compressive stresses, mineral faces are dissolved by intergranular fluid and reprecipitated on surfaces of low compressive stresses (Guren et al. 2020; Marti et al. 2018; Putnis and Ruiz-Agudo 2013; Renard et al. 2019; Wang et al. 2020). The presence of intergranular fluids can also enhance the activity of grain boundary sliding in superplasticity processes by facilitating diffusion along grain boundaries since the activation energy of fluid phase diffusion is significantly lower than diffusion along dry grain boundaries (Fischer and Elliott 1974).

Investigation of these sub-micrometer scale processes requires a correlative approach combining high-spatial resolution analytical techniques. Current conventional techniques for sub-micrometer scale analysis include electron channeling contrast imaging (ECCI), electron backscatter diffraction (EBSD) and transmission electron microscopy (TEM). Such techniques are very effective at obtaining qualitative and quantitative information about the characteristics of crystal defects such as structure, morphology, and distribution, but they are limited in their ability to quantify elemental compositions at the same scale. Advances in analytical microscopy have now enabled the quantification of elemental compositions at the sub-nanometer scale. One of these novel techniques is atom probe tomography (APT), which has the ability to provide 3D quantitative compositional measurements and spatial imaging of materials at the near-atomic scale (Gault et al. 2012). Although APT was initially developed in the materials sciences for the investigation of metals, the introduction of laser-assisted APT has enabled the analysis of semi-conducting and insulating materials such as natural minerals (Reddy et al. 2020). This tool has since been increasingly applied to understand sub-micrometer scale geological processes, more specifically focussing on the spatial relationship between crystal defects and trace element distribution (e.g., Fougerouse et al. 2019; Piazolo et al. 2016; Schirmer et al. 2020; Wu et al. 2019). For example, in our recent study on pyrite, we investigated the role that crystal-deformation plays on trace element mobility by combining EBSD, ECCI and APT and we were able to document evidence of a dislocation-impurity-pair diffusion mechanism (Dubosq et al. 2019).

Herein, we present data that suggests fluid inclusions can induce mechanical hardening in minerals during deformation. By combining a succession of high spatial resolution analytical techniques on a naturally deformed polycrystalline pyrite aggregate from the Abitibi Subprovince in Canada, we document the interaction between crystal defects and trace element distribution. The multiscale information is then used to discuss the impact that dislocations and fluid inclusions have on mineral rheology. We propose a fluid hardening model based on the pinning of dislocations at fluid inclusions and their subsequent stabilization by pipe diffusion of trace elements from the inclusions into the dislocation cores.

4.3 Geology of the Abitibi Subprovince

The Neoarchean Abitibi Subprovince is located in the southernmost region of the Superior Province in Canada. The region is well-known for its abundance in economic base- and precious-metal mineral deposits including volcanogenic sulphide, epigenic gold, and orogenic gold deposits (Dubé and Gosselin 2007; Eckstrand and Hulbert 2007; Galley et al. 2007). The subprovince is subdivided into eight volcanic episodes: (1) Pacaud (2750 to 2735 Ma); (2) Deloro (2730 to 2724 Ma); (3) Stoughton-Roquemaure (2723 to 2720 Ma); (4) Kidd-Munro (2719 to 2710 Ma); (5) Tisdale (2710 to 2703 Ma); (6) Blake River (2701 to 2697 Ma); (7) Porcupine (2696 to 2692 Ma); and (8) Timiskaming (2687 to 2675 Ma; Figure 4.1; Ayer et al. 2002; Thurston et al. 2008). Each episode consists of mafic to ultramafic volcanic rocks with lesser felsic to intermediate volcanic rocks intruded by syn-volcanic tonalite and gabbrodiorite dikes and plutons. These assemblages are intercalated with, and overlain by, thin sedimentary horizons comprised of iron formations,

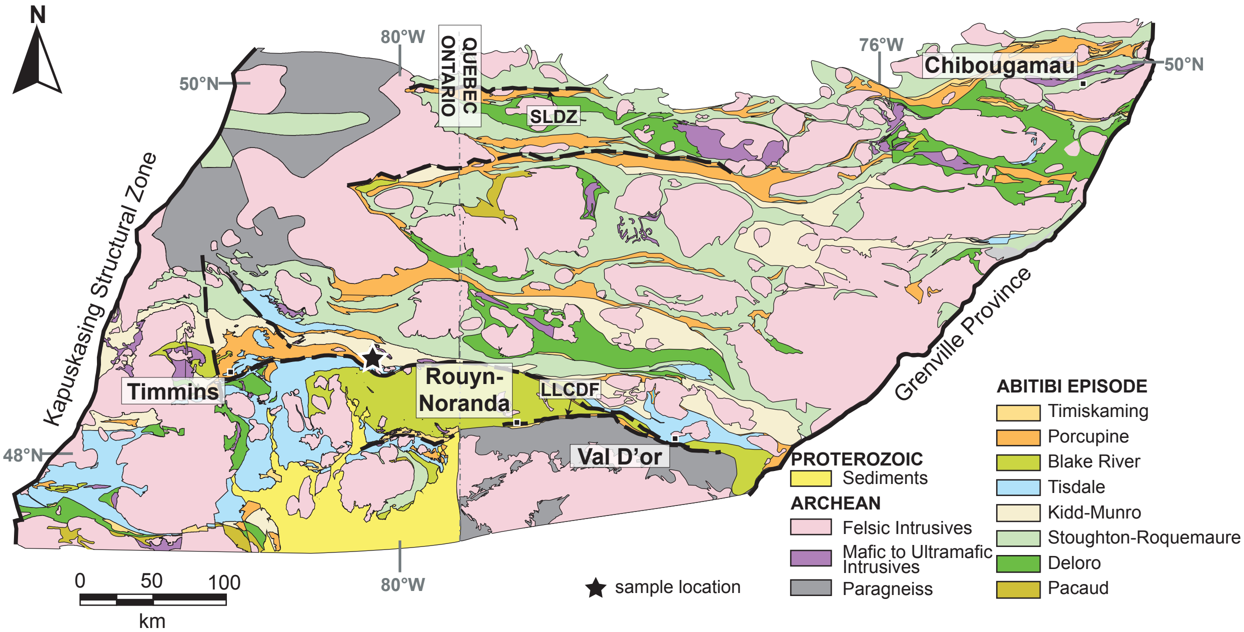

Figure 4.1. Simplified geological map of the Abitibi Subprovince of eastern Canada showing the location of the investigated sample within the Kidd-Munro Assemblage of the Abitibi Greenstone Belt. Larder Lake-Cadillac Destor Fault: LLCDF; Sunday Lake Deformation Zone: SLDZ. (Source: modified from Thurston et al. 2008).

chert breccia, heterolithic debris flows, sandstone, conglomerates and argillites representing brief, punctuated quiescent periods between volcanic episodes (Ayer et al. 2008).

The volcanic belt has been deformed by three major events (Bateman et al. 2008): (1) the collision between the Abitibi and the northern subprovinces of the Superior Province, which resulted in cleavage and folds with north-trending axial planes that pre-date the deposition of the Porcupine Assemblage at ca. 2690 Ma; (2) the refolding and transposition of the pre-Porcupine Assemblage folds, which pre-dates the ca. 2690 Ma Timiskaming Assemblage; and (3) post-Timiskaming folding and faulting. The belt was later subjected to lower-middle greenschist facies metamorphism between 2677 and 2643 Ma (Powell et al. 1995a, 1995b; Thompson 2003).

The sample under investigation in this study comes from the Kidd-Munro Assemblage, a 5 km thick volcanic and sedimentary assemblage involving mostly basalts, komatiites, calc-alkaline basalts to rhyolites and tholeiitic rhyolites overlain by younger sedimentary packages with an age range of 2719 to 2710 Ma (Ayer et al. 2002; Barrie 1999). The volcanic successions of the Kidd-Munro Assemblage can be subdivided into two suites of metavolcanic rocks: (1) a mafic to ultramafic suite of tholeiitic to komatiitic affinity; and (2) an intermediate to felsic metavolcanic suite of calc-alkalic affinity, which conformably underlies the tholeiitic to komatiitic metavolcanic suite (Ayer et al. 1999; Epp 1997; Epp and Crocket 1999). The intercalated sedimentary packages consist of moderately to strongly graphitic argillite horizons that comprise lithic wackes, argillite, black chert, sphalerite-bearing turbidites and lapillistones (Bleeker and Parrish 1996). These horizons are heavily enriched in base- and precious-metals including Pb, Ag, Au, Cd, Ga, As, Bi, Co, Cu, Cr, Hg, In, Mn, Mo, Ni, Sb, Sn, and Zn, with accessory Pt, Te and Se (Bleeker and Breeman 2011). The detritus of these horizons has been interpreted to be locally derived and reflect the reworking of contemporaneous black smoker debris contributing to the complex history of ore formation in the region (Bleeker and Parrish 1996).

4.4 Materials and methods

4.4.1 Sample petrography

The investigated sample is a polycrystalline pyrite aggregate hosted within a graphitic argillite horizon in the Kidd-Munro Assemblage. The host rock consists of a dark grey to black, fissile carbonaceous slate. The matrix is composed mostly of fine grained (5-20 μm) graphite, white mica, and quartz, with graphite and white mica defining a weak foliation. Pyrite occurs as large (800-1000 μm) and several smaller (100-300 μm), less developed nodules consisting of fine grained subhedral cores and larger grained rims. These nodules are surrounded by quartz-rich pressure haloes containing calcite, white mica, and minor chalcopyrite. In addition to nodules, pyrite also occurs as polycrystalline aggregates within intergranular pockets (50-300 μm) filled with quartz and calcite as well as minor chalcopyrite and sphalerite.

The studied pyrite aggregate measures ~200 by 250 μm, and is made up of anhedral to subhedral pyrite crystals ranging between 10 to 50 μm and a secondary growth forming a 2-10 μm wide porous rim (Figure 4.2). Raman spectroscopy of carbonaceous material yielded a peak temperature of 302 ± 27°C for the sample (Dubosq et al. 2020). The host rock foliation wraps around the aggregate (Figure 4.2b) suggesting pre- to syn-deformational crystallization. The presence of minor subgrain development within the surrounding intergranular quartz (Figure 4.2a) also suggests the pre- to syn-deformational crystallization of the pyrite aggregate.

4.4.2 Electron backscatter diffraction and electron channelling contrast imaging

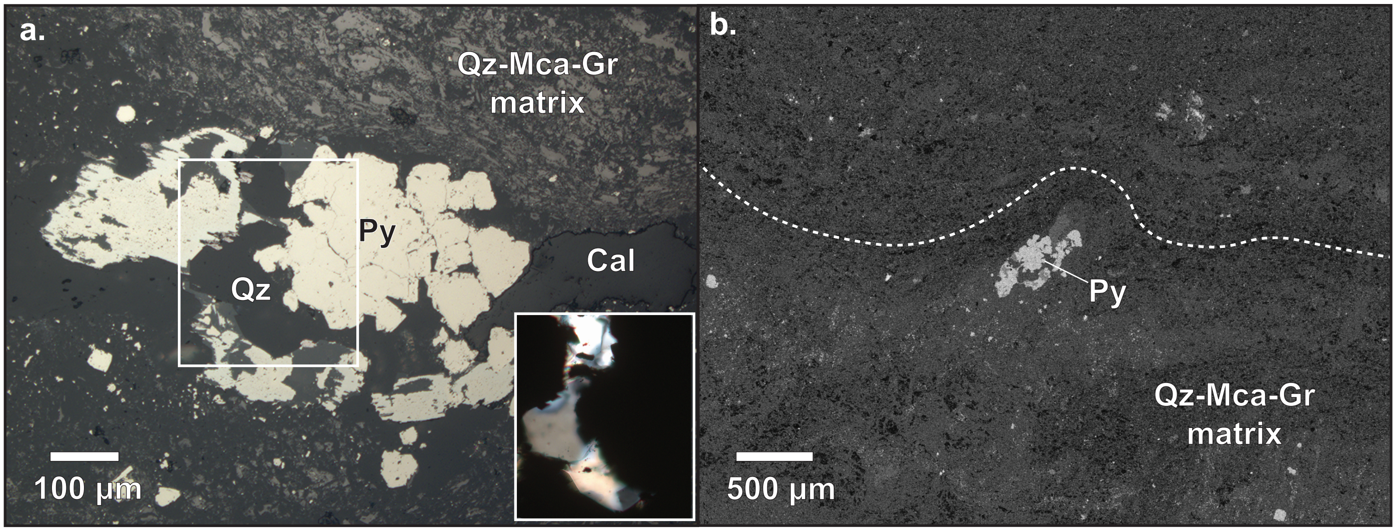

Figure 4.2. a. Reflected light photomicrograph of pyrite aggregate showing quartz-calcite (Qz-Cal) pressure shadow and minor subgrain development in quartz (white box inset). **b.** Overview BSE image of pyrite (Py) aggregate showing the foliation (dashed white line) wrapping around the pyrite. Graphite: Gr; Mica: Mca.

Primary characterization of the investigated pyrite aggregate was performed by combining EBSD mapping and ECC imaging to obtain quantitative and qualitative information of the crystalline structure and deformation state of the sample. All crystallographic data were collected at the Department of Lithospheric Research (University of Vienna, Austria) using a FEI Quanta 3D FEG instrument equipped with a field-emission electron source and an EDAX Pegasus Apex 4 System consisting of a Digiview IV EBSD camera and an Apollo XV silicon drift detector for EDX-spectroscopy. Prior to analysis, the thin section was chemomechanically polished with an alkaline colloidal silica suspension (SYTON©) and carbon-coated to establish conductivity. EBSD mapping was conducted first with analytical conditions set to an accelerating voltage of 15 kV with a spot size of 1.5 in analytical modus and a probe current of 4 nA. The sample was tilted to 70° and brought to a working distance of 14 mm. Mapping was performed by using a hexagonal grid and a step size of 26 nm. EBSD data was cleaned using the OIM Data Collection and Analysis software by combining the neighbour orientation correlation (clean-up level: 2) and confidence index standardization (CI: 0.1) functions. Misorientation deviation angle (misorientation of each pixel relative to grain average) and grain boundary maps were then created using the MTEX toolbox in MATLAB® (Bachmann et al. 2010).

ECC imaging was subsequently conducted at specific pyrite domains identified in EBSD maps to further investigate the targeted microstructures. This imaging was also performed on the FEI Quanta 3D FEG instrument at the University of Vienna. Analytical conditions for imaging were set to a 30 kV accelerating voltage, a spot size of 2 in analytical modus, a 2–4 nA probe current and a working distance between 7.5 and 8 mm, allowing for the direct observation of crystal defects.

4.4.3 Atom probe tomography

A series of specimens were prepared from the investigated pyrite by *in situ* lift-out (Thompson et al. 2007) for APT in an attempt to investigate the detailed composition of some of the microstructural features at the near-atomic scale. The needle-shaped specimen was sharpened by annular milling at 30 kV on a dual-beam scanning electron microscope (SEM)/focused ion beam (FIB) FEI Helios Nanolab 600i at the Max-Planck-Institut für Eisenforschung GmbH (Düsseldorf, Germany) and subsequently cleaned using the Ga-beam at 2 kV to remove regions potentially severely damaged by the implantation of energetic Ga ions. The specimens were then analysed by APT in a CAMECA LEAP 5000 XR (Table S4.1) fitted with a reflectron-lens with a detector efficiency of ~50%. The specimen was analysed in laser pulsing mode at 55 K with a laser pulse energy of 45 pJ focused on an area estimated to be <3 μm in diameter, a detection rate of 0.5 ion detected for 100 pulses and a laser pulse repetition rate of 125 kHz. The data processing and reconstruction were done with the commercial software package IVAS® 3.8.2. Compositional profiles presented herein were generated from cylindrical regions of interest using the 1D concentration profile function and computed using the fixed bin width profile, atomic, and decompose complex ions options. The bin size was adjusted for each profile (0.2–0.4 nm) to maximize the ratio of the peak signal to the statistical fluctuations. Ion identities within the measured dataset were assigned by defining ranges within the mass spectrum that best fit theoretical isotopic ratios (Blum et al. 2018; Exertier et al. 2018; Reddy et al. 2020). The ranged mass spectrum used for the specimens is shown in Figure S4.1.

4.4.4 Scanning transmission electron microscopy

A TEM specimen adjacent to the APT targets was prepared by *in situ* lift-out using a Thermo Scientific Helios™ G4 UXe DualBeam™ Plasma-FIB/SEM at the Canadian Centre for Electron Microscopy at McMaster University (Hamilton, Canada). The region of interest was marked by an electron-deposited tungsten layer and subsequently protected by xenon deposition of tungsten and mixture of carbon and platinum. A ~1 μm thick lamella was obtained by trenching adjacent areas and was then attached to a copper grid. The lamella was thinned to ~80 nm by an ion beam with gradually decreased currents at 30 keV and cleaned with progressively reduced low voltages until 5 keV in order to remove the amorphorized layers resulting from ion bombardment.

High-angle annular dark field (HAADF) imaging was performed using a FEI Titan 80-300 transmission electron microscopy (TEM) equipped with a CEOS probe and image corrector operated in STEM mode at a convergence angle of 19.1 mrad. The microscope was operated at an acceleration voltage of 300 kV and micrographs captured using a Fischione high-angle annular dark field detector. The images were collected using a dwell time of 4 μs, a total frame time of 20.1 s, a camera length of 185 mm, a spot size of 11 and a screen current of ~100 pA.

4.5 Results

4.5.1 Microstructural analysis

EBSD analysis of the pyrite aggregate evinces mostly minor crystal-plastic deformation, displaying a heterogeneous misorientation pattern with a maximum average misorientation of <2° relative to the mean orientation, with the exception of two grains that reveal moderate crystal plasticity in the form of low angle grain boundaries and a maximum deviation angle of 9° (Figure 4.3a, 4.4c). In ECCI, dislocations appear as white dots with short bright line segments whereas low-angle grain boundaries, not all observed by EBSD, are revealed by partially aligned dislocation walls with varying crystal orientation on either side (Figure 4.3b, c). In ECC images of the higher strained region, we observe mostly microfractures at the 2–5° low-angle grain boundaries imaged by EBSD. Microfractures are documented as discrete line segments, some of which are delineated by fluid inclusions (Figure 4.4a). Trace analysis of the microfractures in

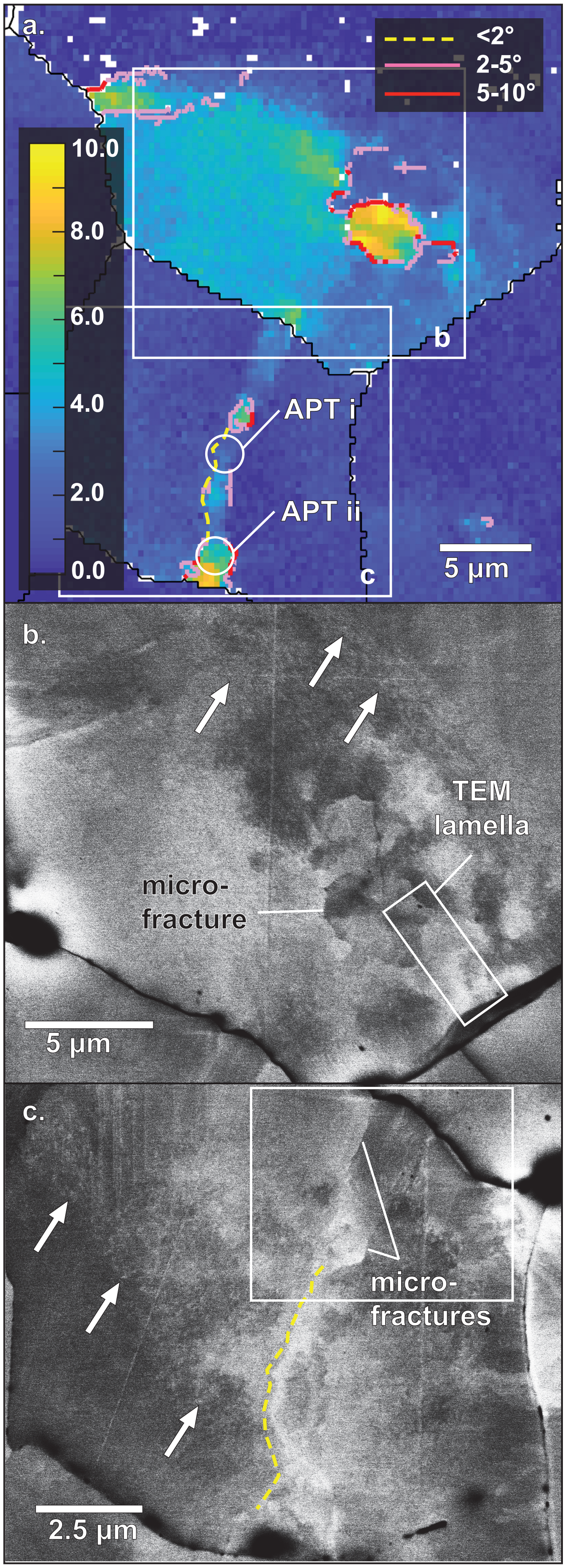

Figure 4.3. a. EBSD misorientation deviation angle and grain boundary map of pyrite region of interest revealing a heterogeneous misorientation pattern with a maximum misorientation of 9° relative to the average grain orientation and low-angle grain boundaries (pink, red and dashed yellow lines). The <2° low-angle grain boundaries were observed in the ECC images as aligned dislocations and were added onto the EBSD map. The white circles indicate the locations of APT specimens (i and ii) and white boxes indicate the location of (**b.** and **c.**) ECC images of the pyrite. These images reveal increased dislocation density (white arrows), micro-fracturing and associated low-angle grain boundaries (dashed yellow lines). White box in b. indicates the location of the TEM lamella lift-out. White box in c. indicates the location of figure 4.4a.

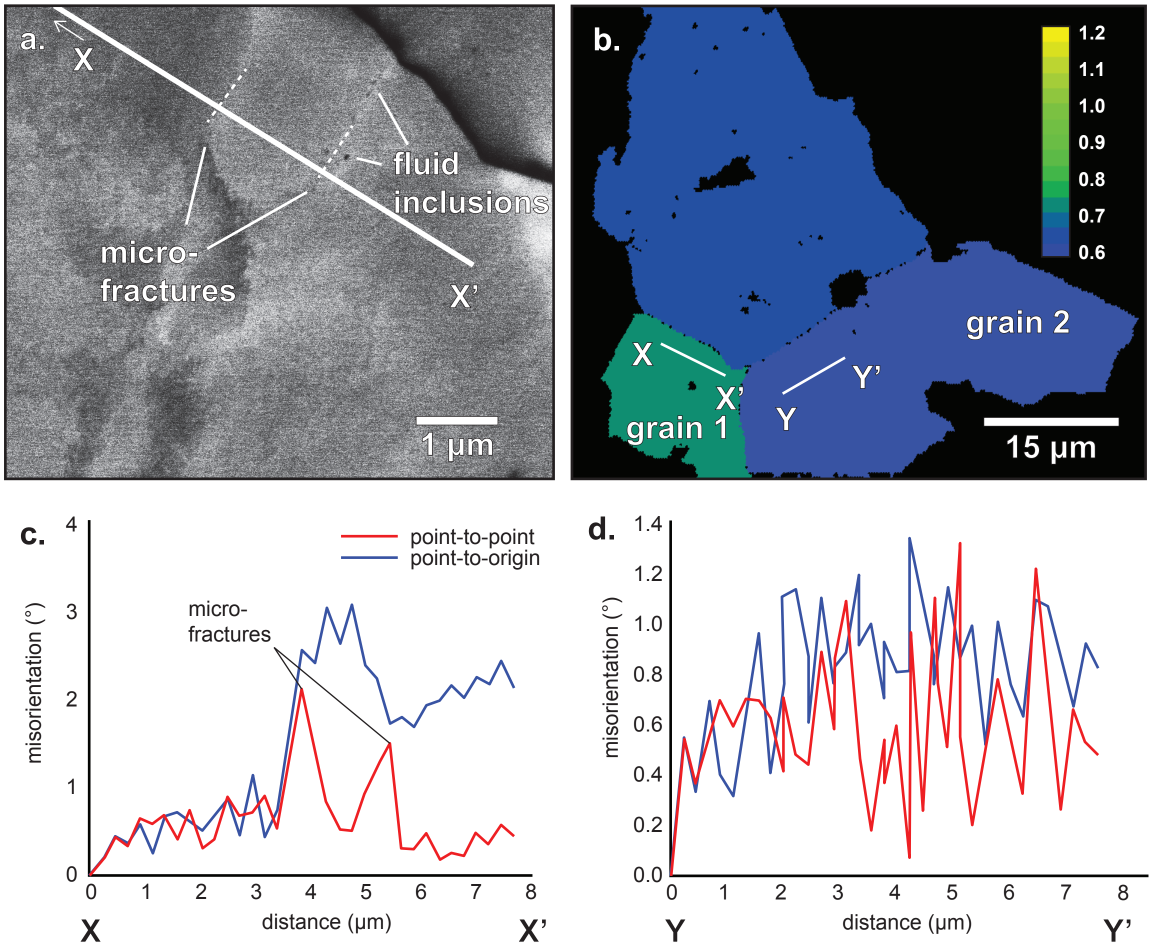

Figure 4.4. a. ECC image of the pyrite revealing microfracturing tracing (001) planes (dashed white lines). Microfractures are delineated by trapped fluid inclusions. The white line (X-X') displays the line of the misorientation profile shown in c. **b.** EBSD grain misorientation average map revealing an average misorientation of ~1° for the region of interest (grain 1) and almost no misorientation in surrounding microfracture-free grains. White lines X-X' and Y-Y' display the location for the misorientation profiles shown in c. and d. **c.** Misorientation profile across X-X' in grain 1 showing continuous misorientation on either side of the microfractures with a maximum deviation of 4° to the origin. **d.** Misorientation profile across Y-Y' in grain 2 showing minor misorientation with a maximum deviation of 1.4° to the origin.

Figure 4.4a reveal an orientation tracing the (001) plane. The low-angle grain boundary in the ECC image (Figure 4.3c) occurs at the tip of microfractures. Misorientation profiles across the more highly strained domains reveal continuous linear misorientation on either side of microfractures and low-angle grain boundaries (Figure 4.4c, S4.2). Note, the grain average misorientation map and misorientation profile (Y-Y' Figure 4.4b, d) of a pyrite grain (grain 2) adjacent to the higher strained domain (grain 1) reveal almost no misorientation in the absence of microfractures.

4.5.2 Nanostructural and chemical analyses

Two APT specimens from these highly strained domains were analyzed (Table S4.1) and their 3D reconstructions reveal a homogeneous distribution of Fe and S (Figure S4.3a-b). In contrast, As and O form ubiquitous clusters, exhibiting a point-density twice that of the surrounding matrix (Figure 4.5a, 4.6a, S4.3c-d). Their apparent diameter is 4–12 nm, with As forming spheroids and O disc-shapes overlain on the As spheres in the analysis direction. By combining experiments and image simulations, we concluded that these features are fluid inclusions within pyrite (Dubosq et al. 2020). Individual linear tubular features in both specimens, linked to one or two larger (15–31 nm) inclusions, appear as high As compositions (0.80–2.10 at%) with minor Co and Cu enrichment, which are interpreted as dislocations (Figure 4.5a-b, 4.6a-b, S4.3f; Dubosq et al. 2019; Fougerouse et al. 2019). Composition profiles across the larger inclusions reveal elevated As, O, Na and K compositions in the range of 3.0–4.2 at%, 3.1–16.1 at%, 0.1–0.2 at%, and 0.1–0.6 at%, respectively, compared to matrix values of 0.11–0.15 at% As and 0.08–0.13 at% O, with no Na and K, and only minor enrichment of Co (0.1–1.1 at%) and Cu (0–0.4 at%; Figure 4.5c, 4.6c, S4.3g). The elevated compositions are accentuated by narrow (2–5 nm) O, Na and K composition peaks preceding (in the order of evaporation) or slightly overlapping a wider (8–13 nm) As composition peak at the imaged inclusion (Figure 4.5c, 4.6c, S4.3e). Note,

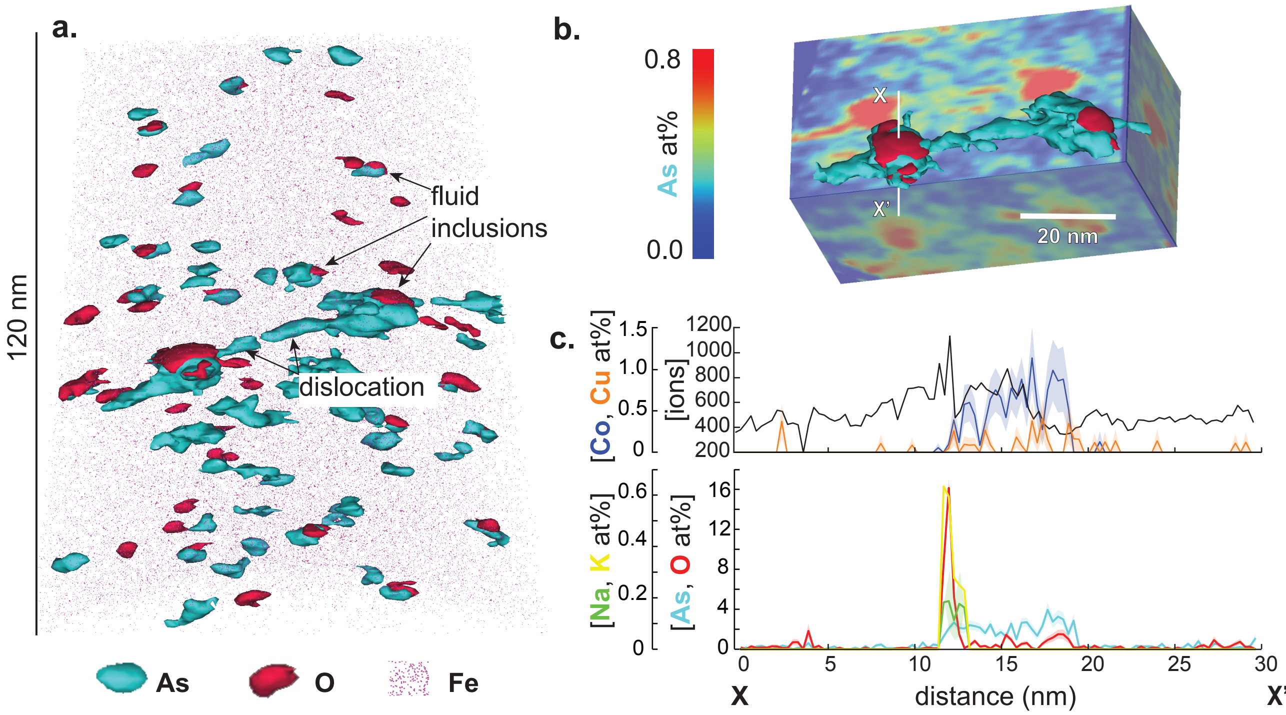

Figure 4.5. a. Reconstruction of APT specimen i displaying the distribution of Fe ions (pink dots), and elevated As (turquoise isosurfaces; 1.10 at% isovalue) and O (red isosurfaces; 1.10 at% isovalue) compositions, revealing globular high-density features (fluid inclusions) and one linear feature linking two larger high-density features. **b.** Clipping of region of interest surrounding linear feature with 2D contour plots of As along x-, y-, and z-axes revealing elevated As concentration along a linear feature and linked high-density features. **c.** Composition profile across high-density feature (X-X') confirming the elevated As- and O-rich compositions and revealing Na (0.23 at%) and K (0.63 at%) within the feature. Note, apparent O-rich or As-rich only inclusions are in fact enriched in both O and As (Figure S4.6).

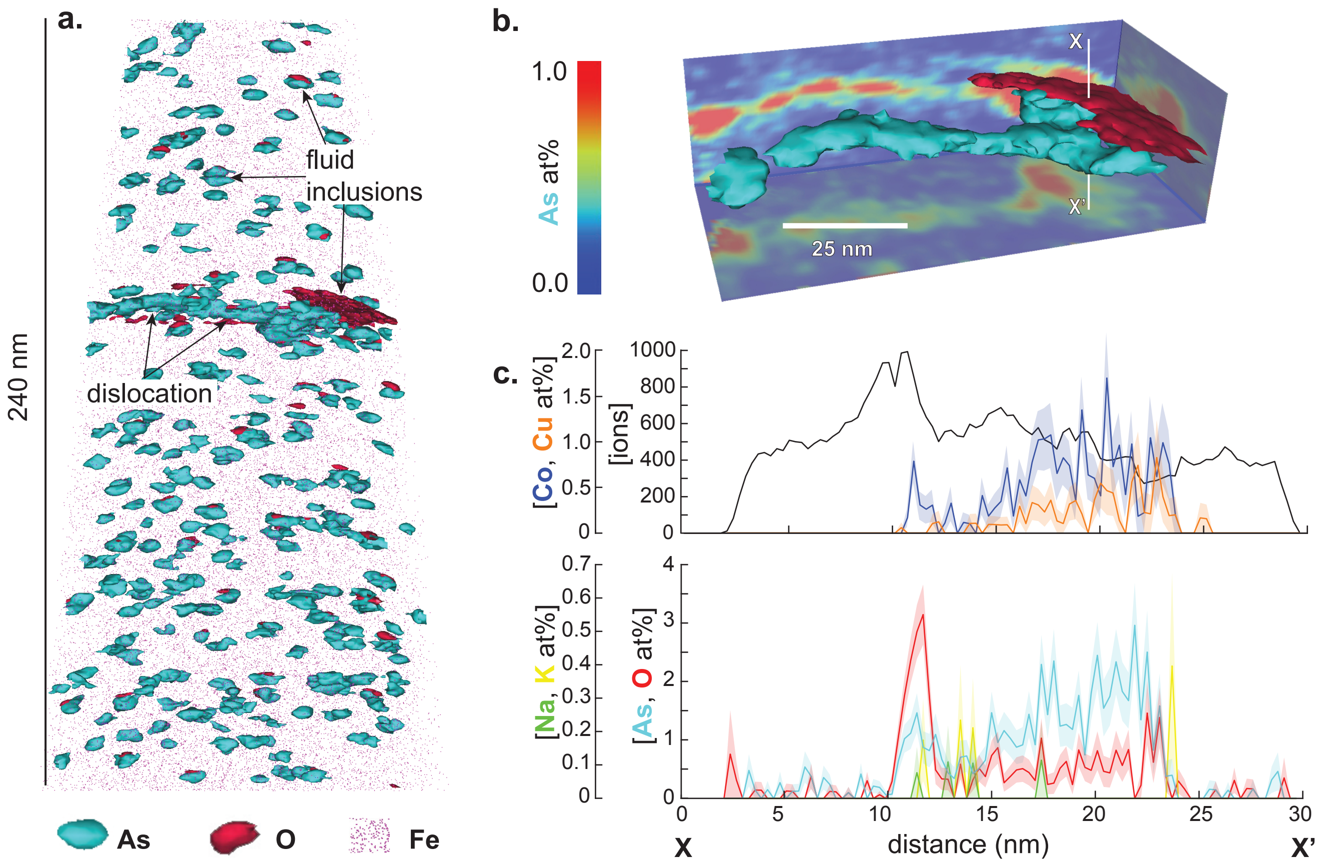

Figure 4.6. a. Reconstruction of APT specimen ii displaying the distribution of Fe ions (pink dots), and elevated As (turquoise isosurfaces; 0.95 at% isovalue) and O (red isosurfaces; 1.15 at% isovalue) compositions, revealing globular high-density features (fluid inclusions) and one linear feature linked to a larger high-density features. **b.** Clipping of region of interest surrounding linear feature with 2D contour plots of As along x-, y-, and z-axes revealing elevated As concentration along a planar feature and linked high-density feature. **c.** Composition profile across high-density feature (X-X') confirming the elevated As- and O-rich compositions and revealing Na (0.11 at%) and K (0.40 at%) compositions within the feature.

O compositions were obtained by decomposing all O-bearing ions (5.1–8.8% O; 1.3–2.3% OH; ~11.3% H_2O; 3.8–9.0% H_3O; 66.5–68.0% FeO; 1.0–1.1% Fe_3O; ~0.5% MnO; 0.5–1.5% CoOH and 3.3–4.7% OS_2).

A similarly strained domain was imaged by STEM to support the identification of the inclusions and dislocations analysed by APT (Figure 4.3a, b). The HAADF images reveal ubiquitous nearly-spherical dark features corresponding to closed-cell pores (Figure 4.7; Dubosq et al. 2020). The pores are 3–20 nm in diameter, are heterogeneously distributed within the sample, and found along healed microfractures revealed by several sets of planar features (sharp line segments with a greyscale gradient on one side) at 60° to each other (Figure S4.4**;** Leroux et al. 1999). Although the sample appears to be dominated by pores and microfractures, a few faint, curved, white line segments that are 95–210 nm in length correspond to dislocations (Phillips et al. 2011; Figure 4.7). These are all linked to one or more pores (Figure 4.7) and the bright contrast indicates segregation of elements heavier than the matrix, likely As based on the APT data.

4.6 Discussion

4.6.1 Origin of micro- and nanostructures

The observed microstructures within the EBSD maps and ECC images suggest dominantly brittle to brittle-plastic deformation mechanisms. The relatively low degree of misorientation within the sample (<2°) and the direct linkage to microfractures (Figure 4.3, 4.4) indicates a dominantly brittle regime with minor strain accommodation via crystal-plasticity where dislocations are mostly emitted by the propagating fracture (Cervellon et al. 2020; Rogowitz et al. 2018). The continuous linear misorientation on either side of microfractures (Figure 4.4c) and the lack of misorientation within a pyrite grain free of microfractures adjacent to the more highly deformed domain (Figure 4.4b, d) also suggest that the observed crystal-plasticity within the sample is

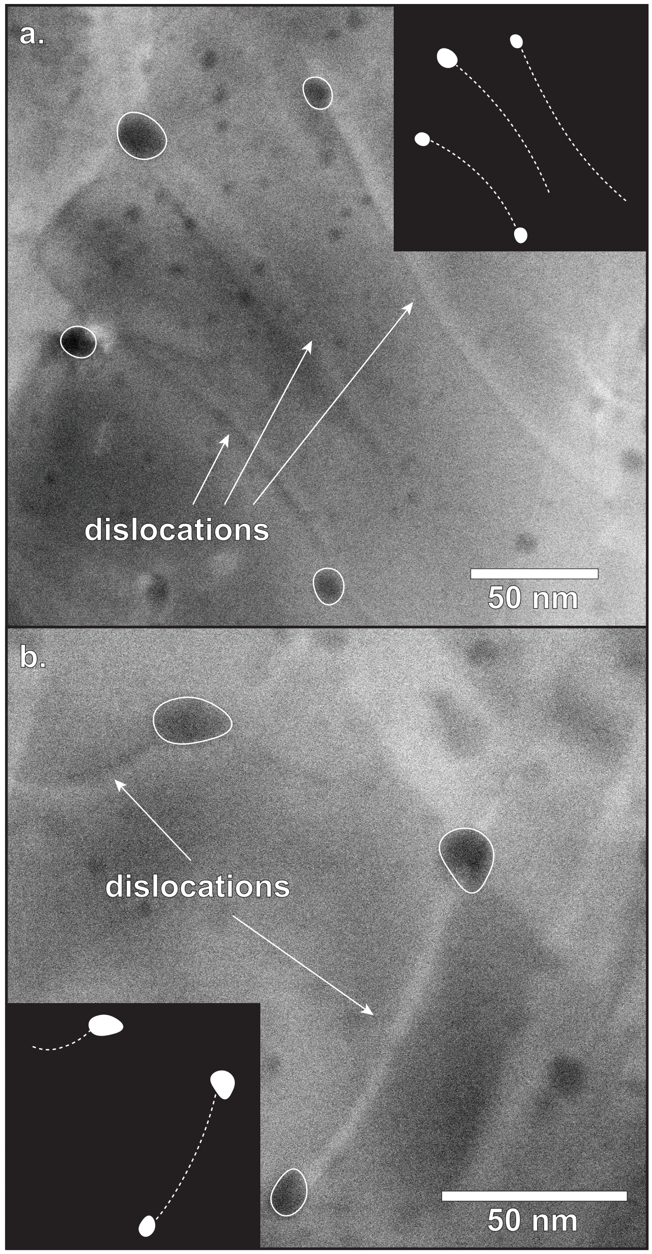

Figure 4.7. HAADF STEM images of pyrite grain adjacent to APT specimens showing curved line defects (white arrows pointing to dislocations) linked to nanovoids (fluid inclusions outlined in white). Inset sketches show the configuration of the nanostructures (white) observed in the respective STEM images.

related to microfracturing. In addition, microfractures are tracing (001), a common cleavage plane for pyrite (Mariano and Beger 1971), and the conjugated sets of microfractures within the STEM data most likely represent micro-cleavage (Leroux et al. 1999). These interpretations are consistent with the peak temperature conditions of the sample estimated at 302 ± 27°C (Dubosq et al. 2020), which falls within the lower range of the brittle to crystal-plastic behaviour of pyrite (260-450°C; Barrie et al. 2011; Cox et al. 1981; Graf et al. 1981).

The fluid inclusions imaged by APT were most likely trapped in the mineral during nucleation and crystallization (Dubosq et al. 2020). Furthermore, fluid inclusions tracing cleavage in our STEM data (Figure S4.4) are probably representing a fast annealing process during a post-crystallization stage. Within the inclusions, we document Na and K compositions that are elements typically found in aqueous brines involved in the formation of orogenic gold deposits (Goldfarb et al. 2001; Zaw et al. 1994). Assuming all the O within the volume corresponds to H_2O molecules, which is supported by their H/O ratio of ~2 (Figure S4.5), the salinity of the fluid inclusions can be estimated by comparing the Na/O and K/O ratios for the approximated fluid inclusion volumes. With Na/O and K/O ratios in the range of 0.05–0.5 and 0.05–0.65, respectively (Figure S4.5), the salinity of the fluid is estimated to range between 14–62 wt% NaCl and 17–73 wt% KCl. Although the ranges are broad, the values exceed the salinity of aqueous brines associated with hydrothermal ore deposits (up to 30 wt% in volcanogenic mass sulphide systems and 15 wt% in orogenic gold systems; Bodnar et al. 2014; Groves et al. 1998; McCuaig and Kerrich 1998). These salinities suggest that either the solution was supersaturated in solutes, which is possible when confined to the nanoscale as a result of the Gibbs-Thompson effect (El Zoka et al 2020), or the solution contained solid salt. However, the salinity measurements cannot be confirmed due to the possibility of water loss during the APT analysis.

4.6.2 Trace element segregation

Trace elements hosted within crystal defects can originate internally within the crystal structure or from an external source such as an interstitial fluid (e.g., Dubosq et al. 2018; Fougerouse et al. 2016), however the exact mechanisms by which they diffuse into these defects remain unclear. Externally sourced trace elements typically diffuse into a mineral's crystal structure by volume diffusion (Klinger and Rabkin 1999; Vukmanovic et al. 2014) or pipe diffusion (Love 1964) to equilibrate the chemical potential of these species and hence reduce the overall free energy of the system, whereas internally source elements can diffuse through the lattice by volume or dislocation-impurity-pair diffusion (DIP; Cahn 2014; Chen et al. 2008; Cottrell and Bilby 1949; Vitik et al. 2000). In the absence of high dislocations densities and at higher temperatures (e.g., when crystals begin to anneal (>500°C for pyrite; McClay and Ellis 1983)), volume diffusion is favored. However, at the lower temperatures experienced by the investigated pyrite (302 ± 27°C), dislocations act as high diffusivity paths – the activation energy for diffusion is significantly lower than through the lattice (Legros et al. 2008; Rabier and Puls 1989). These so-called pipes include individual dislocations and dislocation arrays (Legros et al. 2008; Love 1964). Pipe diffusion occurs when a chemical potential gradient appears between sources of trace elements, for example chemical sinks such as precipitates or chemically-enriched or -depleted zones within, or at either end, of dislocation cores (Legros et al. 2008; Piazolo et al. 2016). Here, the As-rich fluid inclusions act as sources linked via dislocations to the relatively As-poor matrix creating a chemical potential gradient, thereby activating pipe diffusion. This explains the As-enriched dislocations observed in our APT data and demonstrates the migration of As from the fluid inclusions into the dislocation cores through pipe diffusion. Another explanation for As enrichment in the dislocations could be

DIP diffusion of internally sourced As within the pyrite lattice. DIP diffusion is a mechanism by which mobile solutes accumulate in dislocation cores during dislocation creep (Cahn 2014; Chen et al. 2008; Cottrell and Bilby 1949; Vitik et al. 2000). If DIP diffusion were the responsible mechanism, we would expect a depletion of As within the matrix adjacent to the dislocation (e.g., Dubosq et al. 2019), which is not observed in our data. Thus, pipe diffusion is the preferred model to explain the As enrichment within dislocations in our sample.

4.6.3 Dislocation-fluid inclusion interaction and potential implications

The spatial correlation between dislocations and larger (>15 nm) fluid inclusions can be explained by either dislocation nucleation in the local stress field of fluid inclusions or the pinning of migrating dislocations by fluid inclusions. Considering the first scenario, stress concentrations occur at structural defects in crystals including fluid inclusions. The stress distribution and the magnitude of the disturbance in the stress field are dependent on the size and the thermodynamic properties of the inclusion surface (Cahn and Lärché 1982; Sharma et al. 2003). In most cases the maximal stress is concentrated at the equatorial zone around a void (bulk defects comparable to fluid inclusions), which is 90° to the loading axis (Davis et al. 2017; Laatsh et al. 1998; Michler and Schmeling 2013; Tandon and Weng 1986). Previous experimental and numerically simulated studies have shown that dislocation loops can nucleate at void surfaces to accommodate this stress and subsequently migrate away from the void by dislocation glide and creep processes (Hatano 2004; Mitchell et al. 1958; Moriarty et al. 2002; Rudd 2009; Vityk et al. 2000). In these studies however, multiple dislocation loops were associated with each void defect and some were observed distal to the voids, as a result of dislocation glide. In our sample, we only observe one or two dislocations associated with some of the larger (>15 nm) fluid inclusions and none appear to be migrating away from the immediate vicinity of the fluid. For these reasons, it is unlikely that the dislocations observed in this study were nucleated at the fluid inclusions. In the second scenario, gliding dislocations encounter obstacles (e.g., other dislocations, precipitates, grain boundaries, voids) that can arrest their movement or partially immobilize them during crystal-plastic deformation if the disturbance in the stress field exceeds the critical value needed for pinning (Cahn 2014). The dependence of the magnitude of disturbance in the stress field on the size of the inclusions (Cahn and Lärché 1982; Sharma et al. 2003) can potentially explain why dislocations in our APT data (Figure 4.5a, 4.6a) appear only to be spatially correlated with larger (>15 nm) fluid inclusion. When pinning occurs, the portion of the dislocation between the pinning points continues to slightly migrate under the applied stress, resulting in a bowed or scalloped configuration (e.g., Morris et al. 1999; Vityk et al. 2000). This configuration is consistent with our STEM images that show single bowed dislocations linked to one or two fluid inclusions (Figure 4.7).

The observed bowed configuration of the dislocations can be explained by two possible mechanisms by which dislocations move through obstacles: 1) the Orowan mechanism where dislocations loop around the obstacles by bowing, leading to an increase in dislocation density and a decrease in the yield stress necessary for subsequent dislocations to migrate by reducing the effective spacing between obstacles (Orowan 1947); and 2) the Arzt–Rösler–Wilkinson (ARW) model where dislocations migrate through obstacles during creep, reaching a point of maximum deformation resistance that requires a higher yield stress for further movement (Rösler and Arzt 1990). Both mechanisms result in strain hardening. Since the dislocations in our sample are only slightly bowed and we do not observe dislocation loops around the fluid inclusions or the dislocation geometry associated with the ARW mechanism, we cannot discern which of the two mechanisms is occurring. The minor bowing of the dislocations could be a result of low strain in the sample or further dislocation pinning by trace element segregation.

Nevertheless, an aspect consistently overlooked in the literature is the pipe diffusion of impurities that tends to lower the dislocation's stress and its elastic energy, hence stabilizing the dislocation, contributing to hardening and to an overall reduction in the system's free energy (Cahn 2014). In our example, As segregates into the dislocation cores as a result of being pinned at As-rich fluid inclusions by the aforementioned mechanisms. When dislocations incorporate mobile impurities within their core, they can be temporarily arrested or pinned (Butt and Feltham 1993; Cahn 2014). As stress increases and reaches a critical value, the dislocations can be unpinned and move at high velocities. This discontinuous motion of dislocations is known as the Portevin–Le Chatelier (PLC) effect (Portevin and Le Chatelier 1923) and can lead to further hardening of the material and brittle fracturing (Mohles et al. 1999). Although the dominantly brittle behavior of the sample is consistent with its estimated peak temperatures, we do observe two processes that immobilize dislocations and when combined could lead to strain hardening. In light of these observations, we propose that the incorporation of trace element-rich fluid inclusions could have a hardening effect on minerals by pinning dislocations and initiating pipe diffusion of trace elements into dislocation cores (Figure 4.8).

4.7 Conclusions

Our combined multiscale 2D and 3D structural and chemical analyses of pyrite document ubiquitous nanoscale Na- and K-bearing fluid inclusions coated by As. Arsenic-decorated dislocations, linked to the larger fluid inclusions, exhibit a bowed configuration. Based on these observations, we suggest a deformation-induced trace element segregation model where dislocations migrate through the crystal structure by dislocation glide. When dislocations

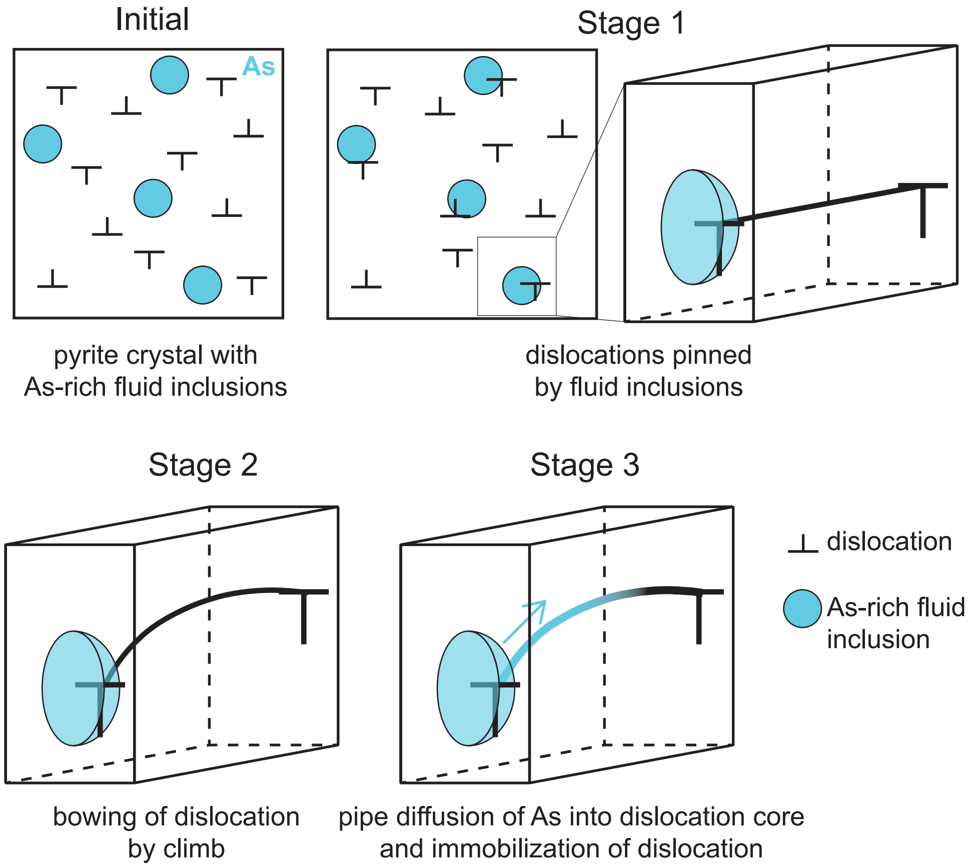

Figure 4.8. Conceptual model of fluid inclusion induced hardening. An initial pyrite crystal with As-rich fluid inclusions is deformed introducing dislocations within the crystal lattice. During stage 1, the dislocations migrate by glide and creep processes and get pinned by fluid inclusions. In stage 2, the dislocation cores continue to migrate by climb while the edges remain pinned by the fluid inclusions, resulting in a bowed configuration. Lastly in stage 3, As from the fluid inclusions diffuse into the dislocation cores by pipe diffusion, further immobilizing the dislocations.

encounter inclusions, they are partially immobilized as trace elements hosted within the fluid inclusions migrate into the dislocations through pipe diffusion. These combined processes lead us to propose that trace element-rich fluids can locally harden deforming minerals.

4.8 Acknowledgements

This project was funded by a Mitacs Globalink award and CCEM seed grant (to RD) and NSERC grant (to DAS). KS acknowledges funding from IMPRS-SurMat. We greatly appreciated discussions with Tyler Blum and Paraskevas Kontis, as well as Chadwich Sinclair. Andreas Sturm, Christian Broß and Uwe Tezins are thanked for their training and support of the APT and FIB facilities at MPIE. We thank Lola Lilensten for assistance during APT experiments, and Hui Yuan and Natalie Hamada for their assistance on PFIB and STEM instruments at CCEM. Steven Reddy, Sandra Piazolo, Daniel Gregory, Manuel Keith, and an anonymous reviewer provided valuable feedback during the review process of the manuscript.

4.9 References

Ahrens TJ, Schubert G (1975) Rapid formation of eclogite in a slightly wet mantle. Earth Planet Sci Lett 27(1): 90–94. doi.org/10.1016/0012-821X(75)90165-X

Ayer JA, Amelin Y, Corfu F, Kamo S, Ketchum J, Kwok K, Trowell N (2002) Evolution of the southern Abitibi greenstone belt based on U-Pb geochronology: Autochtonous volcanic construction followed by plutonism, regional deformation, and sedimentation. Precambrian Res 115: 63–95. doi.org/10.1016/S0301-9268(02)00006-2

Ayer JA, Berger BR, Trowell NF (1999) Geological compilation of the Lake Abitibi area, Abitibi greenstone belt. Ontario Geological Survey, Preliminary Map P.3398, scale 1:100 000.

Ayer JA, Thurston PC, Bateman R, Dubé B, Gibson HL, Hamilton MA, Hathway B, Hocker SM, Houle MG, Hudak G, Ispolatov VO, Lafrance B, Lesher CM, MacDonald PJ, Peloquin AS, Piercey SJ, Reed LE, Thompson PH (2005) Overview of results from the greenstone architecture project: Discover Abitibi initiative. Ontario Geological Survey, Open File Report 6154, 146p.

Ayer JA, Thurston PC, Lafrance B (2008) A special issue devoted to base metal and gold metallogeny at regional, camp, and deposit scales in the Abitibi greenstone belt. Econ Geol 103: 1091–1096. doi.org/10.2113/gsecongeo.103.6.1091

Bachmann F, Hielscher R, Jupp PE, Pantleon W, Schaeben H, Wegert E (2010) Inferential statistics of electron backscatter diffraction data from within individual crystalline grains. J Appl Crystallogr 43: 1338–1355. doi.org/10.1107/S002188981003027X

Bakker RJ, Jansen JBH (1994) A mechanism for preferential H_2O leakage from fluid inclusions in quartz, based on TEM observations. Contrib Mineral Petrol 116: 7–20. doi.org/10.1007/BF00310686

Barrie CT, Corfu F (1999) The Kidd–Munro extension project: results of U–Pb Geochronology for year 1. In: Summary of Field Work and Other Activities, Ontario Geological Survey, Misc Paper 169: 74–81.

Barrie CD, Pearce MA, Boyle AP (2011) Reconstructing the pyrite deformation mechanism map. Ore Geol Rev 39: 265–276. doi.org/10.1016/J.OREGEOREV.2011.03.006

Bateman R, Ayer JA, Dubé B (2008) The Timmins-Porcupine gold camp, Ontario: anatomy of an Archean greenstone belt and ontogeny of gold mineralization. Econ Geol 103: 1285–1308. doi.org/10.2113/gsecongeo.103.6.1285

Bell TH, Etheridge MA (1976) The deformation and recrystallization of quartz in a mylonite zone, Central Australia. Tectonophysics 32: 235–267. doi.org/10.1016/0040-1951(76)90064-0

Bleeker W (2012) Lode gold deposits in ancient deformed and metamorphosed terranes: the role of extension in the formation of Timiskaming basins and large gold deposits, Abitibi greenstone belt—a discussion. Ontario Geological Survey, Open File Report 6280, pp 47.1–47.12.

Bleeker W, van Breemen O (2011) New geochronological, stratigraphic, and structural observations on the Kidd–Munro assemblage and the terrane architecture of the south--central Abitibi greenstone belt, Superior craton, Canada. In Results from the Targeted Geoscience Initiative III Kidd–Munro Project. Ontario Geological Survey, Open File Report 6258, 142p.

Bleeker W, Parrish RR (1996) Stratigraphy and U-Pb zircon geochronology of Kidd Creek: Implications for formation of giant volcanogenic massive sulphide deposits and the tectonic history of the Abitibi greenstone belt. Can J Earth Sci 33: 1213–1231. doi.org/10.1139/e96-092

Blum TB, Darling JR, Kelly TF, Larson DJ, Moser DE, Perez-Huerta A, Prosa TJ, Reddy SM, Reinhard DA, Saxey W, Ulfig RM, Valley JW (2018) Best practices for reporting atom probe analysis of geological materials. In: Moser DE, Corfu F, Darling JR, Reddy SM, Tait K (eds) Microstructuctural geochronology: Planetary records down to atom scale, pp. 369–373. doi.org/10.1002/9781119227250.ch18

Bodnar RJ, Lecumberri-Sanchez P, Moncada D, Steele-MacInnis M (2014) Fluid inclusions in hydrothermal ore deposits. In: Holland HD, Turekian kk (eds) Treatise on geochemistry, second edition, Elsevier, pp 119–142. doi.org/10.1016/B978-0-08-095975-7.01105-0

Butt MZ, Feltham P (1993) Solid solution hardening. J Mater Sci 28: 2557–2576. doi.org/10.1007/BF003 56192

Cahn JW (2014) Reprise: partial chemical strain dislocations and their role in pinning dislocations to their atmospheres. Philos Mag 94(27): 3170–3176. doi.org/10.1080/14786435.2014.951711

Cahn JW, Lärché F (1982) Surface stress and the chemical-equilibrium of small crystals. II. Solid particles embedded in a solid matrix. Acta Metall Mater 30: 51–56. doi.org/10.1016/0001-6160(82)90043-8

Cervellon A, Hémery S, Kürnsteiner P, Gault B, Kontis P, Cormier J (2020) Crack initiation mechanisms during very high cycle fatigue of Ni-based single crystal superalloys at high temperature. Acta Mater 188: 131–144. doi.org/10.1016/j.actamat.2020.02.012

Chen Q, Liu X-Y, Biner SB (2008) Solute and dislocation junction interactions. Acta Mater 56: 2937–2947. doi.org/10.1016/j.actamat.2008.02.026

Chen S, Hiraga T, Kohlstedt DL (2006) Water weakening of clinopyroxene in the dislocation creep regime. J Geophys Res 111: 1–14. doi.org/10.1029/2005JB003885

Cottrell AH, Bilby BA (1949) Dislocation theory of yielding and strain ageing of iron. Proc Phys Soc A 62: 49–62. doi.org/10.1088/0370-1298/62/1/308

Cox SF, Etheridge MA, Hobbs BE (1981) The experimental ductile deformation of polycrystalline and single crystal pyrite. Econ Geol 76: 2105–2117. doi.org/10.2113/gsecongeo.76.8.2105

Cukjati JT, Cooper RF, Parman SW, Zhao N, Akey AJ, Laiginhas FATP (2019) Differences in chemical thickness of grain and phase bouandaries: An atom probe tomography study of experimentally deformed wehrlite. Phys Chem Miner 46: 845–859. doi.org/10.1007/s00269-019-01045-x

Davis T, Healy D, Bubeck A, Walker R (2017) Stress concentrations around voids in three dimensions: The roots of failure. J Struct Geol 102: 193–207. doi.org/10.1016/j.jsg.2017.07.013

Dubé B, Gosselin P (2007) Greenstone-hosted quartz-carbonate vein deposits. In: Goodfellow WD (ed) Mineral deposits of Canada: A synthesis of major deposit-types, district metallogeny, the evolution of geological provinces, and exploration methods, pp 49–74.

Dubosq R, Gault B, Hatzoglou C, Schweinar K, Vurpillot F, Rogowitz A, Rantitsch G, Schneider DA (2020) First observation of nanoscale voids in geological metals by atom probe tomography: Results from direct observations and numerical simulations. Ultramic 218: 1–10. doi.org/10.1016/j.ultramic.2020.113092

Dubosq R, Lawley CJM, Rogowitz A, Schneider DA, Jackson S (2018) Pyrite deformation and connections to gold mobility: Insight from micro-structural analysis and trace element mapping. Lithos 310–311: 86–104. doi.org/10.1016/j.lithos.2018.03.024

Dubosq R, Rogowitz A, Schweinar K, Gault B, Schneider DA (2019) A 2D and 3D nanostructural study of naturally deformed pyrite: assessing the links between trace element mobility and defect structures. Contrib Mineral Petrol 174: 1–16. doi.org/10.1007/s0041 0-019-1611-5

Eckstrand R, Hulbert L (2007) Magmatic nickel-copper-platinum group element deposits. In: Goodfellow WD (ed) Mineral deposits of Canada: A synthesis of major deposit-types, district metallogeny, the evolution of geological provinces, and exploration methods, pp 205–222.

El-Zoka AA, Kim SH, Deville S, Newman RC, Stephenson LT, Gault B (2020) Enabling near-atomic–scale analysis of frozen water. Sci Adv 6: 1–11. doi.org/10.1126/sciadv.abd6324

Epp MS (1997) Geology, petrography and geochemistry of the Potterdoal Cu-Zn deposit, Kidd–Munro assemblage, Munro Township, Ontario. Dissertation, McMaster University, 143 p.

Epp MS, Crocket JH (1999) Geology and geochemistry of the Potterdoal Cu-Zn deposit, Munro Township, Ontario. In: Hannington MD, Barrie CT (eds) The giant Kidd Creek volcanogenic massive sulfide deposit, western Abitibi Subprovince, Canada. Econ Geol Monogr 10: 593-612. doi.org/10.5382/Mono.10

Exertier F, La Fontaine A, Corcoran C, Piazolo S, Belousova E, Peng Z, Gault B, Saxey DW, Fougerouse D, Reddy SM, Pedrazzini S, Bagot PAJ, Moody MP, Langelier B, Moser DE, Botton GA, Vogel F, Thompson GB, Blanchard PT, Chiaramonti AN, Reinhard DA, Rice KP, Schreiber DK, Kruska K, Wang J, Cairney JM (2018) Atom probe tomography analysis of the reference zircon gj-1: An interlaboratory study. Chem Geol 495: 27–35. doi.org/10.1016/j. chemgeo.2018.07.031.

Fischer GW, Elliott D (1974) Criteria for quasi-steady diffusion and local equilibrium in metamorphism. In: Hoffmann AW, Giletti BJ, Yoder HS, Yund R (eds) Geochemical transports and kinetics, Carnegie Inst, Washington Publ., Washington, pp 77–89.

Fougerouse D, Micklethwaite S, Halfpenny A, Reddy SM, Cliff JB, Martin LAJ, Kilburn M, Guagliardo P, Ulrich S (2016) The golden ark: arsenopyrite crystal plasticity and the retention of gold through high strain and metamorphism. Terra Nova 28: 181–187. doi.org/10.1111/ter.12206

Fougerouse D, Reddy SM, Kirkland CL, Saxey DW, Rickard WD, Hough RM (2019) Time-resolved, defect-hosted, trace element mobility in deformed Witwatersrand pyrite. Geosci Front 10: 55–63. doi.org/10.1016/j.gsf.2018.03.01

Galley A, Hannington M, Jonasson I (2007) Volcanogenic massive sulphide deposits. In: Goodfellow WD (ed) Mineral deposits of Canada: A synthesis of major deposit-types, district metallogeny, the evolution of geological provinces, and exploration methods, pp 141–162.

Gault B, Moody MP, Cairney JM, Ringer SP (2012) Atom probe microscopy, vol 160. Springer Science & Business Media, New York.

Goldfarb RJ, Groves DI, Gardoll S (2001) Orogenic gold and geologic time: a global synthesis. Ore Geol Rev 18: 1–75. doi.org/10.1016/S0169-1368(01)00016-6

Graf JL, Skinner BJ, Bras J, Fagot M, Levade C, Couderc JJ (1981) Transmission electron microscopic observation of plastic deformation in experimentally deformed pyrite. Econ Geol 76: 738–742. doi.org/10.2113/gsecongeo.76.3.738

Griggs D (1967) Hydrolytic weakening of quartz and other silicates. Geophys J R Astron Soc 14: 19–31. doi.org/10.1111/j.1365-246X.1967.tb06218.x

Groves DI, Goldfarb RJ, Gebre-Mariam M, Hagemann SG, Robert F (1998) Orogenic gold deposits: A proposed classification in the context of their crustal distribution and relationship to other gold deposit types. Ore Geol Rev 13: 7-27. doi.org/10.1016/S0169-1368(97)00012-7

Guren MG, Putnis CV, Montes-Hernandez G, King HE, Renard F (2020) Direct imaging of coupled dissolution-precipitation and growth processes on calcite exposed to chromium-rich fluids. Chem Geol 552: 1–12. doi.org/10.1016/j.chemgeo.2020.119770

Hansen LN, Kumamoto KM, Thom CA, Wallis D, Durham WB, Goldsby DL, Breithaupt T, Meyers CD, Kohlstedt DL (2019) Low-temperature plasticity in Olivine: Grain size, strain hardening, and the strength of the lithosphere. J Geophys Res B: Solid Earth 124: 5427–5449. doi.org/10.1029/2018JB016736

Hatano T (2004) Dislocation nucleation in shocked fcc solids: Effects of temperature and pre-existing voids. Phys Rev Lett 93: 1–4. doi.org/10.1103/PhysRevLett.93.085501

Hobbs BE (1968) Recrystallisation of single crystals of quartz. Tectonophysics 6: 353–401. doi.org/10.1016/0040-1951(68)90056-5

Hobbs BE, McLaren AC, Paterson MS (1972) Plasticity of single crystals of synthetic quartz. Geophys Monogr Ser 16: 29–53. doi.org/10.1029/GM016p0029

Klinger L, Rabkin E (1999) Beyond the Fisher model of grain boundary diffusion: effect of structural inhomogeneity in the bulk. Acta Mater 47: 725–734. doi.org/10.1016/S1359-6454(98)00420-0

Kovaleva E, Klözli U, Habler G, Huet B, Guan Y, Rhede D (2017) The effect of crystal-plastic deformation on isotope and trace element distribution in zircon: Combined BSE, CL, EBSD, FEG-EMPA and NanoSIMS study. Chem Geol 450: 183–198. doi.org/10.1016/j.chemgeo.2016.12.030

Laatsch J, Kim GM, Michler GH, Arndt T, Süfke T (1998) Investigation of the micromechanical deformation behavior of transparent toughened poly(methylmethacrylate) modified with core-shell particles. Polym Adv Technol 9: 716–720. doi.org/10.1002/(SICI)1099-1581(1998100)9:10/113.0.CO;2-9

Legros M, Dehm G, Arzt E, Balk TJ (2008) Observation of giant diffusivity along dislocation cores. Science 319: 1646–1649. doi.org/10.1126/science.11517-71

Leroux H, Reimold WU, Koeberl C, Hornemann U, Doukhan JC (1999) Experimental shock deformation in zircon: A transmission electron microscopic study. Earth Planet Sci Lett 169: 291–301. doi.org/10.1016/S0012-821X(99)00082-5

Love GR (1964) Dislocation pipe diffusion. Acta Metal Mater 12: 731–737. doi.org/10.1016/0001-6160(64)90220-2

Mariano AN, Beger RM (1971) Cleavage in pyrite and cobalite. Am Miner 56: 1867–1881.

Marti S, Stünitz H, Heilbronner R, Plümper O, Killian R (2018) Syn-kinematic hydration reactions, grain size reduction, and dissolution–precipitation creep in experimentally deformed plagioclase–pyroxene mixtures. Solid Earth 9: 985–1009. doi.org/10.5194/se-9-985-2018

McClay KR, Ellis PG (1983) Deformation and recrystallization of pyrite. Mineral Mag 47: 527–538. doi.org/10.1180/minmag.1983.047.345.14

McCuaig TC, Kerrich R (1998) P-T-t-deformation-fluid characteristics of lode gold deposits: Evidence from alteration systematics. Ore Geol Rev 12: 381–453. doi.org/10.1016/S0169-1368(98)80002-4

McLaren AC, Cook RF, Hyde ST, Tobin RC (1983) The mechanisms of the formation and growth of water bubbles and associated dislocation loops in synthetic quartz. Phys Chem Miner 9: 79–94. doi.org/10.1007/BF00308151

Mei S, Kohlstedt DL (2000) Influence of water on plastic deformation of olivine aggregates 1. Diffusion creep regime. J Geophys Res 105: 457–469. doi.org/10.1029/2000JB900179

Michler GH, von Schmeling HHKB (2013) The physics and micro-mechanics of nano-voids and nano-particles in polymer combinations. Polymer 54: 3131–3144. doi.org/10.1016/j.polymer.2013.03.035

Mitchell JW (1958) Growth and perfection of crystals. In: Doremus RH, Roberts BW and Turnbull D (eds), Wiley, New York, pp 386–389.

Mohles V, Rönnpagel D, Nembach E (1999) Simulation of dislocation glide in precipitation hardened materials. Comput Mater Sci 16(1–4): 144–150. doi.org/10.1016/S0927-0256(99)00056-7

Moriarty JA, Belak JF, Rudd RE, Söderlind P, Streitz FH, Yang LH (2002) Quantum-based atomistic simulation of materials properties in transition metals. J Phys: Condens Matter 14: 2825–2857. doi.org/10.1088/0953-8984/14/11/305

Morris DG, Liu CT, George EP (1999) Pinning of dislocations and the origin of the stress anomaly in FeAl alloys. Intermetallics 7: 1059–1068. doi.org/10.1016/S0966-9795(99)00015-1

Orowan E (1947) Discussion. Symposium on Internal Stresses Institute of Metals, London, p. 451.

Phillips PJ, Brandes MC, Mills MJ, De Graf, M (2011) Diffraction contrast STEM of dislocations: Imaging and simulations. Ultramic 111: 1483–1487. doi.org/10.1016/j.ultramic.2011.07.001

Piazolo S, La Fontaine A, Trimby P, Harley S, Yang L, Armstrong R, Cairney JM (2016) Deformation-induced trace element redistribution in zircon revealed using atom probe tomography. Nat Commun 7: 1–7. doi.org/10.1038/ncomm s1049 0

Portevin A, Le Chatelier F (1923) Sur un phénomène observation lors de l'essai de traction d'alliages en cours de transformation. C R Acad Sci Paris 176: 507–510.

Powell WG, Carmichael DM, Hodgson CJ (1995a) Conditions and timing of metamorphism in the southern Abitibi greenstone belt, Quebec. Can J Earth Sci 32: 787–805. doi.org/10.1139/e95-067

Powell WG, Hodgson CJ, Hanes JA, Carmichael DM, McBride S, Farrar E (1995b) $^{40}Ar/^{39}Ar$ geochronological evidence for multiple postmetamorphic hydrothermal events focused along faults in the southern Abitibi greenstone belt. Can J Earth Sci 32: 768–786. doi.org/10.1139/e95-066

Putnis CV, Ruiz-Agudo E (2013) The mineral–water interface: Where minerals react with the environment. Elements 9: 177–182. doi.org/10.2113/gselements.9.3.177

Rabier J, Puls MP (1989) Atomistic calculations of point-defect interaction and migration energies in the core of an edge dislocation in NaCl. Philos Mag A 59: 533–546. doi.org/10.1080/01418618908229783

Reddy SM, Saxey DW, Rickard WDA, Fougerouse D, Montalvo SD, Verberne R, van Riessen A (2020) Atom probe tomography: Development and application to the geosciences. Geostand Geoanal Res 44: 5–50. doi.org/10.1111/ggr.12313

Renard F, Røyne A, Putnis CV (2019) Timescales of interface-coupled dissolution-precipitation reactions on carbonates. Geosci Front 10: 17–27. doi.org/10.1016/j.gsf.2018.02.013

Rogowitz A, Zaefferer S, Dubosq R (2018) Direct observation of dislocation nucleation in pyrite using combined electron channeling contrast imaging and electron backscatter diffraction: Terra Nova 30: 423–430. doi.org/10.1111/ter.12358

Rösler J, Arzt E (1990) A new model-based creep equation for dispersion strengthened materials. Acta Metal Mater 38:671–683. doi.org/10.1016/0956-7151(90)90223-4

Rudd RE (2009) Void growth in bcc metals simulated with molecular dynamics using the Finnis-Sinclair potential. Philos Mag 89: 3133–3161. doi.org/10.1080/14786430903222529

Sharma P, Ganti S, Bhate N (2003) Effect of surfaces on the size-dependent elastic state of nano-inhomogeneities. Appl Phys Lett 82: 535–537. doi.org/10.1063/1.1539929

Schirmer T, Ließmann W, Macauley C, Felfer P (2020) Indium and antimony distribution in a sphalerite from the "Burgstaetter Gangzug" of the Upper Harz Mountains Pb-Zn mineralization. Minerals 10: 1–19. doi.org/10.3390/min10090791

Tandon GP, Weng GJ (1986) Stress distribution in and around spheroidal inclusions and voids at finite concentration. J Appl Mech 53: 511–518. doi.org/10.1115/1.3171804

Thompson PH (2003) Metamorphism and its relationships to gold deposits in the Timmins-Kirkland Lake area, western Abitibi greenstone belt, Ontario. Discover Abitibi, Metamorphic Subproject Report 1. Ontario Geological Survey, Open File Report 6120, pp 37.1–37.8.

Thompson K, Lawrence D, Larson DJ, Olson JD, Kelly TF, Gorman B (2007) In situ site-specific specimen preparation for atom probe tomography. Ultramic 107: 131–139. doi.org/10.1016/J.ULTRAMIC.2006.06.008

Tielke JA, Zimmerman ME, Kohlstedt DL (2017) Hydrolytic weakening in olivine single crystals. J Geophys Res Solid Earth 122: 3465–3479. doi.org/10.1002/2017JB01400

Tsong TT, Kinkus TJ (1984) Energy distributions of pulsed-laser field-desorbed gaseous ions and field-evaporated metal ions: A direct time-of-flight measurement. Phys Rev B 29: 529–542. doi.org/10.1103/PhysRevB.29.529

Tullis J, Christie JM, Griggs DT (1973) Microstructures and preferred orientations of experimentally deformed quartzites. Geol Soc Am Bull 84: 297–314. doi-org/10.1130/0016-7606(1973)84<297:MAPOOE>2.0.CO;2

Thurston PC, Ayer JA, Goutier J, Hamilton MA (20080 Depositional gaps in Abitibi greenstone belt stratigraphy: a key to exploration for syngenetic mineralization. Econ Geol 103: 1097–1134. doi.org/10.2113/gsecongeo.103.6.1097

Vityk MO, Bodnar RJ, Doukhan JC (2000) Synthetic fluid inclusions. XV. TEM investigation of plastic flow associated with re-equilibration of fluid inclusions in natural quartz. Contrib Mineral Petrol 139: 285–297. doi.org/10.1007/s004100000142

Vukmanovic Z, Reddy S, Godel B, Barnes S, Fiorentini M, Barnes SJ, Kilburn M (2014) Relationship between microstructures and grain-scale trace element distribution in komatiite hosted magmatic sulphide ores. Lithos 184–187: 42–61. doi.org/10.1016/j.lithos.2013.10.037

Wang L, Putnis CV (2020) Dissolution and precipitation dynamics at environmental mineral interfaces imaged by in situ atomic force microscopy. Acc Chem Res 53: 1196–1205. doi.org/10.1021/acs.accounts.0c00128

Wu YF, Fougerouse D, Evans K, Reddy SM, Saxey DW, Guagliardo P, Li JW (2019) Gold arsenic, and copper zoning in pyrite: A record of fluid chemistry and growth kinetics. Geology 47: 641–644. doi.org /10.1130 /G46114.1

Xu J, Zhang D, Fan D, Dera PK, Shi F, Zhou W (2019) Thermoelastic properties of eclogitic garnets and omphacites: implications for deep subduction of oceanic crust and density anomalies in the upper mantle. Geophys Res Lett 46(1): 179–188. doi.org/10.1029/2018GL081170

Zaw K, Huston DL, Large RR, Mernagh T, Hoffman CF (1994) Microthermometry and geochemistry of fluid inclusions from the Tennant Creek gold–copper deposits: implications for ore deposition and exploration. Mineralia Deposita 29: 288–300. doi.org/10.1007/BF00206872

CHAPTER 5

Bubbles and atom clusters in rock melts: a chicken and egg problem

R. Dubosq[1], D.A. Schneider[1], X. Zhou[2], B. Gault[2,3], B. Langelier[4], P. Pleše[1]

[1]Department of Earth and Environmental Sciences, University of Ottawa, Ottawa, Canada

[2]Max-Planck-Institut für Eisenforschung GmbH, Düsseldorf, Germany

[3]Department of Materials, Royal School of Mines, Imperial College London, London, UK

[4]Canadian Centre for Electron Microscopy, McMaster University, Hamilton, Canada

To be submitted to

Journal of Volcanology and Geothermal Research

5.1 Abstract

Bubble and crystal nucleation and growth dynamics play a vital function in determining the eruptive behaviour of a magma. Investigating the initial stages of bubble nucleation and crystallization processes, including their rate and relative timing, can thus give us insight into the rheology of magmas. Although many experiments and numerical simulations of magma decompression have been carried out, the earliest mechanisms of bubble nucleation remain poorly understood. It is widely accepted that there are two ways bubbles can form: either by homogeneous nucleation within a melt, or by heterogeneous nucleation on an imperfection in the material such as a surface, interface, or particle. It has been tentatively suggested that what had been interpreted as homogeneous nucleation in magmas was instead heterogeneous nucleation on the surface of elusive nano- or micro-scale crystals spread throughout the melt. Herein, we have induced bubble nucleation in an experimental andesitic glass sample using radiation damage from a focused ion beam (FIB) to investigate the initial stages of bubble nucleation. Scanning transmission electron microscopy, electron energy-loss spectroscopy and atom probe tomography (APT) data reveal sub-nanometer scale chemical heterogeneities in the form of Fe-, Na-, and/or Ca-rich clusters at the bubble-melt interface of the newly created bubbles. Specimens prepared by cryogenic FIB, in which bubble nucleation is suppressed, are without bubbles; however, APT data shows similar chemical heterogeneities suggesting these clusters existed within the glass prior to bubble formation. Based on these observations, our data demonstrate the existence of nanoscale chemical heterogeneities within the melt and at bubble-melt interfaces, which contributes to the hypothesis that previously described homogeneous nucleation be re-interpreted as a variety of heterogeneous

nucleation. These findings highlight the need to revise the commonly used definition of homogeneous nucleation amongst magma scientists.

5.2 Introduction

Volcanic eruptions involving viscous felsic to intermediate magmas are considered the most violent and unpredictable natural hazards of the solid Earth (Massol and Koyaguchi 2005). In an attempt to mitigate risks associated with these events, modern volcanology mostly aims to predict the eruptive style of volcanoes based on their precursory activity and triggers, including the nucleation of vapour (mainly H_2O) bubbles (Cashman and Blundy 2000). Volcanic eruptions range from effusive to explosive, with magma viscosity as one of the main factors controlling the rheology of magmas, hence their eruptive style (Kedrinskii et al. 2006). Changes in magma viscosity are caused by physico-chemical processes, including melt degassing and crystallization that cause the change from a single liquid phase to a three-phase suspension (melt, gas bubbles, crystals) and significantly increases the viscosity of a magma (Martel et al. 2017). From the nucleation and growth of gas bubbles, degassing alone can increase a magma's viscosity by a few orders of magnitude (Davydov 2012). Therefore, the timing and rate of nucleation for gas bubbles and crystals in a magma can significantly influence its rheology, which in turn controls the ductile versus brittle behaviour of the eruption (e.g., Sparks 1978).

The rate and relative timing of nucleation for gas bubbles and crystals in a magma are, among others, controlled by the magma's ascent rate. In an ascending magma, pressure decreases and the magma becomes superstaturated with H_2O resulting in the nucleation and growth of gas bubbles causing the magma to fragment. The occurrence of fragmentation determines the eruptive style of a magma (Massol and Koyaguchi 2005). For example, the slow ascent of a magma (i.e., cm/s to mm/s; Rutherford and Gardner 2000) allows for the nucleation and continuous growth of gas bubbles and microlites (i.e., microscopic crystals) deep within the conduit, leading to extensive degassing and crystallization, enhancing the chances of an effusive eruption (Martel et al. 2017). On the other hand, the rapid ascent of a magma (i.e., m/s; Rutherford and Gardner 2000) only allows for the nucleation of gas bubbles and microlites at shallow levels within the conduit, with a consequence of gas overpressure and sudden changes in viscosity, causing an explosive eruption (Martel et al. 2017). The nucleation and growth of gas bubbles in a stagnant magma can also trigger an eruption: if a stagnant magma begins to crystallize due to cooling, the magma can become supersaturated with H_2O and cause an eruption (Blake 1984; Pyle and Pyle 1995; Tait et al. 1989). Investigating the initial stages of bubble nucleation is central to our understanding of magma rheology and therefore critical to predicting eruption styles.

Although the timing of bubble nucleation in silicate melts has been extensively studied (e.g., Fiege and Cichy 2015), the mechanisms for bubble nucleation have not received as much attention (e.g., Pleše et al. 2018, 2019a, 2019b). It is currently widely accepted that there are two ways by which gas bubbles can nucleate from a volcanic melt: either by homogeneous nucleation or heterogeneous nucleation. Homogeneous nucleation occurs completely within the melt from a relatively higher degree of volatile supersaturation, whereas heterogeneous nucleation requires a lower degree of volatile supersaturation and occurs on a surface, interface or other imperfection in the crystal organisation that lowers the nucleation energy barrier (Blander and Katz 1975; Gardner 2007; Hurwitz and Navon 1994).

The activation energy for homogeneous nucleation in melts can be described by:

$$\mathit{\Delta G} = \frac{16\pi\sigma^3}{3\Delta {P_{SAT}}^2}$$

where $\mathit{\Delta G}$ is the Helmholtz free energy required for nucleation, σ is the surface tension and ΔP_{SAT} is the supersaturation pressure (Hirth et al. 1970; Hurwitz and Navon 1994; Navon and

Lyakhovsky 1998). For heterogeneous nucleation or a gas bubble on a surface, the activation energy can be described by:

$$\Delta G = \frac{16\pi\sigma^3}{3\Delta p {P_{SAT}}^2}\phi$$

where ϕ is defined as:

$$\phi = \frac{(2 - cos\theta)(1 + cos\theta)^2}{4}$$

and θ is the wetting at the bubble-crystal interface defined as:

$$cos\theta = \frac{(\sigma_{cv} - \sigma_{cm})}{\sigma_{mv}}$$

where σ_{ij} is the σ between two phases: crystal (*c*), bubble (*v*) or melt (*m*) (Landau and Lifshitz 1980; Hurwitz and Navon 1994; Adamson and Gast 1997; Navon and Lyakhovsky 1998). Since σ is significantly reduced in the case of heterogeneous bubble nucleation, the activation energy required for the formation of a nucleus that exceeds the critical size for growth on chemical heterogeneities (i.e., microlites, interfaces, secondary phases or atomic clusters) within melts is significantly lower.

In an attempt to determine how bubbles nucleate heterogeneously in silicate melts, Gardner and Denis (2004) carried out some of the first comprehensive decompression experiments on hydrated high-silica rhyolitic melts and found that although most of the bubbles nucleated on the surface of magnetite and hematite crystals, some bubbles had no visibly attached crystals. They concluded that homogeneous nucleation is simply a variety of heterogeneous nucleation where nucleation occurs on the surface of submicroscopic crystals (Figure 5.1). Instead of attributing those bubbles to homogeneous nucleation, the authors suggested that the bubbles must have nucleated on some type of submicroscopic heterogeneity within the melt. Their interpretation was

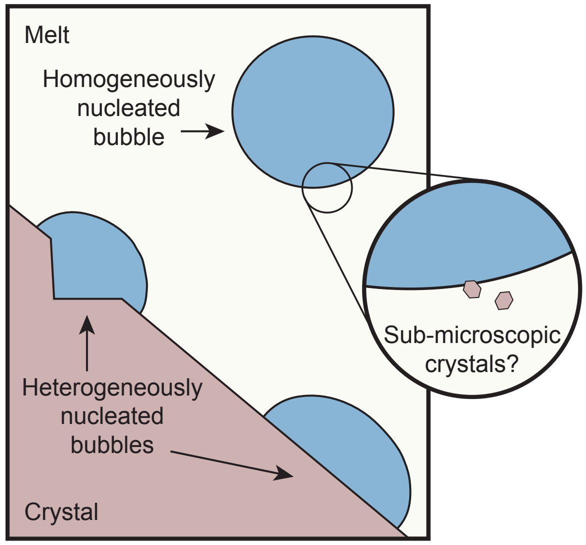

Figure 5.1. Schematic of bubble nucleation model proposed by Gardner and Denis (2004) where homogeneous nucleation is suggested to be a variety of heterogeneous nucleation whereby bubbles nucleate on sub-microscopic crystal (modified from Pleše et al. 2018).

based on work by Hurwitz and Navon (1994), who found similar results and proposed that the nucleation sites were most likely incompletely melted crystals that were left over from hydrating the melt. More recently, Cáceres et al. (2020) used an experimental approach to test the influence of such submicroscopic crystals–termed nanolites–on bubble nucleation and growth dynamics. Although they found that the presence of nanolites is correlated to an increase in the bubble number density, direct evidence of bubble nucleation on nanolites remains equivocal. For our general purposes, we use the term chemical heterogeneities to refer to microlites, nanolites or atomic clusters (i.e., amorphous aggregates).

Herein we combine multiscale 2D and 3D nanostructural and chemical microscopy techniques including scanning transmission electron microscopy (STEM), electron energy-loss spectroscopy (EELS) mapping and atom probe tomography (APT) to investigate the presence of nanometer-scale chemical heterogeneities in the vicinity of gas bubbles within an experimental andesitic glass. APT is a 3D sub-nanometer scale compositional mapping technique with high sensitivity in the range of 10s of parts-per-million. During analyses, a high electrostatic field in the range of tens of V/nm is produced by subjecting needle-shaped specimen to a high voltage (HV) of 2–12 kV. The superimposition of short HV or laser pulses allow for controlling the field evaporation of surface atoms from the specimen's tip. The ionized atoms are then projected onto a time-resolved position sensitive detector with a high detection efficiency (up to 80%). The time-of-flight of the ions is used to determine their mass over charge ratios and deduce their elemental nature. By combining the time-of-flight spectroscopy and the 3D spatial coordinate data of the evaporated atoms, datasets of 10^6–10^8 ions can be converted into 3D atomic point cloud reconstructions of the initial specimens with a spatial resolution typically better than 1nm (De Geuser and Gault 2020; Gault et al. 2021; Jenkins et al. 2020). APT has been used extensively to study gas bubbles or voids resulting from radiation damage in nuclear materials (Edmondson et al. 2011; Wang et al. 2020).

We compare APT data between specimens prepared at room temperature to induce nanoscale gas bubbles within the andesitic glass by agglomeration of point defects associated with FIB irradiation, and prepared under cryogenic conditions to preserve the initial structural integrity of the glass. Our data demonstrate the existence of nanoscale chemical heterogeneities within the melt in both specimens and at the bubble-melt interface of newly created bubbles within the specimen prepared at room temperature, therefore contributing to the proposed hypothesis that what was claimed to be homogeneous nucleation was in fact heterogeneous nucleation on unsuspected nanoscale chemical heterogeneities.

5.3 Materials and methods

5.3.1 Materials

The sample investigated for our study was synthesized and subsequently decompressed using a piston-cylinder apparatus at McGill University (Montreal, Canada; Pleše 2019) with a pressure precision of 25 MPa (Baker 2004). Natural andesite rock powder from Baker and Eggler (1987; Table 5.1) was combined with ~20 vol% cleavage fragments of plagioclase crystals (labradorite An_{67}, Stewart et al. 1966) and ~12 wt% H_2O in order to reach the water-saturation threshold during decompression (Papale et al. 2006). Capsules ($Au_{75}Pd_{25}$; 3 mm diameter, 11 mm in length) were filled with the material and closed by welding in a water bath to minimize water loss and stored in a 110 °C furnace for 1 h. The sample was isothermally decompressed at 1000°C starting with 1 h at 650 MPa to a final pressure of 300 MPa at a decompression rate of 1.8 MPa s^{-1} at which point the sample was immediately isobarically quenched.

Table 5.1. Composition of andesitic rock powder from Baker and Eggler 1987

Oxides	**%**
SiO_2	56.80
TiO_2	1.01
Al_2O_3	16.90
FeO*	8.03
MnO	0.17
MgO	3.09
CaO	7.05
Na_2O	3.99
K_2O	2.05
P_2O_5	0.88
Total	99.37

* All Fe determined as FeO
Data from microprobe analyses of superliquidus glass

5.3.2 Scanning Transmission Electron Microscopy

In an attempt to investigate the initial stages of bubble nucleation processes, two TEM lamellae were prepared from a mostly bubble-free region of interest within the sample at the micron scale (Figure 5.2) by *in situ* lift-out at room temperature with the intent to induce new nanoscale gas bubbles. The lamellae were prepared using a Thermo Scientific Helios™ G4 UXe DualBeam™ Plasma-FIB/SEM at the Canadian Centre for Electron Microscopy at McMaster University (Hamilton, Canada). The regions of interest were marked by an electron-deposited W layer and subsequently protected by Xe-ion deposition of W and a mixture of C and Pt. The ~1 μm thick lamellae were obtained by trenching adjacent areas and were then attached to Cu grids. The lamellae were thinned to ~80 nm by an ion beam with gradually decreased currents at 30 keV and cleaned with progressively reduced low voltages until 5 keV in order to remove the amorphorized layers resulting from the Xe-ion bombardment.

High-angle annular dark field (HAADF) imaging for lamella 1 was performed using a FEI Titan 80-300 transmission electron microscopy (TEM) equipped with a CEOS probe and image corrector operated in STEM mode at a convergence angle of 19.1 mrad. The microscope was operated at an acceleration voltage of 200 kV and micrographs were captured using a Fischione HAADF detector. The images were collected using a dwell time of 4 μs, a total frame time of 20.1 s, a camera length of 185 mm, a spot size of 11 and a screen current of ~100 pA. Electron energy loss spectroscopy (EELS) mapping was also performed on the FEI Titan 80-300 TEM operated at 200 kV using a Gatan Quantum GIF spectrometer with K2 direct electron detector, using a collection angle of 55 mrad and a dispersion of 0.5 eV/ch. HAADF imaging for lamella 2 was performed using a Talos 200X operated at 200 kV in STEM mode at a convergence angle of 10.5 mrad. EELS mapping was performed on the same microscope–equipped with a Gatan Continuums

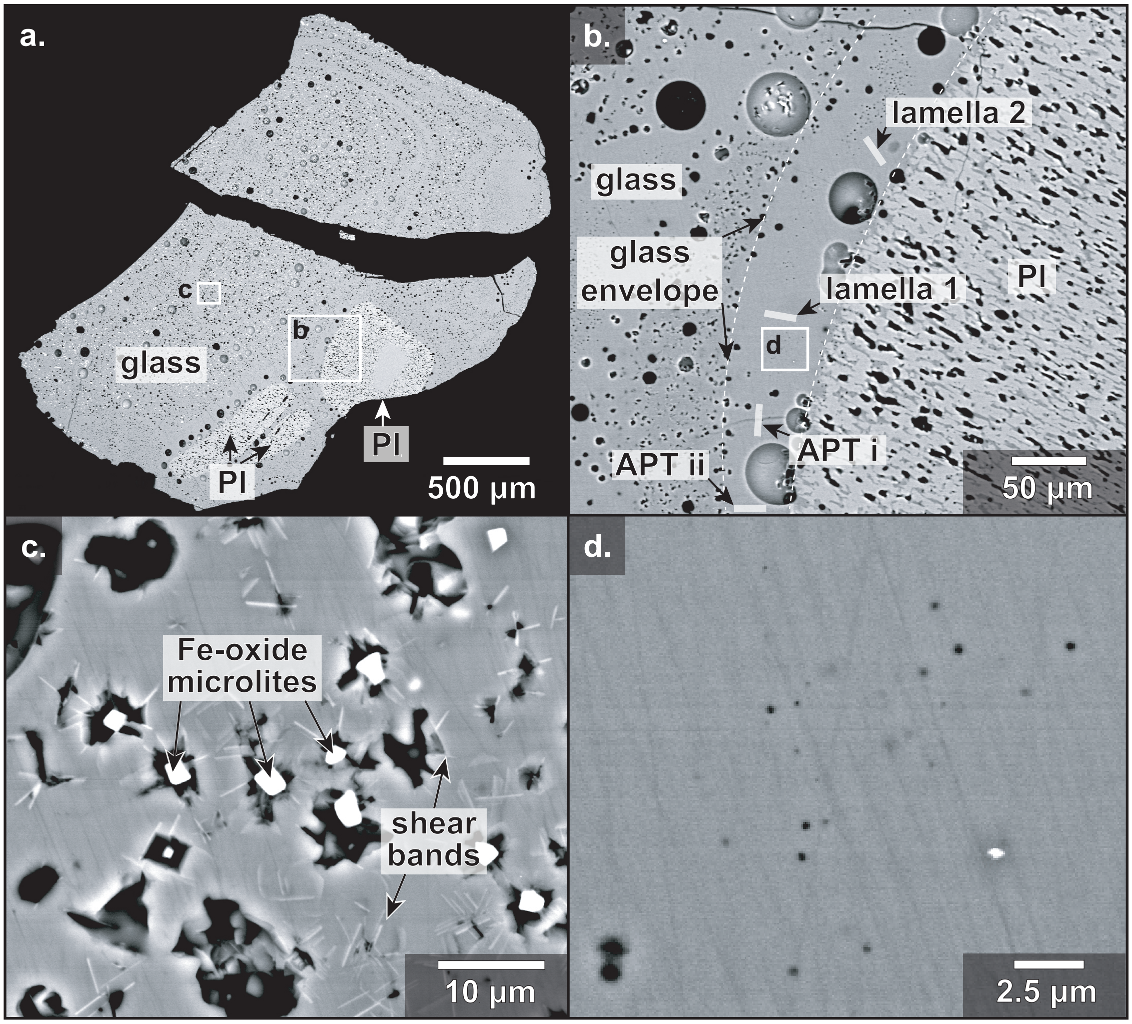

Figure 5.2. BSE images of experimental andesitic glass sample. **a.** Overview of sample showing the heterogeneous distribution of gas bubbles and sieve-rimmed plagioclase crystals. **b.** Close-up view of region of interest at the margin of a plagioclase crystal showing the locality of STEM lamellae 1 and 2 and of the APT lift out for specimens (i) and (ii). **c.** Close-up view of glass sample showing the heterogeneous distribution of Fe-oxide microlites and shear band defects. **d.** Close-up view of glass envelope showing the heterogeneous distribution of nanoscale bubbles.

GIF spectrometer with CMOS detector using a collection angle of 55 mrad and a dispersion of 0.5 eV/ch.

5.3.3 Atom Probe Tomography

For the purpose of this study, a series of specimens was prepared at room temperature from the same nearly bubble-free region of interest by *in situ* lift-out (Thompson et al. 2007) for APT in an attempt to induce nanoscale gas bubbles and investigate the detailed composition of some of the microstructural features at the near-atomic scale. The needle-shaped specimen was sharpened by annular milling at 30 kV on a Thermo Scientific Helios™ G4 UXe DualBeam™ Plasma-FIB/SEM at the Canadian Centre for Electron Microscopy (Hamilton, Canada) and subsequently cleaned using the xenon beam at 2 kV to remove regions potentially severely damaged by the implantation of energetic Xe ions. The specimen was then analysed by APT in a CAMECA LEAP 4000 XR (Table S5.1) fitted with a reflectron-lens with a detector efficiency of ~36%. The specimen was analysed in laser pulsing mode at 59.6 K with a laser pulse energy of 300 pJ focused on an area estimated to be <3 μm in diameter, a detection rate of 0.3 ions detected for 100 pulses and a laser pulse repetition rate of 200 kHz.

A second series of APT specimens was prepared using a FEI Helios 600 at the Max-Planck-Institut für Eisenforschung (Düsseldorf, Germany), and the sharpening was performed under cryogenic conditions to help maintain the structural integrity of the andesitic glass and use as a reference material. The needle-shaped specimen was sharpened at 30kV while the support coupon was directly facing the Ga-ion beam, using the setup described in Rivas et al. (2020). The effect of going to a lower temperature is discussed in detail in Chang et al. (2019) and is in part related to suppressing or hindering thermally-activated diffusion of the incoming ions and of the displaced atoms from within the material (Lilensten and Gault 2020). The specimens were then analysed by

APT in a CAMECA LEAP 5000 XR (Table S5.1) fitted with a reflectron-lens with a detector efficiency of ~52%. The specimen was analysed in laser pulsing mode at 55 K with a laser pulse energy of 400 pJ focused on an area estimated to be <3 μm in diameter, a detection rate of 0.1 ions detected for 100 pulses and a laser pulse repetition rate of 200 kHz.

The data processing and reconstruction were done with the commercial software package IVAS® 3.8.4. Compositional profiles presented herein were generated from cylindrical regions of interest using the 1D concentration profile function and computed using the fixed bin width profile, atomic, and decompose complex ions options. The bin size was adjusted for each profile (~0.2 nm) to maximize the ratio of the peak signal to the statistical fluctuations. Ion identities within the measured dataset were assigned by defining ranges within the mass spectrum that best fit theoretical isotopic ratios (Blum et al. 2018; Exertier et al. 2018; Reddy et al. 2020). The ranged mass spectrum from the analysed specimens is shown in Figure S5.1.

5.4 Results

5.4.1 Sample characterization

Backscatter electron (BSE) imaging of the sample reveals three large sub-rounded plagioclase crystals varying between 130–570 μm in width and 430–770 μm in length within a glassy matrix (Figure 5.2). All three plagioclase crystals have rough surfaces with melt inclusions, herein referred as sieve texture (Pleše 2019a). The largest of the three plagioclase crystals exhibits a sieved rim (3.0–8.5 μm wide) with a smaller intact core. The glassy matrix contains ubiquitous bubbles of varying sizes ranging between 0.4 to 60 μm in diameter and dispersed euhedral Fe-oxide microlites (Figure 5.2c). These oxides occur both within the glassy matrix as well as at bubble-melt interfaces with small (1–5 nm in length) planar defects (i.e., shear bands; Li 2001) propagating from their margins (Figure 5.2c). Furthermore, large (45–60 μm) bubbles occur at or near the plagioclase crystal-bubble interface (Figure 5.2a-b). These crystals are surrounded by 50–100 μm wide glass envelopes with a smaller volume fraction of bubbles that are <2 μm in diameter (Figure 5.2d) and are mostly free of Fe-oxide microlites. One such envelope (Figure 5.2b) was chosen as our region of interest in an attempt to capture a bubble-free volume for our experiments.

5.4.2 2D nano-structural and chemical analysis

HAADF imaging for both lamellae reveal ubiquitous gas bubbles, apparent as darker circles and ellipses relative to the glassy matrix. The bubbles range from 3 to 115 nm in diameter with most of the bubble volume fraction occurring as smaller bubbles (3–35 nm in diameter) in the top 50–80 nm of the lamellae and decreasing in density with depth within the glass (Figure 5.3). Few chemical heterogeneities are also observed within both lamellae, ranging between 10 and 150 nm in length and appear as lighter amoeboid-shaped regions relative to the matrix. These chemical heterogeneities are mostly sporadically distributed within the glass (at 75 nm to >1 μm spacing) or amalgamated together (n>3; at <20 nm spacing), however several of them occur at bubble-melt interfaces. EELS mapping of the heterogeneities at bubble-melt interfaces revealed: 1) Ca-rich clusters with minor O (~20 nm in length; Figure 5.4a), 2) small Fe clusters (~10 nm in diameter; Figure 5.4a), and 3) Fe-rich clusters with minor O, Al, Ca and K (~25 nm in length; Figure 4b). EELS mapping of the heterogeneities within the melt revealed: 1) large amoeboid-shaped Ca-O-Fe-clusters (~100 nm in diameter; Figure 5.5a-b), 2) Fe-rich clusters (Figure 5.5a-b), 3) small amoeboid-shaped Na-rich clusters (10–50 nm in length; Figure 5.5a), and 4) thin and elongated Ca-rich clusters (~50–80 nm in length; Figure 5.5b). The combined STEM data and EELS mapping thus reveal small chemical heterogeneities both at bubble-melt interfaces and within the melt.

5.4.3 3D nano-structural and chemical analysis

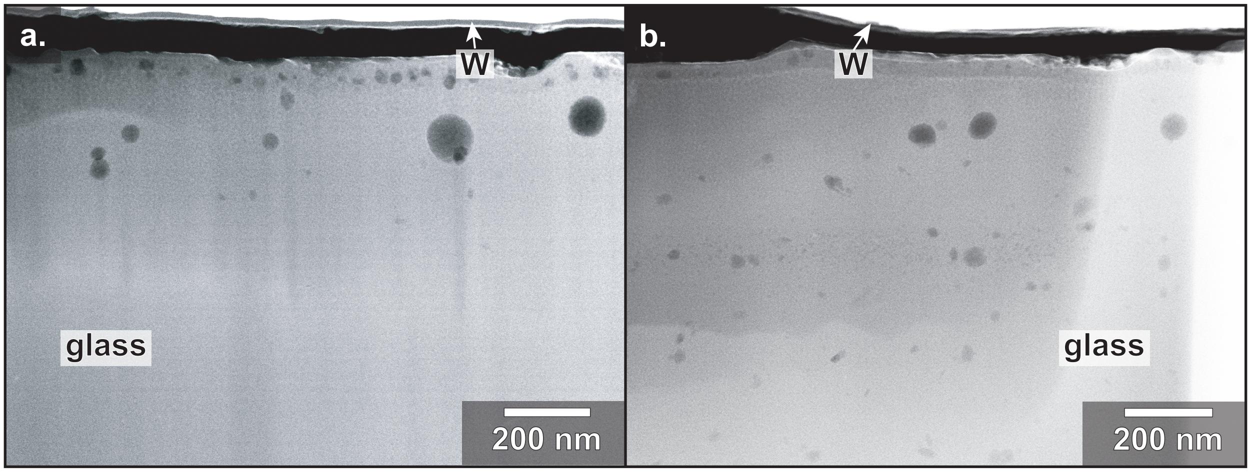

Figure 5.3. HAADF images of STEM lamellae 1 (**a.**) and 2 (**b.**) showing the heterogeneous distribution gas bubbles introduced during room-temperature FIB preparation.

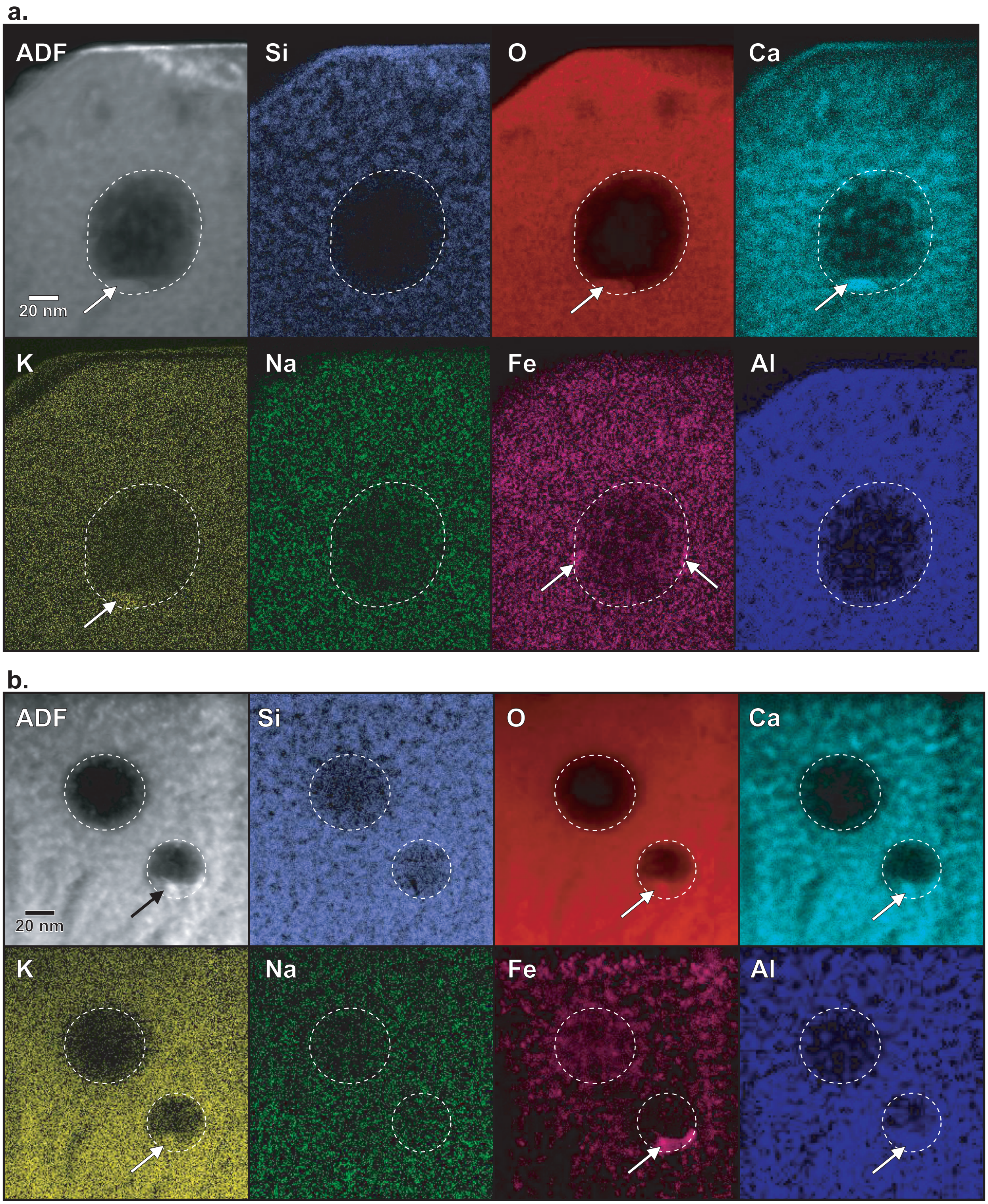

Figure 5.4. ADF and EELS maps of gas bubbles from lamellae 1 (**a.**) and 2 (**b.**) revealing chemical heterogeneities (white arrows) at bubble-melt interfaces. **a.** EELS maps show a Ca- and O-rich cluster and two smaller Fe clusters at the bubble margin. **b.** EELS maps show a Fe-, Ca-, O-, Al-, and K-rich cluster at one bubble margin.

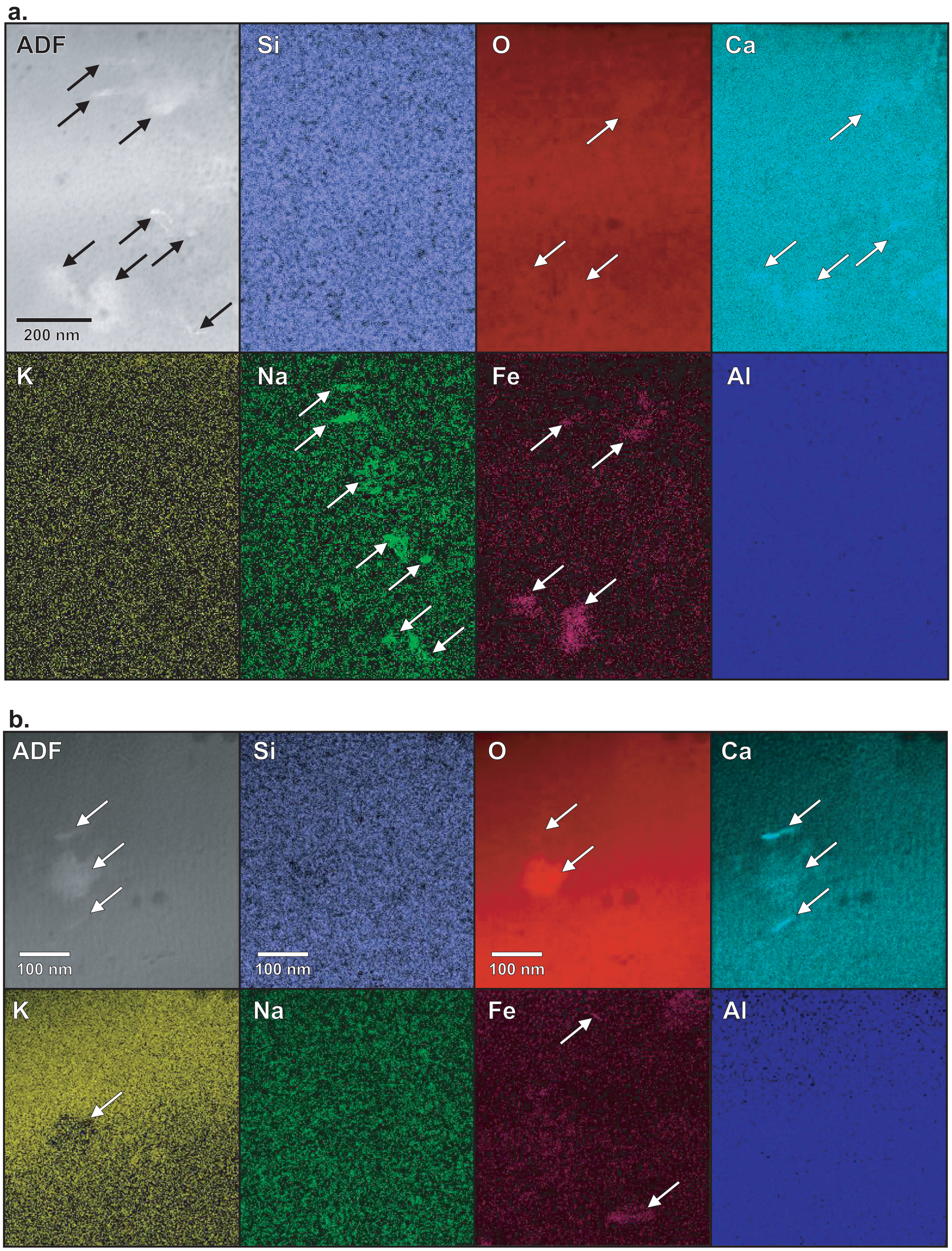

Figure 5.5. ADF and EELS maps of andesitic glass from lamella 2 revealing chemical heterogeneities (white arrows) within the melt. **a.** EELS maps show Na- and Fe-rich clusters within the glassy matrix with minor enrichments in O and Ca. **b.** EELS maps show Ca- and O-rich and K-poor clusters and minor Fe clusters within the melt.

APT analysis of the specimen (i) prepared at room temperature yielded 52 million ions (Table S5.1). The 3D reconstruction of the specimen reveals a homogeneous distribution of its major components Si and O (Figure S5.2). In contrast, Fe and Na form several clusters. Within the APT point cloud, the point-density inside these clusters is ~3.5X and 4X that of the matrix, respectively, which is related to ion trajectory aberrations associated to the local compositional heterogeneity during field evaporation (Dubosq et al. 2020; Wang et al. 2020). The Fe-rich clusters are spherical and have an apparent diameter of 5–8 nm, whereas the Na-rich clusters are disc-shaped or have an amoeboid shape with larger apparent diameters of 15-35 nm.

Furthermore, the specimen exhibits large spherical to elliptical regions of low point density (~25% that of the surrounding matrix; Figure 5.6a-d). Although most of the Fe-rich clusters appear to be heterogeneously distributed within the specimen, few occur in the immediate vicinity of the lower point-density regions (Figure 5.6e). The Na-rich clusters occur mostly directly on top of the lower point-density regions (i.e. bubbles; Miller et al. 2011; Wang et al. 2020) in the direction of evaporation (Figure 5.6e). Composition profiles across Fe clusters reveal peak compositions in the range of 9.4–15.0 at% compared to matrix values <5.0 at% (Figure S5.3). A composition profile across one of the bubbles shows elevated Na, Ca, and K compositions at one of the margins of the bubble with peaks of approximately 7 at%, 9 at%, and 3 at%, respectively, compared to matrix values in the range of 0.6–3.0 at%, 2.0–5.7 at%, and 0–1.4 at% (Figure 5.6f).

APT analysis of the cryo-prepared specimen (ii) yielded 14 million ions (Table S5.1). The 3D reconstruction of the specimen reveals a homogeneous distribution of its major components, Si and O (Figure S5.4), whereas Fe forms several clusters exhibiting a point-density ~5X that of the matrix (Figure 5.7a-b). The clusters range from 3–25 nm in diameter and have a spherical to disc-shaped morphology. Composition profiles across these clusters (e.g., Figure 5.7c) show

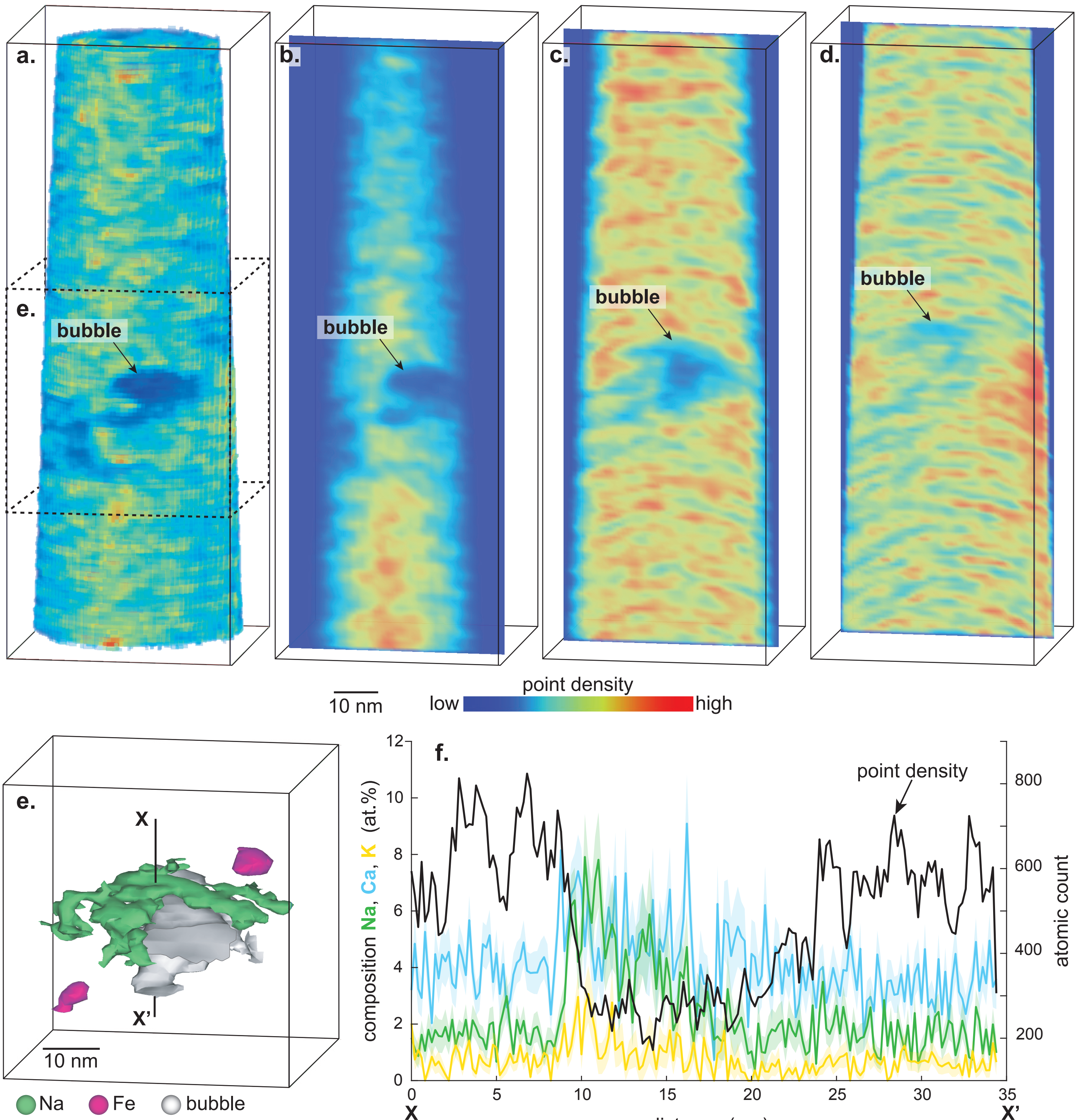

Figure 5.6. a. 3D reconstruction of APT specimen (i) showing the volume point density and revealing a low point density region in the centre of the specimen (i.e., bubble). **b-d.** 2D point density contour plots at 10 nm intervals within the specimen volume showing the apparent geometry of the bubble. **e.** 3D clipping of the bubble (grey isosurface) showing a large Na clusters (green isosurface) on top of the bubble in the direction of evaporation and smaller Fe clusters (pink isosurfaces) in the immediate vicinity on either side. **f.** Composition profiles across the bubble (X-X') showing elevated Na, Ca, and K composition adjacent to the bubble (low point density region show in the black line).

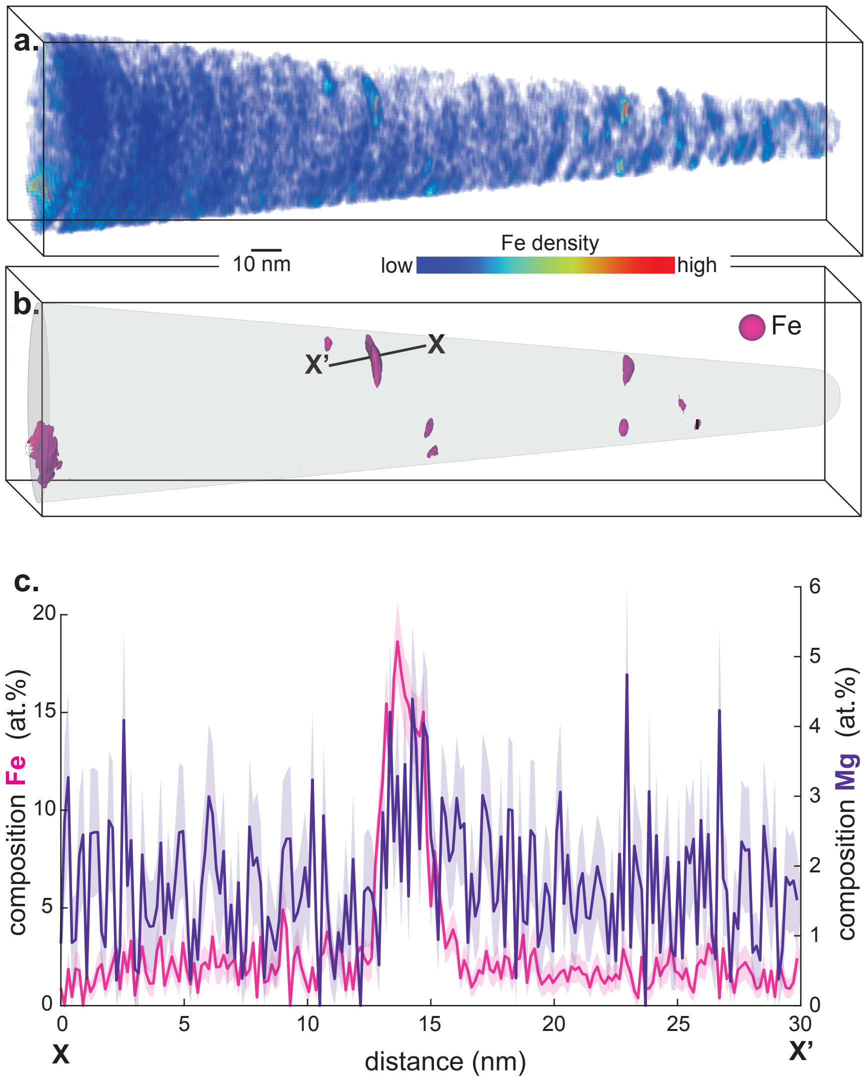

Figure 5.7. a. 3D reconstruction of APT specimen (ii) showing the Fe density and revealing Fe-rich clusters. **b.** 3D reconstruction of APT specimen (ii) showing Fe-rich clusters (pink isosurfaces). **c.** Composition profile across one of the Fe clusters (X-X') revealing minor Mg enrichment.

elevated Fe compositions in the range of 16.1–20.2 at% compared to matrix values <7.0 at%, with minor Mg enrichment with values of up to 4.4 at%. In contrast to specimen (i), specimen (ii) does not reveal any low point-density regions within the analyzed volume.

5.5 Discussion

5.5.1 Validity of analogue model

The bubbles within our experimental andesitic glass specimens were induced by FIB irradiation. Irradiation in solids typically results in the displacement of atoms from their lattice sites, creating vacancies and interstitial point defects. At high temperatures, both vacancies and interstitials can diffuse, and bubble formation can occur (Norris 1972; Russell 1971). Hereafter, the term bubble refers to any free volume or molecular sized space within a material occupied by a vacuum or a gas phase. In a natural magmatic system, bubble nucleation occurs by the agglomeration of exsolved volatiles associated with decompression. Therefore, in this section we compare the nucleation processes of vacuum bubbles in a solid and the nucleation processes of gas bubbles in a liquid to evaluate the validity of our experiments as an analogue model for investigating bubble nucleation processes in natural magmas.

In both scenarios, the vacancy and volatile clusters form microscopic voids that can constitute the nuclei necessary for rupture and growth to macroscopic bubbles. These microscopic voids must exceed the critical radius for nucleation and subsequent growth. In the case of vacuum bubble nucleation by irradiation and vacancy clustering, the critical radius (r_c) is defined by:

$$r_c = \frac{2\sigma \mathrm{V}}{kT \ln\left(\frac{B_v - B_i}{B_{v,o}}\right)}$$

where σ is the surface energy of the void, V is the atomic volume, k is the Boltzmann constant, T is temperature, B_v is the vacancy flux to the void, B_i is the interstitial flux to the void, and $B_{v,o}$ is the vacancy flux for equilibrium vacancy concentration (Norris 1972; Russell 1971). Based on this equation, we can see that the critical radius is very sensitive the interstitial and vacancy fluxes. For nucleation to occur, vacancies must diffuse to voids before being annihilated by interstitials (Norris 1972). In the case of gas bubble nucleation by volatile clustering in a liquid phase, the critical radius is defined by:

$$r_c = \frac{2\sigma}{\Delta P_C}$$

where ΔP_C is the tensile strength of the liquid (Gibbs 1961). When considering gas bubble nucleation in magmas, ΔP_C is equivalent to the supersaturation pressure (ΔP_{SAT}; Hurwitz and Navon 1994). The free energy (ΔG) required to create a nucleus of the critical size can be expressed as the surface energy per unit surface area:

$$\Delta G = \frac{4}{3}\pi {r_C}^2\sigma$$

Therefore, the direct relationship between the critical energy required for vacuum bubble nucleation in a solid can be written as:

$$\Delta G = \frac{16\pi\sigma V^2}{3(kT)^2\left(\ln\frac{B_v - B_i}{B_{v,o}}\right)^2}$$

(Russell 1971), and the direct relationship between the critical energy required for gas bubble nucleation in a liquid can be written as:

$$\Delta G = \frac{16\pi\sigma^3}{3(\Delta P_C)^2}$$

(Gibbs 1961, Skripov 1974). In both cases, the critical energy for bubble nucleation is proportional to the surface energy of the precursor void. In the presence of a heterogeneity (e.g., crystal surface), the activation energy for bubble nucleation decreases by a factor of ϕ due to a decrease in surface energy. As previously described, ϕ is defined as:

$$\phi = \frac{(2 - cos\theta)(1 + cos\theta)^2}{4}$$

and θ is defined as:

$$cos\theta = \frac{(\sigma_{\alpha\delta} - \sigma_{\beta\delta})}{\sigma_{\alpha\beta}}$$

where θ is the contact angle between bubble and heterogeneity, $\sigma_{\alpha\delta}$ is the matrix (α)-heterogeneity (δ) surface energy, $\sigma_{\beta\delta}$ is the bubble (β)-heterogeneity (δ) surface energy and $\sigma_{\alpha\beta}$ is the matrix (α)- bubble (β) surface (Landau and Lifshitz 1980). Although the surface energy of vacuum bubbles may differ from that of gas bubbles, and the diffusion rate of vacancies in a solid may differ from the diffusion rate of volatiles in a liquid, it is evident based on these equations that the processes of irradiation induced bubble nucleation in solids are very similar to gas bubble nucleation in liquids. Therefore, our experiments are plausible analogues of the initial processes of bubble nucleation in natural magmas.

5.5.2 The chicken and egg problem

The combined data from the STEM lamellae and APT specimen (i) prepared at room temperature reveal nanoscale chemical heterogeneities in the form of Fe-, Ca-, and Na-rich clusters at bubble-melt interfaces (Figures 5.4, 5.6, 5.7). Based on these observations, ambiguity remains as to whether the bubbles or chemical heterogeneities occurred first within the melt. Although the presence of chemical heterogeneities is known to facilitate bubble nucleation in magmas by decreasing the required energy barrier (i.e., heterogeneous nucleation; Landau and Lifshitz 1980; Hurwitz and Navon 1994; Adamson and Gast 1997; Navon and Lyakhovsky 1998), pre-existing bubbles are also capable of decreasing the energy barrier required to trigger crystal nucleation (Mollard et al. 2012, 2020). The latter process typically occurs as part of degassing-driven crystallization. For example, as a magma ascends, decompression causes volatiles (i.e., H_2O) to exsolve from the melt, resulting in dehydration and an increase of the liquidus temperature (Hammer and Rutherford 2002; Tuttle and Bowen 1958). Degassing or depressurization of water-saturated melts can therefore lead to an increasing difference between the crystal liquidus temperature and the magma temperature, which is known as effective undercooling and acts as a major driving force for crystal nucleation and growth (Hammer and Rutherford 2002). Degassing-driven crystallization leads to specific crystal textures and morphologies from tabular to skeletal (increasing in complexity with increased undercooling) and common crystal sizes below 100 μm due to rapid growth under thermodynamic disequilibrium (Brandeis and Jaupart 1987; Brugger and Hammer 2010; Couch et al. 2003; Hort 1998; Hammer and Rutherford 2002; Hammer 2004; Lofgren 1974, 1980; Martel 2012; Roselle et al. 1997; Toramaru 2001).

Although the chemical heterogeneities documented in our specimen are characteristically smaller than 100 μm in diameter, we cannot properly describe their textures and morphologies due to the limited spatial resolution of our STEM data and accuracy of APT data reconstructions. The small size of the heterogeneities also raises the question of whether they are amorphous atom clusters within the melt or nanolites with a defined crystal structure, and due to the beam-sensitive nature of the samples we could not focus the beam long enough to obtain a diffraction pattern. However, based on the classical nucleation theory (Becker and Döring 1935; Farkas 1927; Fokin et al. 2006; Frenkel 1946; Kaischew and Stranski 1934; Kashchiev 1969; Kirkpatrick 1981; Turnbull and Fisher 1949; Volmer and Weber 1926), a homogeneous one-component liquid that is held under its liquidus temperature will begin to form pseudo-crystal atom clusters to achieve thermodynamic stability, creating cluster-liquid interfaces. Consequently, regardless of whether the documented chemical heterogeneities are nanolites or amorphous atom clusters, undercooling from bubble nucleation could potentially explain the documented spatial relationship between clusters and bubbles in our sample.

To determine whether the chemical heterogeneities occurred first or as a result of undercooling from bubble nucleation, we compare the specimen prepared at room temperature to the cryo-prepared specimen. The increased bubble volume fraction in the top layer of the STEM lamellae prepared at room temperature suggests that the bubbles were in fact likely created from the initial FIB imaging or potentially by the Xe-ion deposition process, where the top layer was affected by the ion beam, and not by the decompression experiment during the sample synthesis. Additional STEM imaging of APT specimens prepared at room temperature also show higher bubble volume fractions with increasing ion beam damage as a result of the ion milling processes and STEM imaging (Figure S5.5). This suggests that the bubbles observed in the APT specimen (i) prepared at room temperature were also created during the milling process. The absence of bubbles in the cryo-prepared APT specimen suggests that milling under cryogenic conditions did not damage the sample but instead we successfully maintained the structural integrity of the glass and prevented bubble nucleation in this intermediate melt. The observation of the cryo-sharpened APT specimens by STEM was attempted, in order to perform direct correlation (Herbig 2018; Zhou et al. 2021), however the material was too beam sensitive and irradiation by the electrons caused the specimen to be damaged too fast to enable the combined analyses. However, the presence of clusters within the cryo-prepared specimen (ii) therefore suggests that the clusters were present first within the glass and acted as cluster-liquid interfaces that facilitate bubble nucleation in specimen (i). This conclusion is also supported by the observation of such clusters within the matrix away from the immediate vicinity of bubbles in the STEM lamellae prepared at room temperature.

5.5.3 Implications for eruption parameter estimates

Pyroclastic textural measurements, such as bubble number density, and classical nucleation theory have shown great potential for estimating physical parameters of magmas that are essential for the characterization of modern and pre-historical volcanic eruptions. These parameters include supersaturation pressure, decompression rate, magma discharge rate, conduit radius, and eruption column height (e.g., Alfano et al. 2012; Cashman and Mangan, 2014; Gurioli et al. 2008; Houghton et al. 2010; Pardo et al. 2014; Rust and Cashman 2011; Sable et al. 2006; Shea et al. 2013; Toramaru 2006). For example, Toramaru (1989, 1995, 2006) developed a rate-meter based on the nucleation theory and decompression experiments, which uses the number density of bubbles per unit volume melt, to calculate magma decompression rates during ascent. The link between bubble number densities N_V and decompression rate dP/dt is defined by the equation:

$$N_V \approx 34 n_0 \left(\frac{16\pi\sigma^3}{3k_B T P_{SAT}^2}\right)^{-2} \left(\frac{V_{H_2O} P_{SAT}}{k_B T}\right)^{-1/4} \left(\frac{P_{SAT}^2 k_B T n_0 D_{H_2O}}{4\sigma^2 |dP/dt|}\right)^{-3/2}$$

where n_0 is the concentration of water molecules per volume melt, D_{H2O} is the diffusivity of water at the bubble-melt interface, V_{H2O} is the volume of a water molecule in the melt, k_B is the Boltzmann constant, T is the temperature, P_{SAT} is the saturation pressure, and σ is the melt-bubble interfacial energy (surface tension). Surface tension values for homogeneous (σ_{hom}) or heterogeneous (σ_{het}) nucleation can be derived using the nucleation theory after Hirth et al. (1970) in which the nucleation rate J for H_2O bubbles in a magma is defined by:

$$J = J_0 exp\left(-\frac{16\pi\sigma^3}{3k_B T(P_B^* - P_M)^2}\phi\right)$$

where $J_0 = \frac{2{n_0}^2 D_{H_2O} V_{H_2O}}{a_0} \sqrt{\frac{\sigma}{k_B T}}$ is the pre-exponential factor, a_0 is the distance between water molecules in the melt, σ is the melt-bubble interfacial energy, P^*_B is the internal pressure of the bubble nucleus, P_M is the pressure in the surrounding melt, and $\phi = \frac{(2-cos\theta)(1+cos\theta)^2}{4}$ is a geometrical term that defines the nucleation mechanism. For homogeneous nucleation ϕ =1 and for heterogeneous nucleation 0< ϕ <1. These relationships demonstrate that the application of the nucleation theory to natural systems as a tool to extract physical eruption parameters requires an assumption to be made on whether the degassing process was dominated by homogeneous or heterogeneous nucleation.

Current reasoning for the assumption of homogeneous nucleation involves either a visible absence of microlites as possible nucleation sites or a lower abundance of microlites to match the bubble number densities, which are typically based on observations from petrographic microscope or scanning electron microscopy images (e.g., Adams et al. 2006; Alfano et al. 2012; Bouvet de Maisonneuve et al. 2009; Carey et al. 2009; Gondé et al. 2011; Gonnermann and Houghton 2012; Houghton et al. 2010; Klug et al. 2002). Although it has previously been suggested that pyroclasts may contain sub-microscopic crystals or atom clusters that acted as nucleation sites for bubbles (e.g., Cáceres et al. 2020; Gardner and Denis 2004; Hurwitz and Navon 1994; Larsen 2008), direct evidence of their existence remained equivocal. Our combined STEM and APT data not only reveal the existence of such clusters but also demonstrate their spatial relationship with gas bubbles within an experimental melt. These data challenge the use of conventional imaging techniques to discern between homogeneous and heterogeneous nucleation, which is currently a critical piece of information for extracting physical eruption parameters based on textural parameters.

5.5.4 Plausibility of homogeneous bubble nucleation

Recent studies (e.g., Shea 2017) have begun questioning the likelihood of homogeneous bubble nucleation and instead suggest that heterogeneous nucleation may dominate in all magma types. One argument in favor of heterogeneous nucleation is based on estimates of supersaturation pressures (ΔP_N) required for bubble nucleation in magmas. Although values of ΔP_N exceeding 100 MPa are necessary for homogeneous nucleation in rhyolitic melts, heterogeneous nucleation can occur at ΔP_N lower than 50 MPa. Shea (2017) calculated the supersaturation pressures required to trigger homogeneous (ΔP_{Nhom}) and heterogeneous (ΔP_{Nhet}) nucleation of bubbles in highly explosive eruptions (i.e., Vulcanian, sub-Plinian and Plinian) involving magmas of various compositions. Using the Toramaru (2006) model, they yielded ΔP_{Nhom} values of ~40–200 MPa and ΔP_{Nhet} values of ~15–30 MPa. To assess whether the calculated supersaturation pressures were realistic, the author compared the ΔP_N values to the initial pre-eruptive pressures inferred for the various eruptions, which represent the maximum possible pressure ranges for nucleation. The results reveal that the calculated ΔP_{Nhom} are in most instances near to slightly below pre-eruptive pressures with some eruptions yielding ΔP_{Nhom} equal to, or slightly above, pre-eruptive pressures. These estimates suggest that homogeneous nucleation often may not be a realistic degassing mechanism. Considering the results of our study, we can expect that some bubbles that have been assumed to have nucleated homogeneously in order to estimate supersaturation pressures may in fact have nucleated heterogeneously on nanoscale atom clusters. This assumption suggests that we could be significantly underestimating the supersaturation pressures needed for homogeneous nucleation. In reality, the required supersaturation pressures likely exceed realistic pre-eruptive pressures therefore supporting the argument that homogeneous nucleation in natural systems is not prevalent and that bubble nucleation processes in magmas may be dominated by heterogeneous nucleation.

5.5.5 New tools for studying bubble nucleation processes

As highlighted by recent studies (e.g., Gardner and Denis 2004; Larsen 2008; Shea 2017), a complete understanding of the initial stages of bubble nucleation processes requires direct observations to be made at the nanometer- to atomic-scales. Several studies have demonstrated the potential of TEM to characterize microlites in natural pyroclasts (e.g., Besson and Poirier 1994; Schlinger et al. 1991; Sharp et al. 1996), however, there have been fewer efforts to characterize atom clusters as potential bubble nucleation sites. Although TEM has the optimal spatial resolution to resolve structural information including cluster size, morphology, and distribution, it is limited in its ability to quantify elemental compositions at the same scale, in particular for small microstructural features with complex three-dimensional morphologies. Atom probe tomography is being increasingly applied to understand sub-micrometer scale geological processes (Reddy et al. 2020), and the correlation of electron microscopy with techniques such as APT hence has a unique potential as an analytical approach to obtain high resolution compositional information in addition to structural information pertaining to atom clusters in natural and experimental melts, as illustrated by our results.

One of the main limitations for both techniques comes from the structural damage and chemical degradation that is caused by the high-energy ion beam during sample preparation, which is typically achieved through FIB milling at room temperature (e.g., Bassim et al. 2012; Rothmann et al. 2018; Siemons et al. 2014). Damage mitigation becomes especially important when investigating highly-sensitive specimens, such as silicate glasses, as was the case for this study. Recent efforts in the field of electron microscopy and materials science have developed a new specimen preparation approach to considerably minimize ion-milling-induced damage in the case of FIB-based specimen preparation for TEM and APT analyses through cryogenic milling (Chang et al. 2019; Parmenter and Nizamudeen 2021). Milling under cryogenic conditions, typically below 150 K, limits sample heating during the sputtering process, which significantly reduces ion implantation and diffusion as well as preserves the structural integrity of sensitive materials (Bassim et al. 2012; Marko et al. 2007; Medeiros et al. 2018; Rigort et al. 2015; Villa et al. 2013). Whereas these technical developments have mostly been applied for the analysis of aluminium alloys (e.g., Lilensten and Gault 2020), organic-inorganic materials (e.g., perovskite; Lawson et al. 2019; Rivas et al. 2020; Whittle et al. 2018), ceramics (e.g., zirconolite; Blackburn et al. 2020; Mason et al. 2020) and organic or biological specimens (e.g., Marko et al. 2007; Medeiros et al. 2018; Rigort et al. 2015; Villa et al. 2013), our work highlights the potential of cryo-FIB specimen preparation for the analysis of silicate glasses in the context of bubble and crystal nucleation processes.

5.6 Conclusions

Our combined nanoscale structural and chemical analyses of an experimental andesitic melt reveal sub-microscopic Fe-, Na-, and Ca-rich atom clusters at the bubble-melt interface of newly nucleated gas bubbles. The presence of similar atom clusters within a specimen prepared under cryogenic conditions that did not induce gas bubble formation suggest these clusters acted as nucleation sites for gas bubbles induced during the room temperature preparation. Our data support the hypothesis that homogeneous nucleation may simply be a variety of heterogeneous nucleation that occurs at the surface of sub-microscopic crystals or element clusters, which has significant implications for eruption parameter estimates and the plausibility of homogeneous nucleation in natural systems. Lastly, our work demonstrates the potential of cryo-approaches for TEM and APT for the analysis of natural silicate glasses in the context of atom cluster characterization in the early stage of bubble nucleation.

5.7 Acknowledgements

This project was funded by a Geological Society of America student research grant (to RD) and Natural Sciences and Engineering Research Council of Canada grant (to DAS). We thank Hui Yuan and Natalie Hamada for their assistance on PFIB and STEM instruments at CCEM.

5.8 References

Adams NK, Houghton BF, Fagents SA, Hildreth W (2006) The transition from explosive to effusive eruptive regime: the example of the 1912 Novarupta eruption, Alaska. Geol Soc Am Bull 118: 620–634. doi.org/10.1130/B25768.1.

Adamson AW, Gast A (1997) Physical chemistry of surfaces, sixth ed. John Wiley and Sons, New York.

Alfano F, Bonadonna C, Gurioli L (2012) Insights into eruption dynamics from textural analysis: the case of the May, 2008, Chaitén eruption. Bull Volcanol 74: 2095–2108. doi.org. 10.1007/s00445-012-0648-3

Baker DR (2004) Piston-cylinder calibration at 400 to 500 MPa: A comparison of using water solubility in albite melt and NaCl melting. Am Mineral 89(10): 1553–1556. doi.org/10.2138/am-2004-1026

Baker DR, Eggler DH (1987) Compositions of anhydrous and hydrous melts coexisting with plagioclase, augite, and olivine or low-Ca pyroxene from 1 atm to 8 kbar; application to the Aleutian volcanic center of Atka. Am Mineral 72(1–2): 12–28. doi.org/10.1007/BF00402916

Bassim ND, De Gregorio BT, Kilcoyne ALD, Scott K, Chou T, Wirick S, Cody G, Stroud RM (2012) Minimizing damage during FIB sample preparation of soft materials. J Microsc 245(3): 288–301. doi.org/10.1111/j.1365-2818.2011.03570.x

Becker, R., and Döring, W. (1935). Kinetische behandlung der keimbuilding in übersättigten dämpfen. Ann Phys 24: 719–752. doi.org/10.1002/andp.19354160806

Besson P, Poirier J-P (1994) The 3100 BP eruption of the Soufriere of Guadeloupe, a transmission electron microscope study of the cryptodome andesite. Bull Volcanol 56: 184–192. doi.org/10.1007/BF00279603

Blackburn LR, Sun SK, Lawson SM, Gardner LJ, Ding H, Corkhill CL, Maddrell ER, Stennett MC, Hyatt NC (2020) Synthesis and characterisation of $Ca_{1-x}Ce_xZrTi_{2-2x}Cr_{2x}O_7$: Analogue zirconolite wasteform for the immobilisation of stockpiled UK plutonium. J Eur Ceram Soc 40: 5909–5919. doi.org/10.1016/j.jeurceramsoc.2020.05.066

Blake S (1984) Volatile oversaturation during the evolution of silicic magma chambers as an eruption trigger. J Geophys Res 89: 8237–8244. doi.org/10.1029/JB089iB10p08237

Blander M, Katz JL (1975) Bubble nucleation in liquids. J AIChE 21(5): 833–848. doi.org/10.1002/aic.690210502

Blum TB, Darling JR, Kelly TF, Larson DJ, Moser DE, Perez-Huerta A, Prosa TJ, Reddy SM, Reinhard DA, Saxey DW, Ulfig RM, Valley JW (2018) Best Practices for Reporting Atom Probe Analysis of Geological Materials. In: Moser DE, Corfu F, Darling JR, Reddy SM, Tait K (eds) Microstructural geochronology: Planetary records down to atom scale. doi.org/10.1002/9781119227250.ch18

Bouvet de Maisonneuve C, Bachmann O, Burgisser A (2009) Characterization of juvenile pyroclasts from the Kos Plateau Tuff (Aegean arc): insights into the eruptive dynamics of a large rhyolitic eruption. Bull Volcanol 71: 643–658. doi.org/10.1007/s00445-008-0250-x

Brandeis G, Jaupart C (1987) Crystal sizes in intrusions of different dimensions: Constraints on the cooling regime and the crystallization kinetics. In: Mysen BO (ed) Magmatic Processes: Physicochemical Principles. Special Publication of the Geochemical Society 1, pp. 307–318.

Brugger CR, Hammer JE (2010) Crystallization kinetics in continuous decompression experiments: implications for interpreting natural magma ascent processes. J Petrol 51: 1941–1965. doi.org/10.1093/petrology/egq044

Cáceres F, Wadsworth FB, Scheu B, Colombier M, Madonna C, Cimarelli C, Hess KU, Kaliwoda M, Ruthensteiner B, Dingwell DB (2020) Can nanolites enhance eruption explosivity? Geol 48: 997–1001. doi.org/10.1130/G47317.1

Carey RJ, Houghton BF, Thordarson T (2009) Abrupt shifts betweenwet and dry phases of the 1875 eruption of Askja volcano: microscopic evidence formacroscopic dynamics. J Volcanol Geotherm Res 184: 256–270. doi.org/10.1016/j.jvolgeores. 2009.04.003.

Cashman K, Blundy J (2000) Degassing and Crystallization of Ascending Andesite and Dacite. Philos Trans R Soc London A 358(1770): 1487–1513. doi.org/10.1098/rsta.2000.0600

Cashman KV, Mangan MT (2014) A century of studying effusive eruptions in Hawaii. Characteristics of Hawaiian volcanoes. USGS Prof Paper 1801–9: 357–394. doi.org/10.3133/pp18019.

Chang Y, Lu W, Guénolé J, Stephenson LT, Szczpaniak A, Kontis P, Ackerman AK, Dear FF, Mouton I, Zhong X, Zhang S, Dye D, Liebscher CH, Ponge D, Korte-Kerzel S, Raabe D, Gault B (2019) Ti and its alloys as examples of cryogenic focused ion beam milling of environmentally-sensitive materials. Nat Comm 10: 942. doi.org/10.1038/s41467-019-08752-7

Couch S, Sparks RSJ, Carroll MR (2003) The kinetics of degassing-induced crystallization at Soufrière Hills Volcano, Montserrat. J Petrol 44, 1477–1502. doi.org/10.1093/petrology/44.8.1477

Davydov MN (2012) Nucleation and growth of a gas bubble in magma. J Appl Mech Tech Phys 53(3): 324–332. doi.org/10.1134/S0021894412030030

De Geuser F, Gault B (2020) Metrology of small particles and solute clusters by atom probe tomography. Acta Mater 188: 406–415. doi.org/10.1016/j.actamat.2020.02.023

Edmondson PD, Parish CM, Zhang Y, Hallén A, Miller MK (2011) Helium entrapment in a nanostructured ferritic alloy. Scr Mater 65(8): 731–734. doi.org/10.1016/j.scriptamat.2011.07.024

Exertier F, La Fontaine A, Corcoran C, Piazolo S, Belousova E, Peng Z, Gault B, Saxey DW, Fougerouse D, Reddy SM, Pedrazzini S, Bagot PAJ, Moody MP, Langelier B, Moser DE, Botton GA, Vogel F, Thompson GB, Blanchard PT, Chiaramonti AN, Reinhard DA, Rice KP, Schreiber DK, Kruska K, Wang J, Cairney JM (2018) Atom probe tomography analysis of the reference zircon gj-1: An interlaboratory study. Chem Geol 495: 27–35. doi.org/10.1016/j.chemgeo.2018.07.031.

Farkas L (1927) Keimbildungsgeschwindigkeit in übersättigten dämpfen. Zeitschrift für Physikalischee Chemie – Abteilung B –Chemie der Elementarprozesse Aufbau der Materie 125: 236–242. doi.org/10.1515/zpch-1927-12513

Fiege A, Cichy SB (2015) Experimental constraints on bubble formation and growth during magma ascent: A review. Am Mineral 100(11-12): 2426–2442. doi.org/10.2138/am-2015-5296

Fokin VM, Zanotto ED, Yuritsyn NS, Schmelzer JWP (2006) Homogeneous crystal nucleation in silicate glasses: a 40 years perspective. J Non Cryst Solids 352: 2681–2714. doi.org/10.1016/j.jnoncrysol.2006.02.074

Frenkel JI (1946) Kinetic Theory of Liquids. Oxford: Oxford University Press, pp. 488.

Gardner JE (2007) Heterogeneous bubble nucleation in highly viscous silicate melts during instantaneous decompression from high pressure. Chem Geol 236(1–2): 1–12. doi.org/10.1016/j.chemgeo.2006.08.006.

Gardner JE, Denis MH (2004) Heterogeneous bubble nucleation on Fe-Ti oxide crystals in high-silica rhyolitic melts. Geochim Cosmochim Acta 68(7): 3587–3597. doi.org/10.1016/j.gca.2004.02.021

Gault B, Chiaramonti A, Cojocaru-Mirédin O, Stender P, Dubosq R, Freysoldt C, Kumar Makineni S, Li T, Moody MP, Cairney JM (2021) Atom probe tomography. Nat Rev Methods Primers 1, 1–30. doi: 10.1038/s43586-021-00047-w

Gibbs W (1961) The Scientific Papers, Vol. 1. Dover Publ. Inc., NY.

Gondé C, Martel C, Pichavant M, Bureau H (2011) In situ bubble vesiculation in silicic magmas. Am Mineral 96: 111–124. doi.org/10.2138/am.2011.3546

Gonnermann HM, Houghton BF (2012) Magma degassing during the Plinian eruption of Novarupta, Alaska, 1912. Geochem Geophys Geosyst 13: 1–20. doi.org/10.1029/2012GC004273.

Gurioli L, Harris AJL, Houghton BF, Polacci M, Ripepe M (2008) Textural and geophysical characterization of explosive basaltic activity at Villarrica volcano. J Geophys Res 113: B08206. doi.org/10.1029/2007JB005328.

Hammer JE (2004) Crystal nucleation in hydrous rhyolite: experimental data applied to classical theory. Am Mineral 89: 1673–1679. doi.org/10.2138/am-2004-11-1212

Hammer JE, Rutherford MJ (2002) An experimental study of the kinetics of decompression-induced crystallization in silicic melts. J Geophys Res 107: 1–23. doi.org/10.1029/2001JB000281

Herbig M (2018) Spatially correlated electron microscopy and atom probe tomography: Current possibilities and future perspectives. Scr Mater 148: 98–105. doi.org/10.1016/j.scriptamat.2017.03.017

Hirth G, Pound GM, St Pierre GR (1970) Bubble nucleation. Metall Trans A 1(4): 939–945.

Hort M (1998) Abrupt change in magma liquidus temperature because of volatile loss or magma mixing: effects on nucleation, crystal growth and thermal history of the magma. J Petrol 39: 1063–1076. doi.org/10.1093/petrology/39.5.1063

Houghton BF, Carey RJ, Cashman KV, Wilson CJN, Hobden BJ, Hammer JE (2010) Diverse patterns of ascent, degassing, and eruption of rhyolite magma during the 1.8 ka Taupo eruption, New Zealand: evidence from clast vesicularity. J Volcanol Geotherm Res 195: 31–47. doi.org/10.1016/j.jvolgeores.2010.06.002

Hurwitz S, Navon O (1994) Bubble nucleation in rhyolitic melts: Experiments at high pressure, temperature, and water content. Earth Planet Sci Lett 122(3–4): 267–280. doi.org/10.1016/0012-821X(94)90001-9

Jenkins BM, Danoix F, Gouné M, Bagot PAJ, Peng Z, Moody MP, Gault B (2020) Reflections on the analysis of interfaces and grain boundaries by atom probe tomography. Microsc Microanal 26(2): 247–257. doi.org/10.1017/S1431927620000197

Kaischew R, Stranski IN (1934) On the kinetic deflection rate of germ formation. Zeitschrift für Physikalischee Chemie – Abteilung B – Chemie der Elementarprozesse Aufbau der Materie 26: 317–236.

Kashchiev D (1969) Solution of the non-steady state problem in nucleation kinetics. Surf Sci 14: 209–220. doi.org/10.1016/0039-6028(69)90055-7

Kedrinskii VK, Davydov MN, Chernov AA, Takayama K (2006) The initial stage of explosive volcanic eruptions: The dynamics of magma state in unloading waves. Dokl Akad Nauk 407 (2): 1–4.

Kirkpatrick RJ (1981) Kinetics of crystallization of igneous rocks. In Lasagna AC, Kirkpatrick RJ (eds.) Kinetics of Geochemical Processes. Mineralogical Society of America, pp. 321–398. doi.org/10.1515/9781501508233-012

Klug C, Cashman KV, Bacon C (2002) Structure and physical characteristics of pumice from the climactic eruption of Mount Mazama (Crater Lake), Oregon. Bull Volcanol 64: 486–501. doi.org/10.1007/s00445-002-0230-5

Landau L, Lifshitz E (1980) Statistical physics, Vol. 1. Oxford: Pergamon 24: 31–57.

Larsen JF (2008) Heterogeneous bubble nucleation and disequilibrium H_2O exsolution in Vesuvius K-phonolite melts. J Volcanol Geotherm Res 275: 278–288. doi.org/10.1016/j.jvolgeores.2008.03.015

Lawson SM, Hyatt NC, Whittle KR, Gandy AS (2019) Resistance to amorphisation in $Ca_{1-x}La_{2x/3}TiO_3$ perovskites e a bulk ion-irradiation study. Acta Mater 180: 180–188. doi.org/10.1016/j.actamat.2019.09.006

Li JCM (2001) Plastic deformation of noncrystalline materials. In: Jürgen Buschow KH, Cahn RW, Flemings MC, Ilschner B, Kramer EJ, Mahajan S, Veyssière P (eds) Encyclopedia of Materials: Science and Technology. Elsevier, pp. 7071–7078. doi.org/10.1016/B0-08-043152-6/01253-5.

Lilensten L, Gault B (2020) New approach for FIB-preparation of atom probe specimens for aluminum alloys. PLoS ONE 15(4): e0231179. doi.org/10.1371/journal.pone.0231179

Lofgren G (1974) An experimental study of plagioclase crystal morphology: isothermal crystallization. Am J Sci 274: 243–273. doi.org/10.2475/ajs.274.3.243

Lofgren G (1980) Experimental studies on the dynamic crystallization of silicate melt. In: Hargraves, R. B. (ed.) Physics of Magmatic Processes. Princeton, NJ: Princeton University Press, pp. 487–565.

Marko M, Hsieh C, Schalek R, Frank J, Mannella C (2007) Focused-ion-beam thinning of frozen-hydrated biological specimens for cryo-electron microscopy. Nat Methods 4(3): 215–217. doi.org/10.1038/nmeth1014

Martel C (2012) Eruption dynamics inferred from microlite crystallization experiments: Application to Plinian and dome-forming eruptions of Mt Pelée (Martinique, Lesser Antilles). J Petrol 53: 699–725. doi.org/10.1093/petrology/egr076

Martel C, Brooker RA, Andújar J, Pichavant M, Scaillet B, Blundy JD (2017) Experimental simulations of magma storage and ascent. In: Gottsmann J, Neuberg J, Scheu B (eds)

Volcanic Unrest. Advances in Volcanology. Springer, Cham. doi.org/10.1007/11157_2017_20

Mason AR, Tocino FY, Stennett MC, Hyatt NC (2020) Molten salt synthesis of Ce doped zirconolite for the immobilisation of pyroprocessing wastes and separated plutonium. Ceram Int 46: 29080–29089. doi.org/10.1016/j.ceramint.2020.08.080

Massol H, Koyaguchi T (2005) The effect of magma flow on nucleation of gas bubbles in a volcanic conduit. J Volcanol Geotherm Res 143: 69–88. doi.org/10.1016/j.jvolgeores.2004.09.011

Medeiros JM, Bock D, Pilhofer M (2018) Imaging bacteria inside their host by cryo-focused ion beam milling and electron cryotomography. Curr Opin Microbiol 43: 62–8. doi.org/10.1016/j.mib.2017.12.006

Miller MK, Longstreth-Spoor L, Kelton KF (2011) Detecting density variations and nanovoids. Ultramic 111: 469–472. doi.org/10.1016/j.ultramic.2011.01.027

Mollard E, Martel C, Bourdier J-L (2012) Decompression-induced experimental crystallization in hydrated silica-rich melts: I. Empirical models of plagioclase nucleation and growth kinetics. J Petrol 53: 1743–1766. doi.org/10.1093/petrology/egs031

Mollard E, Martel C, Le Trong E, Rogerie G (2020). Theoretical models of decompression-induced plagioclase nucleation and growth in hydrated silica-rich melts. Front Earth Sci 8(203): 1–15. doi.org/10.3389/feart.2020.00203

Navon O, Lyakhovsky V (1998) Vesiculation processes in silicic magmas. J Geol Soc Lond Special Publications 145(1): 27-50. doi.org/10.1144/GSL.SP.1996.145.01.03

Norris DIR (1972) Voids in irradiated metals (Part I). Radiat Eff Defects Solids 14(1–2), 1–37. doi.org/10.1080/00337577208230470

Papale P, Moretti R, Barbat, D (2006) The compositional dependence of the saturation surface of H_2O + CO_2 fluids in silicate melts. Chem Geol 229(1–3): 78–95. doi.org/10.1016/j.chemgeo.2006.01.013

Pardo N, Cronin SJ, Wright HMN, Schipper CI, Smith I, Stewart B (2014) Pyroclast textural variation as an indicator of eruption column steadiness in andesitic Plinian eruptions at Mt. Ruapehu. Bull Volcanol 76: 822. doi.org/10.1007/s00445-014-0822-x

Parmenter CD, Nizamudeen ZA (2021) Cryo-FIB-lift out: practically impossible to practical reality. J Microsc 281(2): 157–174. doi.org/10.1111/jmi.12953

Pleše P (2019) Interactions between gas bubbles and crystals in silicate melts. Université du Québec à Chicoutimi, 284p.

Pleše P, Higgins MD, Baker DR, Kudrna Prašek M (2019a) Nucleation and growth of bubbles on plagioclase crystals during experimental decompression degassing of andesitic melts. J Volcanol Geotherm Res 388: 106679. doi.org/10.1016/j.jvolgeores.2019.106679

Pleše P, Higgins MD, Baker DR, Lanzafame G, Kudrna Prašek M, Mancini L, Rooyakkers SM (2019b) Production and detachment of oxide crystal shells on bubble walls during experimental vesiculation of andesitic magmas. Contrib Mineral Petrol 174: 21. doi.org/10.1007/s00410-019-1556-8

Pleše P, Higgins MD, Mancini L, Lanzafame G, Brun F, Fife JL, Casselman J, Baker DR (2018) Dynamic observations of vesiculation reveal the role of silicate crystals in bubble nucleation and growth in andesitic magmas. Lithos 296–299: 532–546. doi.org/10.1016/j.lithos.2017.11.024

Pyle DM, Pyle DL (1995) Bubble migration and the initiation of volcanic eruptions. J Volcanol Geotherm Res 67: 227–232. doi.org/10.1016/0377-0273(94)00111-S

Reddy SM, Saxey DW, Rickard WDA, Fougerouse D, Montalvo SD, Verberne R, van Riessen A (2020) Atom probe tomography: Development and application to the geosciences. Geostand Geoanal Res 44: 5–50. doi.org/10.1111/ggr.12313

Rigort A, Plitzko JM (2015) Cryo-focused-ion-beam applications in structural biology. Arch Biochem Biophys 581: 122–30. doi.org/10.1016/j.abb.2015.02.009

Rivas NA, Babayigit A, Cornings B, Shwarz T, Sturm A, Manjón AG, Cojocaru-Mirédin O, Gault B, Renner FU (2020) Cryo-focused ion beam preparation of perovskite based solar cells for atom probe tomography. PLoS ONE 15(1): e0227920. doi.org/10.1371/journal.pone.0227920

Roselle GT, Baumgartner LP, Chapman JA (1997) Nucleation-dominated crystallization of forsterite in the Ubehebe peak contact aureole, California. Geol 25: 823–826. doi.org/10.1130/0091-7613(1997)025<0823:NDCOFI>2.3.CO

Rothmann MU, Li W, Zhu Y, Liu A, Ku ZL, Bach U, Etheridge J, Cheng Y-B (2018) Structural and Chemical Changes to $CH_3NH_3PbI_3$ Induced by Electron and Gallium Ion Beams. Adv Mater 30(25): 1800629. doi.org/10.1002/adma.201800629

Russell KC (1971) Nucleation of voids in irradiated metals. Acta Metal 19, 753–758. doi.org/10.1016/0001-6160(71)90131-3

Rust AC, Cashman KV (2011) Permeability controls on expansion and size distributions of pyroclasts. J Geophys Res 116: B11202. doi.org/10.1029/2011jb008494.

Rutherford MJ, Gardner JE (2000) Rates of magma ascent. In: Sigurdsson H (ed.) Encyclopedia of volcanoes. Academic San Diego, California, pp 207–217.

Sable JE, Houghton BF, Wilson CJN, Carey RJ (2006) Complex proximal sedimentation from Plinian plumes: the example of Tarawera 1886. Bull Volcanol 69: 89–103. doi.org/10.1007/s00445-006-0057-6

Schlinger CM, Veblen DR, Rosenbaum JG (1991) Magnetism and magnetic mineralogy of ash flow tuffs from Yucca Mountain, Nevada. J Geophys Res 96: 6035–6052. doi.org/10.1016/0148-9062(92)91184-7

Sharp T, Stevenson R, Dingwell DB (1996) Microlites and “nanolites” in rhyolitic glass: microstructural and chemical characterization. Bull Volcanol 57: 631–640. doi.org/10.1007/s004450050116

Shea T (2017) Bubble nucleation in magmas: A dominantly heterogeneous process?. J Volcanol Geotherm Res 343: 155–170. doi.org/10.1016/j.jvolgeores.2017.06.025

Shea T, Hammer JE, First E (2013) Magma balloons or bombs? Nat Geosci 6: 802–803. doi.org/10.1038/ngeo1971

Siemons W, Beekman C, Fowlkes JD, Balke N, Tischler JZ, Xu R, Liu W, Gonzales CM, Budai JD, Christen HM (2014) Focused-ion-beam induced damage in thin films of complex oxide $BiFeO_3$. Apl Mater 2(2): 1–9. doi.org/10.1063/1.4866051

Skripov VP (1974) Metastable Liquids. John Wiley and Sons.

Sparks RSJ (1978) The dynamics of bubble formation and growth in magmas: A review and analysis. J Volcanol Geotherm Res 3: 1–37. doi.org/10.1016/0377-0273(78)90002-1

Stewart DB, Walker GW, Wright TL, Fahey JJ (1966) Physical properties of calcic labradorite from Lake County, Oregon. Am Mineral: J Earth Planet Mater 51(1-2): 177–197.

Tait S, Jaupart C, Vergniolle S (1989) Pressure, gas content and eruption periodicity of a shallow crystallizing magma chamber. Earth Planet Sci Lett 92: 107–123. doi.org/10.1016/0012-821X(89)90025-3

Toramaru A (1989) Vesiculation process and bubble size distributions in ascending magmas with constant velocities. J Geophys Res 94: 17523–17542. doi.org/10.1029/JB094iB12p17523

Toramaru A (1995) Numerical study of nucleation and growth of bubbles in viscous magmas. J Geophys Res 100: 1913–1931. doi.org/10.1029/94JB02775

Toramaru A (2001) A numerical experiment of crystallization for a binary eutectic system with application to igneous textures. J Geophys Res Solid Earth 106: 4037–4060. doi.org/10.1029/2000JB900367

Toramaru A (2006) BND (bubble number density) decompression rate meter for explosive volcanic eruptions. J Volcanol Geotherm Res 154: 303–316. doi.org/10.1016/j.jvolgeores.2006.03.027

Turnbull D, Fisher JC (1949) Rates of nucleation in condensed systems. J Chem Phys 17: 71–73. doi.org/10.1063/1.1747055

Tuttle OF, Bowen NL (1958) Origin of granite in the light of experimental study in the system NaAlSi3O8-KAlSi3O8-SiO2-H2O. Geol Soc Am Mem 74. doi.org/10.1130/MEM74-p1

Villa E, Schaffer M, Plitzko JM, Baumeister W (2013) Opening windows into the cell: focused-ion-beam milling for cryo-electron tomography. Curr Opin Struct Biol 23: 771–777. doi.org/10.1016/j.sbi.2013.08.006.

Volmer M, Weber A (1926) Germ-formation in oversaturated figures. Zeitschrift für Physicalische Chemie – Stochiometrie und Verwandtschaftslehre 119: 227–301. doi.org/10.1515/zpch-1926-11927

Wang X, Hatzoglou C, Sneed B, Fan Z, Guo W, Jin K, Chen D, Bei H, Wang Y, Weber WJ, Zhang Y, Gault B, More KL, Vurpillot F, Poplawsky JD (2020) Interpreting nanovoids in atom probe tomography data for accurate local compositional measurements. Nat Comm 11:1022. doi.org/10.1038/s41467-020-14832-w

Whittle KR, de los Reyes M, Aughterson RD, Blackford MG, Smith KL, Baldo P, Ryan EP, Zaluzec NJ, Lumpkin GR (2018) In-situ irradiation of $Ca_{1-x}La_{2/3x}TiO_3$ defect perovskites: The role of vacancies in recovery. Mater 3: 186–191. doi.org/10.1016/j.mtla.2018.08.016

Zhou X, Mianroodi JR, Kwiatkowski da Silva A, Koenig T, Thompson GB, Shanthraj P, Ponge D, Gault B, Svendsen B, Raabe D (2021) The hidden structure dependence of the chemical life of dislocations. Sci Adv 7(16). doi.org/10.1126/sciadv.abf0563

CHAPTER 6

Synthesis, conclusions and outlook

My thesis focused on the application and development of high-spatial resolution analytical techniques to investigate nanometer scale processes in geological materials including sulphide minerals and rock melts. This research combined innovative 2D and 3D structural and geochemical mapping methods such as electron channeling contrast imaging (ECCI), electron backscatter diffraction (EBSD) mapping, scanning transmission electron microscopy (STEM) and atom probe tomography (APT) to interrogate the atomic structure and composition of such geomaterials. Although these tools were initially developed for research in materials science, my innovative research presents new applications for understanding long-standing questions in Earth sciences, fundamentally discussing possible implications for rheology, and builds bridges between materials science and geoscience. The topics discussed herein included interrogating the feedbacks between deformation and trace element diffusion processes, more specifically, investigating the influence of deformation and associated nanostructures on the remobilization of trace elements and, in turn, the influence of trace elements on the nucleation and mobility of nanostructures.

Atom probe tomography is a 3D sub-nanometer scale compositional mapping technique with high sensitivity in the range of tens of parts-per-million. The introduction of laser-assisted APT in the late 2000's has enabled the analysis of semi-conducting and insulating materials such as natural minerals, advancing a technique that had previously been restricted to the analysis of conducting materials (Larson et al. 2008, Chen et al. 2009, Marquis et al. 2010, Chen et al. 2011). The 3D tool has since been growing in popularity within the field of geosciences, allowing geoscientists to investigate the local composition of geomaterials at the sub-nanometer scale in order to better understand mechanisms of growth, trace element mobility and chemical reactions, and gain insight into larger tectonic-scale geological processes. The majority of studies that have used APT to study geological materials have focused on minerals with applications for geochronology, petrology, planetary science and economic geology. Although a large portion of the published work using APT on geological materials falls within the four aforementioned disciplines, this thesis presented new interdisciplinary, innovative, and provocative applications and developments to the technique.

In an attempt to better understand the underlying diffusion processes that mobilize trace elements during crystal-plastic deformation, ECCI, EBSD and APT were combined on naturally deformed pyrite from the Detour Lake gold deposit located in the Archean Abitibi Subprovince, Canada (Dubosq et al. 2019). The combined results reveal deformation-induced micro- and nanostructures in the form of dislocations, stacking faults and low-angle grain boundaries that are enriched in As and Co. Composition profiles across the dislocations exhibiting As-depleted 'capture zones' on one side best support a dislocation-impurity-pair (DIP) diffusion model (Cottrell and Bilby 1949; Petukhov and Klyuchnik 2012) in which deformation-induced dislocations attract impurities (i.e., As) within their cores due to their strain field during glide and creep processes, leading to their concentration in low-angle grain boundaries. This study is the first to document direct evidence for DIP diffusion in the context of metallic ore paragenesis and challenges current models of trace element remobilization.

Prevailing models of metallic ore paragenesis suggest that metamorphism and crystal-plastic deformation of sulphides causes the liberation, remobilization and subsequent concentration of these trace elements into viable economic deposits (Craig and Vokes 1993; Tomkins and Mavrogenes 2001; Large et al. 2007). For instance, a recent study on arsenopyrite demonstrated that crystal-plastic deformation creates microstructures in the form of low-angle grain boundaries that act as conduits for fluids leading to leaching of lattice-bound Au from the host mineral and resulting in discrete, intra-crystalline Au-depleted zones within the host mineral

(Fougerouse et al. 2016). In one of my previous investigations (Dubosq et al. 2018), which led to this thesis research, a comparable investigation of pyrite revealed contrasting results and demonstrated that low-angle grain boundaries induced by crystal-plastic deformation can instead act as traps for base- and precious-metals, challenging the widely accepted models. These results showed a clear spatial relationship between deformation-induced microstructures and trace elements, however, the specific geochemical and mechanical processes that led to the concentration of trace elements into the micro- to nanostructures remained elusive until now. Additionally, it is well known that sulphide minerals including pyrite can incorporate significant concentrations of base- and precious-metals such as Au, Ag, Bi, and Te as lattice-bound and/or ultrafine inclusions (Cook and Chryssoulis 1990; Reich et al. 2005). Dubosq et al. (2019) is the first to suggest a new type of metal occurrence hosted within nanostructures. The results also led to proposing a new exsolution model for lattice-bound Au where As segregation into nanostructures leads to As-depletion in the crystal, therefore reducing the solubility of Au.

To further investigate deformation-induced trace element segregation including the role of fluids during deformation-related trace element mobility, EBSD, ECCI, STEM and APT were performed on a naturally deformed pyrite aggregate with nanoscale fluid inclusions from the Kidd-Munro Assemblage in the Archean Abitibi Subprovince, Canada (Dubosq et al 2021). The combined results revealed nanoscale fluid inclusions enriched in As, O, Na and K that are linked to bowed As-rich dislocations. The link between As-rich dislocations and fluid inclusions in addition to the bowed configuration of the dislocations visible in both STEM and APT data suggest that the dislocations were pinned by the stress field of the fluid inclusions. The elevated As compositions within the dislocation cores that are linked to As-rich fluid inclusions suggests that the As diffused from the fluid inclusions into the dislocation cores by pipe diffusion, which was driven by the chemical potential gradient created between the trace element-rich fluid inclusions and the trace element-poor dislocation and matrix (Dubosq et al 2021). This model differs from the diffusion mechanism documented in the previous study where instead, the As was found to have diffused into the nanostructures via dislocation-impurity pair diffusion (Dubosq et al 2019). Strain hardening can occur from the pinning of dislocations by the strain fields of immobile defects and from the accumulation of mobile solutes in dislocation cores (Cahn 2014; Chen et al. 2008; Cottrell and Bilby 1949; Vityk et al. 2000). When the latter occurs, dislocations can be unpinned and move at high velocities as stress increases and reaches a critical value. This discontinuous motion of dislocations is known as the Portevin–Le Chatelier effect (Portevin and Le Chatelier 1923) and can lead to further hardening of the material and brittle fracturing (Mohles et al. 1999). The integrated data documented both processes and led to proposing a new fluid inclusion-hardening model based on the pinning of dislocations at fluid inclusions and their subsequent stabilization by pipe diffusion of trace elements from the inclusions into the dislocation cores (Dubosq et al. 2021; Figure 6.1). Until now, it has been widely accepted that fluids typically have a weakening or softening effect on minerals–for example the compression and subsequent expansion of fluid inclusions under increasing temperature resulting in the nucleation of dislocation loops and mechanical softening (Bakker and Jansen 1994; McLaren et al. 1983). The results of this work documented a process that contradicts the more common result that an increase in fluid content leads to rheological softening and instead suggests that fluids can lead to strain hardening. Despite proposing a new fluid-inclusion induced hardening model, the dominantly brittle behaviour of the investigated pyrite sample is consistent with its estimated peak temperatures. Therefore, the data does not reveal evidence of hardening within the sample, but rather documents two processes that immobilize dislocations and when combined could lead to

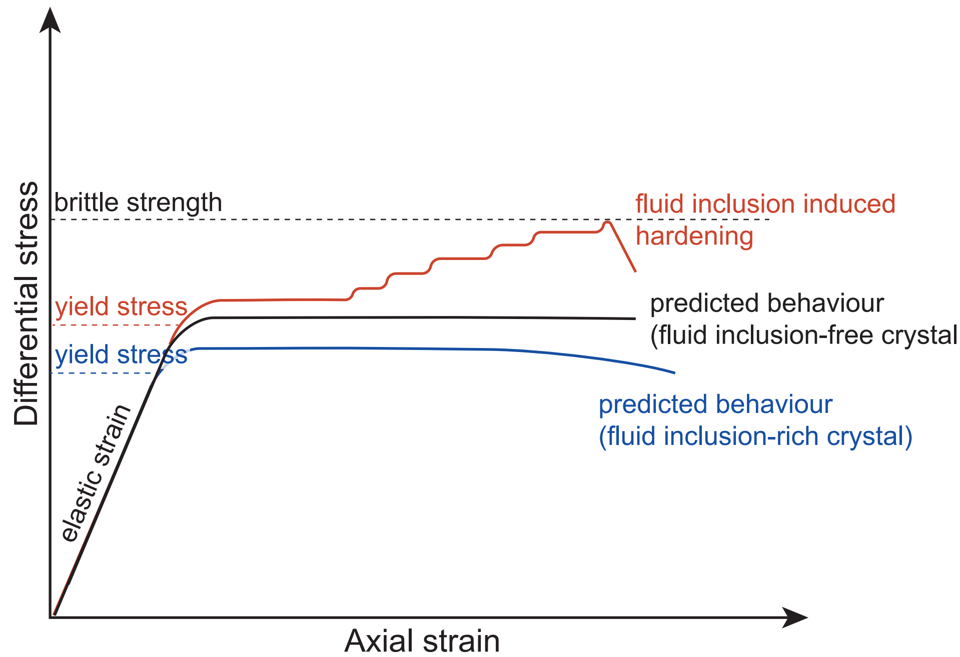

Figure 6.1. Idealised stress-strain curve based on proposed fluid inclusion induced hardening model compared to the predicted stress-strain curves based on prevailing fluid softening and weakening models.

strain hardening. Hence, a complementary experimental study comparing the rheology between fluid inclusion-rich and fluid inclusion-free crystals could help test this new fluid-hardening model.

On another note, although Dubosq et al (2019) and (2021) successfully documented two different diffusion mechanisms for trace element mobility in pyrite i.e., DIP diffusion (Dubosq et al. 2019) and pipe diffusion (Dubosq et al. 2021), the specific P-T conditions under which one mechanism dominates over the other remain elusive. This knowledge gap could be closed by conducting an investigation in which different pyrite crystals, or other sulphide minerals, doped with trace elements are experimentally deformed under varying P-T conditions. The same combination of 2D and 3D nanostructural and geochemical analyses could be applied to the experimental samples in order to identify the dominant diffusion mechanisms in each sample and determine the range of P-T conditions under which each mechanism can occur during deformation.

In addition to proposing a new fluid inclusion-induced hardening model, the thesis is the first to combine APT experiments and field evaporation simulations on pyrite in an attempt to document trace element segregation associated with nanovoids (i.e., fluid inclusions; Dubosq et al. 2020). The combined data documented the first direct evidence of nanoscale fluid inclusions in geomaterials as high point-density core-shell particles. Ion trajectory aberrations associated with nanovoids had been recently discovered in materials sciences (Perrin-Pellegrino 2020; Wang 2020), but the complex atomic displacements around nanovoids and their limiting effect on the accuracy of APT data reconstructions, more specifically when voids are filled with fluids, continued to be poorly understood. With these results, we now have developed a systematic methodology to identify and interpret nanovoids and fluid inclusions in APT data, which have often been misinterpreted as atom clusters or precipitates. The characterization of fluid inclusions has significant implications for understanding the growth of minerals and inclusion of impurities in minerals; providing information about the temperature, pressure and composition of ore forming fluids; and understanding how the presence of such crystalline features can affect the physical properties of geomaterials.

The successful documentation of nanovoids in APT reconstructions inspired the last part of the thesis, which aimed at investigating the influence of nanoscale chemical heterogeneities on the nucleation of structural defects (i.e., gas bubbles) in amorphous rock melts (Dubosq et al. in prep). Investigating the initial stages of bubble nucleation processes can give insight into the rheology of magmas and therefore help to better understand the ductile (effusive) versus brittle (explosive) behaviour of volcanic eruptions. More specifically, the study combined STEM and APT on an experimental intermediate rock melt to test a hypothesis that suggests homogeneous bubble nucleation (within a melt) is simply a variety of heterogeneous bubble nucleation (on a surface) whereby nucleation occurs on the surface of submicroscopic crystals (Gardner and Denis 2004; Hurwitz and Navon 1994). Recent studies have shown that the presence of such crystals in a melt correlates to higher bubble number densities in experiments (Cáceres et al. 2020), however, direct evidence of bubble nucleation on these submicroscopic crystals remained equivocal. The new data presented in this thesis reveals chemical heterogeneities in the form of Fe-, Na-, and/or Ca-rich atom clusters at the bubble-melt interface of the newly created bubbles as well as within the initial melt, therefore supporting the hypothesis that homogeneous nucleation could in fact be a variety of heterogeneous nucleation that occurs at the surface of sub-microscopic crystals or atom clusters and highlighting the need to redefine homogeneous nucleation. These results have significant implications for eruption parameter estimates and the plausibility of homogeneous nucleation in natural systems. In addition, this work demonstrated the potential of cryo-approaches for TEM and APT for the analysis of sensitive geomaterials, including natural silicate glasses in the context of atom cluster characterization in the early stage of bubble nucleation.

While there has been significant progress for developing cryogenic TEM and APT techniques, current approaches are limited and site-specific liftout preparation techniques remain challenging. Thus, further technique development is needed for the site-specific fabrication of APT specimens from sensitive geomaterials. In addition, since TEM is very effective at acquiring qualitative and quantitative information about the characteristics and APT has the ability to provide 3D quantitative compositional measurements and spatial imaging of materials at the near-atomic scale. A correlative approach combining these two techniques on the same specimen would be ideal for documenting the interaction between trace elements, fluids and defects. However, challenges that arise by conducting TEM imaging before APT analysis, such as carbon contamination, absorption of gaseous species, and formation of oxide layers, can cause embrittlement of the specimen and a reduction of the yield during APT analysis (Herbig et al. 2015). These challenges could also be mitigated by further developing cryogenic specimen preparation and transfer approaches.

In summary, the research in this thesis has explored the many interactions between trace elements, fluids and structural defects in geomaterials. Although the links between deformation-induced micro- and nanostructures and trace element mobility in minerals has been well documented in the Earth sciences, the physico-chemical processes that concentrate trace elements in deformation-induced nanostructures is poorly understood. Investigating these processes had been previously limited by the lack of micro-analytical tools with adequate high-spatial resolution. With the development of novel 3D nanostructural and nanochemical analytical techniques in the materials sciences, such as STEM and APT, these tools can now be applied to geomaterials for identifying the specific mechanisms responsible for the nanoscale chemical heterogeneities. My thesis has successfully found new applications for these innovative tools in the geosciences as well as developed new data processing techniques in an attempt to address the aforementioned knowledge gaps. By applying innovative techniques, these studies succeeded in identifying two diffusion mechanisms by which trace elements are remobilized in pyrite during crystal-plastic deformation: (1) dislocation-impurity-pair (Dubosq et al 2019) and (2) high-diffusivity pathway diffusion (Dubosq et al. 2021). The innovative approaches also led to documenting the first direct evidence of nanovoids (nanoscale fluid inclusions) in geomaterials as high point-density features in both experimental and simulated 3D APT specimen reconstructions. This discovery allowed for the documentation of two processes that, when combined, led to proposing a new model where fluids can have a hardening effect on minerals rather than the more commonly reported weakening effect. The successful documentation of nanovoids in APT data led to investigating initial bubble nucleation processes in rock melts and to verifying nanoscale chemical heterogeneities at bubble-melt interfaces, suggesting that homogeneous bubble nucleation could simply be a variation of heterogeneous nucleation.

References

Bakker RJ, Jansen JBH (1994) A mechanism for preferential H_2O leakage from fluid inclusions in quartz, based on TEM observations. Contrib Mineral Petrol 116: 7–20. doi.org/10.1007/BF00310686

Cáceres F, Wadsworth FB, Scheu B, Colombier M, Madonna C, Cimarelli C, Hess KU, Kaliwoda M, Ruthensteiner B, Dingwell DB (2020) Can nanolites enhance eruption explosivity? Geol 48: 997–1001. doi.org/10.1130/G47317.1

Cahn JW (2014) Reprise: partial chemical strain dislocations and their role in pinning dislocations to their atmospheres. Philos Mag 94(27): 3170–3176. doi.org/10.1080/14786435.2014.951711

Chen Q, Liu X-Y, Biner SB (2008) Solute and dislocation junction interactions. Acta Mater 56: 2937–2947. doi.org/10.1016/j.actam at.2008.02.026

Chen YM, Ohkubo T, Kodzuka M, Morita K, Hono K (2009) Laser-assisted atom probe analysis of zirconia/spinel nanocomposite ceramics. Scr Mater 61: 693–696. doi.org/10.1016/j.scriptamat.2009.05.043

Chen YM, Ohkubo T, Hono K (2011) Laser assisted field evaporation of oxides in atom probe analysis. Ultramic 111: 562–566. doi.org/10.1016/j.ultramic.2010.12.013

Cook NJ, Chryssoulis SL (1990) Concentrations of invisible gold in the common sulphides. Can Mineral 28: 1–16.

Cottrell AH, Bilby BA (1949) Dislocation theory of yielding and strain ageing of iron. Proc Phys Soc A 62: 49–62. doi.org/10.1088/0370-1298/62/1/308

Craig JR, Vokes FM (1993) The metamorphism of pyrite and pyritic ores: An overview. Mineral Mag 57: 3–18. doi.org/10.1180/minmag.1993.057.386.02

Dubosq R, Gault B, Hatzoglou C, Schweinar K, Vurpillot F, Rogowitz A, Rantitsch G, Schneider DA (2020) Analysis of nanoscale fluid inclusions in geomaterials by atom probe tomography: experiments and numerical simulations. Ultramic 218: 1–10. doi.org/10.1016/j.ultramic.2020.113092

Dubosq R, Lawley CJM, Rogowitz A, Schneider DA, Jackson S (2018) Pyrite deformation and connections to gold mobility: Insight from micro-structural analysis and trace element mapping. Lithos 310–311: 86–104. doi.org/10.1016/j.lithos.2018.03.024

Dubosq R, Rogowitz A, Schneider DA, Schweinar K, Gault B (2021) Fluid inclusion induced hardening: Nanoscale evidence from naturally deformed pyrite. Contrib Mineral Petrol 176: 1–14. doi.org/10.1007/s00410-021-01774-9.

Dubosq R, Rogowitz A, Schweinar K, Gault B, Schneider DA (2019) A 2D and 3D nanostructural study of naturally deformed pyrite: Assessing the links between trace element mobility and defect structures. Contrib Mineral Petrol 174(72): 1–16. doi.org/10.1007/s00410-019-1611-5

Fougerouse D, Micklethwaite S, Halfpenny A, Reddy SM, Cliff JB, Martin LAJ, Kilburn M, Guagliardo P, Ulrich S (2016) The golden ark: Arsenopyrite crystal plasticity and the retention of gold through high strain and metamorphism. Terra Nova 28: 181–187. doi.org/10.1111/ter.12206

Gardner JE, Denis MH (2004) Heterogeneous bubble nucleation on Fe-Ti oxide crystals in high-silica rhyolitic melts. Geochim Cosmochim Acta 68(7): 3587–3597. doi.org/10.1016/j.gca.2004.02.021

Herbig M, Choi P, Raabe D (2015) Combining structural and chemical information at the nanometer scale by correlative transmission electron microscopy and atom probe tomography. Ultramic 153: 32–39. doi.org/10.1016/j.ultramic.2015.02.003

Hurwitz S, Navon O (1994) Bubble nucleation in rhyolitic melts: Experiments at high pressure, temperature, and water content. Earth Planet Sci Lett 122(3–4): 267–280. doi.org/10.1016/0012-821X(94)90001-9

Large RR, Maslennikov VV, Robert F, Danyushevsky LV, Chang Z (2007) Multistage sedimentary and metamorphic origin of pyrite and gold in the Giant Sukhoi log deposit, Lena Gold Province, Russia. Econ Geol 102: 1233–1267. doi.org/10.2113/gsecongeo.102.7.1233

Larson DJ, Alvis RL, Lawrence DF, Prosa TJ, Ulfig RM, Reinhard DA, Clifton PH, Gerstl S, Bunton JH, Lenz DR, Kelly T, Stiller K (2008) Analysis of bulk dielectrics with atom probe tomography. Microsc Microanal 14: 1254–1255. doi.org/10.1017/S1431927608083657

Marquis EA, Yahya NA, Larson DJ, Miller MK, Todd RI (2010) Probing the improbable: Imaging C atoms in alumina. Mater Today 13: 34–36. doi.org/10.1016/S1369-7021(10)70184-X

McLaren AC, Cook RF, Hyde ST, Tobin RC (1983) The mechanisms of the formation and growth of water bubbles and associated dislocation loops in synthetic quartz. Phys Chem Miner 9: 79–94. doi.org/10.1007/BF003 08151

Mohles V, Rönnpagel D, Nembach E (1999) Simulation of dislocation glide in precipitation hardened materials. Comput Mater Sci 16(1–4): 144–150. doi.org/10.1016/S0927-0256(99)00056-7

Perrin-Pellegrino C, Dumont M, Keita MF, Neisius T, Mikaelian G, Mangelink D, Carlot D, Maugis P (2020) Characterization by APT and TEM of Xe nano-bubbles in CeO_2. Nucl Instrum Methods Phys Res B 469: 24–27. doi.org/10.1016/j.nimb.2020.02.032

Petukhov BV, Klyuchnik PA (2012) Dynamic interaction of dislocations with impurity subsystem in crystalline materials. Crystallogr Rep 57: 388–392. doi.org/10.1134/S106377451 2030169

Portevin A, Le Chatelier F (1923) Sur un phénomène observation lors de l’essai de traction d’alliages en cours de transformation. C R Acad Sci Paris 176: 507–510.

Reich M, Kesler S, Utsunomiya S, Palenik C, Chryssoulis S, Ewing R (2005) Solubility of gold in arsenian pyrite. Geochim Cosmochim Acta 69(11): 2781–2796. doi.org/10.1016/j.gca.2005.01.011

Tomkins AG, Mavrogenes JA (2001) Redistribution of gold within arsenopyrite and löllingite during pro- and retrograde metamorphism: application to timing of mineralization. Econ Geol 96: 525–534. doi.org/10.2113/gseco ngeo.96.3.525

Vityk MO, Bodnar RJ, Doukhan JC (2000) Synthetic fluid inclusions. XV. TEM investigation of plastic flow associated with re-equilibration of fluid inclusions in natural quartz. Contrib Min Petrol 139: 285–297. doi.org/10.1007/s0041 00000 142

Wang L, Putnis CV (2020) Dissolution and precipitation dynamics at environmental mineral interfaces imaged by in situ atomic force microscopy. Acc Chem Res 53: 1196–1205. doi.org/10.1021/acs.accounts.0c00128

APPENDIX A–Supplementary information for chapter 2

A 2D and 3D Nanostructural Study of Naturally Deformed Pyrite: Assessing the Links Between Trace Element Mobility and Defect Structures

R. Dubosq[1], A. Rogowitz[2], K. Schweinar[3], B. Gault[3,4], D.A. Schneider[1]

[1]Department of Earth and Environmental Sciences, University of Ottawa, Ottawa, Canada

[2]Department of Geology, University of Vienna, Vienna, Austria

[3]Max-Planck-Institut für Eisenforschung GmbH, Düsseldorf, Germany

[4]Department of Materials, Royal School of Mines, Imperial College London, London, UK

Table S2.1. Atom Probe Tomography Data Acquisition Settings and Data Summary

Specimen/Data Set	Specimen i	Specimen ii	Specimen iii
Instrument Model	LEAP 5000 XS	LEAP 5000 XR	LEAP 5000 XS
Instrument settings			
Laser wavelength (nm)	355	355	355
Laser pulse energy (pJ)	45	45	45
Voltage pulse fraction (%)	n.a.	n.a.	n.a.
Pulse frequency (kHz)	200	125	125
Evaporation control	detection rate	detection rate	detection rate
Target detection rate (ions/pulse)	0.01	0.01	0.01
Nominal flight path (mm)	100	382	100
Set point temperature (K)	55	55	55
Chamber pressure (Torr)	2.30E-11	4.10E-11	2.90E-11
Data summary			
LAS root version	15.43.393	15.43.393	15.43.393
CAMECAROOT version	18.46.428	18.46.428	18.46.428
Analysis software	IVAS 3.8.2	IVAS 3.8.2	IVAS 3.8.2
Total ions:	89999837	37555819	29064356
Single (%)	40	52	38.4
Multiple (%)	59.3	47.4	60.8
Partial (%)	0.8	0.7	0.8
Reconstructed ions:			
Ranged (%)	83.42	96.83	51.19
Unranged (%)	16.58	3.17	48.81
Volt./bowl corr. peak (Da)	32	32	32
Mass calib. (peaks/interp.)	5/Lin.	5/Lin.	5/Lin.
($M/\Delta M$) for ^{56}Fe	415	1255	352
($M/\Delta M_{10}$)	79	313	65
Time-independent background (ppm/ns)	3.3	3.3	2.8
Reconstruction			
Final specimen state	intact	fractured	intact
Pre-/post-analysis imaging	SEM/n.a	SEM/n.a	SEM/n.a
Radius evolution model	voltage	voltage	voltage
Field factor (k)	2	3.3	3.3
Image compression factor	1.74	1.5	1.71
Assumed E-field (V/nm)	33	30	30
Detector efficiency (%)	80	52	80
Avg. atomic volume (nm^3)	species specific volume used (see range file)		
Vinitial; Vfinal (V)	2627; 7834	1306; 8170	1170; 6255

Table S2.2. Bulk compositions of APT specimens

		Fe	Co	Se	S	O	H	As	Total
Specimen i									
	counts	4.85E+07	281849	13867	7.41E+07	152100	20895	35664	1.23E+08
	%	39.40	0.23	0.01	60.19	0.12	0.02	0.03	
Matrix									
	%	40.71	0.21	0.01	58.94	0.08	0.01	0.03	
Specimen ii									
	counts	2.09E+07	64151	123395	3.79E+07	3602	33225	24778	5.91E+07
	%	35.41	0.11	0.21	64.17	0.01	0.06	0.04	
Matrix									
	%	30.90	0.06	0.00	68.90	0.06	0.04	0.04	
Specimen iii									
	counts	1.49E+07	225837	3020	2.56E+07	11934	43114	12689	4.09E+07
	%	36.58	0.55	0.01	62.70	0.03	0.11	0.03	

*Matrix compositions are calculated from a large ROI in between decorated microstructures

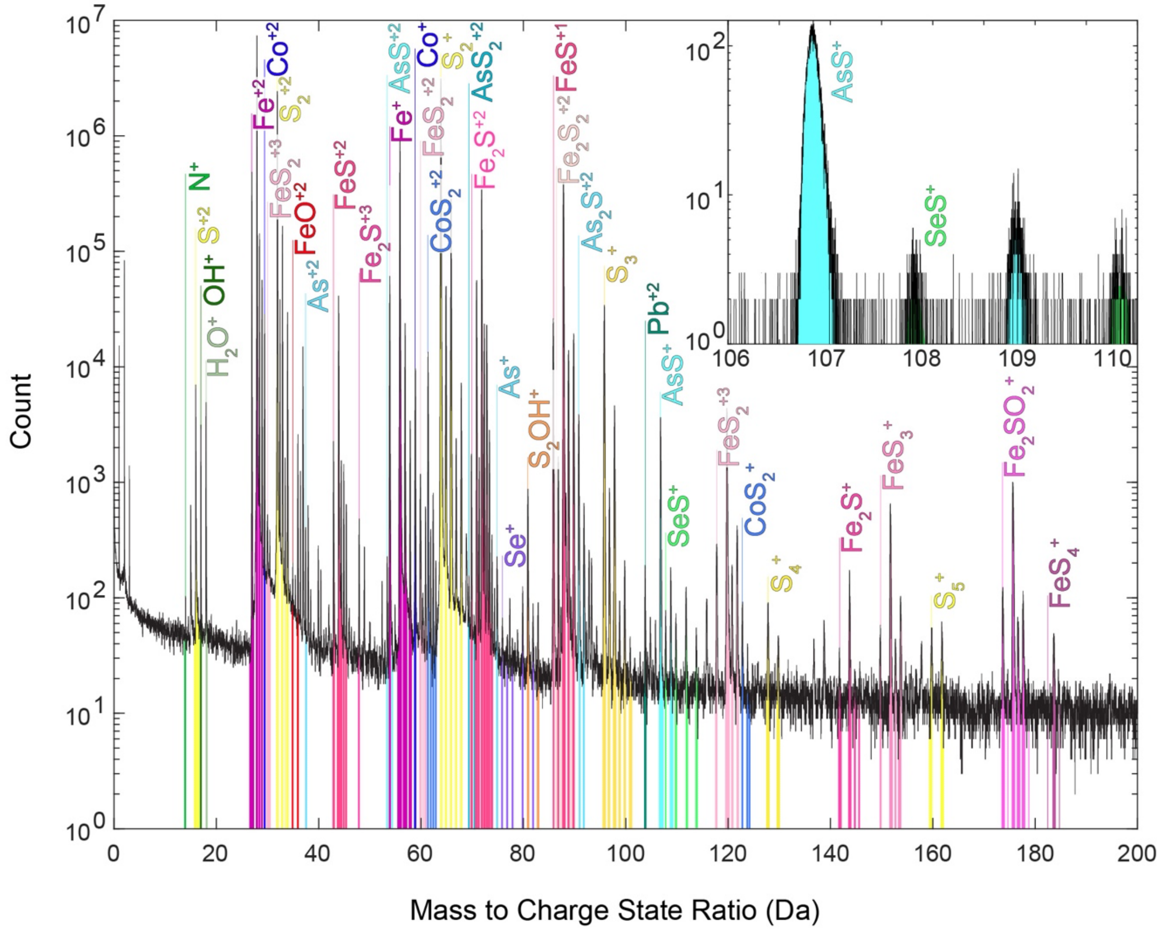

Figure S2.1. Atom probe mass spectrum of pyrite. Representative atom probe microscopy mass spectrum.

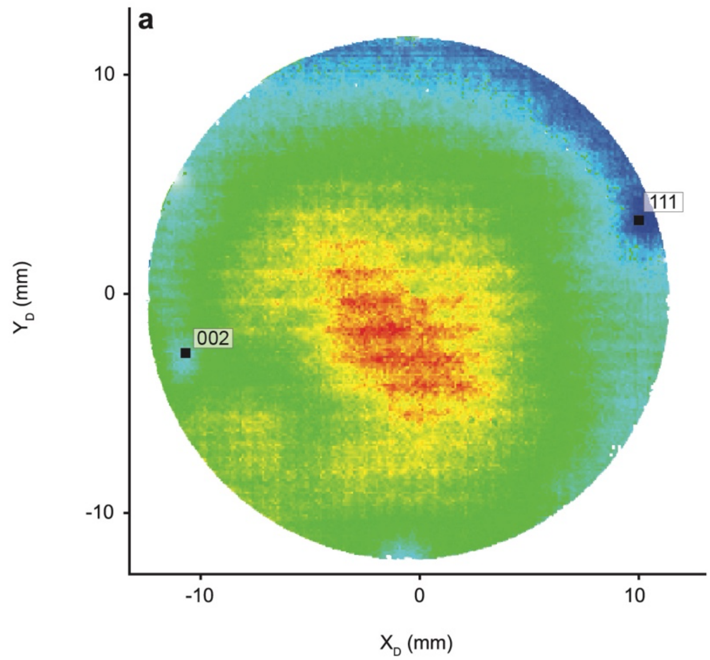

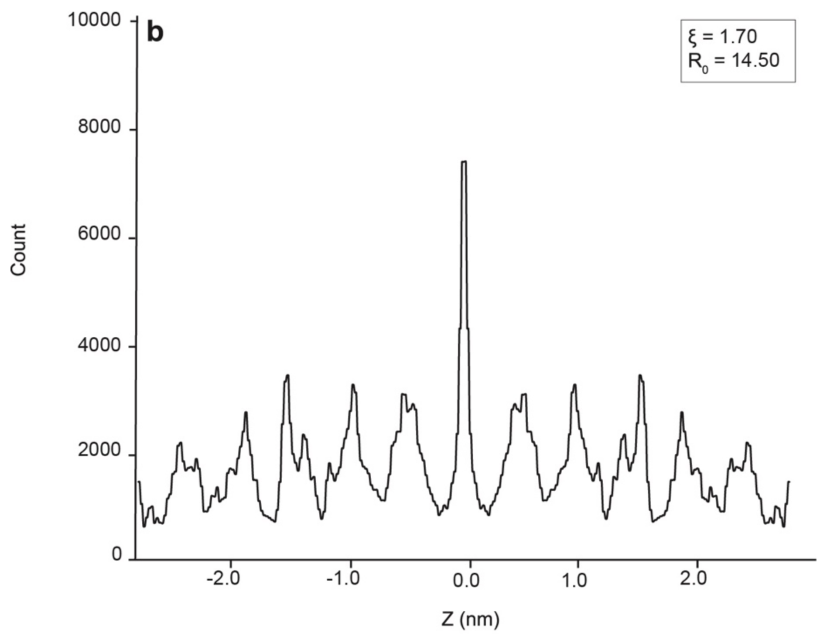

Figure S2.2. a. Detector event histogram of specimen 'i' showing the positioning of poles 111 and 002 (warmer colors represent elevated number of hits). b. Spatial distribution map of specimen 'ii' along the 111 pole showing an interplanar spacing of ~0.54 nm.

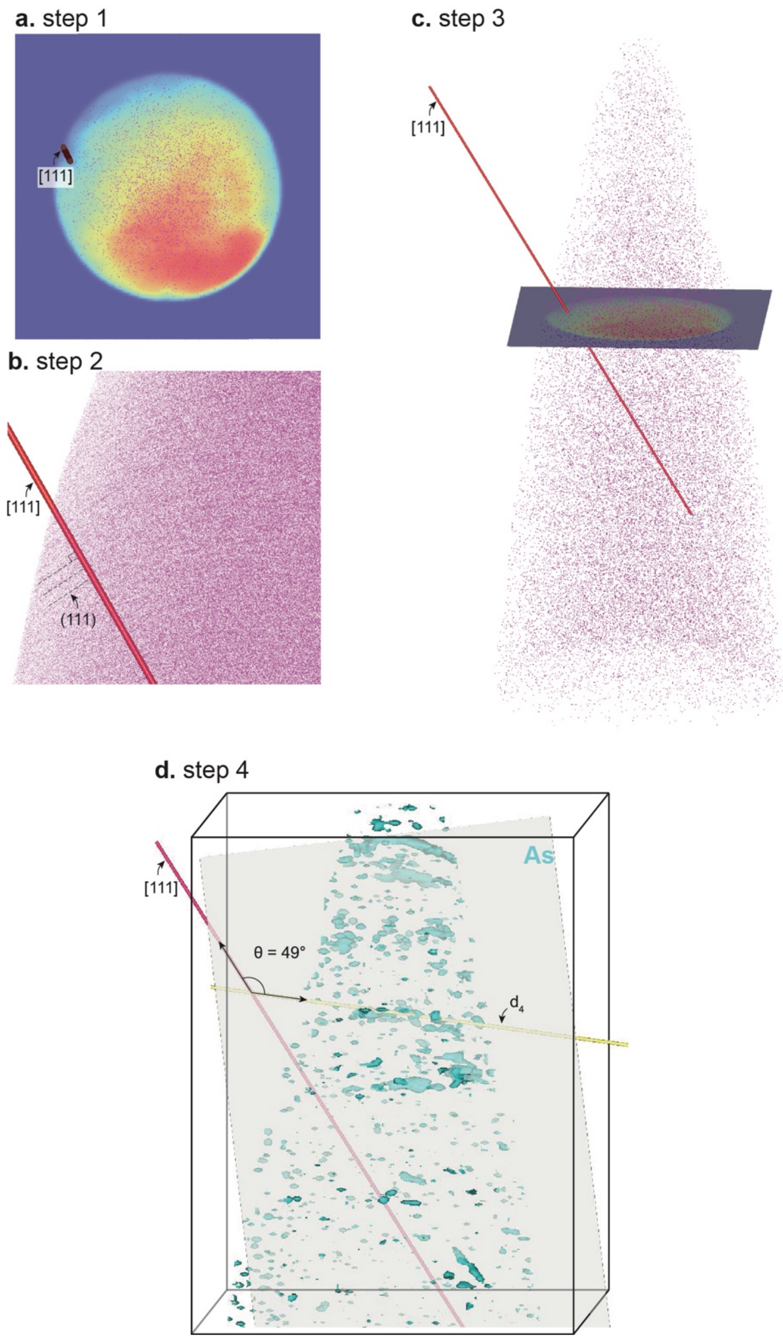

Figure S2.3. Upper section of specimen 'i' reconstruction showing As isosufaces and dislocation 4 (d4; yellow cylinder) at a 49° angle to pole 111 (red cylinder). The 111 pole was inserted manually by using the detector event histogram and the crystal-lattice planes. The yellow cylinder was also put in manually paralleling the dislocation to facilitate the measurement of its angle relative to the 111 pole. The grey plane is a surface, which parallels the 111 pole and the dislocation to ensure the angle is measured correctly.

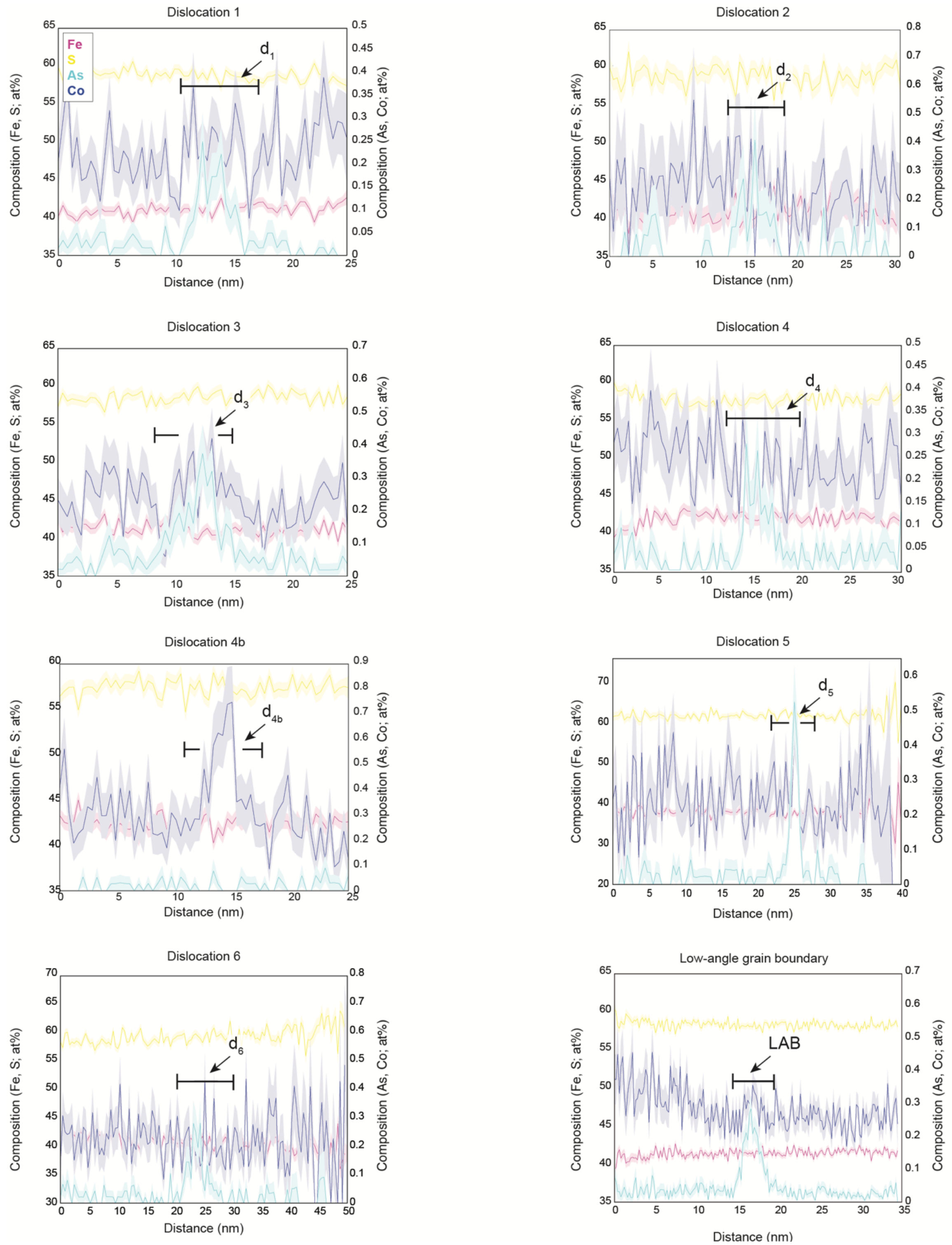

Figure S2.4. Composition profiles across all dislocations and subgrain boundary observed in specimen 'i' showing Fe (pink), S (yellow), As (turquoise), and Co (blue) compositions.

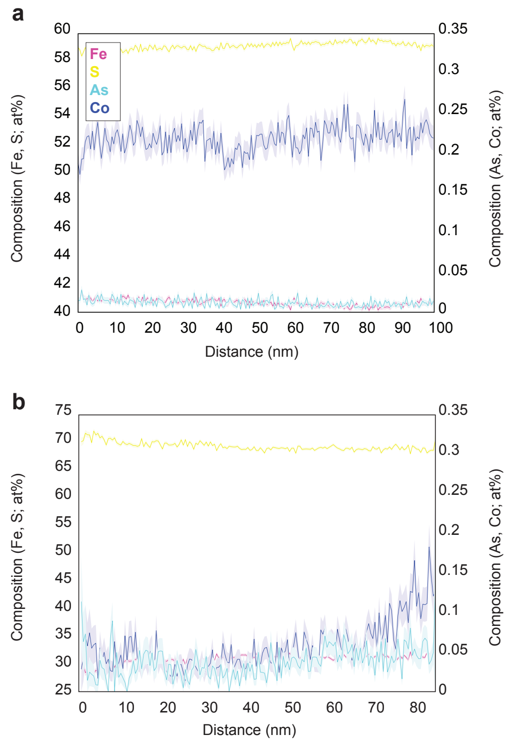

Figure S2.5. Composition profiles across the matrix of **a.** specimen ‘i’ and **b.** specimen ‘ii’ between nanostructures showing Fe (pink), S (yellow), As (turquoise), and Co (blue) compositions.

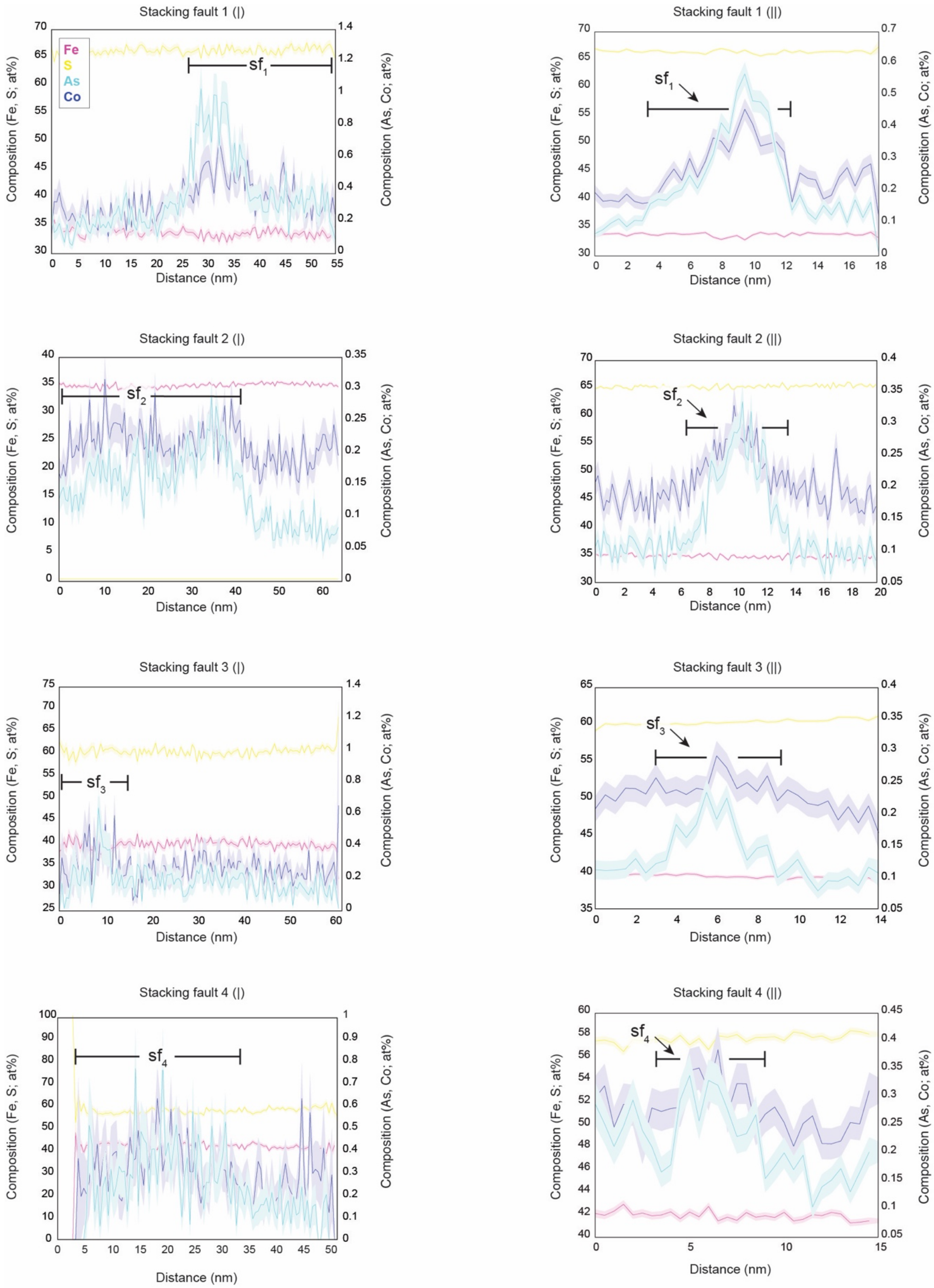
Stacking fault 1 (|)
Stacking fault 1 (||)
Stacking fault 2 (|)
Stacking fault 2 (||)
Stacking fault 3 (|)
Stacking fault 3 (||)
Stacking fault 4 (|)
Stacking fault 4 (||)
Fe
S
As
Co
sf1
sf2
sf3
sf4
Composition (Fe, S; at%)
Composition (As, Co; at%)
Distance (nm)

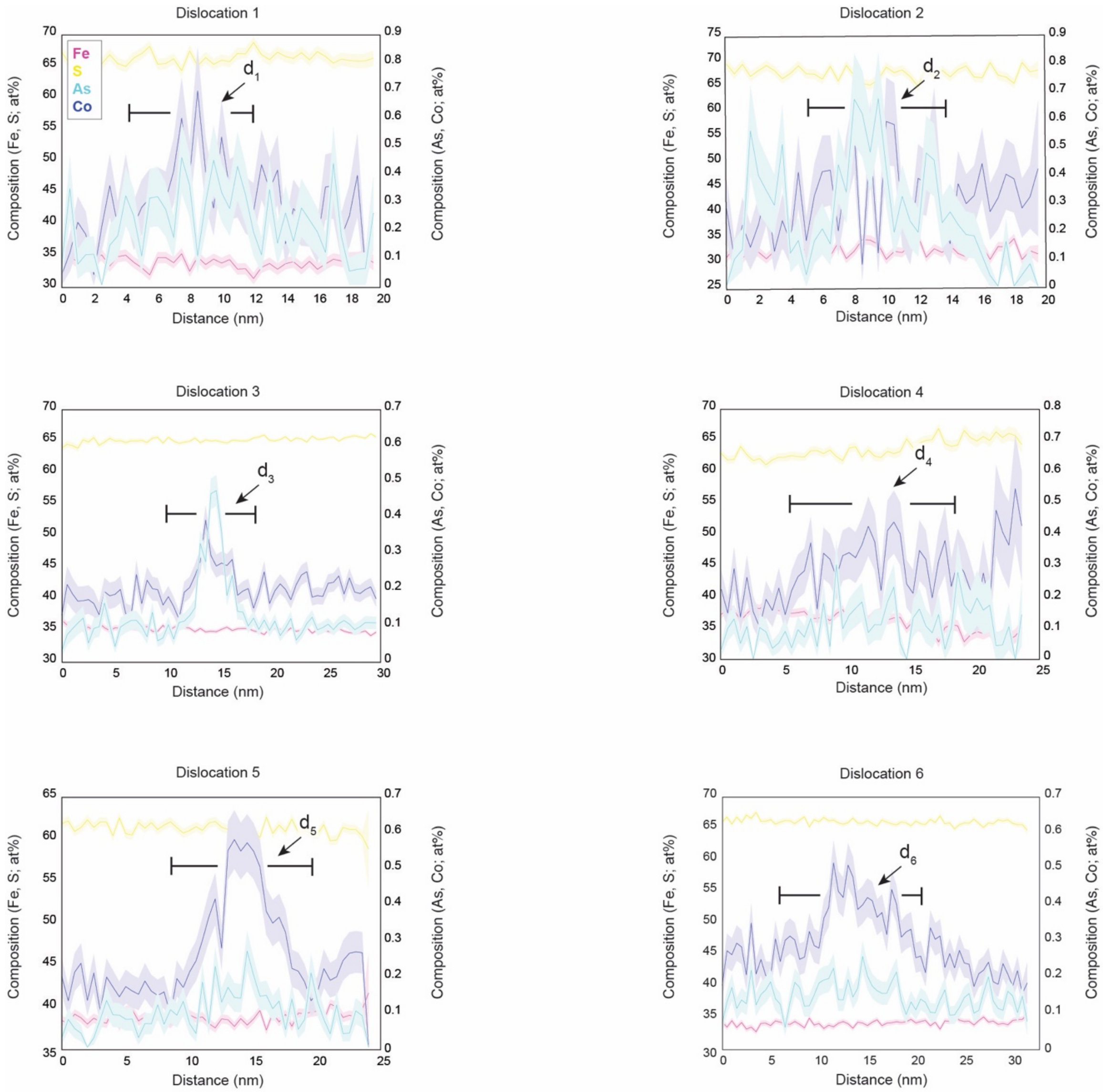

Figure S2.6. Composition profiles along (||) and across (|) all stacking faults and dislocations observed in specimen 'ii' showing Fe (pink), S (yellow), As (turquoise), and Co (blue) compositions.

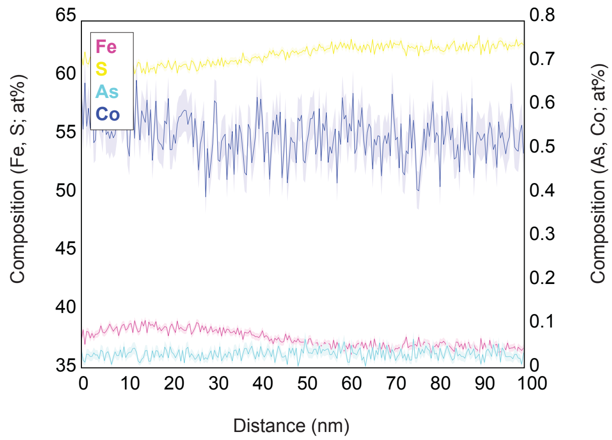

Figure S2.7. Composition profiles across the matrix of specimen ‘iii’ showing Fe (pink), S (yellow), As (turquoise), and Co (blue) compositions.

APPENDIX B–Supplementary information for chapter 3

Analysis of nanoscale fluid inclusions in geomaterials by atom probe tomography: experiments and numerical simulations

R. Dubosq[1], B. Gault[2,3], C. Hatzoglou[4], K. Schweinar[2], F. Vurpillot[4], A. Rogowitz[5], G. Rantitsch[6], D.A. Schneider[1]

[1]Department of Earth and Environmental Sciences, University of Ottawa, Ottawa, Canada

[2]Max-Planck-Institut für Eisenforschung GmbH, Düsseldorf, Germany

[3]Department of Materials, Royal School of Mines, Imperial College London, London, UK

[4]Normandie Université, UNIROUEN, INSA Rouen, CNRS, Groupe de Physique des Matériaux, 76000 Rouen, France.

[5]Department of Geology, University of Vienna, Vienna, Austria

[6]Department of Geology and Economic Geology, University of Leoben, Leoben, Austria

Table S3.1. Raman parameter according to Lünsdorf et al. (2017)

Sample	sample type	N	D_STA	std	G_STA	std	G_shape_factor	std	Dmax_pos	std	Gmax_pos	std	Dmax/Gmax-ratio	std	Temp (°C)	+/-
4084.00	powder	20.00	130.02	8.03	166.42	5.22	2.05	0.06	1334.30	2.24	1587.52	2.65	1.28	0.06	302.00	27.00

Table S3.2. Atom Probe Tomography Data Acquisition Settings and Data Summary

Instrument Model	**LEAP 5000 XR**
Instrument settings	
Laser wavelength (nm)	355
Laser pulse energy (pJ)	45
Voltage pulse fraction (%)	n.a.
Pulse frequency (kHz)	125
Evaporation control	detection rate
Target detection rate (ions/pulse)	0.005
Nominal flight path (mm)	382
Set point temperature (K)	55
Chamber pressure (Torr)	4.30E-11
Data summary	
LAS root version	15.43.393
CAMECAROOT version	18.46.428
Analysis software	IVAS 3.8.2
Total ions:	25017160
Single (%)	60.6
Multiple (%)	37.2
Partial (%)	2.2
Reconstructed ions:	
Ranged (%)	98.8
Unranged (%)	1.2
Volt./bowl corr. peak (Da)	56
Mass calib. (peaks/interp.)	5/Lin.
$(M/\Delta M)$ for ^{56}Fe	1117.4
$(M/\Delta M_{10})$	280.8
Time-independent background (ppm/ns)	2.1
Reconstruction	
Final specimen state	fractured
Pre-/post-analysis imaging	SEM/n.a
Radius evolution model	voltage
Field factor (k)	3.3
Image compression factor	1.54
Assumed E-field (V/nm)	33
Detector efficiency (%)	52
Avg. atomic volume (nm^3)	species specific volume used (see range file)
Vinitial; Vfinal (V)	2660; 5724

Table S3.3. Decomposed atomic bulk composition of APT specimen

Ion Type	Decomposed Count	Decomposed Fraction (%)	Decomposed Fraction (sigma)
Fe	15918325.17	40.18%	1.19E-04
As	61293.86	0.15%	6.25E-06
Co	2356.6	0.01%	1.23E-06
S	23602954.79	59.58%	1.55E-04
Cu	593.75	0.00%	6.15E-07
Te	734.2	0.00%	6.84E-07
Ni	273.24	0.00%	4.17E-07
Zn	5943.9	0.02%	1.95E-06
Cr	83.72	0.00%	2.31E-07
C	1829.05	0.00%	1.08E-06
H	6403.46	0.02%	2.02E-06
O	16221.47	0.04%	3.22E-06
K	342.17	0.00%	4.67E-07

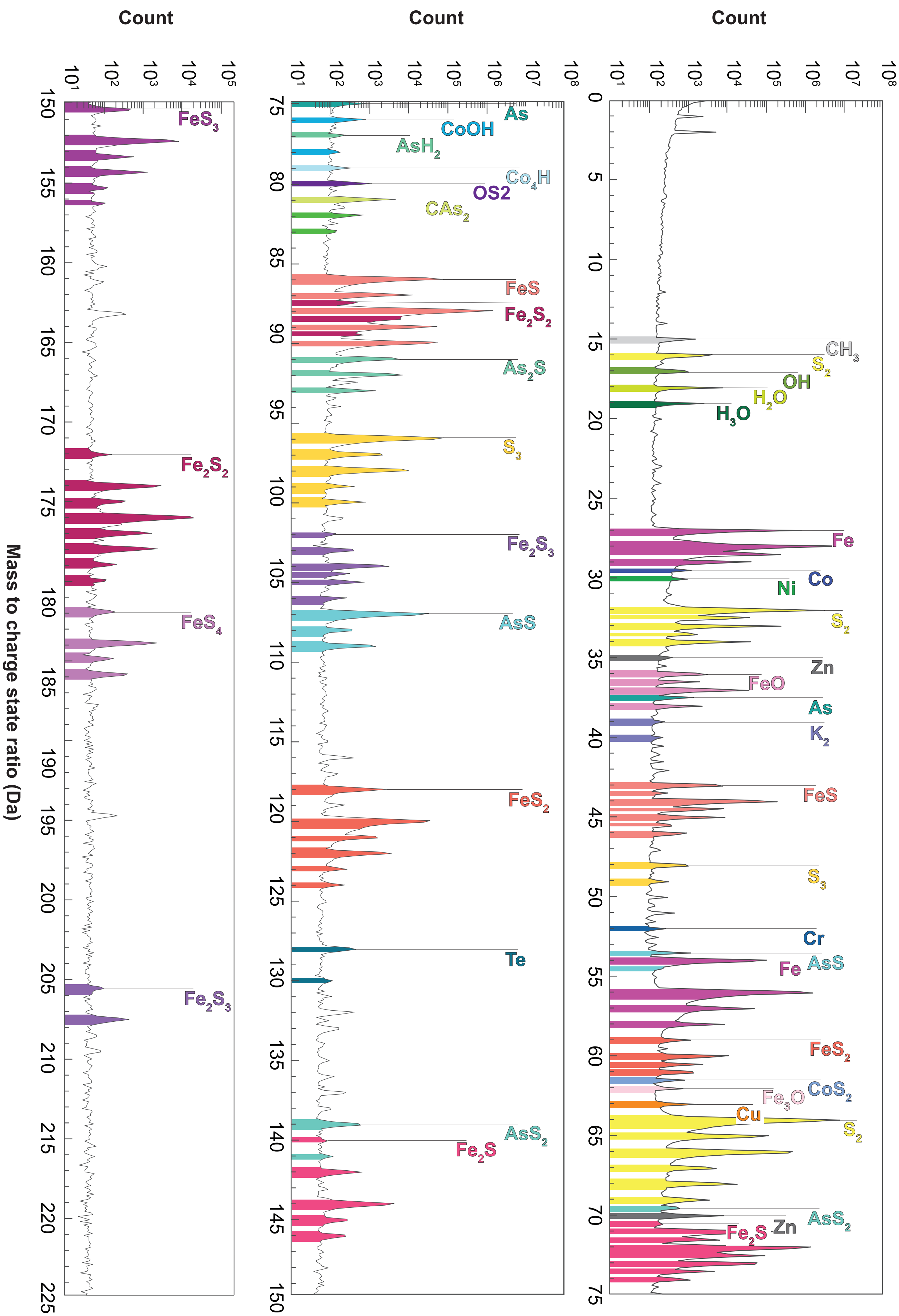

Figure S3.1. Atom probe mass spectrum of pyrite. Representative atom probe microscopy mass spectrum.

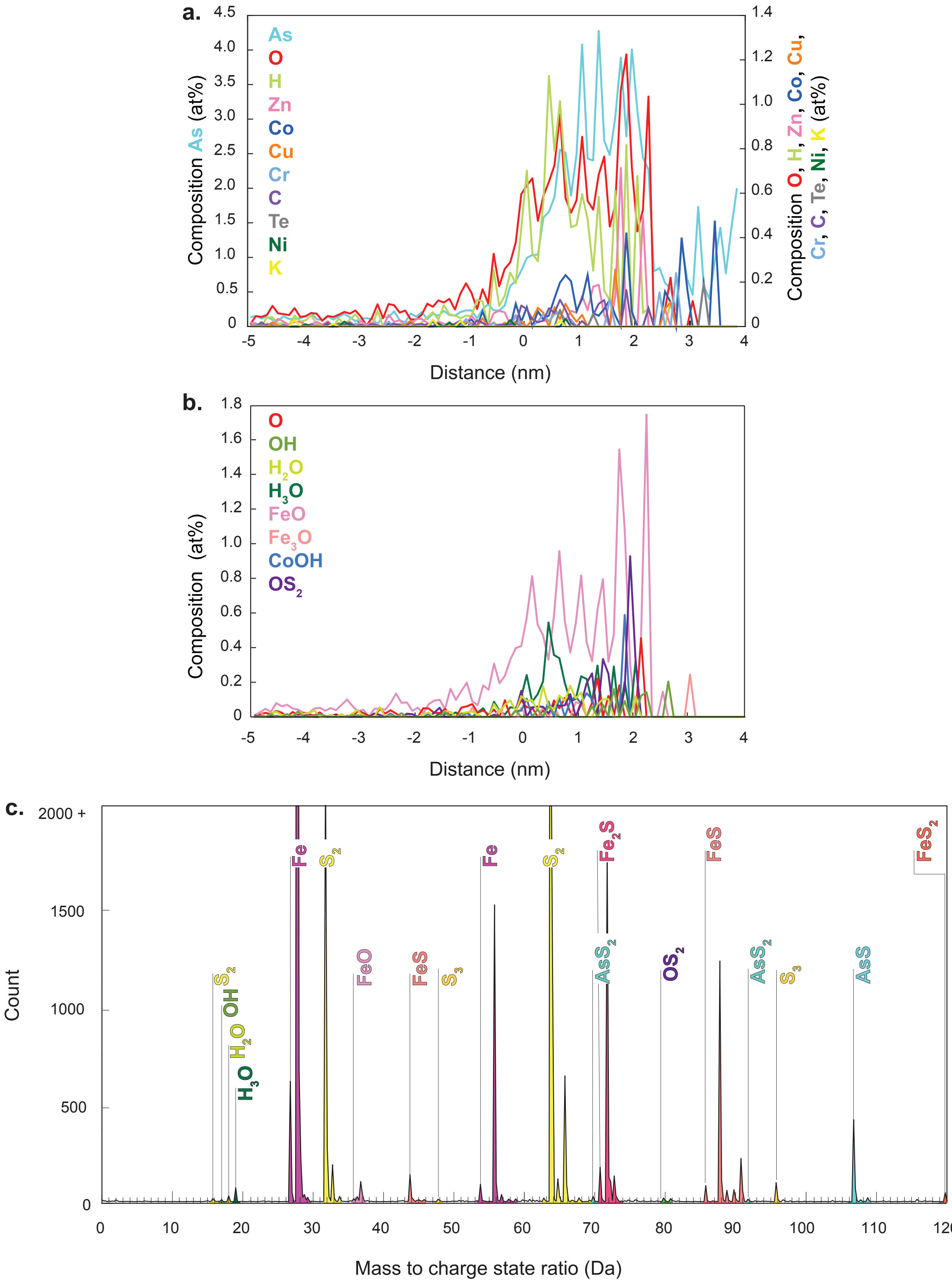

Figure S3.2. **a**. Proxigram of 10 fluid inclusions revealing the elevated composition of trace elements. **b.** Proxigram of 10 fluid inclusions revealing the ionic compositions of O-bearing elements. **c.** Mass spectrum extracted from 10 fluid inclusions.

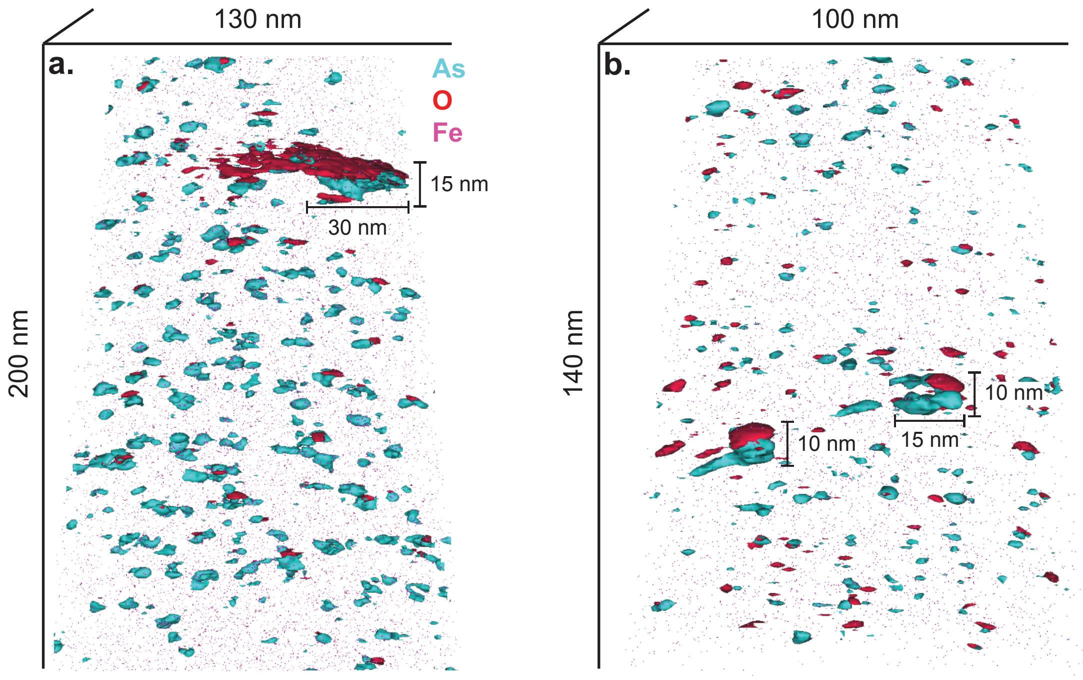

Figure S3.3. a-b. Reconstruction of APT specimens displaying the distribution on Fe ions (pink dots) and As (turquoise isosurfaces; 1.53 (**a.**) and 1.96 (**b.**) at% isovalue) and O compositions (red isosurfaces; 1.37 (**a.**) and 1.68 (**b.**) at% isovalue), revealing a grain boundary and other high-density features.

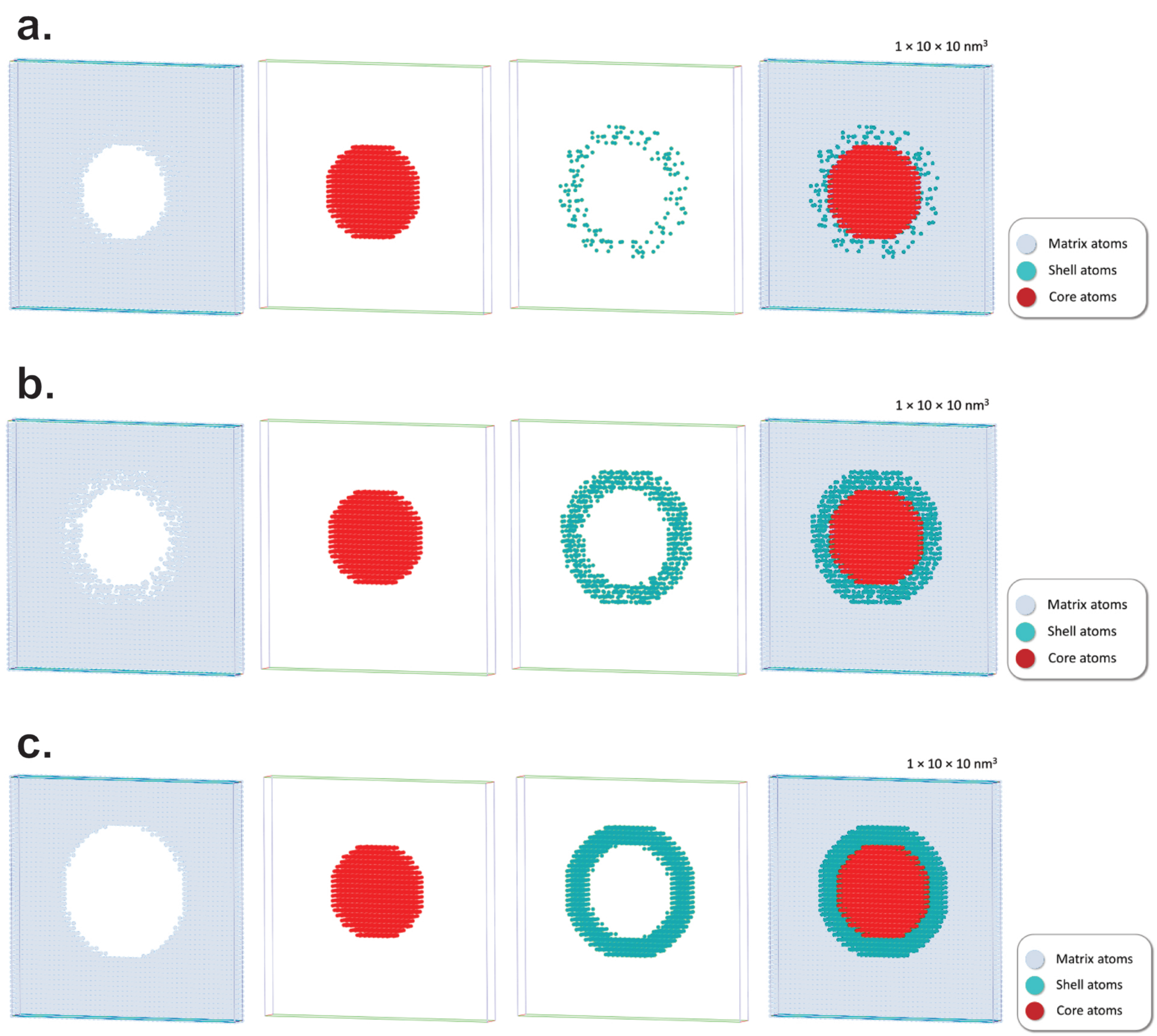

Figure S3.4. Simulated core-shell particle embedded in a pure matrix (in blue). The particle core is also pure (in red). The shell is composed of two elements: shell atoms (in green) and matrix ones, with a varying composition in shell atoms of XS (matrix atoms are in balance): **a.** Xs = 10 at %, **b.** XS = 50 at% and **c.** XS = 100 at% (i.e. pure in shell atoms)

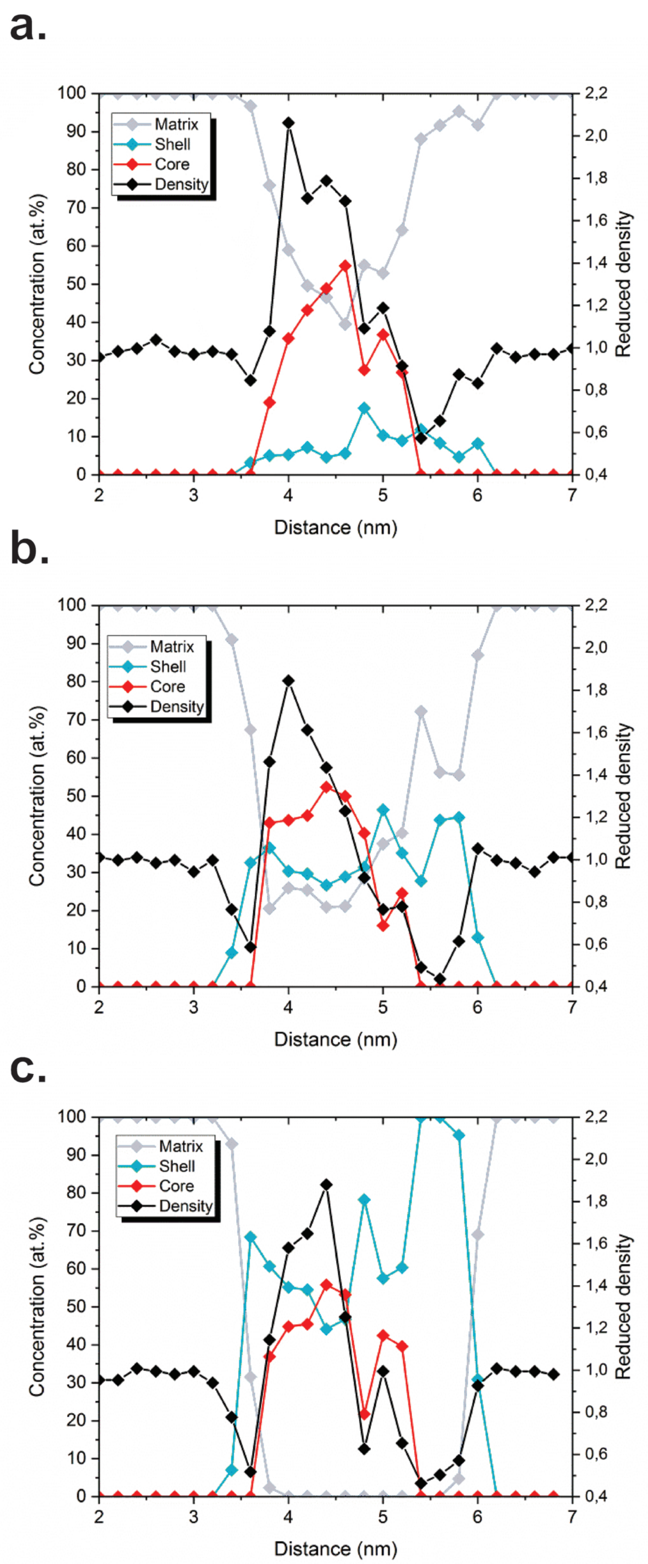

Figure S3.5. Concentration profile after field evaporation simulation through the particle (RS = 9.1%) in the evaporation direction in matrix, shell and core atoms (in at%) and also the reduced density as a function of the shell atoms concentration: **a.** 10, **b.** 50 and **c.** 100 at% (matrix atoms are in balance).

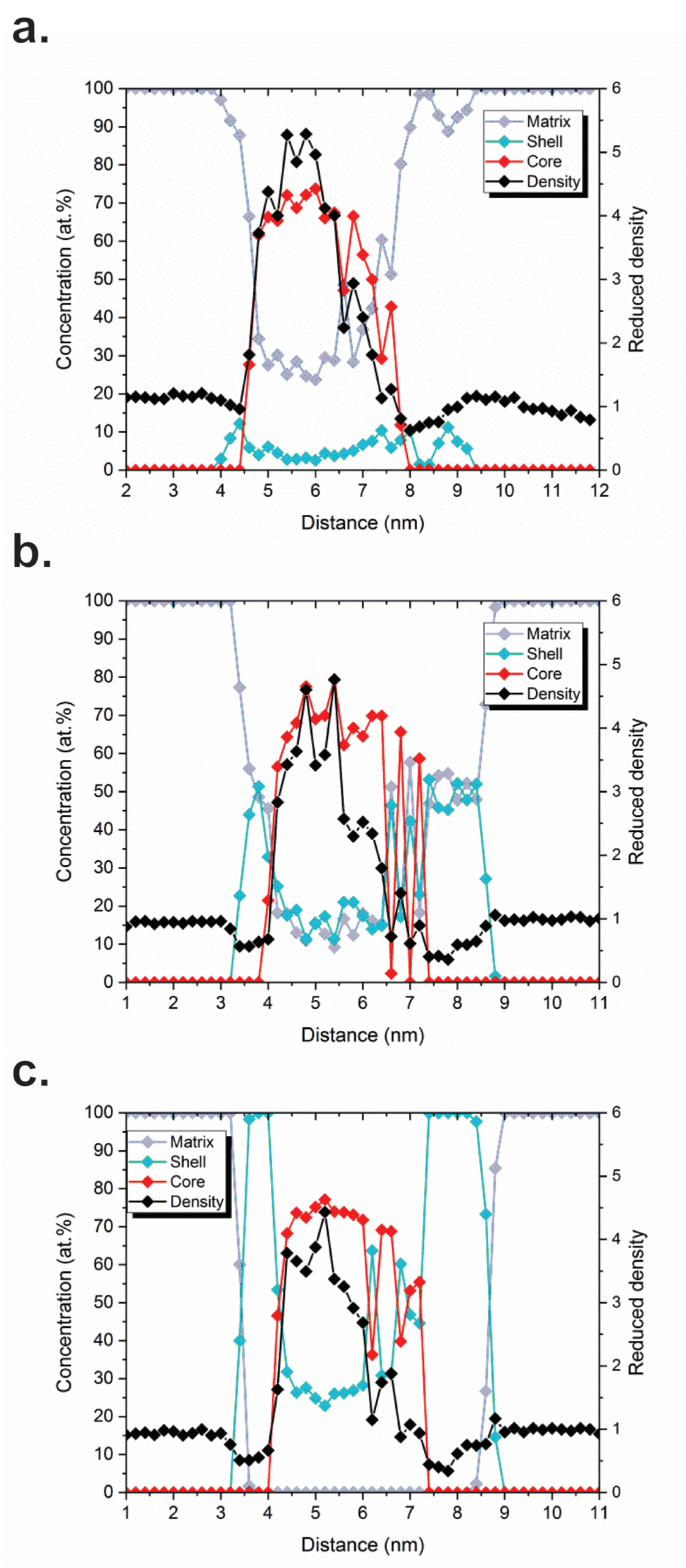

Figure S3.6. Concentration profile after field evaporation simulation through the particle (RS = 20.6%) in the evaporation direction in matrix, shell and core atoms (in at%) and also the reduced density as a function of the shell atoms concentration: **a.** 10, **b.** 50 and **c.** 100 at% (matrix atoms are in balance).

APPENDIX C–Supplementary information for chapter 4

Fluid inclusion induced hardening: Nanoscale evidence from naturally deformed pyrite

R. Dubosq[1], A. Rogowitz[2], D.A. Schneider[1], K. Schweinar[3], B. Gault[3,4]

[1]Department of Earth and Environmental Sciences, University of Ottawa, Canada

[2]Department of Geodynamics and Sedimentology, University of Vienna, Austria

[3]Max-Planck-Institut für Eisenforschung GmbH, Germany

[4]Department of Materials, Royal School of Mines, Imperial College London, UK

Table S4.1. Atom Probe Tomography Data Acquisition Settings and Data Summary

Specimen/Data Set	**Specimen i**	**Specimen ii**
Instrument Model	LEAP 5000 XR	LEAP 5000 XR
Instrument settings		
Laser wavelength (nm)	355	355
Laser pulse energy (pJ)	45	45
Voltage pulse fraction (%)	n.a.	n.a.
Pulse frequency (kHz)	125	125
Evaporation control	detection rate	detection rate
Target detection rate (ions/pulse)	0.01	0.01
Nominal flight path (mm)	382	382
Set point temperature (K)	55	55
Chamber pressure (Torr)	4.00E-11	3.80E-11
Data summary		
LAS root version	15.43.393	15.43.393
CAMECAROOT version	18.46.428	18.46.428
Analysis software	IVAS 3.8.2	IVAS 3.8.2
Total ions:	1.88E+07	43561686
Single (%)	61.1	57.9
Multiple (%)	35	39.8
Partial (%)	3.9	2.4
Reconstructed ions:		
Ranged (%)	90.8	97
Unranged (%)	9.2	3
Volt./bowl corr. peak (Da)	32	32
Mass calib. (peaks/interp.)	5/Lin.	5/Lin.
$(M/\Delta M)$ for ^{56}Fe	1026.2	1141.9
$(M/\Delta M_{10})$	200	225.1
Time-independent background (ppm/ns)	2.3	1.7
Reconstruction		
Final specimen state	fractured	fractured
Pre-/post-analysis imaging	SEM/n.a	SEM/n.a
Radius evolution model	voltage	voltage
Field factor (k)	3.3	3.3
Image compression factor	1.5	1.5
Assumed E-field (V/nm)	33	33
Detector efficiency (%)	52	52
Avg. atomic volume (nm^3)	species specific volume used (see range file)	
V initial; V final (V)	2153; 4162	1145; 5837

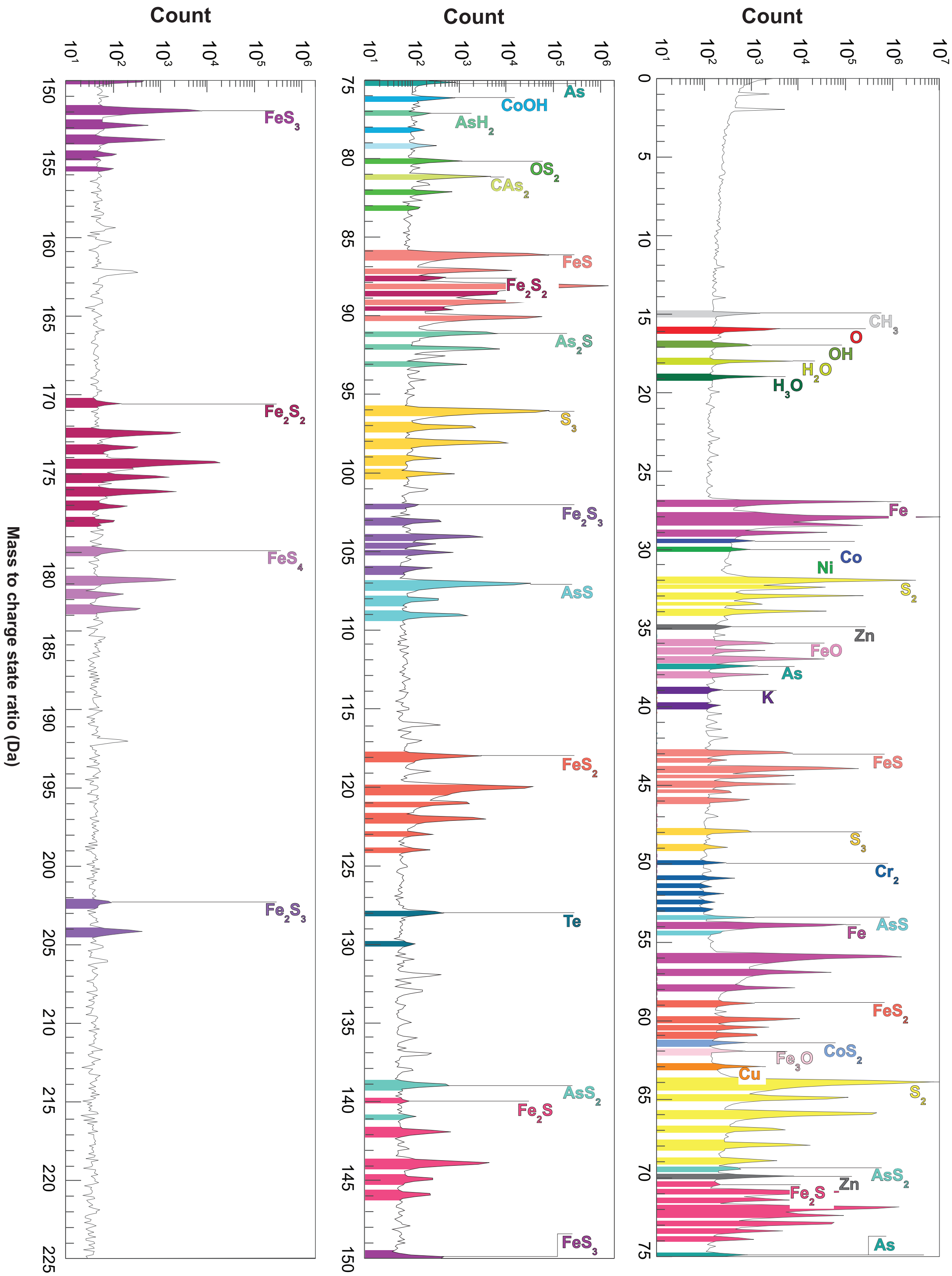

Figure S4.1. Atom probe mass spectrum of pyrite. Representative atom probe microscopy mass spectrum

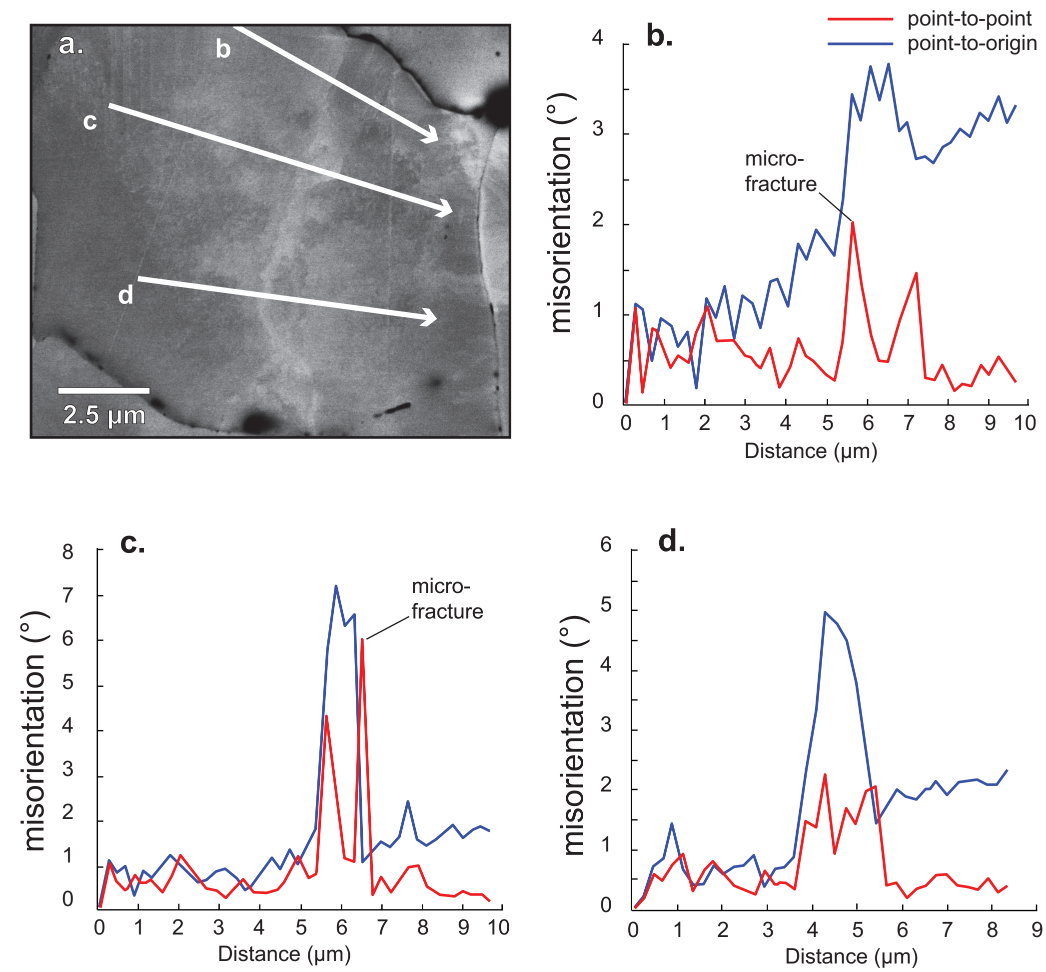

Figure S4.2. a. ECC image of the pyrite grain showing the orientation of the misorientation profiles (white arrows). **b-d.** misorientation profiles across pyrite grain revealing crystal plasticity in the form of linear misorientation related to microfracturing.

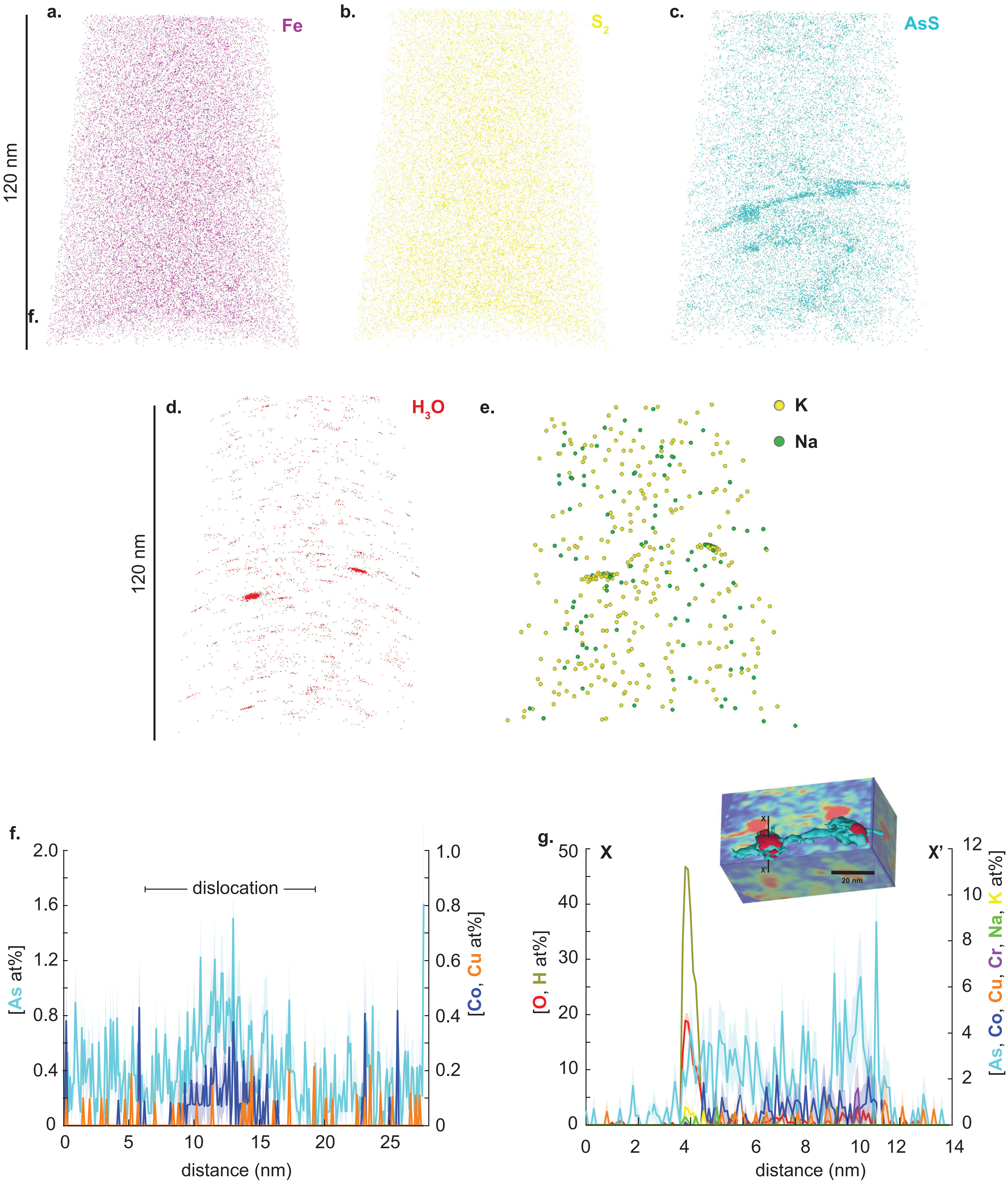

a.
Fe
b.
S_2
c.
AsS
120 nm
f.
d.
H_3O
120 nm
e.
K
Na
f.
dislocation
[As at%]
[Co, Cu at%]
distance (nm)
g.
X
X'
[O, H at%]
[As, Co, Cu, Cr, Na, K at%]
distance (nm)
20 nm

Figure S4.3. a-e. Reconstruction of APT specimen i displaying the homogeneous distribution of Fe and S_2 ions and the clustering of AsS, H_3O, Na and K ions. **f.** Composition profile across the dislocation in APT specimen i showing a significant increase of As and minor increase in Co and Cu within the feature. **g.** Composition profile across a high-density feature (X-X') within APT specimen i revealing a narrow peak of O and H followed by a wider band of elevated As, Co, Cu, Cr, Na, and K compositions in the order of evaporation.

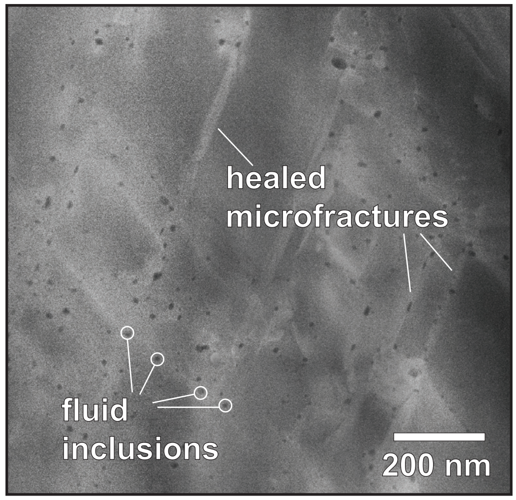

Figure S4.4. High-angle annular dark field STEM images of pyrite grain adjacent to APT specimens showing healed microfractures linked to nanovoids (fluid inclusions). Microfractures are visible at sharp straight line segments with a grayscale gradient on one side.

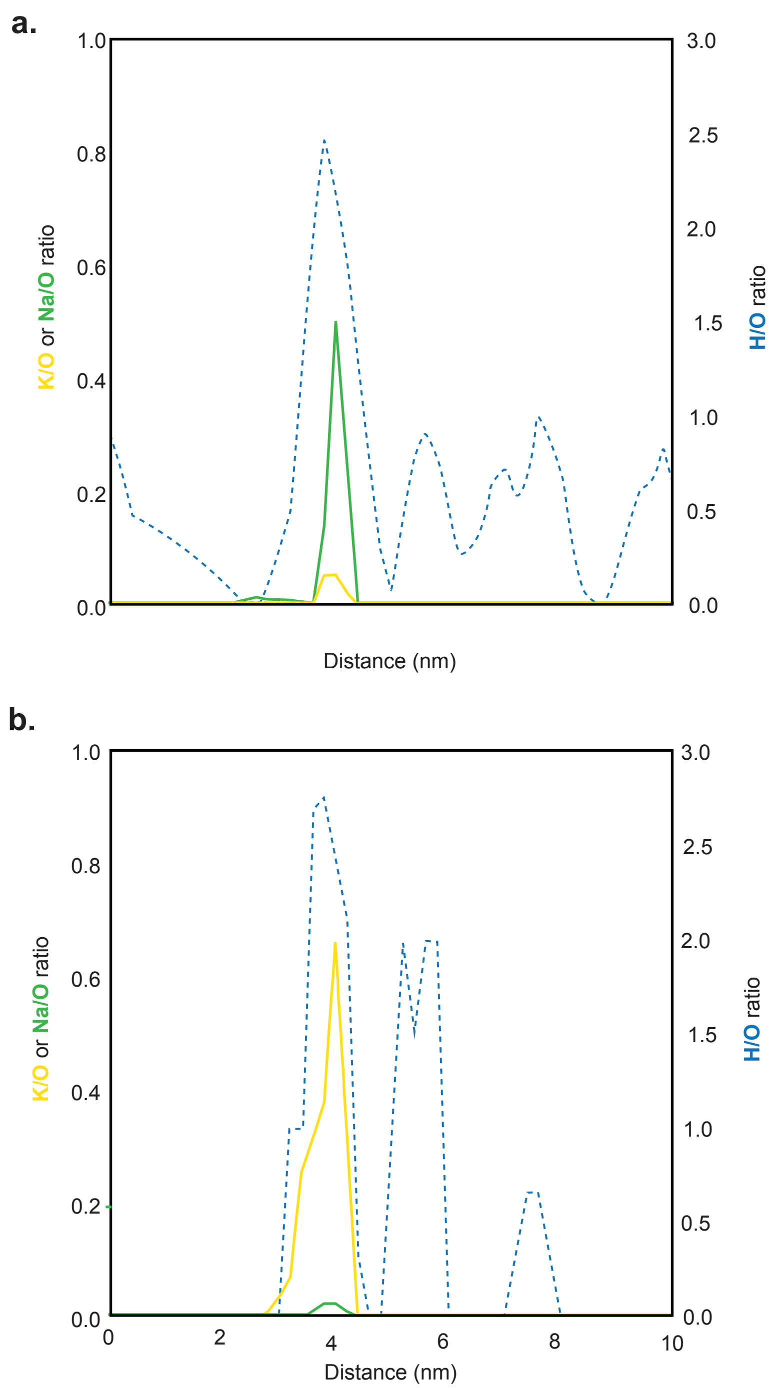

Figure S4.5. a. and **b.** profiles of the Na/O, K/O, and H/O ratios across 2 large fluid inclusions.

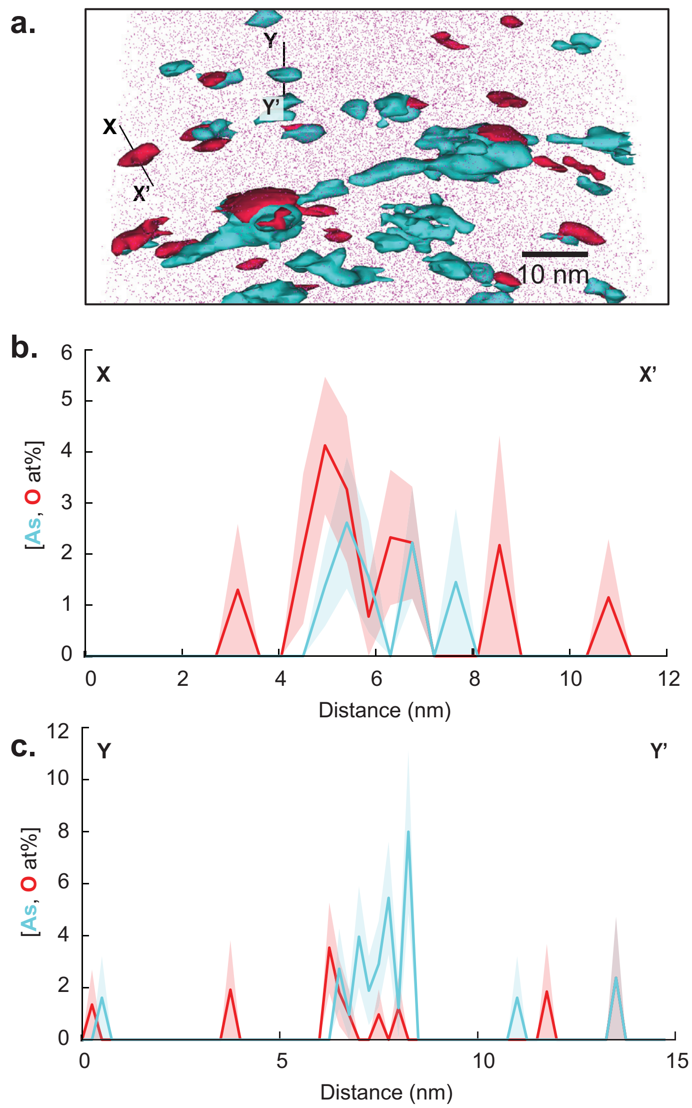

Figure S4.6. a. Close-up of the reconstruction of APT specimen 'i' presented in Fig. 2a displaying the orientation of the composition profiles shown in **b.** and **c. b-c.** Composition profiles across apparent O-rich (**b.**) and As-rich (**c.**) clusters revealing both As and O peaks for each cluster.

APPENDIX D–Supplementary information for chapter 5

Bubbles and atom clusters in rock melts: a chicken and egg problem

R. Dubosq[1], D.A. Schneider[1], X. Zhou[2], B. Gault[2,3], B. Langelier[4], P. Pleše[1]

[1]Department of Earth and Environmental Sciences, University of Ottawa, Ottawa, Canada

[2]Max-Planck-Institut für Eisenforschung GmbH, Düsseldorf, Germany

[3]Department of Materials, Royal School of Mines, Imperial College London, London, UK

[4]Canadian Centre for Electron Microscopy, McMaster University, Hamilton, Canada

Table S5.1. Atom Probe Tomography Data Acquisition Settings and Data Summary

Specimen/Data set	**Specimen i**	**Specimen ii**
Instrument Model	LEAP 4000 XR	LEAP 5000 XR
Instrument settings		
Laser wavelength (nm)	355	355
Laser pulse energy (pJ)	300	400
Voltage pulse fraction (%)	n.a.	n.a.
Pulse frequency (kHz)	200	200
Evaporation control	detection rate	detection rate
Target detection rate (ions/pulse)	0.003	0.001
Nominal flight path (mm)	382	382
Set point temperature (K)	59.6	55
Chamber pressure (Torr)	3.40E-11	5.10E-11
Data summary		
LAS root version	15.41.342j	18.46.533
CAMECAROOT version	18.46.452d	18.46.533
Analysis software	IVAS 3.8.4	IVAS 3.8.4
Total ions:	52802782	14499953
Single (%)	73.6	77.0
Multiple (%)	25.5	20.9
Partial (%)	0.9	2.0
Reconstructed ions:	31658925	13905181
Ranged (%)	96.0	51.2
Unranged (%)	4.0	48.8
Volt./bowl corr. peak (Da)	16	16
Mass calib. (peaks/interp.)	5/Lin.	5/Lin.
($M/\Delta M$)	965.7	772.3
($M/\Delta M_{10}$)	452.6	417.9
Time-independent background (ppm/ns)	93	112.56
Reconstruction		
Final specimen state	intact	intact
Pre-/post-analysis imaging	SEM/n.a	SEM/n.a
Radius evolution model	tip profile	tip profile
Field factor (k)	3.3	3.3
Image compression factor	1.65	1.65
Assumed E-field (V/nm)	33	15
Detector efficiency (%)	36	52
Avg. atomic volume (nm^3)	species specific volume used (see range file)	
Vinitial; Vfinal (V)	2840; 3580	2000; 3200

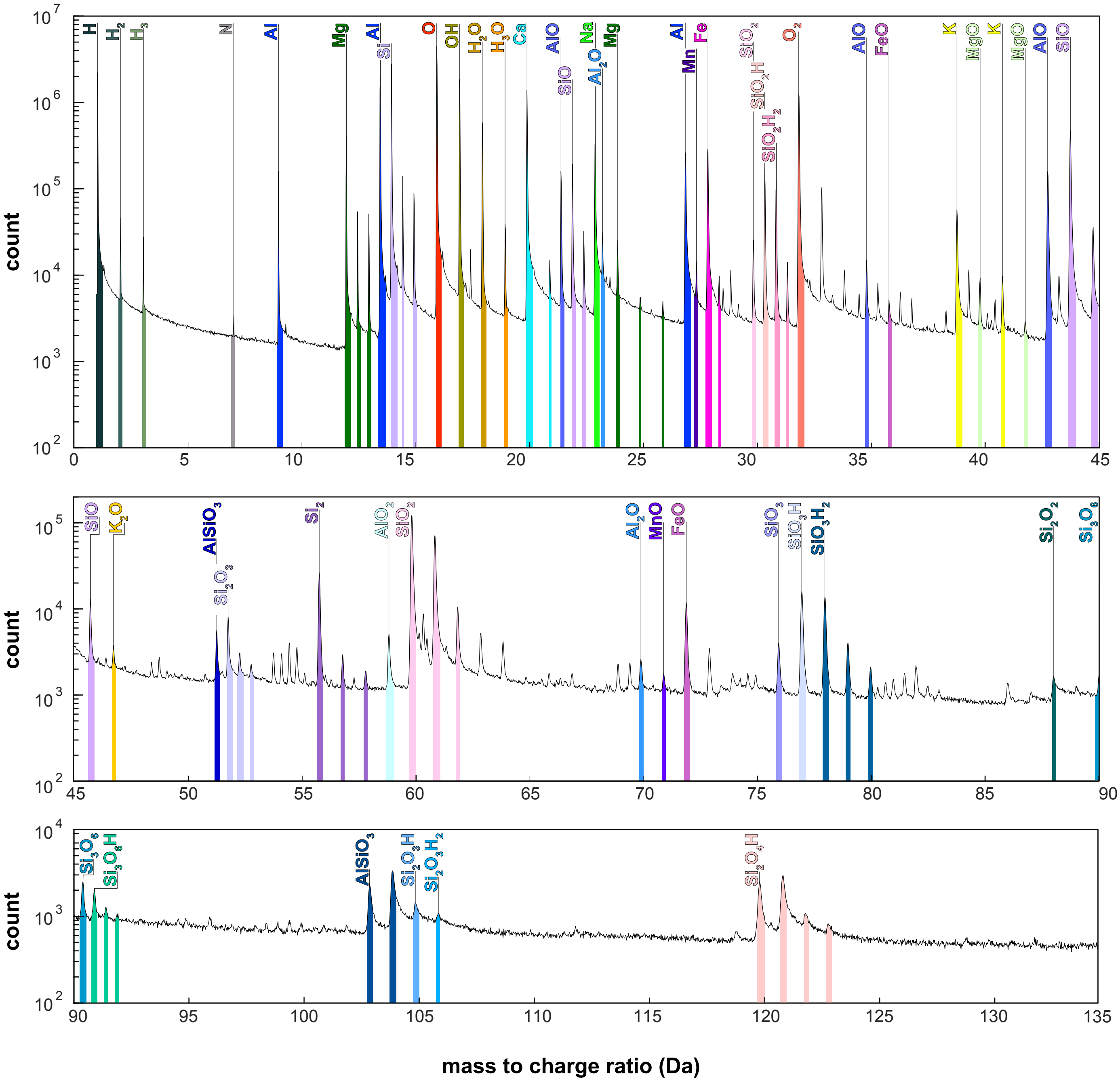

Figure S5.1. Atom probe mass spectrum of andesitic rock melt.

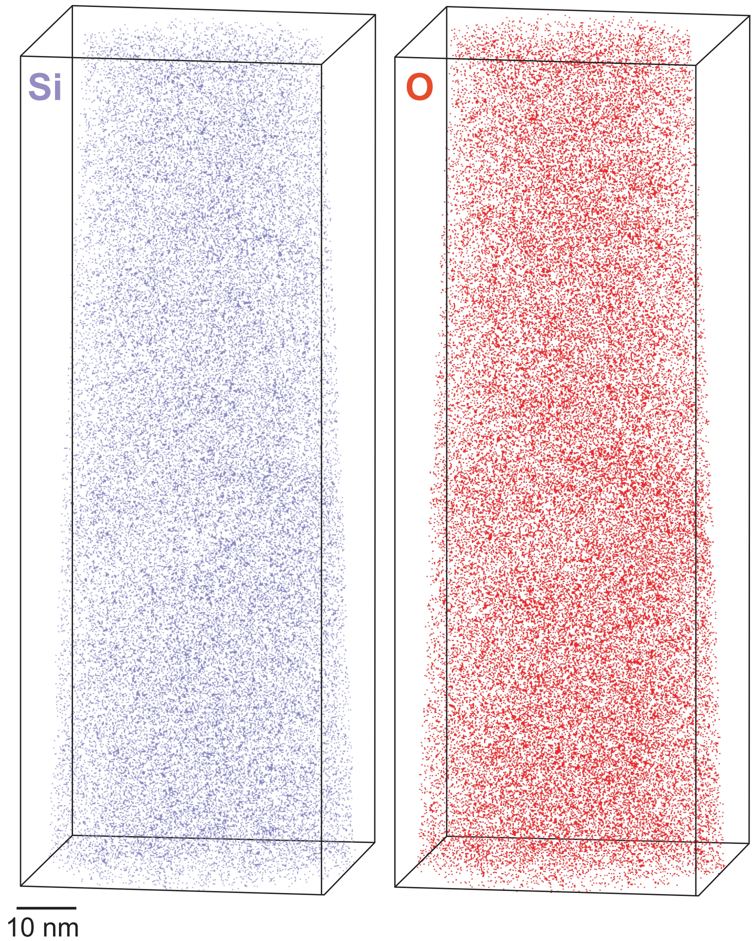

Figure S5.2. 3D reconstruction of APT specimen i showing the homogeneous distribution of Si and O atoms.

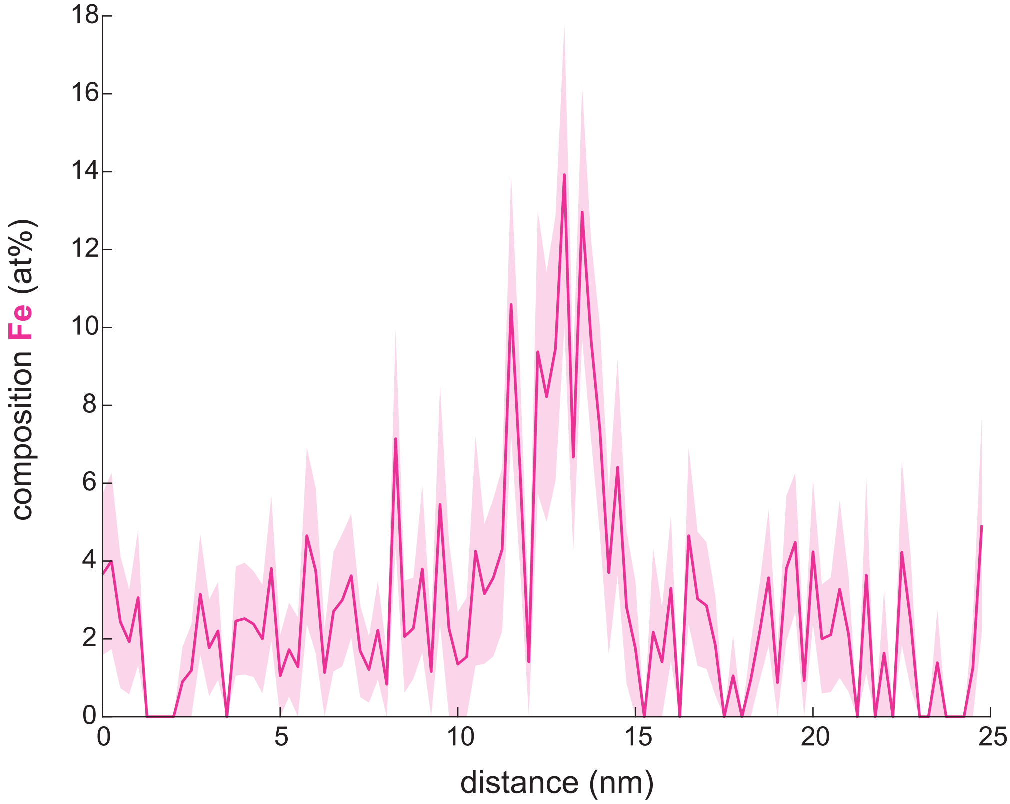

Figure S5.3. Composition profile across a Fe cluster from specimen i.

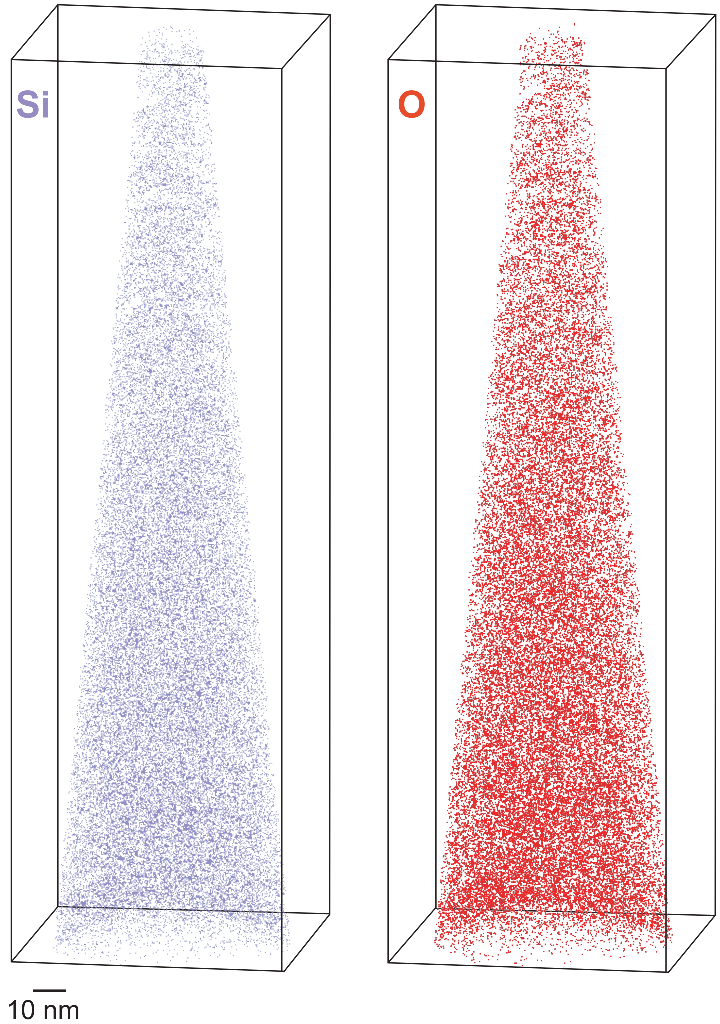

Figure S5.4. 3D reconstruction of APT specimen ii showing the homogeneous distribution of Si and O atoms.

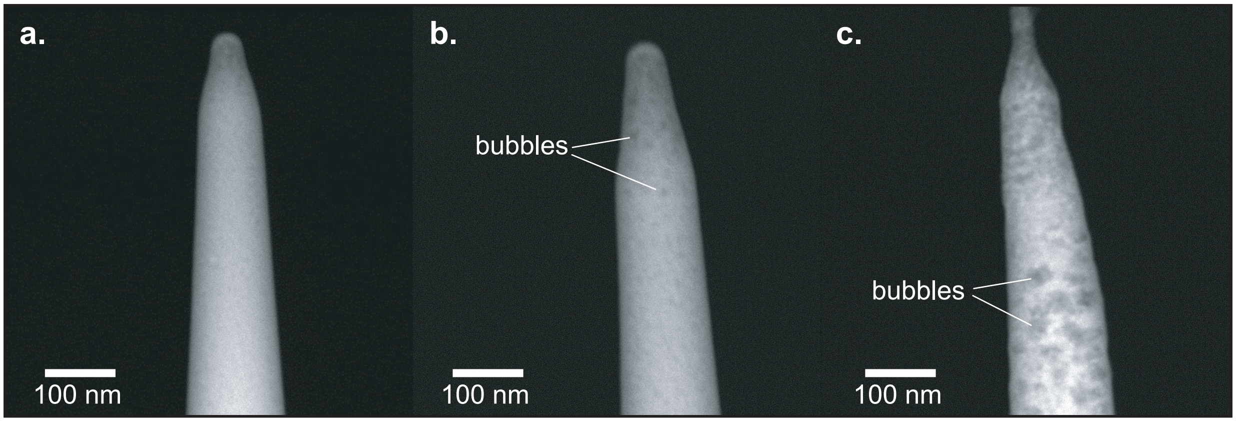

Figure S5.5. HAADF STEM images of andesitic rock melt specimens showing light **(**a**)**, moderate **(**b**)**, and heavy **(c)** beam damage from the room temperature FIB ion milling process and subsequent STEM imaging**.**